

**A scanning ion conductance microscopy assay  
to investigate interactions between  
cell penetrating peptides and  
pore-suspending lipid membranes**

Dissertation

for the award of the degree

“Doctor rerum naturalium”

of the Georg-August-Universität Göttingen

within the doctoral program: Physics of Biological and Complex Systems

of the Georg-August University School of Science (GAUSS)

submitted by

**Christoph Saßen**

from Viersen

Göttingen 2013

**THESIS COMMITTEE**

Prof. Dr. Claudia Steinem

Institute for Organic and Biomolecular Chemistry, Georg-August Universität Göttingen

Prof. Dr. Ulf Diederichsen

Institute for Organic and Biomolecular Chemistry, Georg-August Universität Göttingen

Dr. Iwan Schaap

Third Institute of Physics, Georg-August Universität Göttingen

**MEMBERS OF THE EXAMINATION BOARD**

Referee: Prof. Dr. Claudia Steinem

Institute for Organic and Biomolecular Chemistry, Georg-August Universität Göttingen

2<sup>nd</sup> Referee: Prof. Dr. Ulf Diederichsen

Institute for Organic and Biomolecular Chemistry, Georg-August Universität Göttingen

**FURTHER MEMBERS OF THE EXAMINATION BOARD**

Dr. Iwan Schaap

Third Institute of Physics, Georg-August Universität Göttingen

Prof. Dr. Martin Suhm,

Institute for Physical Chemistry, Georg-August Universität Göttingen

Prof. Dr. Michael Meinecke

European Neuroscience Institute, Georg-August-Universität Göttingen

Prof. Dr. Kai Tittmann

Albrecht-von-Haller-Institute for Plant Sciences, Georg-August-Universität Göttingen

DATE OF ORAL EXAMINATION:

22 October 2013

I, Christoph Saßen, hereby certify that my doctoral thesis entitled “A scanning ion conductance microscopy assay to investigate interactions between cell penetrating peptides and pore-suspending lipid membranes” has been written independently and with no other sources and aids than quoted.

Göttingen, 2013

---

Christoph Saßen



*Meiner Familie*

*Ueberall, wo man sich ganz sicher fühlt,  
hat der Zustand schon etwas Verdächtiges,  
denn da weiß man Etwas gewiß, also Etwas, was schon da ist,  
wird nur gehandhabt, wird wiederholt angewendet.  
Dies ist schon eine halb todtte Lebendigkeit.*

Karl Friedrich Schinkel



**ABSTRACT** Scanning ion conductance microscopy (SICM) provides a technique for the investigation of surface topography as well as the local ion conductance of a surface without any mechanical contact between probe and sample. This avoidance of interaction is particularly advantageous for the examination of highly flexible structures such as lipid membranes, e.g. living cells or artificial membranes. Pore-suspending membranes (PSMs) as a model system combine high stability with close mimicking of natural structures with respect to lateral mobility and the existence of aqueous compartments on both sides of the bilayer. A major field of research focuses on the interaction of lipids or other membrane constituents with peptides, in recent years notably cell penetrating peptides (CPPs). Among most prominent examples are melittin as the major venom component of the honey bee *Apis mellifera* and penetratin as the third helix of the *Drosophila melanogaster* Antennapedia homeodomain.

Generalised protocols for the preparation of solvent-free PSMs are reported. Giant unilamellar vesicles (GUVs) of various lipid compositions were spread on porous silicon nitride ( $\text{Si}_3\text{N}_4$ ) substrates which had been functionalised with cholesteryl polyethylenoxy thiol (CPEO3, hydrophobically) or with mercaptoethanol (ME, hydrophilically). Lipid compositions comprised purely zwitterionic phosphatidylcholine (PC) lipids as well as mixtures of PC lipids with cholesterol and PC lipids with phosphatidylserine (PS) lipids. Successful spreading was proven by means of confocal laser scanning microscopy (CLSM) and SICM imaging.

The main part of this thesis dealt with the development and application of CPP titration assays based on both the CLSM and SICM techniques aiming at the elucidation of the influence of substrate functionalisation and membrane composition on interactions of melittin and penetratin with PSMs. The CLSM assay was performed with melittin on PSMs of every lipid composition on both hydrophobically and hydrophilically functionalised substrates and with penetratin on PSMs of every lipid composition on hydrophilically functionalised substrates. Rupturing of bilayers on hydrophilically functionalised substrates was observed at comparable concentrations of 1–3  $\mu\text{M}$  for both peptides. Comparison of experiments on hydrophilically and hydrophobically functionalised substrates reveals three times higher melittin concentrations in the former case. On both functionalisation types, a cholesterol content of 10% resulted in an increase in melittin concentration sufficient for membrane rupturing, while 20% PS lipids resulted in a decrease. SICM experiments were performed with melittin on PC/cholesterol PSMs on hydrophobically and on hydrophilically functionalised substrates as well as with pure PC PSMs on hydrophilically functionalised substrates. There was not any significant difference found for membrane rupturing inducing peptide concentrations. These were of the same order as found in CLSM experiments. Prior to rupturing, an increase in pore depth hinting at an increase in membrane permeability was observed.

ZUSAMMENFASSUNG Die Rasterionenleitfähigkeitsmikroskopie (*scanning ion conductance microscopy, SICM*) stellt eine kontaktfreie Methode zur Ermittlung sowohl der Topographie als auch lokalen Ionenleitfähigkeit einer Oberfläche dar. Besonders vorteilhaft ist die Vermeidung mechanischer Beeinflussung bei der Untersuchung flexibler Strukturen, z.B. Lipiddoppelschichten wie Zellen oder künstlich erzeugter Lipidmembranen. Porenüberspannende Membranen (*pore-suspending membranes, PSMs*) verbinden als ein Beispiel für Modellsysteme eine hohe Stabilität mit lateraler Mobilität und dem Vorhandensein wässriger Kompartimente ober- und unterhalb der Doppelschicht, wie sie auch in der Natur gefunden werden. Ein wichtiges Forschungsgebiet stellt die Untersuchung der Wechselwirkung von Peptiden, besonders zellpenetrierenden Peptiden (*cell penetrating peptides, CPPs*), mit Lipiden und anderen Membranbestandteilen dar. Häufig untersuchte Beispiele sind Melittin, Hauptbestandteil des Giftes der Honigbiene *Apis mellifera*, sowie Penetratin, dritte Helix der Antennapedia Homöodomäne von *Drosophila melanogaster*.

Generalisierte Protokolle zur Herstellung lösungsmittelfreier *PSMs* werden vorgestellt. Riesige unilamellare Vesikel (*giant unilamellar vesicles, GUVs*) unterschiedlicher Lipidzusammensetzung wurden hierzu auf porösem Siliziumnitrid ( $\text{Si}_3\text{N}_4$ ), welches mit Cholesterylpolyethylenoxythiol (CPEO3, hydrophob) bzw. Mercaptoethanol (ME, hydrophil) funktionalisiert worden war, gespreitet. Verwendet wurden *GUVs* aus reinen Phosphatidylcholin (PC)-Lipiden sowie aus Mischungen von PC-Lipiden mit Cholesterol und PC-Lipiden mit Phosphatidylserin (PS)-Lipiden. Der Erfolg des Spreitvorgangs wurde durch Abbilden mittels konfokaler Rasterlasermikroskopie (*confocal laser scanning microscopy, CLSM*) und *SICM* verifiziert.

Der Hauptteil dieser Arbeit behandelte die Entwicklung und Anwendung *CLSM*- und *SICM*-basierter *CPP*-Titrationsassays zur Aufklärung des Einflusses der Substratfunktionalisierung und der Lipidzusammensetzung der Membranen auf die Wechselwirkung zwischen Melittin bzw. Penetratin und den Lipiddoppelschichten. *CLSM*-Experimente wurden mit Melittin auf allen zur Verfügung stehenden *PSMs* sowohl auf hydrophob als auch hydrophil funktionalisierten Substraten durchgeführt, während Penetratin auf den drei unterschiedlichen *PSMs* auf hydrophil funktionalisierten Substraten verwendet wurde. Ein Reißen der Membranen wurde im Fall hydrophil funktionalisierter Substrate für beide Peptide im Bereich von 1–3  $\mu\text{m}$  beobachtet. Bei hydrophob funktionalisierten Substraten induzierte eine dreifach geringere Melittinkonzentration die Zerstörung der Membranen. Sowohl auf hydrophob als auch auf hydrophil funktionalisierten Substraten wurde bei einem Cholesterolanteil von 10% eine Erhöhung der zum Reißen notwendigen Melittinkonzentration erhalten, während bei 20% PS-Anteil eine Verschiebung zu geringeren Konzentrationen evident wurde. *SICM*-Experimente wurden mit Melittin auf PC/Cholesterol-*PSMs* auf hydrophob und hydrophil funktionalisierten Substraten und mit reinen PC-*PSMs* auf hydrophil funktionalisierten Membranen durchgeführt. Es wurden keine signifikanten Konzentrationsunterschiede beobachtet; die gefundenen Konzentrationsbereiche jedoch stimmten mit denen der *CLSM*-Experimente überein. Darüberhinaus wurde vor dem Reißen der Membranen ein Ansteigen der Porentiefe gefunden, das mit einer erhöhten Membranpermeabilität korrespondiert.







# TABLE OF CONTENTS

1	INTRODUCTION .....	1
1.1	Scanning probe microscopy.....	1
1.1.1	Principle .....	2
1.1.2	Advantages.....	2
1.1.3	Disadvantages .....	3
1.2	Scanning ion conductance microscopy (SICM).....	4
1.2.1	Scanning modes .....	4
1.2.2	Resolution.....	9
1.2.3	SICM theoretics .....	10
1.2.4	Hybrid techniques.....	16
1.2.5	A selection of applications .....	18
1.3	Artificial membrane model systems.....	19
1.3.1	Vesicles .....	20
1.3.2	Solid supported membranes.....	21
1.3.3	Black lipid membranes.....	22
1.3.4	Pore-suspending membranes .....	23
1.4	Membrane active peptides .....	24
1.4.1	Mechanisms of cellular uptake .....	25
1.4.2	Melittin.....	27
1.4.3	Penetratin .....	29
2	SCOPE OF THESIS.....	33
3	MATERIALS AND METHODS.....	35
3.1	Materials .....	35
3.1.1	Buffers & solutions.....	35
3.1.2	Lipids, thiols and fluorescent dye.....	35
3.1.3	Peptides.....	37
3.2	Preparative methods .....	38

# TABLE OF CONTENTS

3.2.1	Preparation of giant unilamellar vesicles .....	38
3.2.2	Preparation of pore-suspending membranes .....	39
3.2.3	Preparation of Ag/AgCl electrodes .....	41
3.2.4	Preparation of nanopipettes.....	41
3.3	Analytical methods.....	42
3.3.1	Fluorescence microscopy .....	42
3.3.2	Scanning ion conductance microscopy .....	45
3.3.3	UV/Vis spectroscopy .....	52
3.4	Matlab analysis .....	53
4	RESULTS.....	57
4.1	Investigation of pore-suspending membranes on hydrophobically functionalised substrates.....	58
4.1.1	Establishment of a spreading procedure .....	58
4.1.2	SICM imaging of pore-suspending membranes.....	59
4.1.3	Time frame definition for experiments.....	61
4.1.4	Fluorescence titration experiments .....	63
4.1.5	SICM titration experiments.....	67
4.2	Investigation of pore-suspending membranes on hydrophilically functionalised substrates.....	73
4.2.1	Establishment of a spreading procedure .....	73
4.2.2	SICM imaging of pore-suspending membranes.....	75
4.2.3	Time frame definition for experiments.....	76
4.2.4	Fluorescence titration experiments .....	77
4.2.5	SICM titration experiments.....	82
5	DISCUSSION .....	87
5.1	Assay development .....	87
5.2	Preparation of pore-suspending membranes .....	88
5.3	Imaging of pore-suspending membranes .....	90
5.3.1	CLSM imaging .....	90
5.3.2	SICM imaging .....	90
5.4	CLSM titration experiments.....	94
5.4.1	The influence of lipid composition and substrate functionalisation in melittin experiments.....	94

## TABLE OF CONTENTS

5.4.2 The influence of lipid composition and substrate functionalisation in penetratin experiments.....	99
5.4.3 Comparative discussion of melittin and penetratin titrations with particular consideration of the substrate functionalisation influence.....	101
5.5 SICM titration experiments.....	104
5.5.1 Melittin titrations on DPhPC/chol (9:1) membranes on hydrophobically functionalised substrates.....	104
5.5.2 Melittin titrations on POPC and DPhPC/chol (9:1) membranes on hydrophilically functionalised substrates.....	107
5.6 Comparison of CLSM and SICM titration experiments.....	109
6 SUMMARY OF THESIS.....	113
APPENDIX.....	117
A. Abbreviations.....	117
B. Symbols.....	118
C. Chemicals.....	120
D. Materials.....	121
E. Hardware.....	121
F. Software.....	122
BIBLIOGRAPHY.....	125



# 1 INTRODUCTION

For millennia, humans have strived for understanding of phenomena beyond their borders of vision as becomes obvious at the large scale from prehistoric astronomic sites and calendars around the earth as well as at the small scale from medicinal, physical and alchemistic knowledge gathered by shamans and early natural scientists.

Spectacles, for instance, have been used as tools to enhance vision in Florence since the 13<sup>th</sup> century unerringly and most probably in ancient times in form of water filled goblets as historical texts reveal. Zacharias Jansen developed a compound microscope in the 16<sup>th</sup> century and as the early 17<sup>th</sup> century experienced the advent of high quality lenses his design became evident as superior compared to single lens microscopes by Anton van Leeuwenhoeck [Singer 1914].

In addition to these lens-based microscopies, a variety of imaging techniques based on other phenomena than electromagnetic waves in the ultraviolet/visible (UV/Vis) range has been developed, mainly in the 20<sup>th</sup> century, such as electron microscopy and scanning probe microscopy (SPM).

Structures and features of cells have posed highly interesting research foci for a long time. Investigations have aimed at the elucidation of cell topographies, of membrane compositions and building blocks (lipids, carbohydrates, proteins) and their distribution within membranes. A reductionist approach has led to the development and utilisation of artificial membrane systems since the 1960s, aiming to achieve deeper understanding of particular phenomena and properties. An important branch of studies is the investigation of interactions between membranes and proteins such as ligands corresponding to membrane-embedded receptor molecules or translocating molecules. The utilisation of SPMs allows here for the investigation of changes in membrane characteristics on the nanometre scale induced by membrane affecting proteins.

## 1.1 SCANNING PROBE MICROSCOPY

The family of SPMs was originated in the early 1980s when Binnig and Rohrer developed the scanning tunneling microscope (STM) [Binnig et al. 1982] based on publications on the topographiner by Young et al. ten years before [Young et al. 1971; Young et al. 1972]. Ideas on the visualisation of surface topographies, however, date back to as early as 1929 when the stylus profilometer was developed by Schmalz [Schmalz 1929]. The STM's relevance and footprint within the scientific world was reflected by the Nobel Prize in Physics earned merely half a decade after its development [Binnig and Rohrer 1987].

# INTRODUCTION

In the past 30 years, a great variety of techniques and principles employed for novel scanning probes extended the range of samples subjected to SPM, of tolerated measuring conditions and of resolution limits. SPM studies have thus developed into an important contribution to progress in physics, chemistry, biology and especially interdisciplinary fields. Well over 20 different SPM techniques have been developed to date, the most prominent being the original STM and atomic force microscopy (AFM).

## 1.1.1 PRINCIPLE

The common principle of SPMs displayed in Figure 1.1 is a probe whose position is accurately controlled by means of piezo transducers. The probe geometry and features vary with different SPM techniques and the physical phenomena exploited. As the probe is scanned across the sample, its topography and properties are detected by measuring a parameter  $P$  as function of the probe-sample distance  $z$ . A setpoint  $P_0$  is set for  $P$  by the operator and the probe is kept at a constant  $z$  via a feedback system, which changes the probe's position by means of piezo transducers as soon as  $P \neq P_0$  is detected. These changes, indicating surface deviations from an ideal plane, are translated into the surface topography, which is displayed as a scanning probe micrograph [Mironov 2004].

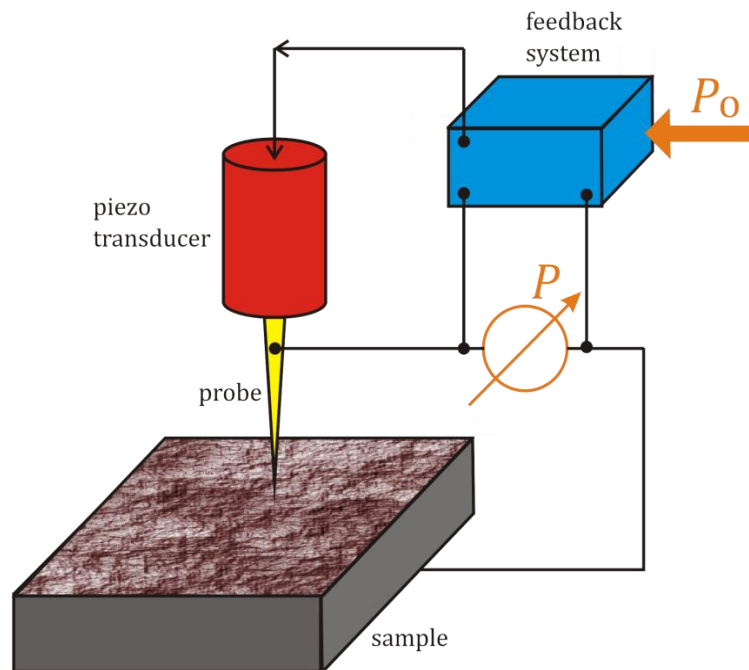


**Figure 1.1: Principle of scanning probe microscopy. The probe is scanned across the sample and measures a probe-sample distance  $z$  dependent parameter  $P$ , which is compared to an operator set value  $P_0$ . Deviations of  $P$  from  $P_0$  cause a change of the probe's vertical position and is interpreted as surface topography (adapted from V. L. Mironov, *Fundamentals of Scanning Probe Microscopy* [Mironov 2004]). Examples for  $P$  are the tunneling current in STM or forces between probe and sample in AFM.**

## 1.1.2 ADVANTAGES

Prior to the development and establishment of SPM as commonly used techniques, electron microscopy techniques such as scanning electron microscopy (SEM) delivered nanometre



resolution images of surface topographies. As electron microscopy (EM) techniques need to be operated under low pressure or vacuum conditions, they are rarely suitable for the investigation of living specimen. Biological samples need to be prepared in order to be visualised by means of EM, but changes of the samples' properties cannot be precluded. These disadvantages of existing high resolution imaging techniques are overcome by several SPM techniques which tolerate or even prefer operation under standard conditions in air or liquid environments.

Another branch of imaging – although not necessarily surface topography imaging – techniques is fluorescence microscopy, which has recently overcome its disadvantageous diffraction limitation in the shape of stimulated emission depletion (STED) and related techniques [Hell and Wichmann 1994; Betzig et al. 2006; Hess et al. 2006; Rust et al. 2006]. The superiority of SPM in comparison to fluorescence microscopy can be found – like in the comparison with EM – in the field of sample preparation. While fluorescence microscopy is well suitable for the investigation of samples in their natural environment, i.e. within cells or whole tissues, a manipulation of the sample is necessary such that attachment of a fluorophore to the investigated entity is inevitable. This kind of interference can be excluded for SPM experiments.

Another interesting feature is the SPMs' potential to manipulate samples by means of sample-probe interactions. While most biophysical investigations will be interested in a lifelike visualisation of the sample's topography, SPM is also well suited for nanolithography experiments [Tseng and Li 2007].

### 1.1.3 DISADVANTAGES

The aforementioned sample-probe interaction is one of the major drawbacks of most SPMs. While piconewton forces being exerted on samples by AFM probes do not pose a severe problem for the investigation of hard surfaces, e.g. in material sciences, they have to be considered a significant alteration of soft samples' features. Scanning electrochemical microscopy (SECM), which avoids mechanical contact between probe and sample, comprises another branch of the SPM family. There are, however, electrochemical interactions with the investigated surface, which may change sample properties as well.

A, with respect to the original purpose of SPM, minor disadvantage is the limitation of systems that can be investigated. As the probe is of a finite volume and needs to be brought into proximity of the investigated entity for any kind of SPM, experiments at solid/solid interfaces are inherently stymied. Liquid/liquid interfaces are subjectable to few SPMs such as SECM which has been used to study ion transfer between immiscible liquids. Similarly, molecule transport across lipid monolayers at a gas/liquid interface has been studied by means of SECM, whereas topographies of such interfaces may be studied by means of scanning ion conductance microscopy (SICM).

# INTRODUCTION

## 1.2 SCANNING ION CONDUCTANCE MICROSCOPY (SICM)

SICM is a 1989 by Hansma and co-workers developed new member of the SPM family [Hansma et al. 1989]. Its basic principle as originally devised is displayed in Figure 1.2. It bears on a nanopipette containing an Ag/AgCl electrode scanning over the investigated insulating surface, which is covered by an electrolyte solution. An ion current is constituted between the electrode inside the pipette and another in the bath surrounding sample and pipette. This ion current is highly dependent on the pipette tip-sample distance in a distance regime resembling the inner diameter of the pipette. Using the ion current as a feedback signal, adjustment of the pipette's z position is converted into topographic information, while the pipette is scanned in x and y directions. Despite the promising potential revealed in the first publications in the late 1980s [Hansma et al. 1989; Prater et al. 1991] (Fig. 1.3 A)), further development of the technique itself and applications to more complex or even biological samples were published slowly, starting in the late 1990s only [Proksch et al. 1996; Korchev et al. 1997a; Korchev et al. 1997b; Zhang et al. 1999] (Fig. 1.3 B)).

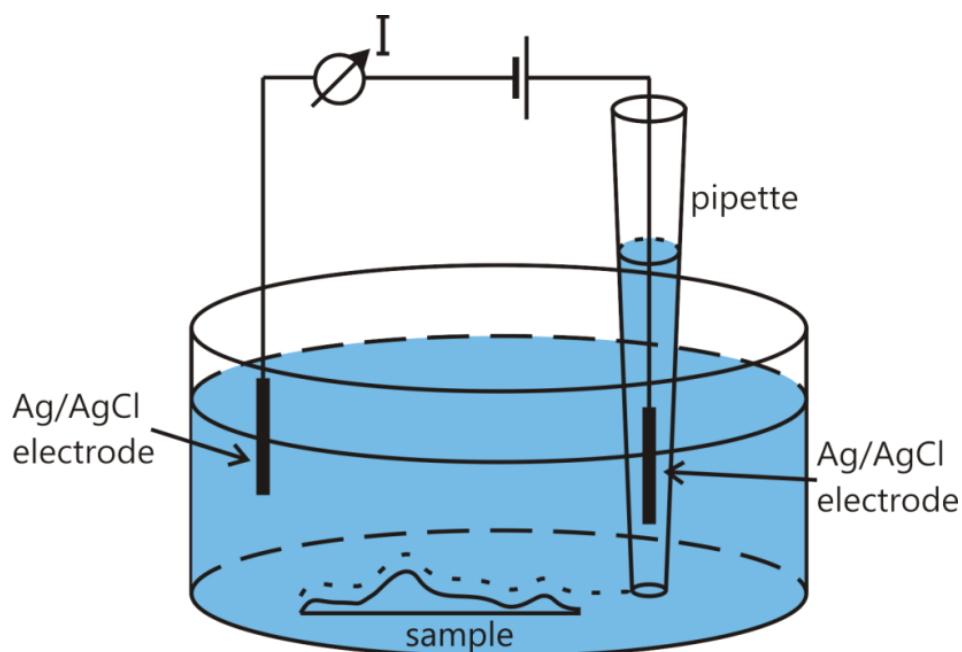


**Figure 1.2: Schematic SICM as developed by Hansma et al. [Hansma et al. 1989; Mironov 2004]. The pipette is kept at a constant distance to the insulating surface and thus follows the sample's contours, imaging its topography.**

### 1.2.1 SCANNING MODES

The original SICM as presented by Hansma et al. is operated in what is in retrospect called the nonmodulated mode. A later innovation involves a short vertical oscillation of the probe, which is referred to as the distance-modulated mode. A further development in this direction is the institution of the hopping mode (also backstep or standing approach mode), where the pipette performs a larger vertical movement. As this comes at the expense of imaging velocity, a fast SICM mode has been developed recently.

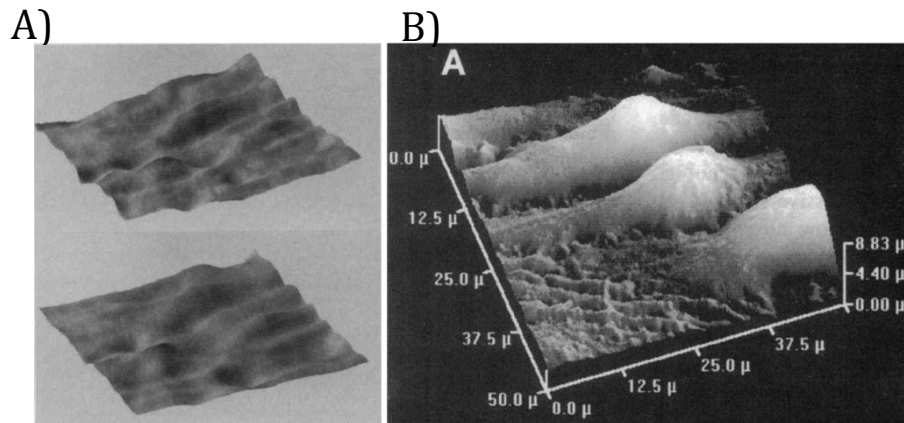


Figure 1.3: Early SICM images. A) First published SIC micrographs. A comparison of two  $(4 \times 4) \mu\text{m}^2$  topography images of an acetate film to demonstrate pipette tips not damaging samples [Hansma et al. 1989]. B) SICM image of living murine melanocyte line melan-b from one of the first publications in the late 1990s [Korchev et al. 1997b].

### Nonmodulated mode

The nonmodulated mode is operated in analogy to AFM's contact mode (constant force): a constant voltage is applied between the two electrodes in the bath solution and the pipette. While the pipette is scanned across the sample, the direct current (dc) is used for feedback control as shown in Figure 1.4, which displays the dependence of the measured current  $I_{dc}$  of the pipette-surface distance  $z$  calculated after Nitz et al. [Nitz et al. 1998] (equation [1.20], cf. Ch. 1.2.3).  $I_{dc}$  is constantly equal to a maximum value  $I_{dc,sat}$  over a wide range of  $z$ . Only at short distances, i.e. small  $z$  values, the ion flow through the pipette tip is stymied. This significant decrease in dc is utilised for the feedback control mechanism such that  $z$  is kept constant via keeping  $I_{dc}$  constant at a specific value below  $I_{dc,sat}$ .

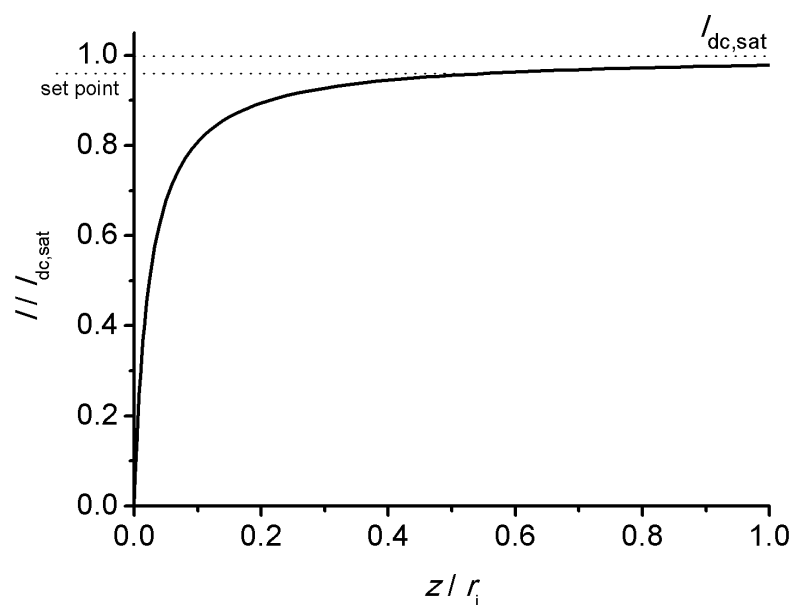


Figure 1.4: A typical current/distance ( $I/z$ ) curve as calculated from equation [1.20] (cf. Ch. 1.2.3). Values inserted are:  $r_0 = 0.3 \text{ mm}$ ,  $r_1 = 50 \text{ nm}$ ,  $r_a = 85 \text{ nm}$ ,  $L_p = 10 \text{ mm}$ ,  $\kappa = 0.92 \text{ Sm}^{-1}$ ,  $U = 100 \text{ mV}$ .

## INTRODUCTION

Problems, however, have arisen, namely an increased probability of breaking the pipette, when investigated samples feature sudden height changes, since pipettes are very likely to get into contact with the surface or protruding obstacles when operating at  $z < r_i$ .

Nevertheless, the early days of SICM experiments in nonmodulated mode have already provided topographies with sub-micrometre resolutions, including biological samples such as living cells [Hansma et al. 1989; Korchev et al. 1997b; Korchev et al. 1997c; Schraml 2003] (cf. Fig. 1.3). Due to the described problem, SICM research has aimed at the development of an other measurement mode, which is neither as slow to react to rapid changes in  $z$  nor as susceptible to current drifts, changes in ionic strength, contamination of electrodes or even partial obstruction of ion flow through the pipette.

### *Distance-modulated mode*

The crucial difference between distance modulated and nonmodulated mode is a vertical oscillation of the pipette with oscillation amplitudes in the range of (20–30) nm and frequencies of (0.1–10) kHz. This modulation of the  $z$  position of the pipette results in an oscillating component – i.e. alternating current (ac) – added onto the dc measured in nonmodulated mode, if the pipette is sufficiently close to the sample. Utilisation of a lock-in amplifier recovers the oscillating current  $I_{ac}$  which is then used for feedback control. While the dc decreases when the pipette approaches the surface,  $I_{ac}$  does not exist in the regime where  $I_{dc} = I_{dc,sat}$ , but increases when short pipette-sample distances are reached as demonstrated in Figure 1.5 [Mannelquist et al. 2001; Pastré et al. 2001; Shevchuk et al. 2001].

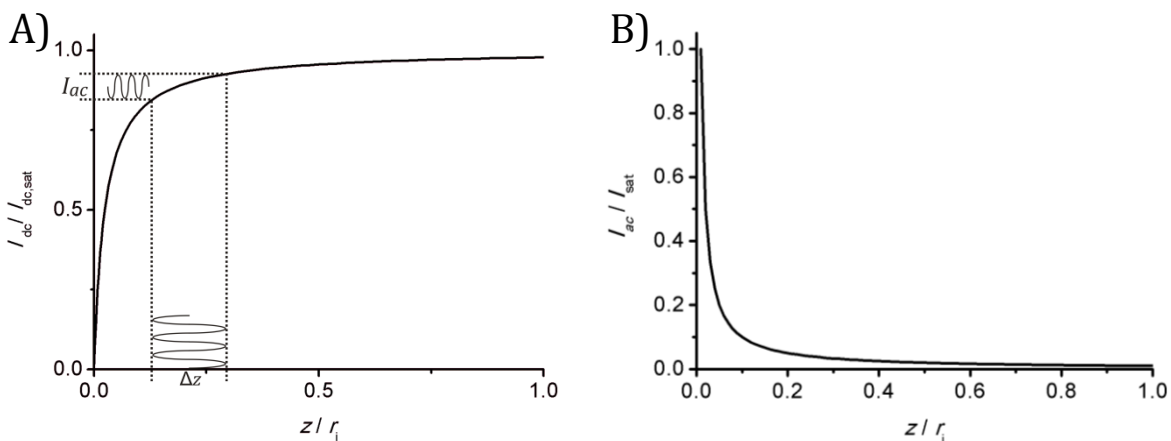


**Figure 1.5: Characteristic  $I/z$  curves for distance-modulation mode. A) The current compound  $I_{ac}$  is created via modulation of the pipette's vertical position by  $\Delta z$ . B)  $I_{ac}$  increases with decreasing probe-sample distances  $z$ . It provides enhanced stability for feedback control as the feedback parameter remains in a suitable range even for larger changes in  $I_{dc}$ . This is due to the fact that  $I_{ac}/I_{dc}$  scales with  $I_{dc}$  rather than  $I_{ac}$  scaling with  $I_{dc}$ . (adapted from Shevchuk et al. [Shevchuk et al. 2001]).**

Distance-modulated mode experiments provide enhanced pipette  $z$  position control. As the set point used for feedback control works best at (97–99.8)% of  $I_{sat}$  (i.e.  $I_{dc}$  or  $I_{ac} = (0.2–3)\%$ ) a large change in  $I_{dc}$  results in problems – if not loss of feedback control – while the  $I_{ac}/I_{dc}$  ratio scales with  $I_{dc}$ . This means that a 100% increase in  $I_{dc}$  exceeds the suitable set point range while  $I_{ac}$  does not as it increases from e.g. 1% to 2%. Moreover, current changes out of phase

with the oscillation frequency are neglected for feedback control, and thus problems described above are largely circumvented by modulating the pipette's z position.

The development of distance-modulated mode has facilitated long-term experiments over 24 h and longer [Gorelik et al. 2004; Zhang et al. 2005] (Fig. 1.6 A)), especially of living cells, as well as experiments involving changing ionic conditions in the bath solution [Shevchuk et al. 2001; Gorelik et al. 2004; Zhang et al. 2005] or hybrid scanning near-field optical microscopy (SNOM)/SICM techniques [Mannelquist et al. 2001; Mannelquist et al. 2002]. Furthermore, the highest resolution imaging by means of SICM has been performed in distance-modulated mode, where individual proteins on a mica surface have been visualised [Shevchuk et al. 2006] (Fig. 1.6 B)).

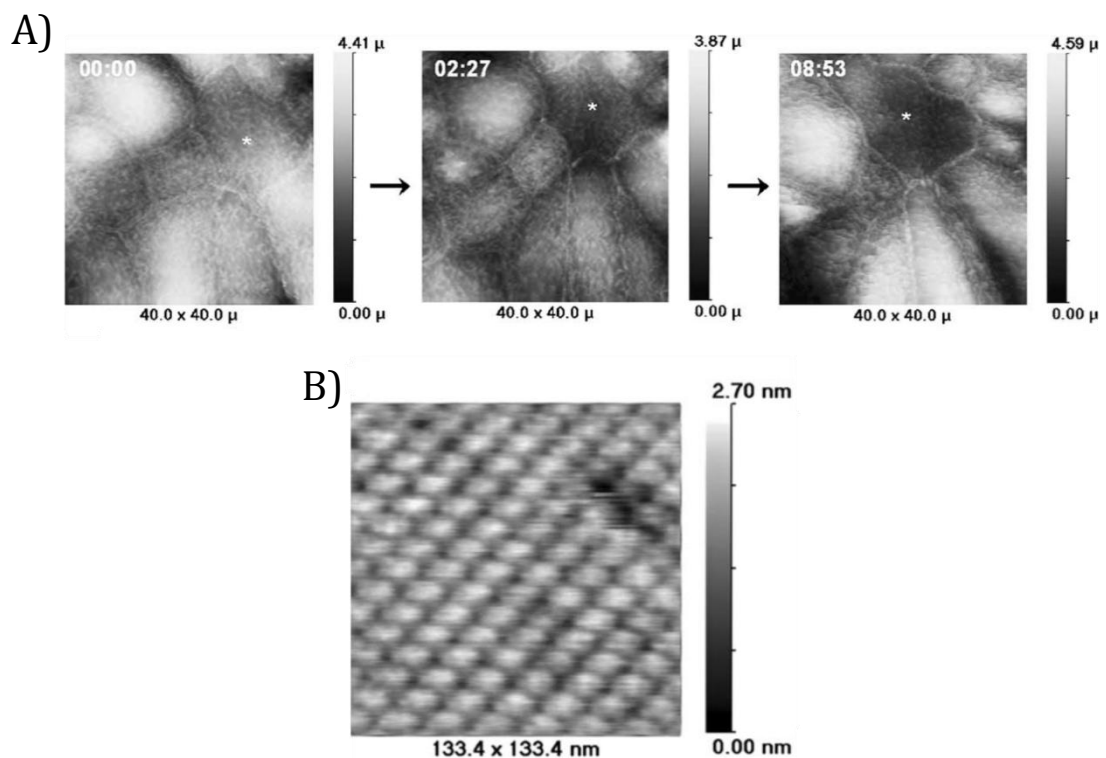


**Figure 1.6: Examples for studies conducted in distance-modulated mode. A) A series of SICM images of an A6 cell monolayer, taken every 20 min over a period of 10 h. The asterisk marks the same cell in every image [Gorelik et al. 2004]. B) The highest resolution achieved with SICM to date reveals individual S-layer proteins from *Bacillus sphaericus* CCM 2177 [Shevchuk et al. 2006].**

### *Hopping mode*

Imaging samples exhibiting high topography complexity has been a difficult task even after development of distance-modulated mode. As a consequence, an operation mode has been introduced in various research groups that relies on a large vertical oscillation of the pipette after which this mode is named and described as hopping [Novak et al. 2009], backstep [Mann et al. 2002; Happel et al. 2003] or standing approach [Takahashi et al. 2010a]. This mode can be regarded as analogous to intermittent contact mode in AFM. Low resolution experiments have been conducted ten years ago [Mann et al. 2002; Happel et al. 2003], while

## INTRODUCTION

high resolution measurements of living cells date back four years only [Novak et al. 2009] (Fig. 1.7).

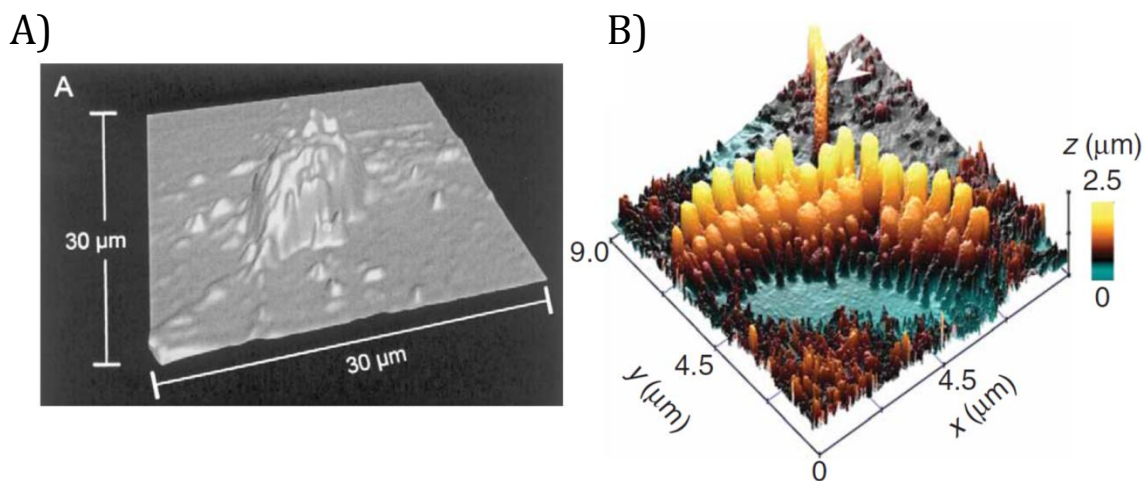


**Figure 1.7: Examples for backstep or hopping mode experiments. A) A hippocampal cell from postnatal rat brain recorded by Mann et al. with a lateral step size of 500 nm [Mann et al. 2002]. B) A sample with steep surface topography. Hopping mode experiments allow for imaging of highly demanding samples like the depicted stereocilia of auditory hair cells, recorded by Novak et al. The arrow indicates a true cilium [Novak et al. 2009].**

While pipettes have usually scanned line by line, scanning in hopping mode is typically performed in small squares that build a line: the pipette approaches the corners of each square to determine its roughness, i.e. height differences of its corners. The number of data points within the squares and the hopping height are then adjusted according to the prescan of the corners. The pipette starts at a point well above the investigated specimen and measures the maximum  $I_{dc,max}$  current at a great probe-sample distance. It then approaches the surface until a specified decrease in current is reached and is withdrawn subsequently to its starting height. This measurement mode ensures that protruding features of the sample do not constitute dangerous obstacles for the pipette unless their  $z$  dimension is larger than the hopping amplitude which can be set to values in the  $10^1$  micrometre range.

A major drawback the hopping mode is attended by is the increase in measuring time. In comparison to the earlier modes, the pipette consumes time to measure  $I_{dc,max}$  and needs to travel by micrometre distances twice for every data point at speeds of typically  $10 \text{ nm ms}^{-1}$ . This is another reason for pre-scanning squares as its roughness may be an indicator for its relevance. Low interest squares are thus measured at lower resolution and higher speed, while relevant areas of the specimen are recorded at higher resolution [Novak et al. 2009].

### *Fast scanning ion conductance microscopy*

In this case, the first pixels of the first line are scanned in hopping mode to obtain thorough topography information. From then on, the pipette is scanned at constant height, and the feedback system does not correct the vertical pipette position during, but only after completion of a line scan. To this end, two current set points are used: the first is similar to that used in hopping mode, which indicates too close proximity of the pipette to the surface

so that the  $z$  position is changed for the next scan of this line; the second is  $I_{\text{sat}}$  indicating too large a distance between probe and sample.

Problems at imaging high spatial frequency topographies are overcome via implementation of a scaled convolution of error function and a fixed width Gaussian function rendering post-scan procession of data a crucial part of the experiment. Every pixel's ion current is translated into height information by feeding it into the equation for the  $I/z$  curve. This height information is added to (or, depending on the sign of the approach curve, subtracted from) the pixel's  $z$  coordinate, which is then used to display the correct sample topography. This measurement mode has achieved remarkably high scanning velocities despite recording of even more pixels than in hopping mode, reaching 10 s for a  $(20 \times 20) \mu\text{m}^2$  image of an AFM calibration standard or a 10 min scan (600 lines, 1024 pixels each) of A6 cells, while hopping mode imaging at  $(512 \times 512)$  pixels would have consumed 5 h [Zhukov et al. 2012].

### 1.2.2 RESOLUTION

Resolution is one of an SPM's features, that defines its application range. Little has been known about resolution for SICM, except for the fact that it depends on the pipette tip geometry. Experimental evidence led Hansma et al. to the conclusion, the lateral resolution was given as  $1/3$  of the inner diameter  $r_i$  of the pipette tip, when they were able to image regularly ordered groves utilising a pipette with  $r_i$  equalling the threefold inter groove distance [Hansma et al. 1989]. Measurements, however, were performed with pipettes featuring micrometre sized tips and results merely extrapolated towards nanopipettes. This assumption was later believed to be validated when Shevchuk et al. imaged a monolayer of proteins on a mica surface [Shevchuk et al. 2006] (cf. Fig. 1.6 B)). By utilisation of a tip of  $r_i = 12.5$  nm, identification of single proteins with inter protein distances of 13.1 nm and a resolution of (3–6) nm, i.e.  $1/3$  of  $r_i$ , were achieved.

A thorough theoretical investigation of SICM resolution was performed by means of finite element modelling by Rheinländer and Schäffer [Rheinlaender and Schäffer 2009]. Based on calculations of ion current density, they found SICM resolution – defined as the 'smallest distance at which two individual particles can clearly be resolved from each other' – to be three times the inner diameter of the pipette tip. This is highly contrary to the findings based on experimental approaches described above, which were regarded insufficient by Rheinlaender and Schäffer because of the perfect periodicity of the surfaces used.

# INTRODUCTION

## 1.2.3 SICM THEORETICS

Besides the resolution problem, another aspect worth investigating is the current and its behaviour for various experimental situations. Few attempts have been conducted to develop mathematical models for SICM measurements to gain further insight into processes and to better understand results obtained from experimental approaches.

A first important approach displayed below has been published by Nitz et al. [Nitz et al. 1998]. The total resistance  $R_{\text{tot}}$  of a SICM system can be separated threefold into:

- the electrolyte resistance  $R_r$  between the bath electrode and the borders of the cylinder below the pipette tip with a base radius equalling the outer pipette radius  $r_a$
- the distance-dependent leakage resistance  $R_l$  between the borders of the aforementioned cylinder and its top, a circle with its radius equalling  $r_i$
- the pipette resistance  $R_p$  between the pipette tip and the electrode inside the pipette:

$$R_{\text{tot}} = R_r + R_l + R_p \quad [1.1]$$

Figure 1.8 displays a schematic representation of assumptions made by Nitz and co-workers. The SICM implicates that the bath solution consists of a conductive electrolyte,  $R_r$  can thus be neglected in comparison to  $R_l$  and  $R_p$  such that equation [1.1] can be simplified into:

$$R_{\text{tot}} = R_l + R_p \quad [1.2]$$

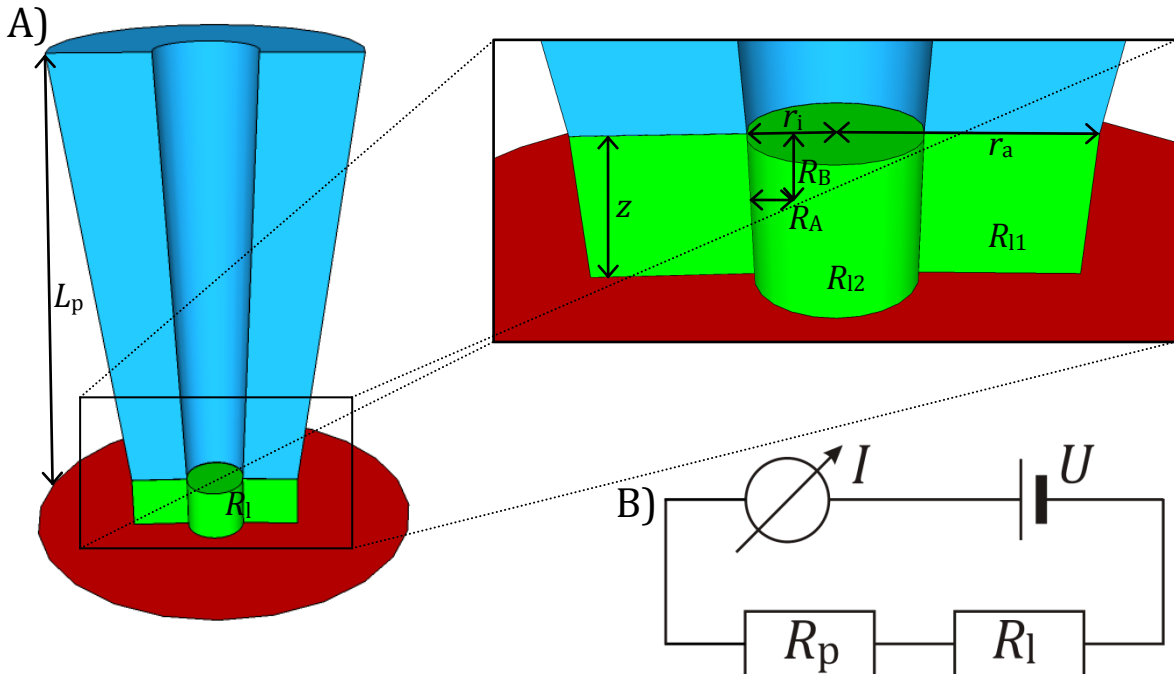


Figure 1.8: Calculation of  $I(z)$ . A) Resistances and parameters determining these resistances involved. The conical pipette tip (blue), the sample surface (red) and the electrolyte volume influencing the access resistance (green) are displayed. Tip parameters determining its resistance  $R_p$  are the length  $L_p$  as well as  $r_a$ ,  $r_i$  and  $r_0$ , representing the outer and the inner radii at the bulk solution border and the pipette electrode border, respectively. The leakage resistance  $R_l$  can be bisected into  $R_{l1}$  and  $R_{l2}$ .  $R_{l2}$  consists of  $R_A$  and  $R_B$ . B) The equivalent circuit for the typical SICM situation after Nitz et al. [Nitz et al. 1998] is displayed as a series circuit, the total resistance  $R_{\text{tot}}$  consisting of  $R_p$  and  $R_l$ .



An electrolytic cylinder's resistance  $R$  can be described by:

$$R = \frac{1}{\kappa} \cdot \frac{l}{A} = \frac{l}{\kappa \pi r^2} \quad [1.3]$$

where  $\kappa$  is the electrolyte's specific conductance while  $l$ ,  $A$  and  $r$  represent the cylinder's length, cross section and radius, respectively. As the pipette is of conical shape,  $r$  is a function of its position along the cone's axis:

$$r(L) = r_i + (r_0 - r_i) \frac{L}{L_p} \quad [1.4]$$

where  $r_i$  and  $r_0$  are the tip's inner radius and inner radius at the top of the cone, respectively, while  $L$  represents the examined position along the axis and  $L_p$  the cone's length (cf. Fig. 1.8). Consideration of the axis position change results in:

$$dR_p(L) = \frac{1}{\kappa} \cdot \frac{dL}{\pi [r(L)]^2} \quad [1.5]$$

which can be solved to:

$$\begin{aligned} R_p &= \int_{R_p(0)}^{R_p(L_p)} dR_p(L) \\ &= \frac{1}{\pi \kappa} \int_0^{L_p} \left[ r_i + (r_0 - r_i) \frac{L}{L_p} \right]^{-2} dL = \frac{L_p}{\pi \kappa r_0 r_i} \end{aligned} \quad [1.6]$$

The second contributor to  $R_{\text{tot}}$ , the leakage resistance  $R_l$ , describes the  $z$  dependent part of  $R_{\text{tot}}$ , the resistance met by ions trespassing the circular area right beneath the pipette opening and its glass surface parallel to the sample surface. It can be bisected in accordance to these two volumes (beneath pipette opening and glass, respectively):

$$R_l = R_{l1} + R_{l2} \quad [1.7]$$

$R_{l1}$  comprises migration through the hollow cylinder's electric field beneath the pipette tip's glass, which is thus bordered by two circles with radii of  $r_a$  (outer tip radius) and  $r_i$  (inner tip radius), respectively (cf. Fig. 1.8). The current of a hollow cylinder  $I_{\text{cyl}}$  can be described by:

$$I_{\text{cyl}} = \iint_A j dA = \kappa \iint_A E dA = \frac{\kappa Q}{\epsilon_0} \quad [1.8]$$

## INTRODUCTION

with  $j$ ,  $E$ ,  $Q$  and  $\varepsilon_0$  being current density, electric field, charge and electric constant, respectively, while  $R_{11}$ 's voltage  $U_{\text{cyl}}$  is:

$$U_{\text{cyl}} = - \int_{r_a}^{r_i} E dr = - \int_{r_a}^{r_i} \frac{Q}{2\pi\varepsilon_0 z r} dr = \frac{Q}{2\pi\varepsilon_0 z} \ln\left(\frac{r_a}{r_i}\right) \quad [1.9]$$

such that follows:

$$R_{11} = \frac{U_{\text{cyl}}}{I_{\text{cyl}}} = \frac{\frac{Q}{2\pi\varepsilon_0 z} \ln\left(\frac{r_a}{r_i}\right)}{\kappa \frac{Q}{\varepsilon_0}} = \frac{1}{2\kappa\pi z} \ln\left(\frac{r_a}{r_i}\right) \quad [1.10]$$

$R_{12}$  comprises lateral and vertical ( $R_A$  and  $R_B$ , respectively, cf. Fig 1.8 and equation [1.11]) migration through a cylinder with a radius of  $r_i$  between the hollow cylinder described above and entering the pipette interior.  $R_{12}$  is thus bisected:

$$R_{12} = R_A + R_B \quad [1.11]$$

where  $R_A$  is analogous to  $R_{11}$  in equation [1.10]:

$$R_A = \frac{1}{2\kappa\pi z} \ln\left(\frac{r_i}{r_i/2}\right) = \frac{1}{2\kappa\pi z} \ln(2) \quad [1.12]$$

and  $R_B$  analogous to equation [1.3], with estimated averaged path lengths of  $\frac{1}{2} r_i$  for lateral movement and  $\frac{1}{2} z$  for vertical movement:

$$R_B = \frac{1}{\kappa} \cdot \frac{l}{\pi r^2} = \frac{1}{\kappa} \cdot \frac{l}{\pi r_i^2} = \frac{z}{2\kappa\pi r_i^2} \quad [1.13]$$

It follows that:

$$R_{12} = \frac{1}{2\kappa\pi z} \ln(2) + \frac{z}{2\kappa\pi r_i^2} \quad [1.14]$$

The probe-sample distance was reasonably estimated as  $z = \frac{1}{2} r_i$ , and comparison of  $R_A$  and  $R_B$  with  $R_{11}$  leads to  $R_A \approx 1.3 R_{11}$  and  $R_B \approx 0.5 R_{11}$  resulting in an estimation of:

$$R_{12} \approx 2 \cdot R_{11} \quad [1.15]$$

Equation [1.7] can thus be expressed as:

$$R_1 = \frac{1}{2\kappa\pi z} \ln\left(\frac{r_a}{r_i}\right) + \frac{1}{2\kappa\pi z} \ln(2) + \frac{z}{2\kappa\pi r_i^2} \quad [1.16]$$

or be simplified to:

$$R_1 \approx 3 \cdot R_{11} = \frac{3}{2\kappa\pi z} \ln\left(\frac{r_a}{r_i}\right) \quad [1.17]$$

As  $R_1$  becomes small for large probe-sample distances  $z$ , the saturation current  $I_{\text{sat}}$  is determined by the pipette resistance  $R_p$  only:

$$I_{\text{sat}} \approx \frac{U}{R_p} = \frac{U}{\frac{L_p}{\kappa\pi r_0 r_i}} \quad [1.18]$$

As soon as the pipette gets closer to the surface, the dependence on  $z$ , i.e.  $R_1$ , has to be taken into account and

$$I(z) = \frac{U}{R_{\text{tot}}} \approx \frac{U}{R_p + R_1} \approx \frac{U}{\frac{L_p}{\kappa\pi r_0 r_i} + \frac{3}{2\kappa\pi z} \ln\left(\frac{r_a}{r_i}\right)} = I_{\text{sat}} \left[1 + \frac{3r_0 r_i}{2zL_p} \ln\left(\frac{r_a}{r_i}\right)\right]^{-1} \quad [1.19]$$

is obtained. The more exact equation, when one abstains from the approximation given by equation [1.15] but does consider  $R_r$ , the electrolyte resistance (v.s.), as reasonably negligible is then:

$$I(z) = \frac{U}{R_{\text{tot}}} \approx \frac{U}{R_p + R_1} = I_{\text{sat}} \left[1 + \frac{r_0 r_i}{2zL_p} \left[\ln\left(\frac{r_a}{r_i}\right) + \ln 2\right] + \frac{r_0 r_i}{2L_p r_i^2}\right]^{-1} \quad [1.20]$$

A plot (Fig. 1.9) of both the – disregarding  $R_r$ 's contribution – exact equation and the simplified equation for typical values of pipette parameters reveal good mutual accordance.

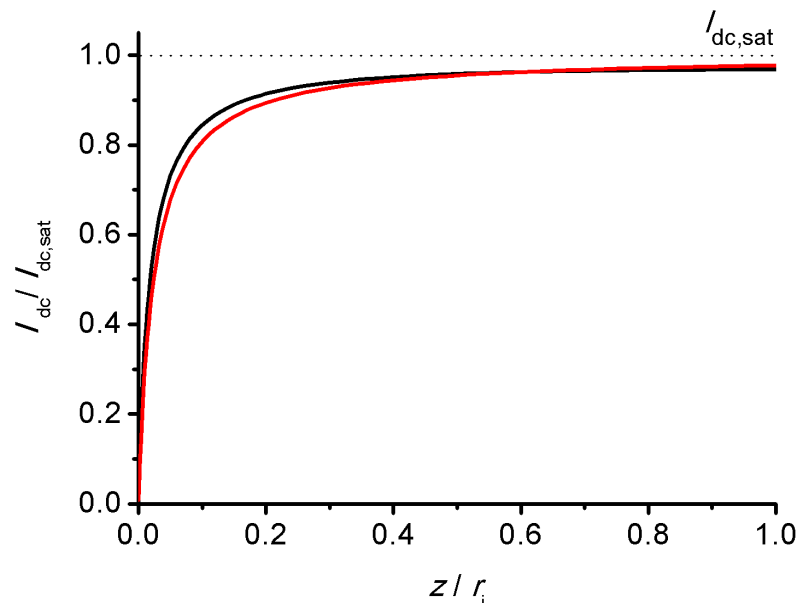
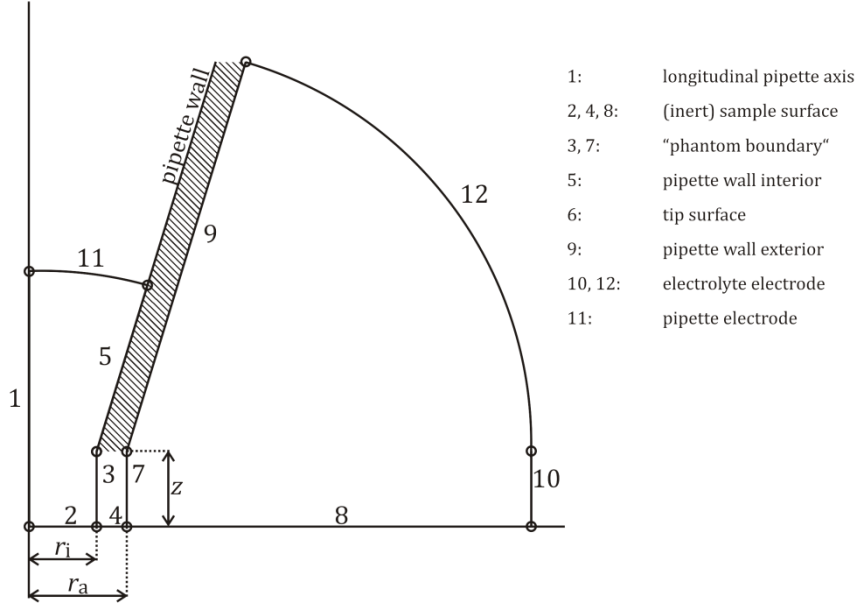


Figure 1.9:  $I/z$  curves obtained from solving the exact and simplified equations based on assumptions by Nitz et al. [Nitz et al. 1998] A comparison of the exact (black) and the simplified (red) solution shows slightly steeper decay of the current at low  $z$  values for the former while negligible differences become obvious in the  $z = r_i$  regime.

## INTRODUCTION

A computationally more demanding approach has been taken by Edwards et al. [Edwards et al. 2009], the key difference being that lateral access to the pipette tip has been taken into account more realistically. Both the 2D and the 3D model are based on a twelve edge geometry of axial symmetry as displayed in Figure 1.10. The bath electrode's dimensions are assumed to be large enough in comparison to the pipette tip that any resistance contribution is negligible. Other assumptions, e.g. representation of the pipette electrode as a circle's arc, have been shown to not affect simulations as well.



**Figure 1.10:** 2D geometry of a pipette close to a sample surface as subjected to finite element modeling by Edwards et al. [Edwards et al. 2009]. The 3D geometry is obtained from a 180° rotation around boundary 1. Numbers specified on the right refer to boundaries used in the simulations.

For the electrolyte solution, Laplace's equation is solved in cylindrical polar coordinates:

$$\nabla^2 \Phi = \frac{\partial^2 \Phi}{\partial r^2} + \frac{1}{r} \frac{\partial \Phi}{\partial r} + \frac{\partial^2 \Phi}{\partial z^2} = 0 \quad [1.21]$$

Integration of flux on the electrode boundary  $\Omega$  (boundary 11, Fig. 1.10) results in a description for the current  $I$ :

$$I = 2\kappa\pi \int_{\Omega} r \nabla \Phi \vec{n} \quad [1.22]$$

where  $\vec{n}$  is the unit normal to the edge. With regard to the pipette, modelling of the entire pipette has been proven inefficient, but a simplification is suggested, which describes the resistance within the conical segment between two concentric, spherical shells of radii  $A$  and  $B$  (outer and inner, respectively):

$$R_{A,B,\gamma} = \frac{B - A}{2\kappa\pi AB(1 - \cos \gamma)} \quad [1.23]$$

with  $\gamma$  representing the semiangle of the conical section. Here, a description in spherical polar coordinates is chosen with  $r$ ,  $\Phi$ ,  $\Psi$  being the radial, azimuthal and polar coordinates, respectively:

$$\begin{aligned} 0 = \nabla^2 \Phi &= \frac{1}{r^2} \frac{\partial}{\partial r} \left( r^2 \frac{\partial \Phi}{\partial r} \right) + \frac{1}{r^2 \sin \theta} \frac{\partial}{\partial \theta} \left( \sin \theta \frac{\partial \Phi}{\partial \theta} \right) + \frac{1}{r^2 \sin^2 \theta} \frac{\partial^2 \Phi}{\partial \theta^2} \\ &= \frac{1}{r^2} \frac{\partial}{\partial r} \left( r^2 \frac{\partial \Phi}{\partial r} \right) \end{aligned} \quad [1.24]$$

The current  $I$  results from integration of the normal flux  $-\kappa\beta r^2$  over the inner shell's part within the pipette ( $\phi < \gamma$ ) with  $\beta$  resulting from the ansatz  $\Phi(r, \phi, \theta) = \Phi(r) = \alpha + (\beta)/(r)$ :

$$I = \int_0^{2\pi} \int_0^\gamma (-\beta/A^2) \kappa A^2 \sin \Phi \, d\Phi \, d\theta = \frac{AB}{(B-A)} 2\pi(1 - \cos \gamma) \quad [1.25]$$

which is exactly reciprocal to the resistance (eq. [1.23]).

The 3D model is based on the volume of a 180° rotation of the 2D model geometry. Cartesian coordinates are used for Laplace's equation:

$$\nabla^2 \Phi = \frac{\partial^2 \Phi}{\partial x^2} + \frac{\partial^2 \Phi}{\partial y^2} + \frac{\partial^2 \Phi}{\partial z^2} = 0 \quad [1.26]$$

The current  $I$  is obtained from the flux integral analogous to equation [1.22]:

$$I = 2\kappa \int_{\Omega} \nabla \Phi \mathbf{n} \quad [1.27]$$

Results of these simulations shall be described below:

The smaller the pipette's semiangle, the less sensitive is the probe to its distance to the sample, which is derived from decreasing steepness of  $I_{dc}/z$ -curves with decreasing semiangles. In addition to this,  $I_{ac}/z$ -curves reveal on the one hand an enhanced sensitivity in comparison to experiments, where  $I_{dc}$  is used as feedback parameter, and on the other hand increasing sensitivity with increasing semiangles. This is due to an increase in pipette resistance  $R_p$  with narrowing the cone (i.e. decreasing semiangle). As  $R_{tot}$  depends on  $R_p$  and  $R_i$ , an increase in  $R_p$  means a decrease of the  $R_i/R_{tot}$  ratio and thus of the  $z$ -dependent  $R_i$  influence.

A similar result is found for the influence the ratio of the pipette's outer and inner radii ( $r_a/r_i$ ) has on probe sensitivity: an increase of  $r_a/r_i$  increases probe sensitivity in both  $I_{dc}$  and  $I_{ac}$  cases. This effect is based on a potential drop in the hollow cylinder below the tip, bounded by  $r_i$  and  $r_a$ . The broader this hollow cylinder, i.e. the larger  $r_a/r_i$ , the higher the leakage resistance  $R_i$  and thus the probe's sensitivity.

## INTRODUCTION

Pipette trajectories for imaging of a step of different heights perpendicular to the surface have been modeled. Evidence is provided that an  $I_{ac}$  based feedback mode is superior to an  $I_{dc}$  based, not merely with respect to feedback control stability but also with respect to the quality of tip response to surface features. Regardless of the feedback control parameter and the step height, it is found that the larger the probe-sample distance  $z$ , at which the set point is reached the more blurred is the image. It has to be taken into account, however, that usual probe-sample distances are higher than those inserted into simulations. These are significant differences to calculations by Nitz et al. [Nitz et al. 1998], who find much narrower pipette trajectories, i.e. trajectories corresponding much better to the step's geometry. Edwards et al. claim these differences to be based on erroneous extrapolation of 2D results to 3D situations, while they consider lateral effects on the resistance as well.

For the imaging of pits it is found that pits with radii  $r_{\text{pit}} < r_i$  ( $r_{\text{pit}} = 0.73 r_i$ ) are invisible to the pipette. Pits with slightly larger radii ( $r_{\text{pit}} = 1.35 r_i$ ) are visible, but caution has to be exercised for all but the shallowest pits with regard to accuracy of pit depth measurements. These appear to be exact only for depths in the range of  $0.1 r_i$ . The imaging of pits much wider than pipette tips ( $r_{\text{pit}} = 5.74 r_i$ ) does not pose any problem for height assessments.

Theoretically approaching typical SICM experiment situations has provided valuable information and has led to better understanding and interpretation of SICM data, underlining its importance for SICM experimentalists.

### 1.2.4 HYBRID TECHNIQUES

As the SICM technique provides a non-interfering approach, it is readily combinable with other techniques. The positioning of the probe with nanometre accuracy has been found to be especially valuable: after SICM imaging of the sample topography, a region of interest can be defined and accessed. The combined technique comes into play then and provides the information it can gather.

#### *Smart patch-clamp*

As SICM is a SPM technique suitable for the investigation of soft biological samples that is based on a glass pipette as a probe, utilisation of the SICM probe as a patch-clamp pipette is self-evident. The patch-clamping technique has provided deep insights into the occurrence of membrane channels in different cell species, e.g. cardiomyocytes [Bustamante et al. 1991; Sigurdson et al. 1992] or neurons [Green and Gillette 1983; Bossu and Feltz 1984; Gao et al. 2009], and into these channels' electrochemical and mechanistic features.

While its temporal resolution has been remarkably high, spatial resolution with regard to localisation of channel proteins has posed significant problems. These problems were overcome when Gu et al. used SICM to image the surface topography of cardiac myocyte sarcolemma and performed patch-clamp experiments with the same nanopipette at specific regions such as T-tubule regions, Z-grooves and scallop crests [Gu et al. 2002]. It was possible

to assign a specific ion channel (L-type  $\text{Ca}^{2+}$  channels) to the T-tubule region, i.e. to localise this ion channel in one specific membrane area. Subsequent studies subjected various cell types successfully to smart patch-clamp and demonstrated its general applicability [Gorelik et al. 2002a]. Furthermore, Duclohier showed neuronal  $\text{Na}^+$  channels to be localised near T-tubule openings in ventricular heart cells [Duclohier 2005], Dutta et al. investigated the spatial distribution of the maxi-anion channels in rat cardiomyocytes, finding them to be concentrated at T-tubule openings and along Z-lines [Dutta et al. 2008], while James et al. were successful in demonstrating clustered appearance of protein kinase A-dependent  $\text{Cl}^-$  channels of ventricular myocytes [James et al. 2010]. This range of experiments reveals the potential to give further insights into cellular membrane architecture via localisation of ion channels.

### *Optical techniques*

SICM is usually performed on an inverted optical microscope such that lateral pipette positioning is facilitated for studies on transparent samples. Combination of SICM with more powerful optical methods has been applied to solve a variety of problems.

The  $\text{Ca}^{2+}$ -sensitive fluorescent probe fluo-3 has been utilised by Shevchuk et al. to image local  $\text{Ca}^{2+}$  concentrations beneath cell membranes of cardiac myocytes during recording of their contraction movement, which takes place on a nanometre scale and is hence hardly resolvable by optical methods, by SICM [Shevchuk et al. 2001]. Similarly, an investigation of the effect of two drugs on taurocholate induced arrhythmia that appears during pregnancies, was conducted by Gorelik et al. [Gorelik et al. 2002b]. The nature of endocytic pits (clathrin-coated, caveolae or other) has been elucidated via GFP-coupling of both clathrin and the putative coating flotillin-1 and -2 by Shevchuk et al., where pits have been identified by topography recording by means of SICM – this hybrid being termed scanning surface confocal microscopy (SSCM) [Shevchuk et al. 2008].

The applicability of combining SICM and SNOM is self-evident. The nanometre precision of z position control is highly valuable for SNOM measurements, where a short probe-sample distance is desired. Studies of Mannelquist et al. [Mannelquist et al. 2001; Mannelquist et al. 2002] and Korchev et al. [Korchev et al. 2000b] displayed this hybrid technique's general applicability using distance-modulated control to keep a pipette, simultaneously used as the light source, in close proximity to the surface. A follow-up study by Bruckbauer et al. used fluo-3 as a light source for  $\text{Ca}^{2+}$  such that delivery of the fluorescent probe was executed through the nanopipette [Bruckbauer et al. 2002].

### *Other methods*

SICM has very early, i.e. prior to the development of distance-modulated mode, been combined with AFM by Proksch et al. [Proksch et al. 1996] Contrary to the hybrid SICM/SNOM examples, where SICM is responsible for probe-sample distance control, the AFM feature is utilised for feedback control. A bent pipette works here as both the cantilever

## INTRODUCTION

and the conductance probe and has been applied in contact and tapping mode to successfully record topographies of polycarbonate membranes based on both AFM and SICM.

Similarly, shear-force microscopy has been combined with SICM and used for distance control by Nitz et al. [Nitz et al. 1998], when precise and reliable control of the pipette's vertical position could not be achieved via the SICM feature. Later, distance control has been facilitated by introduction of distance-modulated shear-force control by Böcker et al. with proof of concept being given by imaging of polycarbonate membranes as well as mammalian cells [Böcker et al. 2007].

SICM has recently been combined with SECM. Here, a nanopipette, with its outside coated with a conductive metal layer (Au or Pt), is utilised as the probe. While SICM provides distance control, the metal ring serves as an electrochemical probe such that the investigation of living cells [Takahashi et al. 2010b] is possible as well as that of Au film electrodes [Comstock et al. 2010].

### 1.2.5 A SELECTION OF APPLICATIONS

While Chapter 1.2.4 covers hybrid techniques, an assortment of specific interesting experiments is presented here.

#### *Embryonic stem cell characterisation*

Embryonic stem cells (ESCs) have evoked growing interest in recent years. A challenging problem has been the dissection and elimination of differentiated cells during cultivation of human ESCs. SICM provides a noncontact method to characterise ESCs and their differentiation state based on topographical measurements and SSCM as described above. Features screened for include the existence of microvilli and elongated surface structures whose disappearance and attainment, respectively, indicate differentiation of ESCs [Gorelik et al. 2008].

#### *Microprocessing*

Proof of concept for the utilisation of SICM for a microprocess method has been delivered by Zhang et al. [Zhang et al. 1999] A copper electrode was used as the anode inside the micropipette with an  $r_1$  of 1.5  $\mu\text{m}$ , filled with 0.5 M  $\text{CuSO}_4$  solution. By means of electrolysis, lines of 2  $\mu\text{m}$  width were deposited on a conductive surface, here an indium tin oxide (ITO) surface, which works as the cathode. Desired is a decrease of linewidths that would provide further progress in addition to achieved enhanced velocities of such electroplating procedures.



*Guidance and redirection of neuronal growth cones*

Another example, where probe-sample interaction is utilised, has been delivered by Pellegrino et al. [Pellegrino et al. 2009] They use SICM to either image neurites or guide their growth depending on the pipette-sample distance: while imaging of neurites is accomplished as has been for a variety of other cells, a reduction of the scanning distance results in manipulation of growth cones' behaviour. It was proven possible to link erstwhile distinct growth cones and thereby shown an approach towards developing networks or linking existing networks to artificial structures.

*Cell volume measurements*

Korchev et al. have utilised SICM with 50 nm  $r_i$  pipettes to measure cell volumes over a range of  $(10^{-19}$ – $10^{-9})$  l with spatial and temporal resolutions of up to  $2.5 \cdot 10^{-21}$  l and 5 ms, respectively, providing a means to investigate mechanisms of cellular homeostasis without mechanic or photonic interference with the subject [Korchev et al. 2000a]. Happel et al. presented long-term monitoring of cell motility and volume changes by utilisation of micropipettes achieving 50 nm standard deviation vertically and 500 nm laterally [Happel et al. 2003].

### 1.3 ARTIFICIAL MEMBRANE MODEL SYSTEMS

Lipid membranes constitute the ubiquitous barrier on  $\mu\text{m}$  and  $\text{nm}$  scales in life. A widely useful idea of the architecture of cell membranes has been developed by Singer and Nicolson in 1972 who describe a membrane as a 2D liquid, where components such as protein molecules are embedded within a phospholipid bilayer comprising the matrix, a fluid mosaic [Singer 1972; Singer and Nicolson 1972]. Recent investigations, however, have refined this model and brought forward the existence of more complex protein-protein associations, the possibility of lipid rafts [Simons and Ikonen 1997; Simons and Toomre 2000; Dietrich et al. 2001; Engelman 2005; Simons and Sampaio 2011] as well as pickets and fences [Fujiwara et al. 2002; Ritchie et al. 2003; Kusumi et al. 2005; Morone et al. 2006] resulting from interactions with the cytoskeleton (Fig. 1.11).

A wide range of experiments has been conducted on cellular and hence lipid membrane systems focusing on medicinal, biological, chemical or physical questions. To circumvent the complexity of *in vivo* studies and to prevent unknown interactions not focused on from influencing the sample's behaviour, *in vitro* studies can be applied, where lipid compositions and interacting molecules are well-known and under the experimenter's control. To this end, model systems for the natural lipid membrane have been developed which shall be introduced below.

# INTRODUCTION

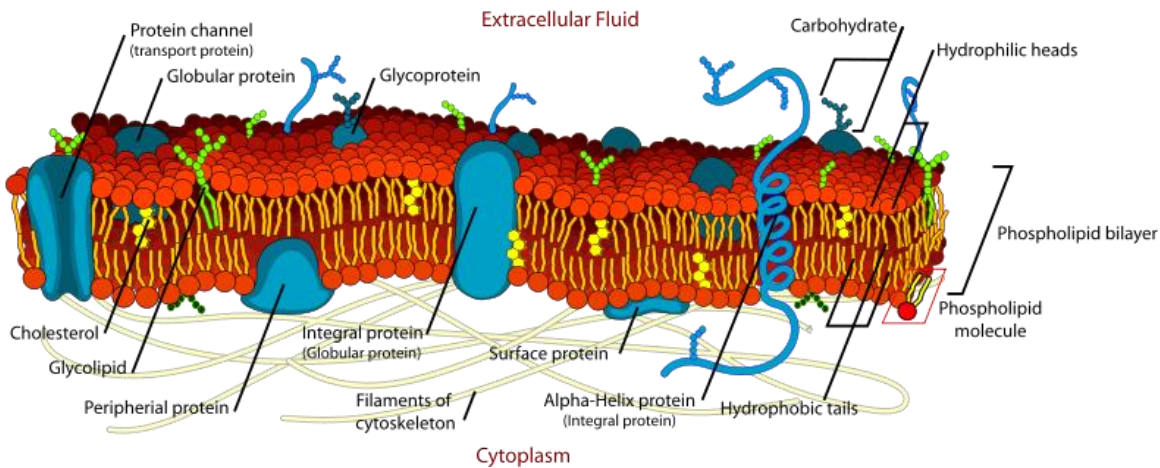


**Figure 1.11: Schematic of a cell membrane depicting its major constituents ((glyco)lipids, (peripheral, integral, surface) proteins, carbohydrates) and the underlying cytoskeleton [Ruiz 2007].**

## 1.3.1 VESICLES

The model system mimicking living cells' geometry best is that of spherical lipid membrane structures separating the aqueous exterior from the aqueous compartment within as displayed in Figure 1.12. Systems with more than one concentric doublelayer – multilamellar vesicles (MLVs) – are distinguished from unilamellar vesicles, which are trisected depending on their diameter: small unilamellar vesicles (SUVs,  $d < 100$  nm), large unilamellar vesicles (LUVs,  $d = (100-500)$  nm) and giant unilamellar vesicles (GUVs,  $d > 1000$  nm) [Ulrich 2002].

Due to easy access to large quantities of vesicles by means of e.g. extrusion [MacDonald et al. 1991] or electroformation [Angelova and Dimitrov 1986; Angelova et al. 1992], bulk experiments, e.g. calcein release experiments from LUVs upon addition of membrane active peptides [Benachir and Lafleur 1995], are readily performed. Moreover, GUVs are well detectable by means of confocal laser scanning microscopy (CLSM), which has been exploited

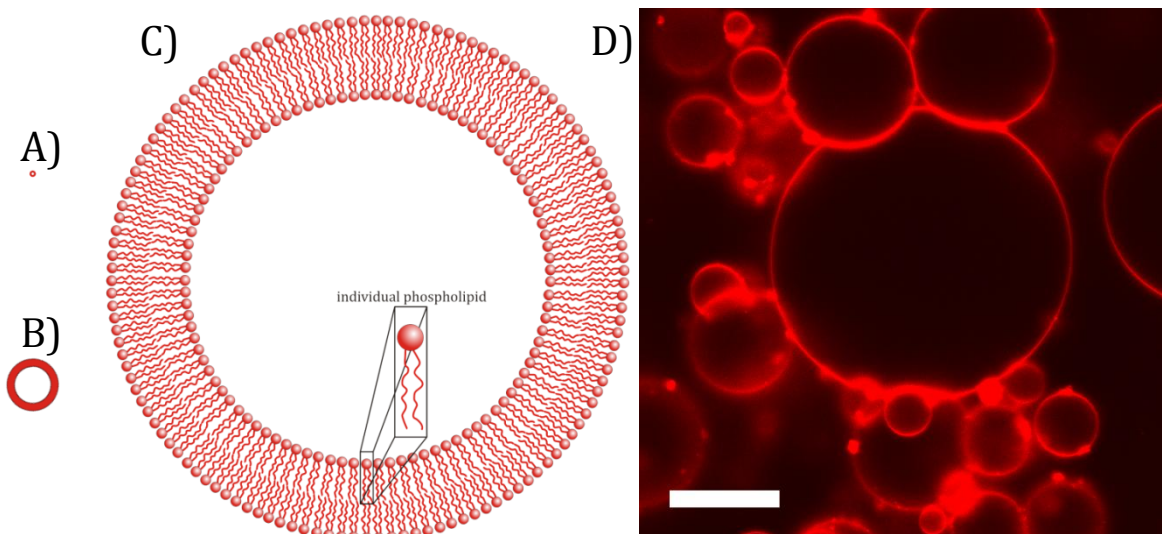


**Figure 1.12: Various phospholipid vesicles: Schematics of a A) SUV (diameter: 50 nm), B) LUV (diameter: 500 nm), C) GUV (diameter: 5  $\mu$ m) are displayed. Vesicle sizes are drawn to scale. D) Fluorescence micrograph of GUVs (scale bar: 27.0  $\mu$ m).**

to investigate the evolution and behaviour of lipid domains [Korlach et al. 1999; Bacia et al. 2005], the activity of ion channels [Girard et al. 2004], the influence of membrane proteins [Windschiegl et al. 2009] or lipid peptide interactions [Boll et al. 2011].

The system's limitations, however, become obvious when SPMs or surface sensitive methods such as surface plasmon resonance (SPR), ellipsometry, or the quartz crystal microbalance (QCM) technique would be the method of choice to solve a specific problem.

### 1.3.2 SOLID SUPPORTED MEMBRANES

To achieve systems where surface based methods can be applied, membrane models have been developed with lipid bilayers immobilised on a solid support (Fig. 1.13). Moreover, solid supported membranes (SSMs) feature high mechanical stability which, however, comes at the expense of a second aqueous compartment and reduced lateral mobility of the lipid molecules ( $(0.3\text{--}4)\ \mu\text{m}^2\ \text{s}^{-1}$  [Lopez et al. 1988; Brozell et al. 2006; Dertinger et al. 2006] compared to  $(13\text{--}20)\ \mu\text{m}^2\ \text{s}^{-1}$  [Ladha et al. 1996; Sonnleitner et al. 1999] for free standing membranes.

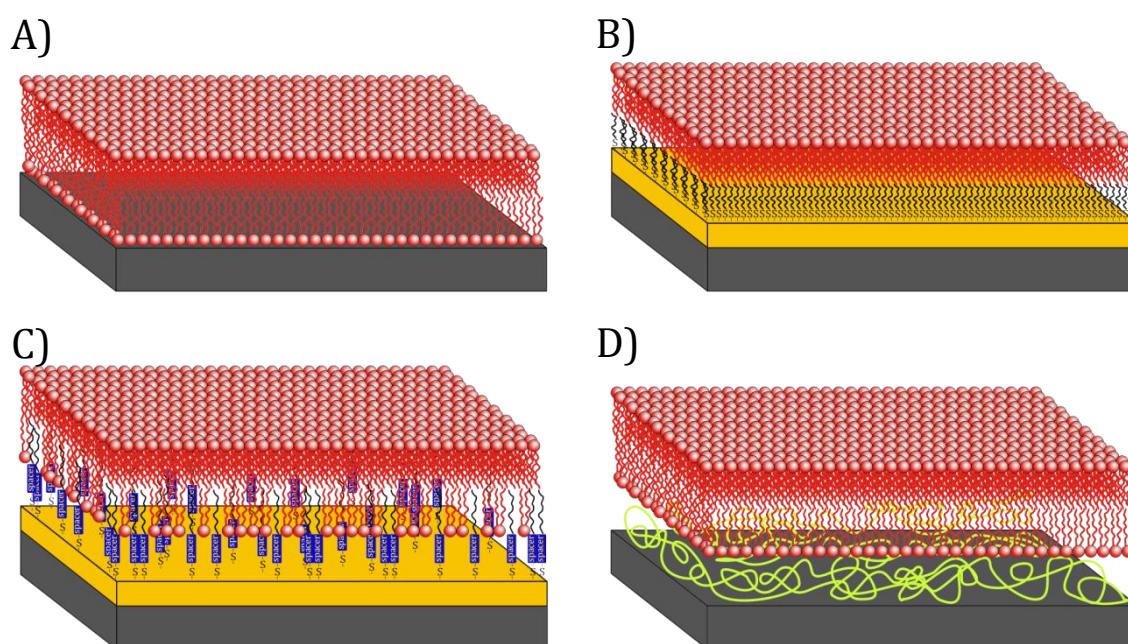


**Figure 1.13: Various types of SSMs are displayed. The bilayers' bottom monolayers are omitted for clarity. A) Membrane prepared directly on a hydrophilic support (dark grey). B) A layer of phospholipids is prepared on thiolipids bound to an Au layer (yellow). C) Tethered membrane: thiolipids containing spacer moieties (blue) are used to achieve an aqueous compartment between the lipid bilayer and the support. D) A polymer cushion (green) is utilised to create H<sub>2</sub>O filled space between the membrane and the support.**

Various techniques can be utilised for the preparation of SSMs. Methods to achieve asymmetry with respect to the lipid composition have been developed by Blodgett [Blodgett 1935] or Langmuir and Schäfer [Langmuir and Schäfer 1938]. Lipids dissolved in an organic solvent can directly be painted onto a surface and self-assemble into bilayers when the solvent evaporates [Florin and Gaub 1993] or unilamellar vesicles can be spread [Cremer and Boxer 1999; Jass et al. 2000; Keller et al. 2000] (Fig. 1.13 A)). Both these ways are equally

## INTRODUCTION

well applicable to chemically modified surfaces, e.g. thiolipid modified gold [Plant 1993; Steinem et al. 1996; Ulman 1996] or silane modified SiO<sub>2</sub> [Köper et al. 2006] substrates (Fig. 1.13 B)).

The lack of a second aqueous compartment (v.s.) has been overcome by means of tethered membranes. To this end, surface modifying molecules feature spacer moieties such as cholesterol (cf. Tab. 3.2) or fatty acids resulting in a free space for an aqueous phase between these spacers which is bordered by the lipid bilayer and the solid support [Lang et al. 1994; Williams et al. 1997; Raguse et al. 1998; Krishna et al. 2001] (Fig. 1.13 C)). A slightly different approach is taken when flexible polymer networks working as cushions are utilised to prevent direct contact of the bilayer with the solid support [Spinke et al. 1992; Tanaka and Sackmann 2005] (Fig. 1.13 D)). Successful development of tethered membranes has allowed for the integration and investigation of transmembrane proteins in SSMS.

### 1.3.3 BLACK LIPID MEMBRANES

Black lipid membranes (BLMs) have been developed by Müller and Rudin by painting lipid molecules dissolved in organic solvent over an aperture of (0.1–2) mm diameter in a hydrophobic wall [Müller et al. 1963]. Due to the large dimension of the aperture, BLMs lack SSMS' stability as they are supported by the rim only. On the contrary, they are a better mimic of natural cells featuring aqueous compartments on both sides of the bilayer. Moreover, access is easy to both sides of the membrane which is an advantage over vesicles whose interior is not readily accessible [Müller et al. 1963] (Fig. 1.14).

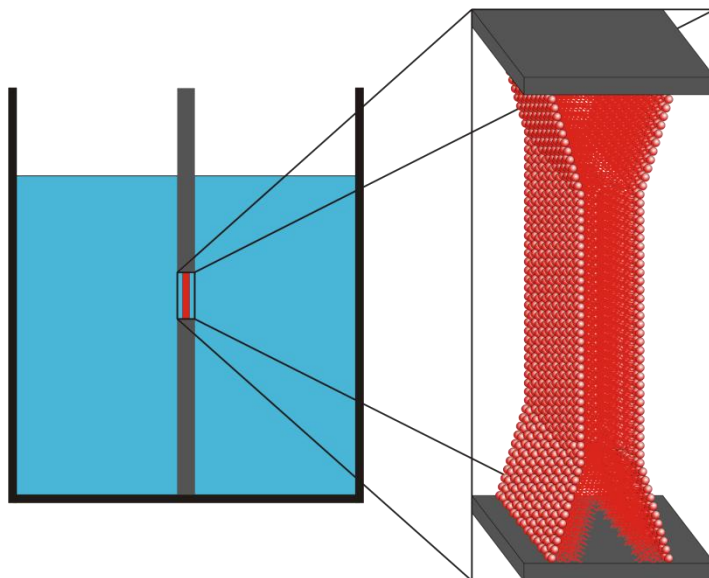


**Figure 1.14: Scheme of a typical BLM setup. Two aqueous compartments are separated by a hydrophobic wall which contains the aperture suspended by the bilayer. The solvent annulus becomes obvious as the free space where the monolayers are attached to the wall.**

A disadvantage of the Müller-Rudin method for BLM preparation is the residual solvent within the membranes. Montal and Müller have overcome this drawback and successfully prepared solvent-free BLMs. To this end, both compartments are filled with aqueous solutions to which lipids in volatile organic solvents are added. After solvent evaporation and monolayer formation in both compartments the water level is risen and a bilayer spanning the aperture results from assembling of the lipids. This method also allows for preparation of asymmetric bilayers as compartments on both sides of the aperture are mutually independent.

BLMs provide a well suited model system for the electrophysiological investigation of a range of membrane components – peptides [Bamberg et al. 1978; Bamberg et al. 1979] and especially ion channels [Gomezlagunas et al. 1989; Alonsoromanowski et al. 1995; Van Gelder et al. 2000] – unless the deficit in membrane stability or residual solvent prevents successful measurements.

#### 1.3.4 PORE-SUSPENDING MEMBRANES

All three membrane model systems described in Chapters 1.3.1–1.3.3 feature particular disadvantages as they either lack mechanical stability (BLMs), a second aqueous compartment and lateral lipid mobility (SSMs) or access to both aqueous compartments and the possibility to subject them to surface based research techniques (vesicles). These disadvantages have been overcome by pore-suspending membranes (PSMs), where lipid bilayers are spanned across apertures of honeycomb-like structures, i.e. porous substrates, such that individual BLMs are formed [Römer and Steinem 2004; Weiskopf et al. 2007]. Depending on the pores' diameter these membranes are referred to as micro- or nano-BLMs. While the former are usually prepared on  $\text{Si}_3\text{N}_4$ - [Weiskopf et al. 2007] or polycarbonate-based [Favero et al. 2005] substrates with pore diameters in the range of (0.8–4)  $\mu\text{m}$ , the latter are spanned across porous alumina with pore diameters of (10–400) nm [Li et al. 1998; Schmitt et al. 2008]. Schemes and a micrograph of typical pore-suspending membranes are shown in Figure 1.15.

To facilitate membrane formation, rims of porous substrates are functionalised in most cases. A major distinction of functionalisations is their polarity, i.e. their hydrophilic or hydrophobic character. Typical molecule classes used for functionalisation are thiolipids (on Au surfaces) or silane moieties bearing alkanes (on  $\text{SiO}_2$ ) and short thioalcohols (on Au), respectively (Fig. 1.15 A, B) [Heinemann and Schwille 2011; Kocun et al. 2011; Lazzara et al. 2011a; Lazzara et al. 2011b]. In general, two methods are applicable for preparation of PSMs: lipids in organic solvents can be painted over or vesicles can be spread on porous substrates. With regard to painting and mimicking natural examples, it has to be taken into account that residual solvent is likely to remain within model membranes. For spreading, the vesicles' size has to be considered since their diameter has to be considerably higher – i.e. several times as high – than the pores' diameter.



## INTRODUCTION

PSMs have been successfully utilised for the reconstitution of challenging ion channels for electrophysiological studies [Gaßmann et al. 2009], for the investigation of microdomains [Orth et al. 2012] and for SPM studies where the PSMs' mechanical features are probed by means of AFM [Mey et al. 2009; Kocun et al. 2011]. It has been revealed that PSMs on hydrophobically functionalised substrates feature a lateral tension termed 'pre-stress', whereas tension is reduced, mimicking plasma membranes more closely, on hydrophilically functionalised substrates. Moreover, the general applicability of SICM for PSM investigations has been demonstrated [Böcker et al. 2009].

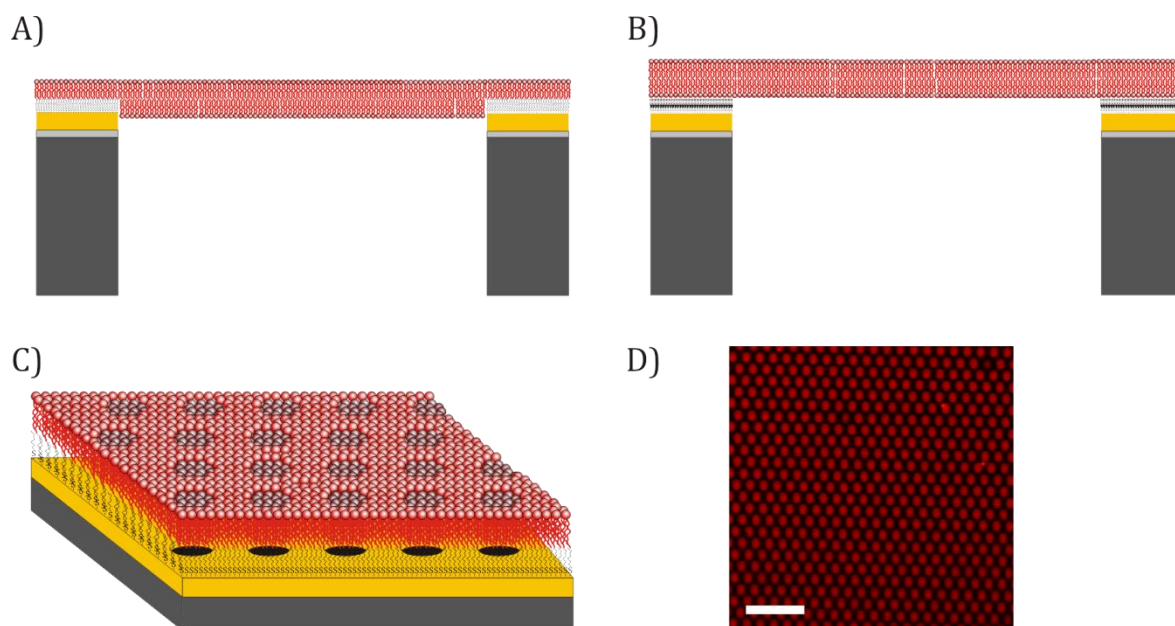


**Figure 1.15: Pore-suspending membranes.** A) Simple schematic cross-section of a PSM on a hydrophobically functionalised substrate. B) Simple schematic cross-section of a PSM on a hydrophilically functionalised substrate. It is known that there is a height difference between membrane on the rims and membrane suspending pores. Exact topographies remain to be elucidated, though. A significant difference is formation of the lower leaflet by CPEO3's cholesterol moieties on the rims, while a symmetric bilayer is formed on top of ME in B). C) Schematic of a small area of a pore-suspending membrane. Height differences are indicated by darker shading of the lipid molecules. The position of the first row's pores is displayed within the gold layer. D) Fluorescence micrograph of a 1,2-diphytanoyl-*sn*-glycero-3-phosphatidylcholine (DPhPC)/cholesterol (chol) (9:1, 0.1 mol% Texas Red) membrane on a CPEO3 (cf. Tab. 3.2) functionalised substrate (scale bar: 7.7  $\mu\text{m}$ ).

## 1.4 MEMBRANE ACTIVE PEPTIDES

Lipid membranes constitute an impermeable barrier to a wide range of polar molecules above a certain size threshold (cf. Ch. 1.3). Certain peptides, however, offer opportunities to translocate through lipid bilayers, and may even not only master membrane penetration themselves but serve as delivery vectors for cargo molecules providing interesting targets for medicinal research. While a family of peptides translocates without causing damage to the barrier, other molecules disturb the membrane structure. The latter are referred to as antimicrobial peptides (AMPs) which are distinguished from the former, most commonly called cell penetrating peptides (CPPs) – other terms found in literature comprise protein

transduction domain, membrane translocating sequence or Trojan peptides. This discrimination, however, has been assigned as an academic artefact to the existence of different peptide communities focusing either on cellular delivery (CPPs) or antimicrobial effects (AMPs) [Henriques et al. 2006; Palm et al. 2006].

CPPs can be classified by various measures [Madani et al. 2011]. A first is their origin such that peptides are distinguished as protein-derived (e.g. TAT [Frankel and Pabo 1988; Green and Loewenstein 1988; Vivès et al. 1997], penetratin [Joliot et al. 1991; Derossi et al. 1994]), chimeric peptides with at least two motifs from other peptides (e.g. transportan [Pooga et al. 1998] or its shorter analogue P10 [Soomets et al. 2000], which contain mastoparan and galanin motifs) or synthetic peptides (e.g. polyarginine) [El-Andaloussi et al. 2005; Zorko and Langel 2005]. Another CPP feature suitable for classification is peptide sequence and binding characteristics which assigns peptides accordingly as primary, secondary or nonamphipathic [Ziegler 2008]: primary amphipathic CPPs (paCPPs, e.g. transportan [Pooga et al. 1998], TP10 [Soomets et al. 2000]) comprise usually more than 20 amino acids with distinct hydrophilic and hydrophobic regions. Secondary amphipathic CPPs (saCPPs, e.g. penetratin [Joliot et al. 1991; Derossi et al. 1994], pVEC [Elmqvist et al. 2001], M918 [El-Andaloussi et al. 2007b]) are shorter than paCPPs and reveal their amphipathy only when undergoing structural changes upon interaction with lipid bilayers. Nonamphipathic CPPs (naCPPs, e.g. R9 [Futaki et al. 2001], TAT(48-60) [Frankel and Pabo 1988; Green and Loewenstein 1988; Vivès et al. 1997]) are even shorter than saCPPs and comprise many cationic amino acid residues, especially arginine.

#### 1.4.1 MECHANISMS OF CELLULAR UPTAKE

Elucidating the translocation mechanism of CPPs is of high interest in order to achieve better understanding of structure activity relationships and become able to predict the behavior of new CPPs or even design unprecedented peptides. Great effort has thus been applied to mechanistic investigations. Definite knowledge, however, has remained scarce, and it is widely believed that difficulties with respect to the assignment of CPPs to specific uptake mechanisms result from the existence of various pathways.

These differences are not only found within the group of CPP molecules or the same class of CPPs but even for individual CPPs, putatively depending on various parameter such as size (and thus cargo), temperature and cell type [Nakase et al. 2004; Boisseau et al. 2006; Tünnemann et al. 2006; El-Andaloussi et al. 2007a]. The two major ways suggested are direct penetration, i.e. energy-independent uptake, and endocytic uptake. The prevalence of energy-independent uptake mechanisms had been concluded from initial experiments, but contradicting results have been found in subsequent studies resulting in an ongoing debate on uptake mechanisms of many CPPs.

## INTRODUCTION

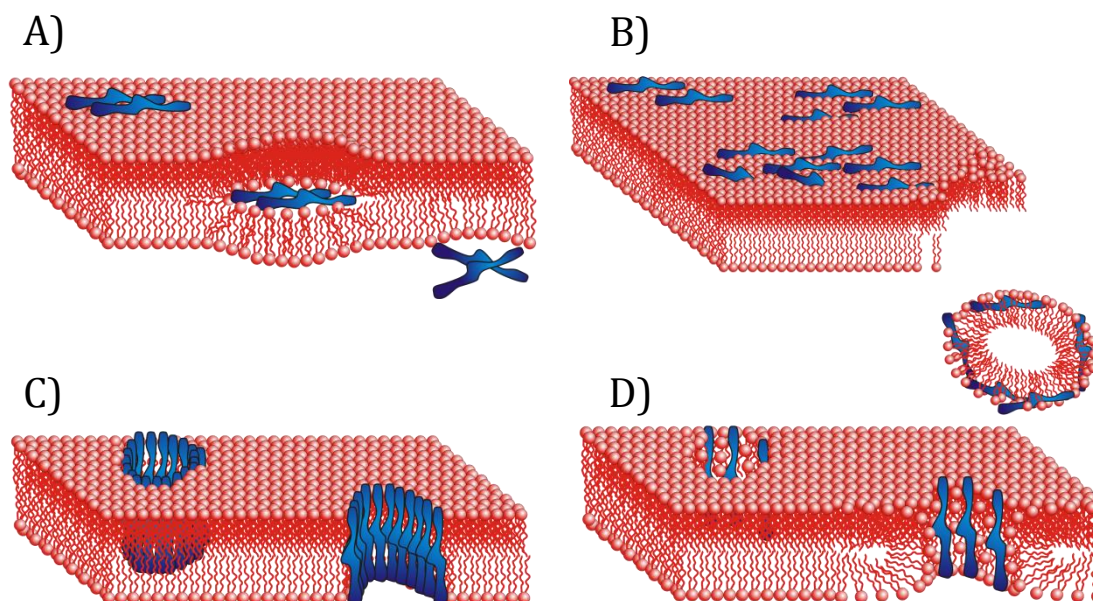


**Figure 1.16: Explanatory models for CPP uptake. A) Inverted micelle formation:** hydrophobic amino acid residues interact with phospholipid chains (top left) and the CPP invades the upper leaflet. An inverted micelle with hydrophilic and hydrophobic moieties facing the CPP and the bilayer's fatty acids, respectively, forms (middle) and translocates through the membrane where CPPs are released (bottom right). **B) Carpet-like model:** CPPs are attracted by phospholipid head groups (top left) and bind to them (top right). CPPs accumulate and form a 'carpet' (bottom left) until a threshold concentration is reached and the bilayer disassembles into micelles. **C) Barrel-stave:** CPPs enter the membrane and form a pore entirely lined with CPP molecules. **D) Toroidal:** CPPs enter the membrane. The resulting pore's walls consist of CPP molecules and lipid head groups after tilting of phospholipids by up to 90°.

### *Direct penetration*

Direct penetration itself comprises various ways having been described as inverted micelle formation, pore formation, the carpet-like and the membrane-thinning model, which are depicted in Figure 1.16 [Pouny et al. 1992; Derossi et al. 1996; Matsuzaki et al. 1996; Lee et al. 2005]. All four given pathways share a common first step which constitutes CPP-membrane interactions, i.e. electrostatic interactions between positively charged CPP moieties and negatively charged membrane components.

Inverted micelle formation (Fig. 1.16 A)) relies on hydrophobic interactions of mainly tryptophan residues with phospholipid chains in addition to the first electrostatic interaction step, rendering this mechanism an unlikely way for highly cationic, i.e. especially naCPPs. The tightened CPP-lipid interactions allow for invasion of the membrane where the membrane's hydrophobicity and repulsion towards the CPP molecule is attenuated by the lipid molecules forming the inverted micelle. Having translocated to the membrane ulterior, the inverted micelles release the CPPs into the aqueous environment.

Pore formation can be further bisected into the barrel stave (Fig. 1.16 C)) and the toroidal model (Fig. 1.16 D)), which differ from each other in a way that there is only lateral rearrangement of phospholipids in the former case where CPP molecules form a barrel and thus a pore, whereas lipids forming the pore border need to tilt up to 90° in case of the latter such that the pore is lined by lipid head groups and CPPs [Matsuzaki et al. 1996]. While CPPs interact only with phosphate groups in the toroidal model, hydrophobic interactions take



place in the barrel stave model between CPPs and lipid chains. Pore formation starts in both cases when CPP concentrations reach a certain threshold.

Explanatory approaches for the concentration threshold, at which CPPs begin to have an effect are the carpet-like [Pouny et al. 1992] and the membrane-thinning [Lee et al. 2005] model. The former simply describes an accumulation of CPP molecules on the membrane surface, eventually resulting in micellisation of the membrane (Fig. 1.16 B)). From the sigmoidal concentration dependence of CPP activities it becomes obvious that single CPP molecules do not affect the membrane's structure. Rather, an accumulation and a certain concentration of CPP molecules are needed to allow for measurable effects, i.e. translocation. The membrane thinning model, on the contrary, is based on the observation that a simple aggregation model does not reflect experimental results sufficiently adequately as it predicts weaker cooperativity than measured. It assumes an increase in average intermolecular distances on the lipid chain level as CPPs are embedded into the bilayer at the phospholipid head group level giving rise to an increase in free energy. The effect of a pore on the membrane's free energy is less destabilising than that of single CPP molecules embedded and thus favoured above a threshold concentration.

### *Endocytosis*

Endocytosis, similar to direct penetration mechanisms, comprises a variety of possible pathways: clathrin [Säälik et al. 2004]- or caveolin [Fittipaldi et al. 2003]-dependent, pit-coating-independent endocytosis [Mayor and Pagano 2007] as well as macropinocytosis [Nakase et al. 2004; Jones 2007]. A major difference between the latter and the former is the size of the vesicles formed during endocytosis. While macropinosomes can reach several micrometers in diameter, clathrin- and caveolin-coated vesicles exhibit diameters of few 100 nm and (50–80) nm, respectively. Furthermore, as macropinocytosis is initiated by the formation of 'ruffles' via actin polymerisation perpendicular to the cell surface, extracellular fluid is taken up eventually.

### 1.4.2 MELITTIN

Melittin comprises the major component (50% dry weight) of the honey bee (*Apis mellifera*) venom. It has been discovered in the 1950s and termed 'direct lytic factor' by Neumann et al. due to lecithin-independence of hemolysis [Neumann et al. 1953]. A wide range of studies has been conducted in the last 60 years rendering melittin one of the most extensively studied membrane active peptides; the reader is hence referred to the review by Raghuraman and Chattopadhyay for a comprehensive overview [Raghuraman and Chattopadhyay 2007], whereas a short characterisation of melittin is given below.

The 2.8 kDa peptide comprises 26 amino acids: GIGAVLKVLTTGLPALISWIKRKRQQ [Habermann and Jentsch 1967]. At physiological pH 7.4 it is highly cationic (charge +5 to +6, pI = 12.02 [Gasteiger et al. 2003]) due to three lysine and two arginine residues. Its

## INTRODUCTION

amphipathy results from 19 apolar amino acids within amino acids 1–20 opposed to four charged and two polar residues at the C-terminus (residues 21–26) such that the molecule is predominantly hydrophobic, but also water soluble due to its high charge. In an aqueous environment, melittin adopts a random coil structure at low concentrations. Higher melittin concentrations, however, lead to association up to tetramers as do high salt concentrations and basic pH values [Faucon et al. 1979; Talbot et al. 1979; Bello et al. 1982; Quay and Condie 1983; Raghuraman and Chattopadhyay 2006]. Figure 1.17 depicts a dimer of predominantly  $\alpha$ -helical melittin molecules.

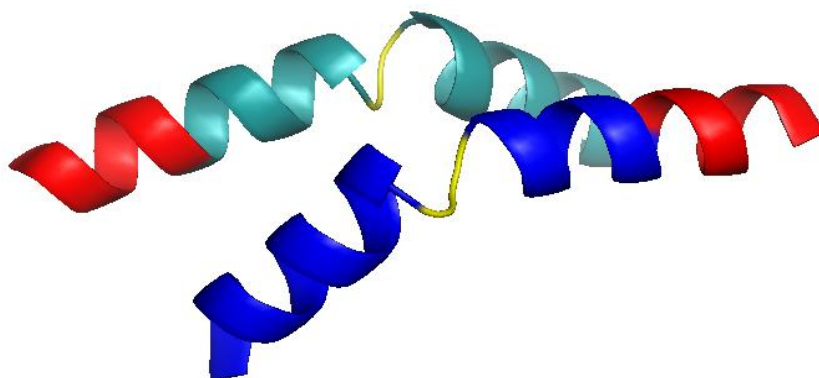


**Figure 1.17:** X-ray structure of a dimer of melittin molecules (PDB code: 2MLT). Two  $\alpha$ -helical regions, separated by a short randomly oriented segment (yellow) become apparent in each molecule. The highly hydrophilic C-termini are labelled in red.

Similarly to structural changes upon aggregation of melittin molecules, the peptide adopts an  $\alpha$ -helical structure when inserted into lipid membranes [Brown and Wüthrich 1981; Ghosh et al. 1997; Yang et al. 2001]. A difference, however, is found for the angle between melittin's  $\alpha$ -helical segments, being increased from  $120^\circ$  in solution to  $\sim 140^\circ$  or  $\sim 160^\circ$  [Naito et al. 2000]. The peptide's affinity for lipid membranes has been shown to depend on the phospholipids such that negatively charged lipids result in a 100-fold increase of membrane-affinity [Batenburg et al. 1988; Lee et al. 2001]. On the other hand, this increased affinity does not entail increased lysis; several studies have shown that negatively charged lipids guard lipid bilayers from lysis [Benachir and Lafleur 1995; Monette and Lafleur 1995; Hinch and Crowe 1996; Ghosh et al. 1997; Pott et al. 2001]. It has been suggested that this guarding effect stems from an altered microenvironment of the tryptophan residue [Chattopadhyay and Rukmini 1993; Ghosh et al. 1997; Raghuraman and Chattopadhyay 2004]. A similar effect has been reported for cholesterol, which has been found to inhibit melittin binding to the membrane. The depth to which tryptophan invades the bilayer is reduced in the presence of cholesterol which putatively decreases melittin's lytic activity [Benachir et al. 1997; Raghuraman and Chattopadhyay 2004; Allende et al. 2005]. Further possible reasons suggested are the formation of a complex of melittin's tryptophan with cholesterol's rigid ring structure or increased deformation energy induced by tightened packing of the lipids. Cholesterol's influence becomes significant in the light of its high natural occurrence in erythrocytes ( $\sim 45$  mol%), melittin's primary target [Yeagle 1985; Raghuraman and Chattopadhyay 2005].

A wide range of experiments has been conducted investigating the effect of melittin on various membrane systems such as erythrocytes, liposomes or solid supported membranes. In general, two different notations have been applied to report melittin concentrations at which the peptide affects lipid bilayers: either as an independent concentration [ $\text{mol l}^{-1}$ ], or depending on the lipid amount as a peptide:lipid (P:L) ratio. Concentration values at which membranes are affected such that leakage or micellisation is observed are reported in the range of (0.2–1)  $\mu\text{M}$  [Sessa et al. 1969; DeGrado et al. 1982; Katsu et al. 1989; Dempsey 1990; Oren and Shai 1997; van den Bogaart et al. 2008]. On the other hand, P:L ratios commonly found are in the range of 1:2000–1:15 [Ohki et al. 1994; Ladokhin et al. 1997; Matsuzaki et al. 1997; Klocek et al. 2009].

Studies on melittin's orientation within lipid bilayers have revealed that transmembrane pores exist only in case of perpendicular alignment relative to the membrane plane, hinting at melittin molecules lining the pore walls in this orientation. Diameters of these pores have been determined in the range between 10 Å and 60 Å by means of vesicle leakage and neutron diffraction experiments [Rex 1996; Ladokhin et al. 1997; Matsuzaki et al. 1997; Yang et al. 2001]. While studies in the late 1980s concluded a barrel-stave model for melittin-induced pores (cf. Fig. 1.16 C) [Vogel and Jähnig 1986; Sansom 1991], later oriented circular dichroism, neutron diffraction and vesicle leakage experiments, as well as molecular dynamics simulations, have disclosed results consistent with a toroidal model (cf. Fig. 1.16 D) [Lin and Baumgaertner 2000; Yang et al. 2001; Allende et al. 2005]. Evidence for a carpet-like model, however, has been found as well for zwitterionic SSMs [Steinem et al. 2000] and liposomes containing negatively charged lipids [Ladokhin and White 2001]. Another study has revealed effects depending on melittin concentrations such that membrane micellisation is achieved at high P:L ratios only, whereas lower ratios lead to leakage from liposomes [Ohki et al. 1994].

### 1.4.3 PENETRATIN

Penetratin comprises amino acids 43–58 of the third helix of the *Drosophila melanogaster* Antennapedia homeodomain (AntHD) allowing for the homeoprotein's internalisation and DNA binding of the homeodomain. The translocation of AntHD and Penetratin has been found in the 1990s [Joliot et al. 1991; Derossi et al. 1994; Derossi et al. 1996] as the second CPP, only preceded by TAT [Frankel and Pabo 1988; Green and Loewenstein 1988].

The 2.2 kDa peptide comprises 16 amino acids: RQIKIWFQNRRMKWKK [Derossi et al. 1994]. Featuring four lysine and three arginine residues, it bears a charge of +7 at physiological pH 7.4 ( $\text{pI} = 12.31$  [Gasteiger et al. 2003]). In an aqueous environment a random coil structure is prevalent for penetratin. In the presence of anionic phospholipids, specifically at low peptide/lipid ratios (1:325), its structure changes to an  $\alpha$ -helical conformation (Fig. 1.18) [Berlose et al. 1996; Derossi et al. 1996; Drin et al. 2001; Magzoub et al. 2001; Lindberg et al. 2003]. At higher peptide/lipid ratios (1:10), anti-parallel  $\beta$ -sheets are formed [Bellet-Amalric et al. 2000; Magzoub et al. 2001; Persson et al. 2001]. Occurring structural changes, however,

## INTRODUCTION

are mutually dependent, indicated by the formation of hexagonal phases [Berlose et al. 1996] or changes in the orientation of fatty acids [Zhang and Smith 2005] in the lipid bilayer.

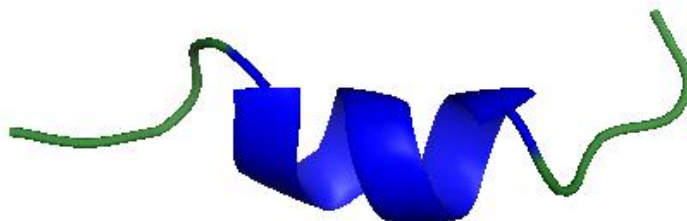


**Figure 1.18: Structure of penetratin (third helix of AnthD) in membrane-mimetic environment. An  $\alpha$ -helical region is bordered by two randomly oriented segments [Czajlik et al. 2002].**

To date, the translocation mechanisms of penetratin remain rather obscure. While first experiments have hinted at an energy-independent uptake mechanism for penetratin [Derossi et al. 1994], recent studies reflect a more complex picture, i.e. predominantly endocytic pathways [Nakase et al. 2004; Maiolo et al. 2005; Duchardt et al. 2007].

The investigation of ways to exploit the CPPs' features has started soon after their exploration. In the beginning, AnthD has been utilised: oligonucleotides (against the  $\beta$ -amyloid precursor protein) and protein domains (C-terminus of rab3a to inhibit the release of the peptide hormone prolactin) have been fused to the homeodomain and successfully internalised by cell cultures [Perez et al. 1994; Allinquant et al. 1995] as well as *in vivo* (induction of T-cell response through a cytotoxic-T-cell epitope) [Schutze-Redelmeider et al. 1996]. Further development has led to the application of penetratin instead of AnthD resulting in successful delivery of both oligopeptides and oligonucleotides [Theodore et al. 1995; Troy et al. 1996]; an overview is given by Dupont et al. [Dupont et al. 2005]. Interest in penetratin as a delivery system has never ceased and continues to inspire new studies until today aiming at combined systems providing enhanced pharmacokinetics, e.g. in the field of brain drug delivery [Xia et al. 2012] or transdermal delivery of drugs [Cohen-Avrahami et al. 2012].





## 2 SCOPE OF THESIS

Scanning ion conductance microscopy (SICM) provides a most suitable tool for the investigation of topography and ion conductance features of flexible structures as it avoids mechanical contact between probe and sample. Interactions of cell penetrating peptides (CPPs) with lipid membranes are of growing interest with respect to questions of mechanisms or peptide concentrations which affect lipid membranes as well as possible applications, e.g. for drug delivery. Pore-suspending membranes (PSMs) represent a highly versatile member of the range of membrane model systems which allow for detailed and controlled investigation of specific membrane features.

The main objective of this thesis is the development and application of an assay combining the three components named above, i.e. a SICM based assay providing a tool to investigate interactions between peptides and pore-suspending membranes. To gain insights into these interactions and thereby facilitating establishment of the SICM assay, a confocal laser scanning microscopy (CLSM) based assay is developed.

A first objective is the establishment of a generalised protocol for the preparation of PSMs comprising various lipid compositions on both hydrophobically and hydrophilically functionalised substrates. Proof of successful preparation is provided via imaging of lipid membranes by means of CLSM and SICM. The latter also yields topography information for PSMs.

Once reliable preparation of PSMs is established and proven, the CLSM assay is developed. It allows for the investigation of melittin and penetratin titration experiments which aim at elucidation of the influence of PSM composition as well as substrate functionalisation on the PSM peptide interactions, notably peptide concentrations at which membrane rupturing occurs and kinetics of the rupturing process. PSM compositions vary between purely zwitterionic lipids, zwitterionic lipids with 10% cholesterol content and zwitterionic lipids with 20% negatively charged lipids as these are expected to induce variations in the membrane melittin interactions. Substrates are functionalised hydrophobically or hydrophilically. Penetratin is employed to demonstrate general applicability of the assay.

Information provided by the CLSM assay is utilised to develop the SICM assay. In general, the same range of experiments as performed by means of CLSM is conducted by means of SICM. PSM compositions and substrate functionalisations are varied to examine and quantify their influence on melittin interactions with the lipid bilayers to proof successful establishment of the assay, i.e. substrates are functionalised hydrophobically or hydrophilically and PSMs are prepared from lipid compositions described above.





## 3 MATERIALS AND METHODS

### 3.1 MATERIALS

#### 3.1.1 BUFFERS & SOLUTIONS

Different solutions were used for different experiments and purposes in the present study which are shown in Table 3.1. Every aqueous solution was prepared with ultrapure water ( $R > 18.2 \text{ M}\Omega\text{m}$ ) from a Milli-Q Gradient A10 (Millipore, Eschborn, Germany).

**Table 3.1: Buffers and solutions used in this study.**

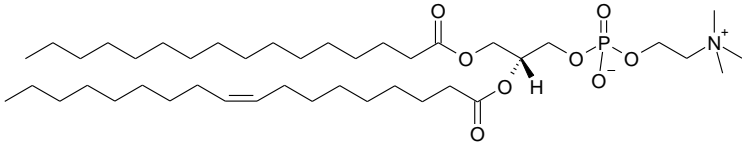
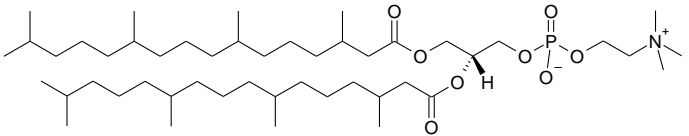
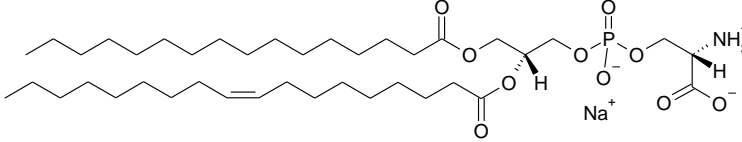
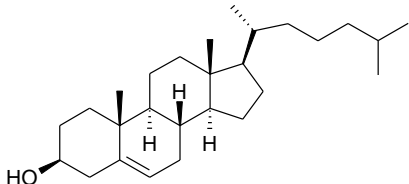
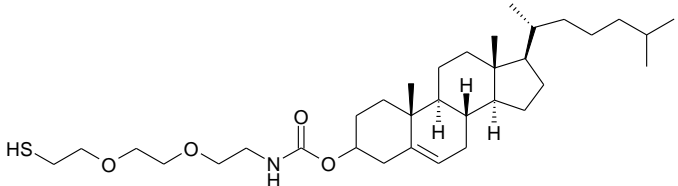
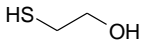
<b>name</b>	<b>content</b>
spreading buffer	100 mM KCl 10 mM Tris pH 7.4
spreading buffer with $\text{Ca}^{2+}$	100 mM KCl 10 mM Tris 50 mM $\text{CaCl}_2$ pH 7.4
sucrose solution	300 mM sucrose
bleach solution	1.6 M NaClO

#### 3.1.2 LIPIDS, THIOLS AND FLUORESCENT DYE

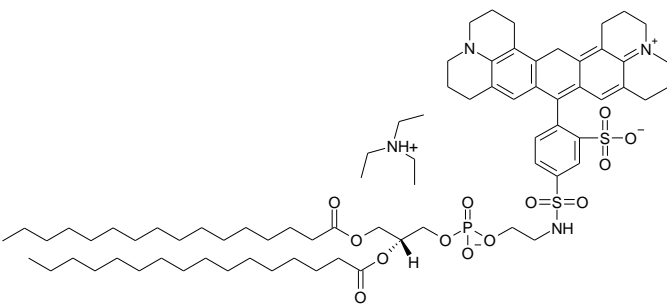
To investigate the interactions of peptides with various lipid membranes, the lipid compositions of the membranes and the functionalisations of the substrates, on which membranes were prepared, were varied. Table 3.2 shows a summary of molecules used in this study for substrate surface functionalisation and membrane preparation comprising zwitterionic phosphatidylcholines (POPC, DPhPC), a negatively charged phosphatidylserine (POPS) and the steroid lipid cholesterol, the thiols used for substrate functionalisation and the fluorescent dye used for membrane labeling (Texas Red DHPE).

# MATERIALS AND METHODS

**Table 3.2: Lipids, thiols and fluorescent dye used in this study.**

name	structure
<p>POPC (1-palmitoyl-2-oleoyl-<i>sn</i>-glycero-3-phosphatidylcholine)</p>	
<p>DPhPC (1,2-diphytanoyl-<i>sn</i>-glycero-3-phosphatidylcholine)</p>	
<p>POPS (1-palmitoyl-2-oleoyl-<i>sn</i>-glycero-3-phosphatidyl-L-serine (sodium salt))</p>	
<p>chol (cholesterol)</p>	
<p>CPEO3 (cholesteryl polyethylenoxy thiol)</p>	
<p>ME (mercaptoethanol)</p>	

**Table 3.2: Lipids, thiols and fluorescent dye used.**

<p>TR DHPE (Texas Red DHPE, <i>N</i>-(Texas Red sulfonyl)-1,2- dihexadecanoyl-<i>sn</i>-glycero- 3-phosphoethanolamine (triethylamine salt))</p>	
--	--

### 3.1.3 PEPTIDES

In this study, fluorescence microscopy experiments (cf. Ch. 3.3.1) were conducted with two different peptides. Melittin was first used to establish the fluorescence assay and to find critical concentration ranges that lead to rupturing of the pore-suspending membranes. It was furthermore applied in this study's central part, i.e. scanning ion conductance microscopy (SICM) experiments (cf. Ch. 3.3.2). In addition to melittin, penetratin was used to test the developed fluorescence assay for its general applicability. Protein concentrations were determined by means of UV/Vis spectroscopy (cf. Ch. 3.3.3).

#### *Melittin*

The 2.8 kDa peptide melittin (Sigma Aldrich, Saint Louis, MO, USA) is the major constituent of the venom of the western honey bee *apis mellifera* and comprises 26 amino acids (GIGAVLKVLTTGLPALISWIKRKRQQ). While the first 20 amino acids are hydrophobic, the C-terminus consists of hydrophilic residues resulting in the peptides amphiphilic features. The used compound was isolated from bee venom with a purity of  $\geq 85\%$  (HPLC).

#### *Penetratin*

The 2.2 kDa peptide penetratin (PolyPeptide Laboratories, Strasbourg, France) is the third helix (residues 43-58) of the homeodomain of *Drosophila melanogaster* and comprises 16 amino acids (RQIKIWFQNRRMKWKK). The C-terminus contains the majority of hydrophilic amino acids, the two, with respect to membrane interaction, important tryptophan residues are residues 48 and 56 of the homeodomain. The used compound was synthesised with a purity of  $\geq 97.5\%$  (HPLC).

## MATERIALS AND METHODS

### 3.2 PREPARATIVE METHODS

#### 3.2.1 PREPARATION OF GIANT UNILAMELLAR VESICLES

A modification of the electroformation protocol described first by Angelova and Dimitrov [Angelova and Dimitrov 1986] and expanded by Angelova and co-workers [Angelova et al. 1992] was used for the preparation of giant unilamellar vesicles (GUVs) resulting in homogeneous vesicle populations with diameters in the range of (10–100)  $\mu\text{m}$ . Dried lipid films are rehydrated and swell in an aqueous, non-conducting solution. Lamellar structures are thought to be disassociated by the application of an alternating electric field, vibrating with this field's frequency. Having grown to a critical size these glass detached lipid structures form giant unilamellar vesicles [Doeven et al. 2005].

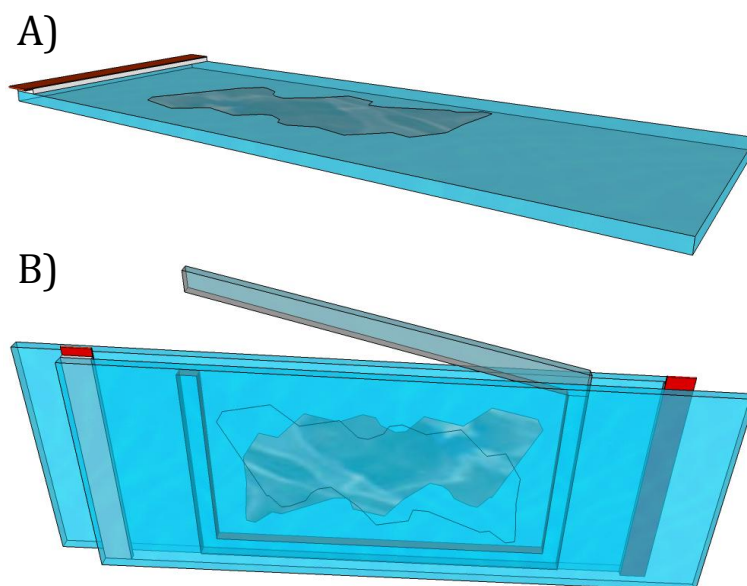


**Figure 3.1: A) Lipid film spread on an indium tin oxide (ITO) covered glass slide with Teflon spacer (white) and Cu tape attached (red); B) GUV electroformation chamber consisting of two ITO slides with a silicon frame containing the lipid film covered areas, which is then filled with 0.3 M sucrose solution.**

20  $\mu\text{l}$  of a 5 mM lipid solution in  $\text{CHCl}_3$  were spread on the conducting side of an ITO covered glass slide (Präzisionsglas & Optik GmbH, Iserlohn, Germany) and dried in a vacuum chamber for at least 3 h. Copper strips were attached to the Teflon spacers on the glass slides. A flexible silicon rectangle with an opening at one corner was placed between two ITO glass slides such that the lipid films were contained by the silicon frame. The assembled GUV chamber was held together by three foldback clamps and the silicon frame was filled with a degassed 300 mM sucrose solution. The rectangle was closed and a fourth clamp was attached to prevent leakage. The frequency generator 33220A (Agilent, Santa Clara, CA, USA) was connected to the copper strips, and a sine-wave voltage of 1.6 V with a frequency of 12 Hz was applied for 3 h. The frequency was then decreased slowly ( $1 \text{ Hz min}^{-1}$ ) to 5 Hz, and a square voltage of 1.6 V was applied for 10 min. The frequency generator was turned off, the resulting GUV solution was transferred into 2 ml Eppendorf cups with a 1 ml pipette to

reduce shear-force induced damage of vesicles and stored at room temperature for up to one week. Used lipid compositions are shown in Table 3.3.

**Table 3.3: Lipid compositions of GUVs used.**

GUV name	lipid composition
POPC	POPC, 0.1-0.5 mol% TR
DPhPC/chol	DPhPC / cholesterol 9:1, 0.1-0.5 mol% TR
POPC/POPS	POPC / POPS 4:1, 0.1-0.5 mol% TR

### 3.2.2 PREPARATION OF PORE-SUSPENDING MEMBRANES

fluXXion substrates (Fig. 3.2) with pore diameters of 1.2  $\mu\text{m}$  (36.2% porosity) were used for every experiment. According to the intended functionalisation type, different procedures (sputter coating, evaporation) and sequences of these procedures were applied.

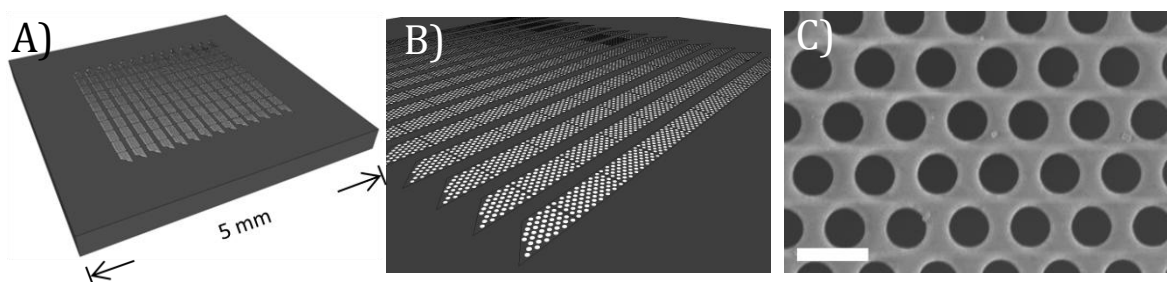


**Figure 3.2:** A) Total schematic view of a porous fluXXion substrate with an edge length of 5 mm. The middle square containing porous regions comprises an area of 3x3 mm<sup>2</sup>. B) Close-up schematic view. 14 stripes of 10 porous regions are visible (inner regions: 75x150  $\mu\text{m}^2$  rectangles, outer regions: mirrored right trapezoids), pore sizes are not true to scale. C) Scanning electron micrograph of a fluXXion substrate with 1.2  $\mu\text{m}$  pore diameter, corresponding to 36.2% porosity (scale bar: 2  $\mu\text{m}$ ).

#### *Preparation of pore-suspending membranes on hydrophobically functionalised substrates*

Substrates were cleaned for 5 min in an argon plasma (Plasma Cleaner PDC 32 G-2, Harrick, Ithaca, NY, USA) to remove any organic contaminants from the surface. They were immediately placed in the Sputter Coater 108 auto (Cressington Scientific Instruments, Watford, UK) which was flushed with argon for 10 s and evacuated for 15 min twice. Substrates were sputter coated with a 2.5 nm thin layer of titanium as an adhesive layer. Argon flushing and evacuation of the chamber was repeated twice before substrates were sputter coated with a 30 nm thin gold layer. After completion of the gold coating substrates were directly placed into a freshly prepared 0.1 mM CPEO3 solution and incubated at room temperature over night. The 0.1 mM CPEO3 solution in 1-propanol was prepared from a 4 mM stock solution in 1-propanol that was kept at -20 °C.

## MATERIALS AND METHODS

Substrates were taken out of the CPEO3 solution and rinsed with 2.5 ml 1-propanol twice. They were then dried under a nitrogen stream and assembled in the SICM chamber (Fig. 3.3) where they were covered with 1 ml ethanol for 15 min to remove residual air bubbles from the pores. Ethanol was then slowly exchanged against spreading buffer (spreading buffer with  $\text{Ca}^{2+}$  in case of POPS containing GUVs): 4 ml buffer were added before 2 ml buffer were subsequently removed and added at least 12 times to ensure complete removal of ethanol. Substrates were kept under spreading buffer for 1 h to allow for straightening up of the cholesterol moieties of the CPEO3 molecules. 50  $\mu\text{l}$  GUV solution were added onto the substrates, and samples were kept at 37 °C for 1 h. Successful spreading was checked by means of fluorescence microscopy. The sample was gently rinsed with 25 ml buffer to remove excess vesicles before subjection to confocal laser scanning microscopy (CLSM) or SICM.

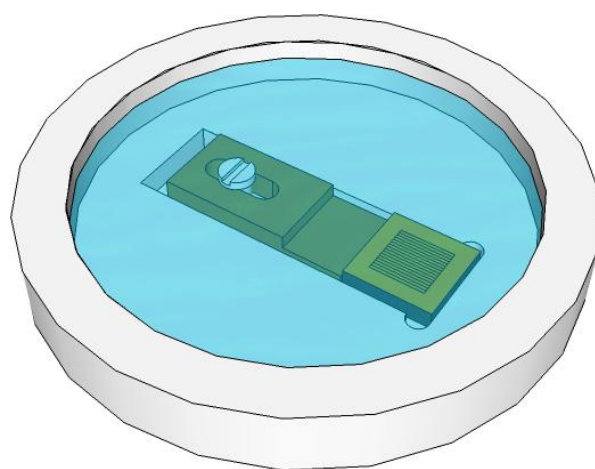


**Figure 3.3: FluXXion substrate assembled in a polytetrafluoroethylene (PTFE) SICM chamber filled with buffer solution.**

### *Preparation of pore-suspending membranes on hydrophilically functionalised substrates*

Substrates were cleaned for 5 min in an argon plasma to remove any organic contaminants from the surface. They were immediately placed in the sputter coater which was flushed with argon for 10 s and evacuated for 15 min twice. Substrates were first sputter coated with titanium for 30 s. Up to nine substrates were placed in the evaporator BAL-TEC MED 020 (Bal-tec, Balzers, Liechtenstein) exactly below the gold carrying vessel. The chamber was evacuated until a pressure of  $p < 5 \cdot 10^{-6}$  bar was achieved. 30-35 nm of gold were evaporated onto the substrates with rates of  $1 \text{ nm s}^{-1}$  (corresponding to currents of  $I = (57-61) \text{ A}$ ). Substrates were stored at room temperature.

A 20 mM ME stock solution in ethanol was produced weekly, and a 1 mM ME solution in ethanol was made from this stock solution immediately before usage. After plasma treatment (30 s (argon) and 5 min (oxygen)) gold coated substrates were incubated with 1 mM ME for 1 h.

Substrates were taken out of the ME solution and rinsed with 1 ml ethanol twice. They were then dried under a nitrogen stream and placed in a Petri dish where they were covered with 2 ml ethanol for 15 min to remove residual air bubbles from the pores. Ethanol was then

slowly exchanged against spreading buffer (spreading buffer with  $\text{Ca}^{2+}$  in case of POPS containing GUVs): 4 ml buffer were added before 2 ml of buffer were subsequently removed and added at least 12 times to ensure complete removal of ethanol. 25  $\mu\text{l}$  GUV solution were added onto the substrates, and samples were kept at 4 °C for 1 h. Successful spreading was checked by means of fluorescence microscopy. The sample was gently rinsed with 25 ml buffer to remove excess vesicles before subjection to CLSM or SICM.

### 3.2.3 PREPARATION OF AG/AGCL ELECTRODES

Currents in the 1 nA range are detected during SICM measurements. Ag/AgCl electrodes are the electrodes of choice as there is no change of polarity caused by electron transitions. A highly conductive metal with a surface as large as possible is desired. For these reasons, silver – featuring the highest electric conductance of all metals [Riedel and Janiak 2007] – is used, and it is sanded prior to chloridation.

Silver wires (1 mm diameter) were sanded and cleaned with ethanol and ultrapure water before they were kept in a NaOCl solution for 30 min. Wires were rinsed with ethanol and ultrapure water prior to usage.

### 3.2.4 PREPARATION OF NANOPIPETTES

Nanopipettes were drawn from borosilicate glass capillaries with filaments with inner diameters of 0.58 mm, outer diameters of 1.00 mm (Science Products, Hofheim, Germany) on a P-1000 micropipette puller with a 2.5 mm box filament (Sutter Instruments, Novato, CA, USA).

To achieve pipettes with short tapers and typical resistances of  $100 \text{ M}\Omega < R < 250 \text{ M}\Omega$ , i.e. currents of  $0.8 \text{ nA} < I < 2 \text{ nA}$  at  $U = 200 \text{ mV}$ , one of the standard protocols had to be custom modified such that the taper was shortened but the tip radius remained small. In general, change in pipette geometries are obtained by variation of four parameters: delay, pressure, heat and velocity. Shorter tapers are achieved by an increase of delay or pressure values – tip diameters are increased alongside – or a decrease of the heat values. Smaller tips and higher resistances can be obtained by an increase in the velocity value. Parameter values used for pipette pulling in this study are shown in Table 3.4.

**Table 3.4: Pulling parameters for SICM pipets produced with the P-1000 micropipette puller.**

<b>parameter</b>	ramp	heat	pull	velocity	delay	pressure	<i>t</i> / s
<b>value</b>	523	ramp - 10	55	110	80	400	10.4-10.5

## 3.3 ANALYTICAL METHODS

## 3.3.1 FLUORESCENCE MICROSCOPY

Fluorescence microscopy is an important method in biological and biophysical research as it enables visualisation of objects in the sub- $\mu\text{m}$  range which cannot be detected by human vision. There is no mechanical contact between probe and sample and sometimes the investigated particles' intrinsic fluorescence can be exploited such that no modification of the sample is needed. In most cases, however, a chemical modification of the molecules to be detected is done, i.e. a fluorescent moiety (fluorophore) is bound to them or fluorescent molecules are added to the otherwise non fluorescent sample [Lichtman and Conchello 2005].

Fluorescence microscopy utilises the fluorophores' ability to absorb light of a specific wavelength and emit light of a specific longer wavelength [Wedler 1997; Lakowicz 2006]. The fundamental principle of fluorescence (Stokes shift [Stokes 1852]) is based on different velocities of nuclear motion and electron transitions taking place upon excitation of the molecule as can be explained on the basis of the Franck-Condon principle (Fig. 3.4) [Condon 1926; Franck and Dymond 1926].

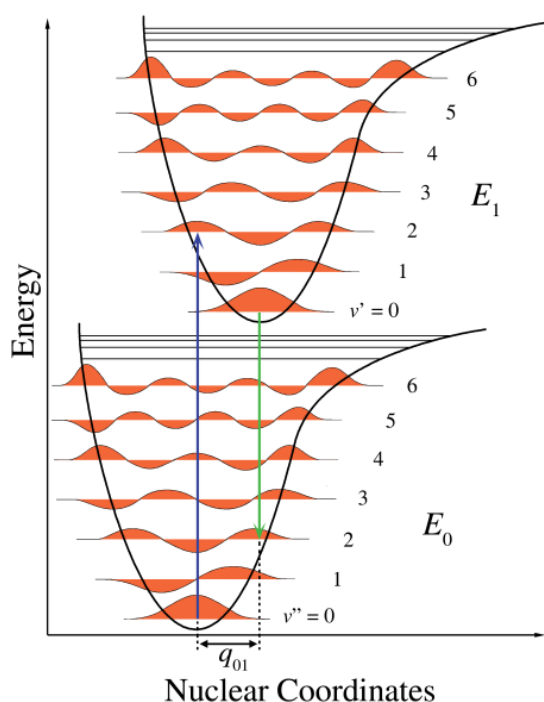


**Figure 3.4; Franck-Condon principle energy diagram depicting vibronic transitions of an electron from its electronic and vibrational ground states  $E_0$  and  $v'' = 0$ , respectively, to excited states  $E_1$  and  $v' > 0$  (here:  $v' = 2$ ) [Gabriel 2007].**

Absorption of a photon causes an electron's transition from its electronic ground state  $E_0$  to the excited state  $E_1$ . This transition is linked to a transition from the vibrational ground state  $v'' = 0$  to an excited state  $v' > 0$  as it is faster than nuclear movements. Excitation (blue,



Fig. 3.4) is caused by light of a wavelength  $\lambda_{\text{abs}}$ . Vibrational relaxation of the system to  $v' = 0$  happens then prior to emission (red arrow, Fig. 3.4) of light of a wavelength  $\lambda_{\text{em}} > \lambda_{\text{abs}}$ .

Time series experiments in this study were conducted on the confocal microscope LSM 710 (Carl Zeiss, Jena, Germany). Images were recorded with a water immersion objective with 63x magnification and a numerical aperture of 1.0 (W Plan-Apochromat, Carl Zeiss, Jena, Germany). Texas Red DHPE was excited at a wavelength of  $\lambda_{\text{abs}} = 561$  nm while emitted light was detected in a range of (574–619) nm.

Checking spreading success was conducted on the LSM 710 under conditions described above or on the BX-51 (Olympus, Hamburg, Germany) with a water immersion objective with 40x magnification. In case of the latter, a mercury-vapour lamp was used for excitation of Texas Red DHPE with an excitation filter to allow passing of light in a range of  $\lambda_{\text{abs}} = (530\text{--}550)$  nm while light emission was detected at  $\lambda_{\text{em}} = 590$  nm.

### *Epifluorescence microscopy*

In case of an epifluorescence microscope, a continuous spectrum is emitted by a light source such as a mercury-vapor lamp, and the desired wavelength is chosen by means of a band-pass filter. A dichroic mirror reflects light of the wavelength  $\lambda_{\text{abs}}$  onto the sample where electrons are excited. Upon fluorescence, light of the wavelength  $\lambda_{\text{em}}$  is emitted and passes the dichroic mirror and another band-pass filter which ensures that wavelengths different from  $\lambda_{\text{em}}$  are prevented from reaching the detector (Figure 3.5).

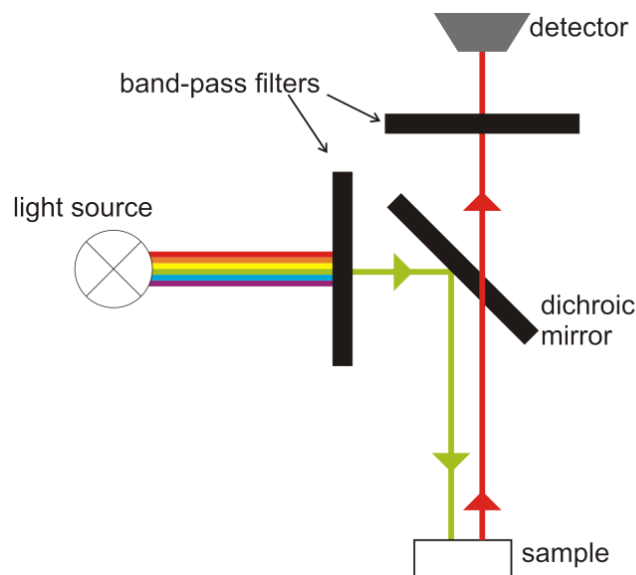


**Figure 3.5: Principle setup of an epifluorescence microscope.** A specific wavelength is chosen by band-pass filters from the continuous spectrum of the light source and before incidence of the reflected light at the detector, respectively. The dichroic mirror reflects light of the wavelength  $\lambda_{\text{abs}}$  (green) while light of the wavelength  $\lambda_{\text{em}}$  (red) is allowed to pass.

As long as super resolution methods of the STED (stimulated emission depletion) [Hell and Wichmann 1994] family (e.g. STORM/PALM [Betzig et al. 2006; Hess et al. 2006; Rust et al. 2006]) are not considered, a fluorescence microscope's resolution  $d$  is defined by Abbe's law

## MATERIALS AND METHODS

[3.1] [Abbe 1882] where  $\lambda$  is the wavelength,  $n$  the medium's refractive index,  $\alpha$  one half of the angular aperture and  $NA$  the numerical aperture:

$$d = \frac{\lambda}{2n \sin \alpha} = \frac{\lambda}{2NA} \quad [3.1]$$

The diffraction limit is therefore  $\frac{1}{2} \lambda_{\text{abs}}$  as the light beam does not only excite an infinitesimal spot but a finite volume of the sample. This excitation of out of focus planes leads to a decrease in quality as images are combinations of sharp images of the focal plane and blurred images of the planes below and above.

### *Confocal laser scanning microscopy*

Confocal laser scanning microscopy as an enhancement of epifluorescence microscopy was devised by Minsky in 1955 [Minsky 1988]. The term refers to the three major differences of a CLSM compared to an epifluorescence microscope. *Confocal* means the utilisation of pinholes having their foci in accordance with the objective's focus. Thus the size of the light beam is decreased resulting in a decrease in sample volume that is excited; light that is emitted from out of focus planes (Fig. 3.6, dotted lines) is restricted from reaching the detector. A *laser* as a source of more coherent light is used and the sample is *scanned* pixel by pixel.

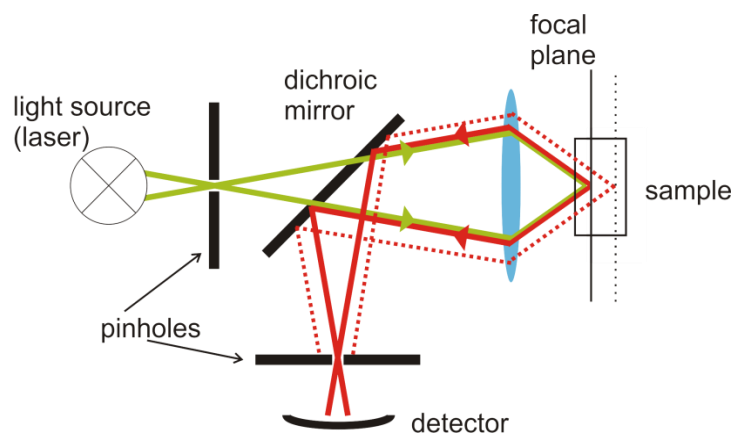


**Figure 3.6: Principle setup of a confocal laser scanning microscope. Pinholes arrange for a decrease in diameter of the light beam and therefore for a decrease in thickness of the excited volume, resulting in enhanced quality of the image recorded, compared to an epifluorescence microscope. Moreover, a laser is used for excitation of the sample with a single wavelength and the sample is scanned pixel by pixel.**

### *Experimental setup*

Porous substrates were glued to the Petri dish bottom prior to addition of GUVs for fluorescence experiments with AFM adhesives. In case of successful spreading, a 3 mm magnetic stir bar, which was driven by a cuvette magnetic stirrer (Variomag Electronicrührer, H + P Labortechnik, Germany) placed underneath the Petri dish, was positioned in the dish (Fig. 3.7). Stirring speeds were usually not varied between experiments. A membrane patch sufficiently large and clean, i.e. lacking lipid debris and

vesicles stuck to the surface, was chosen. The time series function of the CLSM was then used to record a series of images with a frame rate of  $(1-2) \text{ min}^{-1}$ .

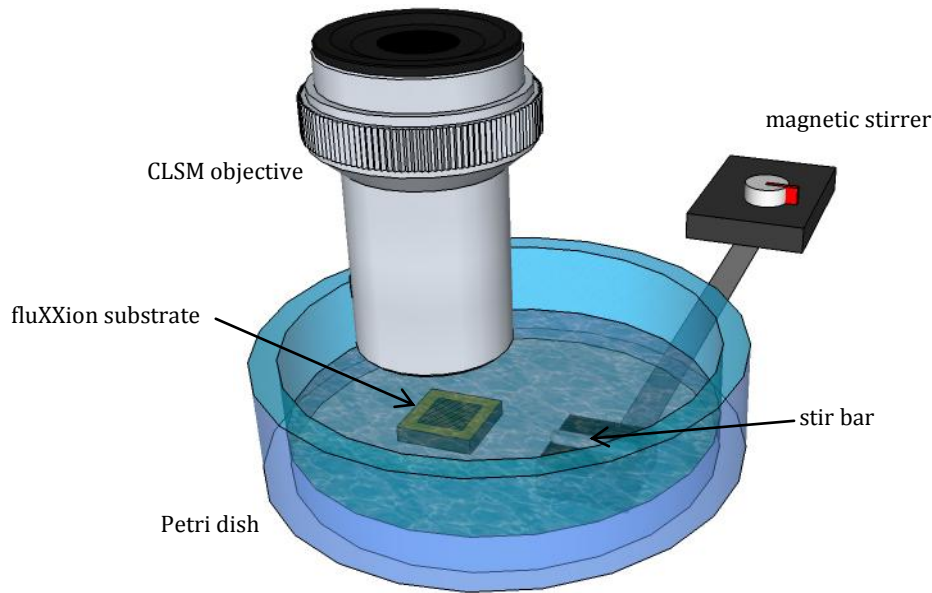


**Figure 3.7: Setup for fluorescence experiments.** A suitable area of the porous substrate is monitored, the surrounding buffer solution is stirred by a 3 mm stirring bar driven by a magnetic stirrer located underneath the Petri dish.

After 15 min of recording, a first volume of peptide solution being kept on ice was added to achieve a suitable peptide concentration. Concentrations were kept constant for (15–20) min before a next titration step was taken, i.e. more peptide solution of the same stock solution was applied. When membrane rupture events were observed the addition of peptide solution was stopped until there was no pore-suspending membrane left or no change in the number of ruptured membranes was discovered.

Analysis of time series was conducted with the software ZEN 2009 LE (Carl Zeiss, Jena, Germany): the number of pores suspended by membrane in image  $N$  were compared to the number of membrane covered pores in image  $N-1$ . Differences in the number of covered pores between images  $N$  and  $N-1$  were summed up for images 1 to  $N$ . The amount of disruption was calculated for every image  $N$  as the ratio of the sum of disrupted membranes and the number of covered pores in image 1.

### 3.3.2 SCANNING ION CONDUCTANCE MICROSCOPY

Scanning ion conductance microscopy is a member of the family of scanning probe microscopies. Its main advantages in comparison to other members are the absence of mechanical contact between sample and probe – at the expense of a reduced resolution being in the  $10^1 \text{ nm}$  range for both lateral and vertical resolution – and the expendability of specific preparations or modifications of the sample as long as it can be kept in a sufficiently conductive medium. Measurements are thus performed under biologically relevant conditions, contrary to methods such as scanning electron microscopy as described in

## MATERIALS AND METHODS

Chapter 1.1. A detailed description of SICM theory and principles can be found in Chapter 1.2, the SICM setup is shown in Fig. 3.8.

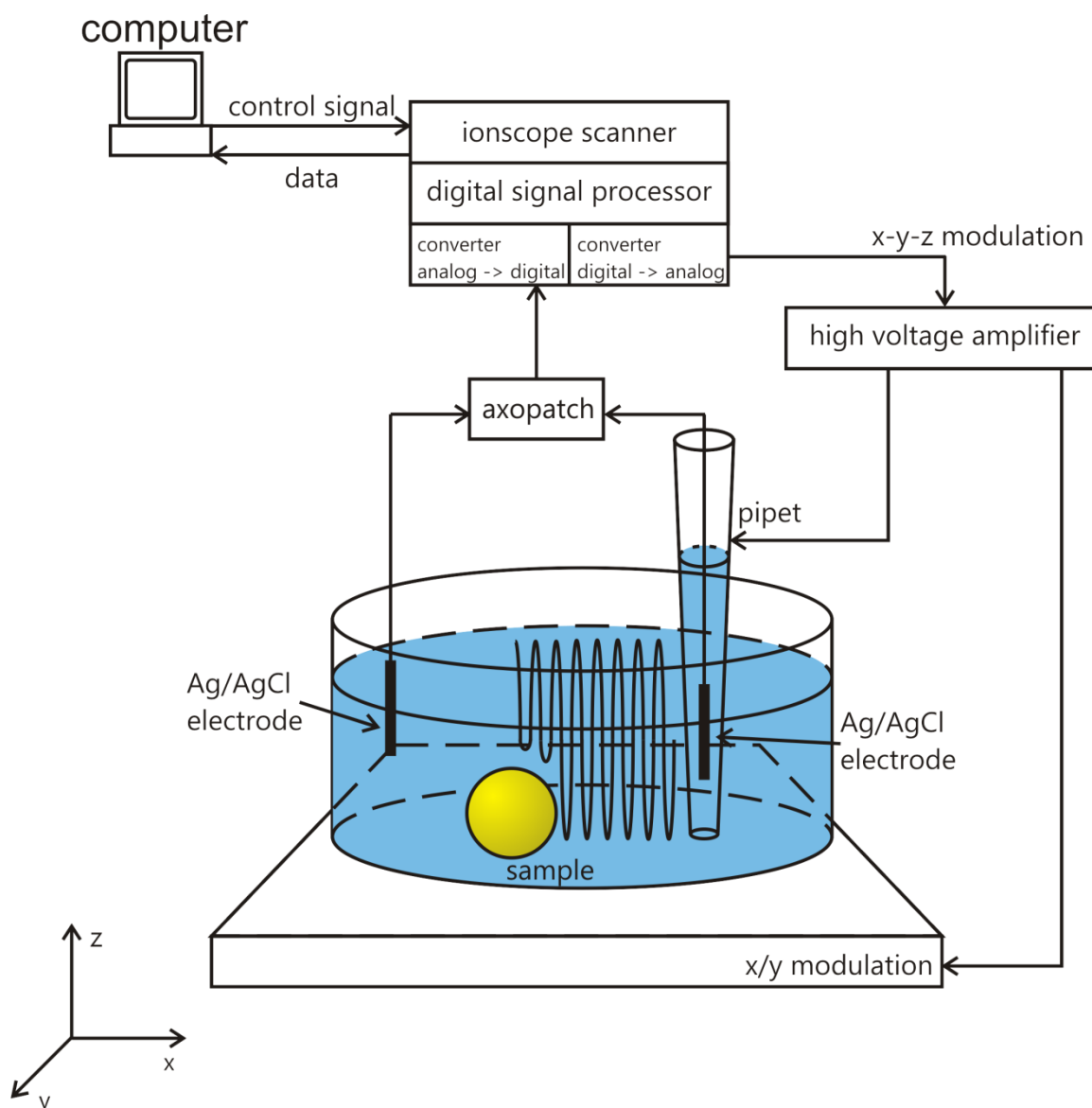


**Figure 3.8:** The current between an electrode in a nanopipette and a counter electrode immersed in the buffer solution is measured with an external amplifier (axopatch) interposed for a better signal-to-noise ratio. The pipette is lowered until the current decreases to a given set-point due to restriction of ion flow between the pipette interior and the bath buffer solution. The pipette carries out a hopping movement approaching and withdrawing from each pixel, and piezo positions in each direction are controlled by a feedback loop.

### *Experimental setup*

In this study, two different SICM instruments were used. Experiments on CPEO3 functionalised substrates and experiments on ME functionalised substrates were performed on an ICnano (ionscope, Melbourn, UK) or ICnano 2000 (ionscope, Melbourn, UK), respectively, except where stated otherwise. In every case an external amplifier (Axopatch 200B, Molecular Devices, Sunnyvale, CA, USA) with a 1 kHz 4-pole lowpass Bessel

filter was interposed to achieve a better signal-to-noise ratio. For experiments on the ICnano the software ICnano Hopping 2, version 1.9.3.73 was used, experiments on the ICnano 2000 were run with the software ICnano 2000.

*Imaging of pore-suspending membranes on CPEO3 functionalised substrates*

Reusable custom-designed PTFE SICM chambers were used for CPEO3 (cf. Tab. 3.2) functionalisations as membrane patches were large enough to ensure quick and easy identification of membrane covered porous regions (Fig. 3.9 A)). In case of successful spreading, the PTFE chambers were placed into the designated position within the Faraday cage, and the counter electrode was lowered into the buffer solution. A freshly pulled pipette (cf. Ch. 3.2.4) was filled with SICM. The optical microscope B3-220 PL (Motic, Wetzlar, Germany) was used to check for residual air bubbles which were removed by application of negative pressure via a syringe which had been connected to the pipette. The pipette electrode was inserted into the buffer filled pipette which was then connected to the headstage, and the Faraday cage was closed.

The pipette position was adjusted by eye such that the pipette was directly above the 9 mm<sup>2</sup> square containing the porous regions by using the software's remote control of the piezos. The pipette was lowered into the buffer solution with a speed of at most 200  $\mu\text{m s}^{-1}$  to avoid damaging it upon hitting the buffer surface. Once it was immersed – which was checked for by observation of the displayed current and the voltage applied to the z piezo displayed on the oscilloscope – it was lowered another 200  $\mu\text{m}$  to prevent surface effects from disturbing the next steps of offset correction. Without further adjustments, the current displayed was  $I \neq 0$  A in most cases when no voltage was applied ( $U = 0$  V). It was corrected by application of an offset voltage such that  $I = 0$  A was displayed for  $U = 0$  V. The voltage was readjusted to  $U = 200$  mV and the displayed current was checked to correspond to a resistance of  $R > 100$  MOhm.

The set-point was then chosen – usually to a value of 5x0.1% - such that the voltage applied to the z piezo was displayed as a regular, periodic signal on the oscilloscope; i.e. a decrease in current of 0.5% compared to  $I_{\text{sat}}$  during the approach phase would result in a rise of the pipette. The pipette was usually allowed to approach the sample at a speed of 1  $\mu\text{m s}^{-1}$ , at most 5  $\mu\text{m s}^{-1}$ . The pipette having reached the surface was indicated by the software stating 'in control' and by a change in the z piezo deflexion displayed on the oscilloscope. Typical values for the parameters needing adjustments for experiments are given in Table 3.5.

In a typical experiment, the pipette was immersed into the buffer solution at 200  $\mu\text{m s}^{-1}$  (immerse velocity). Once immersed, velocity of vertical movement was reduced to 1  $\mu\text{m s}^{-1}$  to prevent crashing of the pipette (approach velocity). A hopping height, usually 2  $\mu\text{m}$ , was chosen such that it exceeded the maximum height differences of the sample. The pipette was lowered at 15  $\text{nm ms}^{-1}$  (fall rate) while risen at 250  $\text{nm ms}^{-1}$  (rise rate) during hopping to ensure fast scanning by a comparatively high rise rate without endangering the pipette (lower fall rate). XY delay time (1 ms) refers to the time span the pipette remains in its

## MATERIALS AND METHODS

upmost position before travelling to the next data point where a background measurement (20 ms) of  $I_{\text{sat}}$  is performed. The z piezo position value refers to the z piezo deflexion in a range between  $-12.5 \mu\text{m}$  (bottom) and  $12.5 \mu\text{m}$  (top). A value of  $-11 \mu\text{m}$  allows for up to  $1.5 \mu\text{m}$  downward travelling as the deflexion range ends at  $-12.5 \mu\text{m}$ . Unidirectional scanning describes the experimental condition that every line is scanned in the same direction, i.e. starting points of lines  $N$  and  $N+1$  differ in their y position but not in their x position. The values of resolution levels describe the distances between data points: an image of  $10 \mu\text{m}$  width comprises  $10000 \text{ nm} / 78.1 \text{ nm} = 128$  data points per line at the  $78.1 \text{ nm}$  resolution level.

**Table 3.5: Values for a typical SICM experiment on the ICnano.**

parameter	value	
$U / V$	0.200	
set-point / 0.1%	5	
immerse velocity / $\mu\text{m s}^{-1}$	200	
approach velocity / $\mu\text{m s}^{-1}$	1	
hopping height / $\mu\text{m}$	2	
fall rate / $\text{nm ms}^{-1}$	15	
rise rate / $\text{nm ms}^{-1}$	250	
XY delay time / ms	1	
background measurement / ms	20	
image size / $\mu\text{m}^2$	10x10	
z piezo position / $\mu\text{m}$	-11	
scan direction	unidirectional	
resolution levels / nm	roughness 1-25000	roughness 0-1
	110.1	78.1

### *Imaging of pore-suspending membranes on ME functionalised substrates*

In case of ME functionalisations, membrane patches showed average diameters of (20–40)  $\mu\text{m}$  which would have rendered adjustment of the pipette relative to the sample by eye very difficult. For this reason, Petri dishes were used where pipette and substrate were identified via the inverted microscope function of the SICM such that membrane covered pores were still found within a time frame of  $< 1 \text{ h}$  in most cases (Fig. 3.8 B)).

In case of successful spreading, the Petri dish was placed into the designated position within the Faraday cage. A freshly pulled pipette (cf. Ch. 3.2.4) was filled with SICM buffer. The optical microscope B3-220 PL (Motic, Wetzlar, Germany) was used to check for residual air bubbles which were removed by application of negative pressure via a syringe which had

been connected to the pipette. The pipette electrode was inserted into the buffer filled pipette which was then connected to the headstage, and the Faraday cage was closed.

The pipette position was adjusted by eye such that the pipette was close to, but not above the sample by using the software's remote control of the piezos. The next steps taken were the same as for CPEO3 functionalised substrates as stated above: pipette immersion, pipette lowering, offset voltage adjustment, current check and choice of set-point.

The inverted objective below the Petri dish was raised to its utmost position and positioned by eye such that it was directly under the pipette which was then searched for manually via the microscope's xy handles. Once the pipette was found, its position in the camera window on the computer monitor was marked and kept constant.

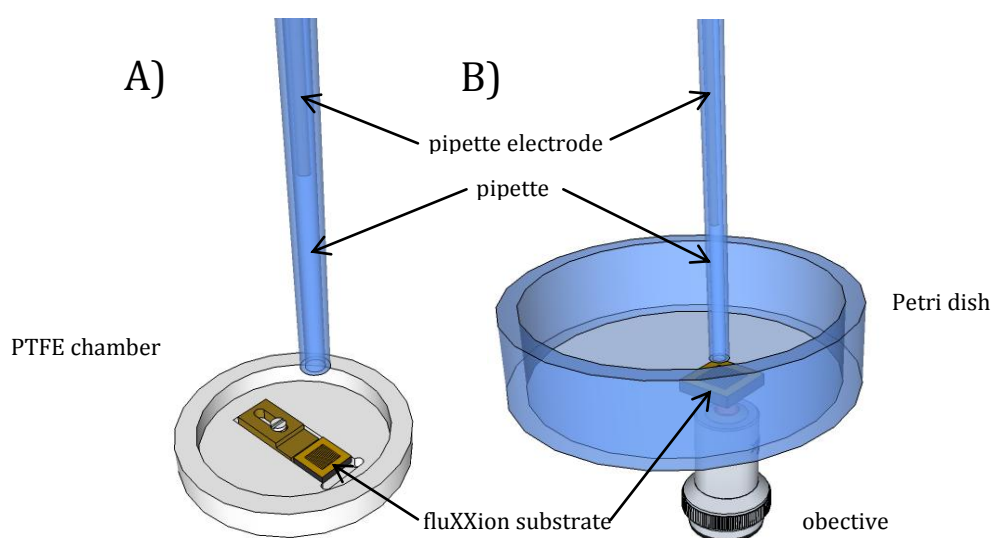


**Figure 3.9: Experimental setup for SICM experiments on A) hydrophobically (CPEO3) functionalised substrates, B) hydrophilically (ME) functionalised substrates. Membrane patches are too small in the latter case to allow for adjustment of the pipette relative to the substrate by eye. The problem is solved by using the inverted microscope to exactly localise the pipette with respect to the membrane covered pores' position.**

The objective's focus was shifted to a plane close to but above the sample surface, and the pipette was allowed to approach at high speeds of  $80 \mu\text{m s}^{-1}$  until its tip reached the chosen focal plane. The substrate was then moved by the software's remote control feature such that the pipette was located above an area where membrane covered pores had been observed with the fluorescence microscope. Further steps again resembled those of the procedure for CPEO3 functionalised substrates: surface approach and parameter adjustment. Typical values are given in Table 3.6 for ICnano 2000 experiments on ME functionalised substrates as notations changed slightly between software versions.

Most values, however, remain the same. Here, the number of data points is chosen directly instead of via the resolution levels indicating the distance between measurement points (v.s.). Furthermore, a limitation of z piezo deflexion is chosen directly (limits) such that the pipette must not be lowered more than it hops: the piezo is set to be deflected to half its maximum when the pipette has approached the surface (approach z target =  $12.5 \mu\text{m}$ ) and the min limit is set such that it differs from the factually reached vertical position by less than  $2 \mu\text{m}$

## MATERIALS AND METHODS

(hopping height). While the immersion process had to be managed manually on the IC nano, it was performed automatically on the IC nano2000, the indicator being the immerse ion threshold typically set to 0.2 V.

**Table 3.6: Values for a typical SICM experiment on the ICnano 2000.**

Parameter	value	
$U / V$	0.200	
set-point / 0.1%	5	
immerse speed / $\mu\text{m s}^{-1}$	200	
approach speed / $\mu\text{m s}^{-1}$	1	
hopping height / $\mu\text{m}$	2	
fall rate / $\text{nm ms}^{-1}$	15	
rise rate / $\text{nm ms}^{-1}$	250	
XY settle / ms	1	
background measurement / ms	20	
image size / $\mu\text{m}^2$	10x10	
scan direction	unidirectional	
total scan measurement points	X	Y
	128	128
limits / $\mu\text{m}$	<b>max</b>	<b>min</b>
	25	11.4-11.9 (hopping height > [abs. z position - min limit])
approach z target / $\mu\text{m}$	12.5	
immerse ion threshold / V	0.2	

### *Titration experiments*

Once a suitable – i.e. containing membrane covered and ideally non covered pores for comparison as well – area was found and imaged, titration experiments were performed. Since stirring was not possible as it was done for fluorescence experiments, large volumes were exchanged to ensure rapid equilibration of peptide concentration throughout the whole sample volume. 1 ml of typically 2.5 ml sample volume were removed with a pipette before 1 ml of peptide solution was added. For peptide concentrations in the added 1 ml, dilution into 1.5 ml of a lower concentration had to be considered, e.g. 1 ml of 200 nM peptide solution was added to 1.5 ml pure buffer ([peptide] = 0 nM) to achieve a final concentration of 80 nM in 2.5 ml sample volume.



The exact sample volume was determined via weighing: SICM chambers and Petri dish were weighed empty and before they were placed into the SICM Faraday cage to determine  $m_{\text{empty}}$  and  $m_{\text{start}}$ , respectively. The difference  $\Delta m_{\text{start}}$  [mg] was used for calculations as the sample volume  $V_{\text{sample,start}}$  [ml]. As experiments were performed over several hours buffer evaporation had to be taken into account. To this end, SICM chambers and Petri dish were weighed when the titration was finished to determine  $m_{\text{final}}$ . The difference in weight with respect to the empty sample holder,  $\Delta m_{\text{final}}$  [mg], was taken as the final sample volume  $V_{\text{sample,final}}$  [ml]. The evaporation rate  $k_{\text{evap}}$  was calculated with [3.2] where  $t_{\text{exp}}$  is the time between weighing of  $m_{\text{start}}$  and  $m_{\text{final}}$ .

$$k_{\text{evap}} = \frac{[V_{\text{sample,start}} - V_{\text{sample,final}}]}{t_{\text{exp}}} \quad [3.2]$$

It was then used to calculate a corrected sample volume  $V_{\text{sample,corr}}$  at the time  $t$ , typically the addition of peptide solution, for losses through evaporation by [3.3] with  $t$  being the time since the measurement of  $m_{\text{start}}$ .

$$V_{\text{sample,corr}} = V_{\text{sample,start}} - k_{\text{evap}} \cdot t \quad [3.3]$$

#### *Image processing and analysis*

A variety of softwares was used to process and analyse SICM images. The ‘Destripe’ and ‘Correct Slope’ features of ScanIC Image were used for destriping and levelling of images where needed and possible, i.e. when there were not any artefacts created.

#### *Histogram analysis*

If the image quality allowed for histogram analysis, the binary .img file resulting from ScanICImage processing was loaded with WSxM [Horcas et al. 2007] and saved as an ASCII matrix file (.txt). This file was then processed with MATLAB (cf. Ch. 3.4), Gaussian curves were fit to the histograms to obtain pore depths for individual pores.

#### *Profile analysis*

If the image quality did not allow for histogram analysis, Gwyddion was used to obtain profile lines with widths of 10 pixel of membrane covered pores. These profile lines were processed with Origin. The profile lines were smoothed by means of the adjacent averaging method, typically with 25 adjacent points. The ‘baseline and peaks’ feature was then used to level pore rims and determine pore depths as the minima of the obtained corrected profile lines.

## MATERIALS AND METHODS

### 3.3.3 UV/VIS SPECTROSCOPY

As peptides were used in this study and experiments were conducted to identify crucial concentrations of these peptides, concentration measurements played a pivotal role for thorough analysis of the experiments. In general, methods to perform concentration determinations comprise colorimetric assays such as those developed by Lowry et al. [Lowry et al. 1951] or Bradford [Bradford 1976] and spectroscopic assays. For peptides containing aromatic amino acids – mainly tryptophan, also tyrosine and phenylalanine – as melittin and penetratin, UV/Vis spectroscopy provides a quick and easy way by measuring absorption spectra ( $\lambda = (200\text{--}800)$  nm) or at a fixed wavelength of  $\lambda = 280$  nm.

As photons are absorbed by sample molecules, the light intensity is reduced. The absorbance  $A$ , equalling the logarithm of the intensities' ratio after and before absorption, is directly proportional to the sample thickness  $d$ , the concentration of absorbent  $c$  and its extinction coefficient  $\epsilon$  as it is described by Beer-Lambert's law [3.4]. The described proportionality is found to be most reliable in a region of  $A$  between 0.1 and 1.0.

$$A = \lg \frac{I}{I_0} = \epsilon \cdot c \cdot d \quad [3.4]$$

In this study, a single beam photometer was used to determine melittin and penetratin concentrations. The principle setup of a single beam photometer is depicted in Fig. 3.10. A monochromator is used to select a single wavelength from the continuous spectrum of the light emitted by the light source. It passes the cuvette containing the peptide solution and reaches the detector. The signal is enhanced by a photomultiplier before it is recorded and digitised by the computer. Reference spectra have to be recorded separately to be subtracted from the sample spectra. In contrast to this setup, dual beam photometers split the light beam to let it pass two cuvettes containing the sample solution and a reference solution, respectively, to directly subtract background signals.

An extinction coefficient of  $\epsilon = 5500 \text{ cm}^{-1} \text{ M}^{-1}$  [Gasteiger et al. 2003] was used for melittin concentration measurements. The concentration of a melittin stock solution was determined at a wavelength of  $\lambda = 280$  nm as  $c = 210 \text{ }\mu\text{M}$  before it was aliquoted into 20  $\mu\text{l}$  portions which were frozen in liquid nitrogen and stored at  $-20 \text{ }^\circ\text{C}$ .

An extinction coefficient of  $\epsilon = 11000 \text{ cm}^{-1} \text{ M}^{-1}$  [Gasteiger et al. 2003] was used for penetratin concentration measurements. A penetratin stock solution was aliquoted into 100  $\mu\text{l}$  portions of an estimated concentration of  $c = 160 \text{ }\mu\text{M}$  which were frozen in liquid nitrogen and stored at  $-20 \text{ }^\circ\text{C}$ . Actual concentrations of each aliquot were determined at a wavelength of  $\lambda = 280$  nm directly before using the peptide solution.

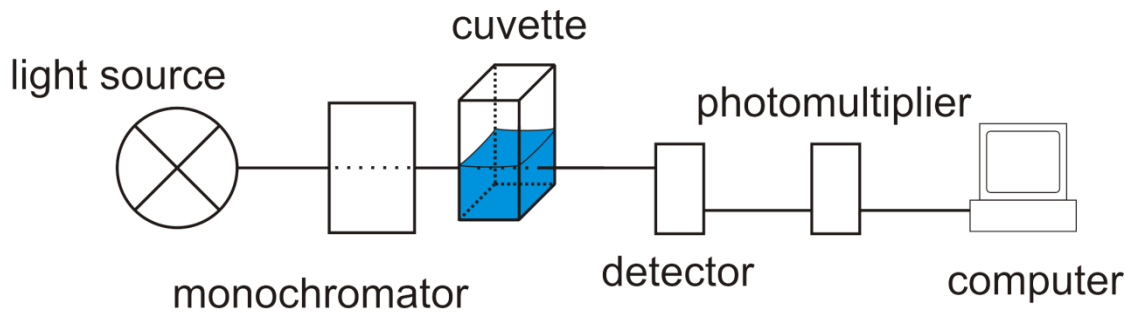


Figure 3.10: Principle setup of a single beam UV/Vis photometer.

### 3.4 MATLAB ANALYSIS

A MATLAB script compiled by Dr. Ingo Mey was used to determine pore depths via histogram analysis as shown in Figure 3.11. ASCII data files resulting from processing with WSxM were loaded, and suitable rectangle areas for histogram analysis were chosen. A Gaussian fit was performed to obtain pore depths, i.e. height differences between rim and covered pore, from SICM experiments.

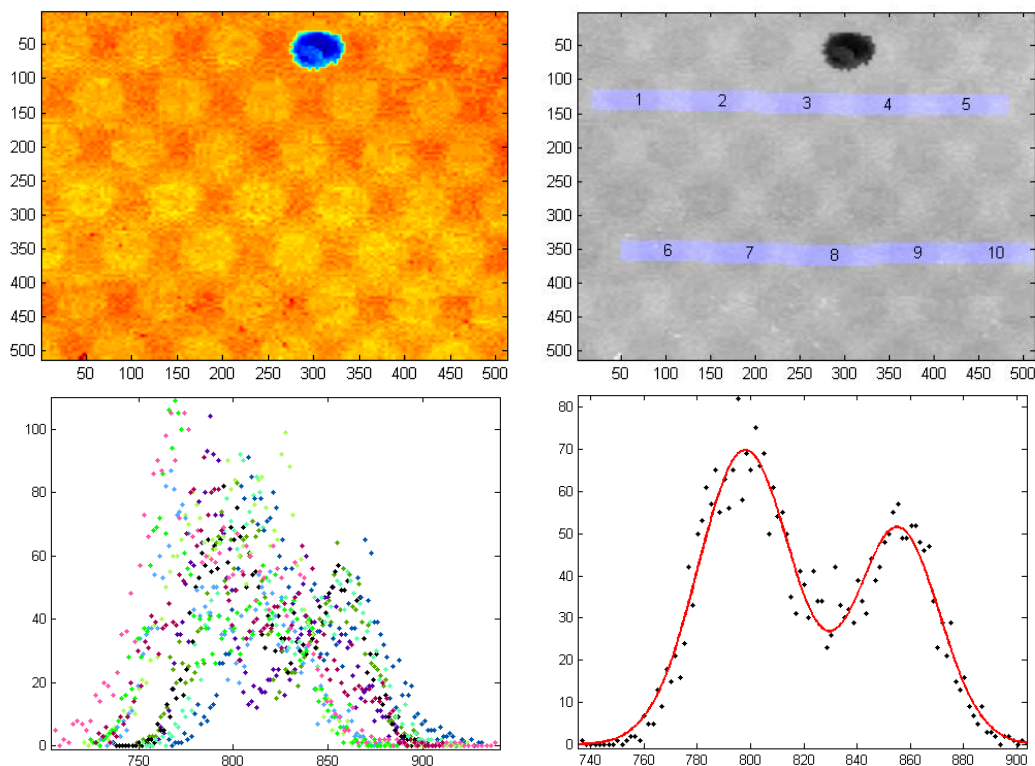


Figure 3.11: Exemplary individual steps of MATLAB analysis: A) image loaded from ASCII file (axis units: pixel), B) rectangles chosen (here: 10, width = 50, height = 20, bins = 40) for histogram data acquisition (axis units: pixel), C) histograms (number of events vs height / nm) obtained - each colour represents one histogram, D) 2<sup>nd</sup> order Gaussian fit of a single histogram (number of events vs height / nm).

## MATERIALS AND METHODS

MATLAB script:

```
function SICMbox(data, name, n, width, height, bins)
% SICMbox(data, name, n, width, height, bins) displays a N*M Matrix as
% image and collects at n positions histograms from an width*height box.
% bins gives the number of bins in the histograms.
%
% All data is stored in Workspace 'base), image and histogram boxed are
% saved in name.fig, the workspace is saved in name.mat
%
% data and name is required,
% default n=1, width=50, height=20, bins=40

if nargin < 2
    disp('more input required')
    return
elseif nargin < 3
    width=50
    height=20
    bins=40
    n=1
elseif nargin < 4
    width=50
    height=20
    bins=40
end

dataBW=mat2gray(data);
img=imagesc(data)
poremids=ginput(n);
wdt=width;
ht=height;
pts=wdt.*2*ht.*2;

maske=zeros(size(data));
dmy=maske;
histdata=[];
for k=1:size(poremids,1)
    mask=strcat('maske',num2str(k));
    for i=1:size(data,1)
        for j=1:size(data,2)
            if j>poremids(k,1)-wdt && j<poremids(k,1)+wdt &&
i>poremids(k,2)-ht && i<poremids(k,2)+ht
                maske(i,j)=1;
                dmy(i,j,k)=1;
            end
        end
    end
end

maske=logical(maske);
dmy=logical(dmy);
over=imoverlay(dataBW,maske,[0 0 1]);
img=image(over);

for i=1:(size(poremids,1))
    text(poremids(i,1),poremids(i,2),num2str(i))
end
saveas(img,name,'fig')
pause(1);
```

```

dmynameporemids=strcat(name,'poremids');
assignin('base',dmynameporemids,poremids);

fits=figure;

fp.func = @(d,p,c) dg(d, p(1), p(2), p(3), p(4), p(5), p(6));
fp.startpar = [255 170 770 830 30 20];
fp.cntrl = 10;
fp.maxiter = 1e4;
fitres.minpar = [-inf -inf -inf -inf 0 0];
fitres.maxpar = [inf inf inf inf inf inf];

for i=1:size(poremids)
    over=imoverlay(dataBW,dmy(:,:,i),[1 0 1]);
    image(over);
    drawnow
    dmy2=data(dmy(:,:,i));
    [dmyy,dmyx]=hist(dmy2,bins);
    dmyname=strcat(name,num2str(i));

    dmynamex=strcat(dmyname,'x');
    dmynamey=strcat(dmyname,'y');
    dmynamemask=strcat(dmyname,'mask');
    dmynamemasklayer=strcat(dmyname,'masklayer');

    assignin('base',dmynamex,dmyx);
    assignin('base',dmynamey,dmyy);
    assignin('base',dmynamemask,maske);
    assignin('base',dmynamemasklayer,dmy);
    pause(0.1)
end
assignin('base','name',name)
expre='save(name)';
evalin('base',expre)

```



## 4 RESULTS

The objective of this study was to establish an assay based on scanning ion conductance microscopy (SICM) to investigate interactions of cell penetrating peptides (CPPs) with pore-suspending lipid membranes (PSMs). PSMs were chosen as the membrane model system as they provide advantages over earlier developed models such as black lipid membranes (BLMs) or solid supported membranes (SSMs) with respect to stability and mimicking natural cellular systems. The SICM allows for investigation of surfaces without mechanical contact which is why the combination of SICM and PSMs appears as very promising. Experiments conducted by means of SICM were accompanied by confocal laser scanning microscopy (CLSM) experiments. Both assays were desired to be applicable to a variety of lipids, peptides and functionalisation types of substrates.

It has been shown previously that there are great differences with regard to mechanical features of PSMs based on the substrate functionalisation they are prepared on: while membranes prepared on hydrophilically functionalised substrates exhibit minor lateral tension only, those prepared on hydrophobically functionalised substrates feature prestress that is larger by a factor of at least 50 compared to unfunctionalised SiO<sub>2</sub> [Mey et al. 2009].

All substrates were functionalised with titanium or chromium and subsequently a gold layer before cholesteryl polyethylenoxy thiol (CPEO3) or mercaptoethanol (ME) were applied which is why substrates are described as CPEO3 or ME functionalised for reasons of readability. It was thus investigated whether different functionalisations cause differences in the effects CPPs on these membranes by means of CLSM and SICM.

To this end, a reliable method to prepare pore-suspending membranes on both hydrophobically and hydrophilically functionalised substrates was needed to be found. Next, the membranes' stability had to be tested such that changes in topography could be ascribed to the application of peptides rather than an inherent membrane instability enhanced or brought forward by the SICM investigation. To narrow down concentration ranges of the CPP in which it affects pore-suspending lipid membranes, a fluorescence assay was set up. The membranes' stability was tested under conditions of fluorescence experiments to allow for correct ascription of observations. When melittin experiments had been conducted successfully on hydrophobically and hydrophilically functionalised substrates, penetratin as another CPP was applied to check for the fluorescence assay's applicability, and SICM experiments were conducted with melittin on both functionalisation types.

As there has been a row of experiments and applications based on pore-suspending membranes prepared on hydrophobically functionalised substrates [Böcker et al. 2009; Gaßmann et al. 2009; Orth et al. 2012], this type of preparation was taken as a starting point to reliably achieve pore-suspending membranes. Later, fluorescence as well as SICM

## RESULTS

experiments were conducted on both hydrophobically and hydrophilically functionalised substrates to investigate the influence of prestress, i.e. the lateral tension, within PSMs.

### 4.1 INVESTIGATION OF PORE-SUSPENDING MEMBRANES ON HYDROPHOBICALLY FUNCTIONALISED SUBSTRATES

This chapter describes experiments with pore-suspending membranes prepared on hydrophobically, i.e. CPEO3 functionalised substrates.

#### 4.1.1 ESTABLISHMENT OF A SPREADING PROCEDURE

In order to mimic natural membrane systems better, the pore-suspending membranes were desired to be prepared solvent-free. To this end, and in contrast to a classical painting technique, GUVs were intended to be spread on functionalised fluXXion substrates. Table 4.1 shows an array of seven parameters initially tested for spreading of 1,2-diphytanoyl-*sn*-glycero-3-phosphatidylcholine (DPhPC) GUVs on CPEO3 functionalised substrates. The screening was conducted in a way that up to two parameters were varied at a time and values resulting in largest and most reliable membrane coverage of pores were adapted to a standard protocol. It therefore did not necessarily result in identification of the globally best conditions but locally best conditions. The benefit, however, was a reduced number of experiments (appr. 50 compared to  $2 \cdot 3 \cdot 3 \cdot 3 \cdot 3 \cdot 4 \cdot 5 = 3240$ ) and time needed to determine suitable spreading conditions, i.e. conditions that reliably (>66% of substrates used) produced membranes with coverage ratios large enough so that the SICM pipette could be positioned above a membrane covered region by eye with a high probability.

**Table 4.1: Parameters screened for spreading conditions of DPhPC GUVs on CPEO3 functionalised substrates. Bold values are those adapted to a standard protocol (cf. Chapter 3.2.2).**

<b>parameter</b>	<b>values tested</b>				
[sucrose] inside GUVs / mM	<b>300</b>		1000		
pore diameters / $\mu\text{m}$	0.8	<b>1.2</b>	2.0		
spreading duration / h	0.5	<b>1</b>	3		
[Ca <sup>2+</sup> ] buffer content / mM	0	40	200		
buffers	<b>100 mM KCl, 10 mM Tris, pH 7.4</b>	100 mM KCl, 10 mM Hepes, pH 7.4	100 mM KCl, 10 mM phosphate, pH 7.4		
$\theta$ / °C	0	ambient	<b>37</b>	50	
lipid composition (DPhPC/cholesterol)	pure DPhPC	95:5	<b>90:10</b>	85:15	80:20

Best results were obtained when substrates with 1.2  $\mu\text{m}$  pore diameters were incubated for 1 h at 37 °C with GUVs with a cholesterol ratio of 10% filled with 300 mM sucrose solution in 100 mM KCl, 10 mM Tris, pH 7.4 buffer (cf. Tab. 4.1). The Ca<sup>2+</sup> content of the buffer system did not have any significant influence on spreading success. Figure 4.1 shows a typical pore-



suspending DPhPC/cholesterol (chol) (9:1) membrane prepared after this standard protocol at different magnifications. The homogeneous coverage of large areas becomes apparent in Figure 4.1 A) while B) and C) show more clearly the regular arrangement of fluorescent areas exactly following the substrate's porous structure (cf. Fig. 3.2) while membrane areas covering rims are not visible due to quenching of fluorescence through the gold layer.

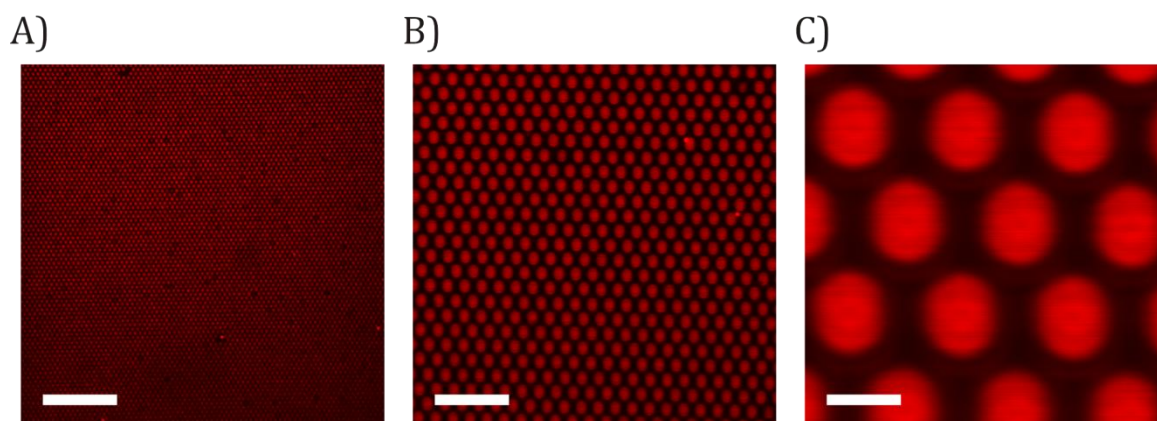


**Figure 4.1:** A DPhPC/chol (9:1) pore-suspending membrane imaged by means of CLSM at different magnifications. Dark spots in A) indicate non covered pores. Scale bars: A) 27.9  $\mu\text{m}$ , B) 7.7  $\mu\text{m}$ , C) 1.2  $\mu\text{m}$ .

#### 4.1.2 SICM IMAGING OF PORE-SUSPENDING MEMBRANES

Fluorescent labelling of lipid membranes is a commonly applied method to achieve visualisation of lipid structures [Edidin et al. 1977; Schlessinger et al. 1977; Derzko and Jacobson 1980; Klausner and Wolf 1980; Struck and Pagano 1980; Spiegel et al. 1984; Weiskopf et al. 2007; Mey et al. 2009; Windschiegl et al. 2009; Kocun et al. 2011; Orth et al. 2012]. The localisation of fluorophore containing PSMs does not pose any problems. Due to the pore diameter of  $> 1 \mu\text{m}$  and the comparably large field of sight provided by the microscope, the existence of membrane patches is checked for easily and fast by means of the live view feature of the instrument. Proof of successful spreading is attended by localisation such that experiments can in principle be begun immediately after checking for the existence of lipid bilayers (cf. Fig. 4.1 A) and Fig. 4.12 A) for CLSM images of PSMs).

The SICM itself, on the contrary, does not allow for easy and fast inspection of a whole substrate ( $(3 \times 3) \text{ mm}^2$ ) due to slower recording speed even for much more confined areas than those examined with the CLSM. It has to be taken into account that synchronous fluorescence and SICM investigation is hardly possible as the SICM pipette takes the space directly above the sample and blocks the light's pathway. An inverted microscope does not provide a solution to this problem as the lipid bilayers are localised on top of the porous substrate which is not transparent. Proof and localisation of fluorescence was consequently done prior to every SICM experiment for time saving reasons, facilitating localisation of PSMs by means of SICM.

## RESULTS

Figure 4.2 illustrates the localisation method applied for SICM use. Porous rectangles containing membrane patches as identified by means of fluorescence microscopy were relocated on the SICM instrument by means of an inverted optical microscope. It reveals the rectangular architecture of the porous stripes and thereby enables approximate identification of the region covered by PSMs. A quick and lowly resolved recording of a large region is usually sufficient to exactly localise membrane patches identified by CLSM before. Proof of the existence of pore-suspending membranes is accomplished when the pore depth, i.e. height difference between rim and suspended region, amounts to values of (50–100) nm [Steltenkamp et al. 2006; Böcker et al. 2009; Mey et al. 2009].

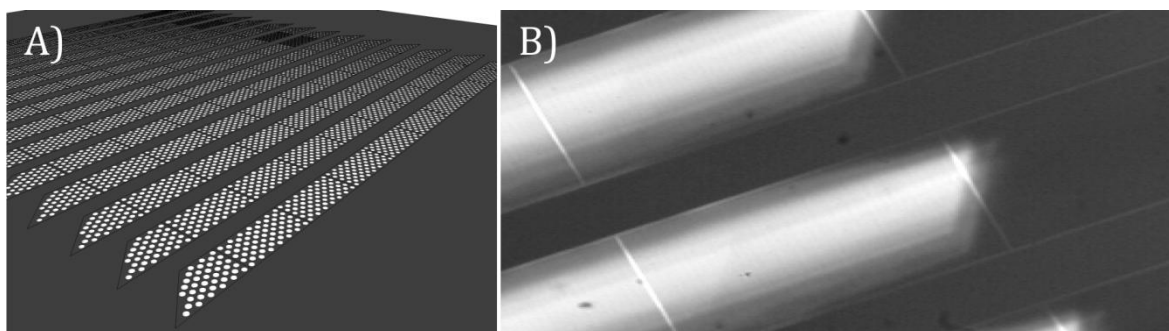


**Figure 4.2:** Close-up views of fluXXion substrates. A) displays a schematic view (cf. Fig. 3.2 B)). 14 stripes of ten porous regions are visible (inner regions:  $75 \times 150 \mu\text{m}^2$  rectangles, outer regions: mirrored right trapezoids), pore sizes are not true to scale. B) shows the view through an inverted optical microscope. The architecture of the substrate with rectangular porous regions is revealed. The two outer porous regions at each end of the stripes appear dark (right side) since these parts are supported at the bottom of the substrate, whereas the inner six rectangles appear bright (left side). The small rims between rectangles become obvious and enable localisation of membrane patches.

Imaging of PSMs on hydrophobically functionalised substrates was achieved relatively straightforward. It was facilitated by the large areas of the porous regions covered by membrane. Pipette adjustment by eye with respect to x and y dimensions was sufficient to find membrane-suspended areas in the majority of experiments with less than ten approaches.

A higher success rate was impeded by several factors. Firstly, there is a possibility  $P > 0$  on porous substrates that the pipette approaches an empty pore and does not finish approaching on the substrate's surface but after having traveled down the pore a significant way – if the current signal reaches the set-point at all. Even if the set-point was reached after some 10 nm down the pore, image recording would be impossible since the pipette remains trapped within the pore either for the whole experiment or until the pipette is driven to a pixel far away enough from the trap such that it breaks free suddenly and breaks most probably. A second problem was an instrument inherent drawback which caused the pipette to not find the surface but to continue approaching although its tip had already traveled to a point below the substrate surface. This behaviour which resulted in pipette breaking was prevented to some amount, though not completely, by reduction of approach velocity. Thirdly, even the large areas covered by PSMs were not sufficient in all cases such that several approaches were necessary until a membrane patch was found, each of the

approaches increasing chances of pipette breaking or other undesired behaviour. Finally, a problem occurred when the pipette scanned across non covered pores as shown in Figure 4.19 (cf. Ch. 4.2.5). It is assumed that in such a case the pipette does not reach its set-point when approaching the open pore. It thus does lose contact to the surface and travels down the pore. For recording of the next pixel, the piezos move the pipette which is trapped in the open pore. The pipette is unable to move laterally and shows the remaining pixels of the line as open as the open pore it is currently in although there is at least the rim if not suspended pores in the open pore's neighbourhood. For unidirectional scanning, the pipette is withdrawn at the end of the line  $N$  and moved back to  $0/N+1$  such that the start of the next line  $N+1$  is recorded correctly until another open pore is hit. For the ICNano instrument, an improvement was reached by indicating a minimum  $z$  position ( $z$  piezo position, cf. Ch. 3.3.2) which reduced the number of incidents slightly. The ICNano2000 instrument provided the option to reliably set a minimum  $z$  position (min limit, cf. Ch. 3.3.2) which solved this problem entirely.

#### 4.1.3 TIME FRAME DEFINITION FOR EXPERIMENTS

As it is the objective to investigate the influence of CPPs on membranes, the ability to distinguish between observations caused by CPPs and those caused by the technique is of great importance. To this end, blank experiments were conducted for the CLSM as well as the SICM since their features differ. In the former case, heating of the sample or the application of laser light might cause undesired effects, whereas in case of the latter, mechanical disturbances close to the membrane surface might interfere with the intended experiment. It was therefore important to find a time frame for the experiments in which experiments could be conducted and effects observed be ascribed to the CPPs.

##### *Fluorescence microscopy*

Blank experiments were conducted on pore-suspending DPhPC/chol (9:1) membranes prepared on CPEO3 functionalised substrates. Two samples were subjected to exactly reproduced titration experiment conditions but melittin solutions were substituted by pure buffer solutions. There was no loss of membranes observed as shown in Figure 4.3.

This timeframe is regarded as sufficient for two reasons. First, experiments can be started directly after location of a suitable membrane covered area and preparation of CPP solutions of the desired concentration. Moreover, CLSM imaging with chosen frame rates of about  $2 \text{ min}^{-1}$  (up to  $6 \text{ min}^{-1}$  possible at the resolutions chosen for most experiments) is fast in contrast to SICM with about 15 min per image.

## RESULTS

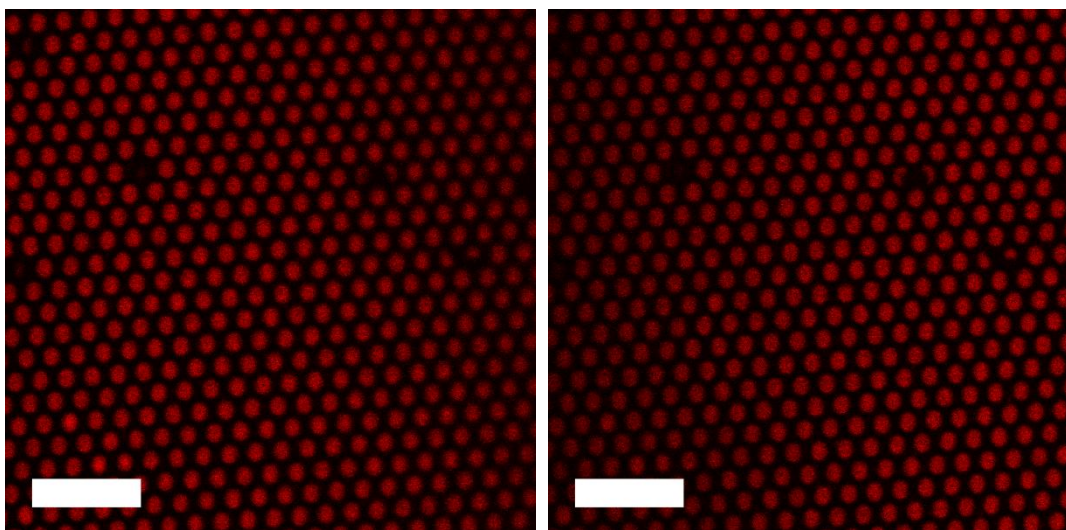


Figure 4.3: Images taken at the beginning ( $t = 0$  min) and the end ( $t = 4$  h) of a blank experiment. Images were taken every 30 s, ice cooled buffer was added every 20 min to mimic a regular CPP titration experiment. Fluorescent spots do not disappear throughout the whole experiment. Slight changes in fluorescence intensity may result from photobleaching or small shifts of the focal plane. Scale bars:  $7.4 \mu\text{m}$ .

### *SICM*

The application of CLSM and SICM may have different influences on samples investigated rendering blank experiments by means of SICM in addition to those by means of CLSM necessary. Furthermore, SICM experiments do require an extended timeframe with regard to fluorescence experiments since identification of a membrane covered area by means of CLSM does not guarantee immediate access to this area with the SICM pipette. Secondly, SICM imaging takes considerably longer than fluorescence imaging (v.s.) resulting in longer experiment duration.

Four experiments were conducted on pore-suspending DPhPC/chol (9:1) membranes prepared on CPEO3 (Tab. 4.1). A  $(10 \times 10) \mu\text{m}^2$  area was imaged for 24 h, and measured pore depths were averaged for each image. Two images at the beginning and the end of the experiment are shown in Figure 4.4 A), revealing no visible difference in pore depths between the two images. Figure 4.4 B) shows the averaged pore depths and reveals a minor change in average pore depths of  $(-0.44 \pm 0.04) \text{ nm h}^{-1}$ . One of the other experiments shows a decrease in pore depths  $((-0.39 \pm 0.04) \text{ nm h}^{-1})$ , while the other two exhibit small increases  $((0.33 \pm 0.04) \text{ nm h}^{-1}$  and  $(0.25 \pm 0.54) \text{ nm h}^{-1})$ , resulting in an overall change of  $(-0.06 \pm 0.40) \text{ nm h}^{-1}$  over the four experiments. This very small change in pore depths provides a timeframe of 24 h after spreading to conduct SICM experiments on pore-suspending membranes.

## 4.1.4 FLUORESCENCE TITRATION EXPERIMENTS

A variety of lipids was used to prepare pore-suspending membranes with different features as described in Chapter 3.2.2. Membranes consisting only of a neutral PC lipid (POPC) are compared to membranes comprising a PC lipid and different additions: either 10% cholesterol in addition to DPhPC, another neutral PC lipid, or 20% POPS, a negatively charged lipid, in addition to POPC. Melittin is used as a CPP and titrated to pore-suspending membranes (POPC, DPhPC/chol (9:1), POPC/POPS (4:1)). This process is monitored by means of CLSM (cf. Fig. 4.5) to investigate at which concentrations of CPP (critical concentration) the observed membranes rupture, i.e. at which [CPP] fluorescent circles indicating lipid bilayers vanish. Disappearance of fluorescence indicates rupturing of the membrane, and the number of ruptured membranes is compared to the overall number of suspended pores and plotted vs  $t$  (cf. Fig. 4.6).

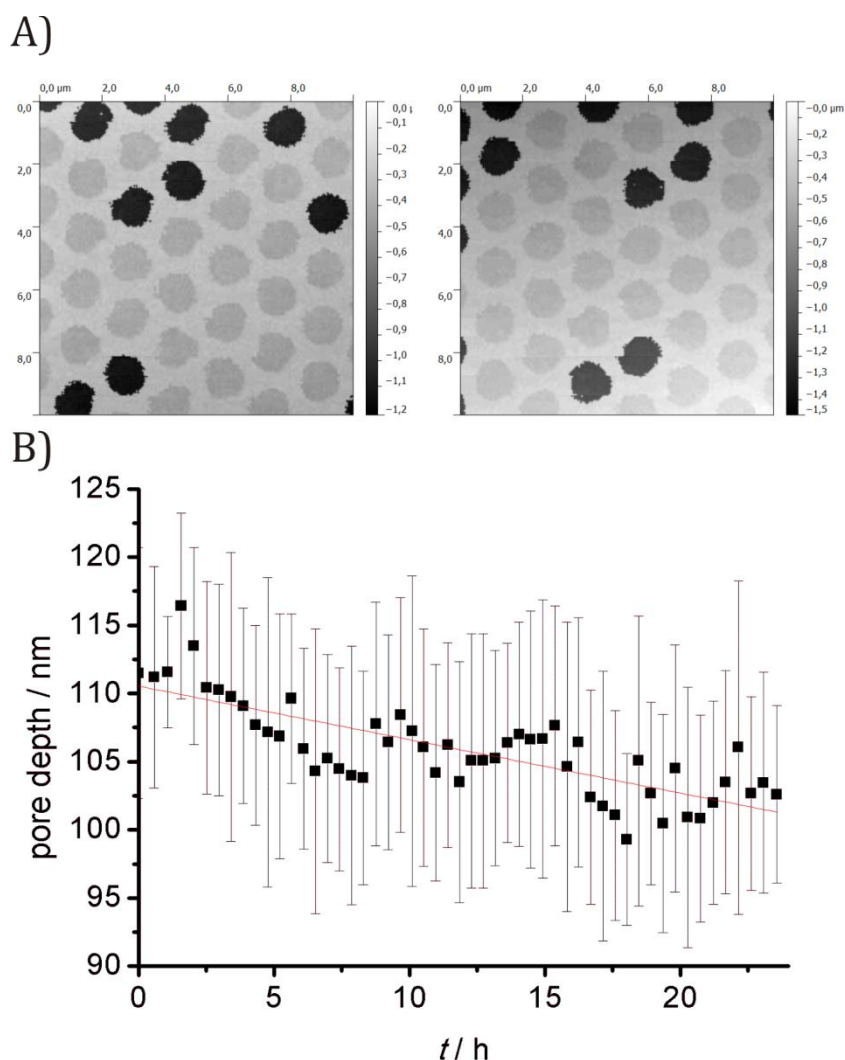


**Figure 4.4:** A  $(10 \times 10) \mu\text{m}^2$  area is imaged for 24 h as a blank experiment. A) Images taken at the beginning and the end of the experiment show no visible differences with respect to pore depths. A lateral drift of few  $\mu\text{m}$  becomes obvious. B) Pore depths determination and averaging for each image reveal a minor decrease in pore depths. Average pore depths for each image are plotted vs.  $t$  (error bars representing standard deviations), the slope of a linear fit reveals the change of pore depth to be  $(-0.44 \pm 0.04) \text{ nm h}^{-1}$ . Further experiments show even smaller deviations from a perfect value of 0.

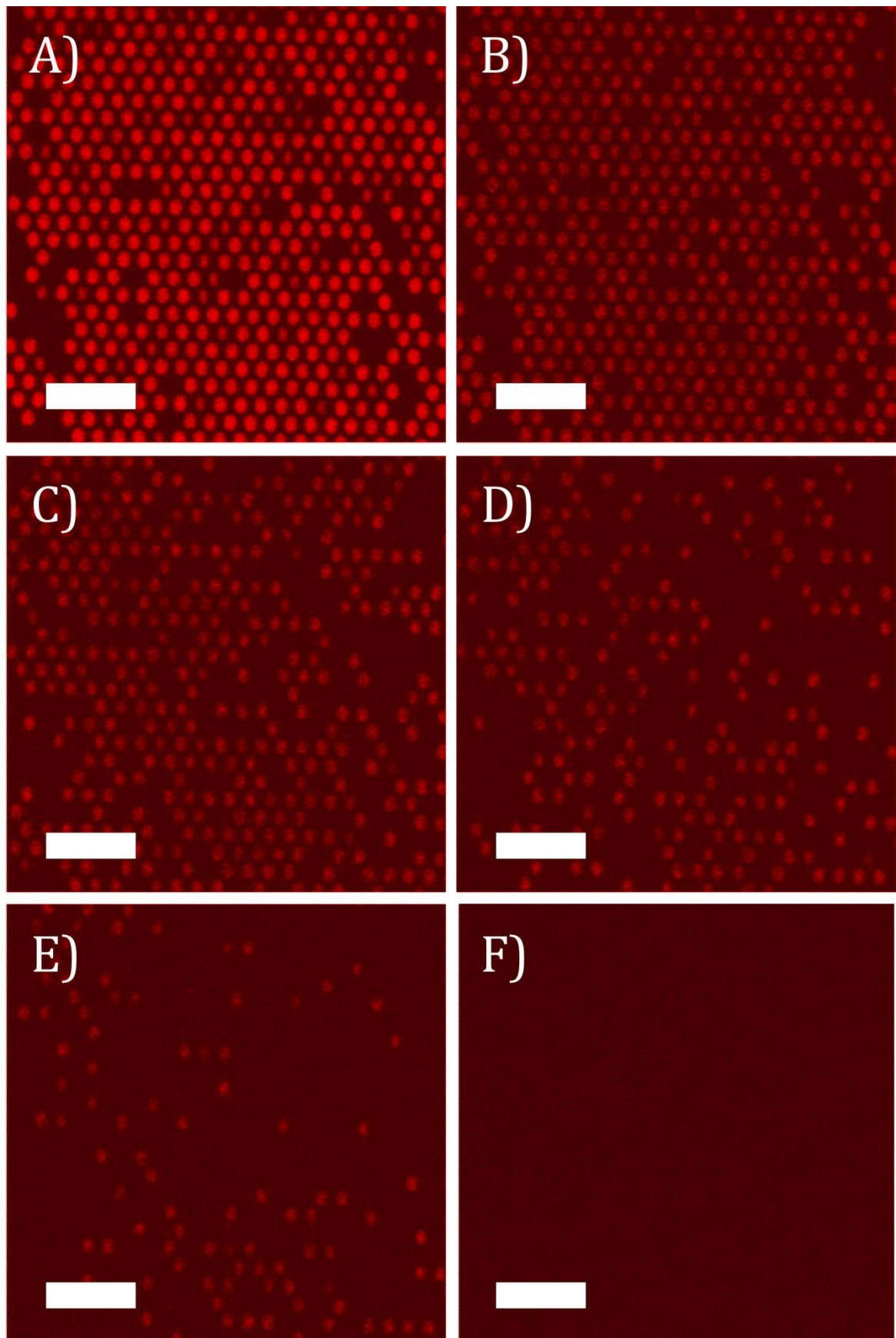
## RESULTS

Figure 4.5 shows a typical series of fluorescence images taken during a titration experiment. The images shown, however, are not taken equidistant in time but are chosen to illustrate the observations during a titration experiment well. It is clearly visible how single pore-suspending membranes rupture at a certain melittin concentration which is reached between Figure 4.5 A) and Figure 4.5 B). Figure 4.5 C)–F) reveal that rupture events do not follow a specific pattern but occur randomly, i.e. there is no cooperativity or interdependence with respect to positions of temporally subsequent rupture events.

Figure 4.6 reveals that different lipid compositions are affected by melittin at different concentrations. While the pure PC membrane (POPC, Fig. 4.5 A)) ruptures at  $[\text{melittin}] = 400 \text{ nM}$ , the addition of a negatively charged lipid (20% POPS) leads to a slightly reduced critical melittin concentration (300 nM, Fig. 4.6 B)). In contrast to this, the addition of 10% cholesterol results in an increase in critical concentration (600 nM, Fig. 4.6 C)). Reproduction of the experiments ( $N = 2\text{--}3$ ) led to the same results for the critical melittin concentration. For error considerations, the reader is referred to Chapter 5.4.1.

Independent from their lipid composition, pore-suspending membranes rupture within approximately 25 min once rupturing events start. Moreover, the shape of the curve resulting from plotting the number of ruptured membranes vs.  $t$  is the same throughout the whole range of experiments on hydrophobically functionalised substrates. A sigmoidal curve is obtained, i.e. the velocity of the increase in the number of ruptured membranes rises until approximately 50% of the investigated area is uncovered where the curve shows an inflexion point (Fig. 4.6).





**Figure 4.5:** A series of CLSM images taken during a typical CPP titration experiment. The critical melittin concentration is reached between A) and B). C)-F) show that rupturing events are randomly distributed. Fluorescence intensities differ from A) to B) due to photobleaching. The corresponding diagram with ruptured membranes plotted vs. time is shown in Figure 4.5 A). Scale bars: 7.6  $\mu\text{m}$ .

## RESULTS

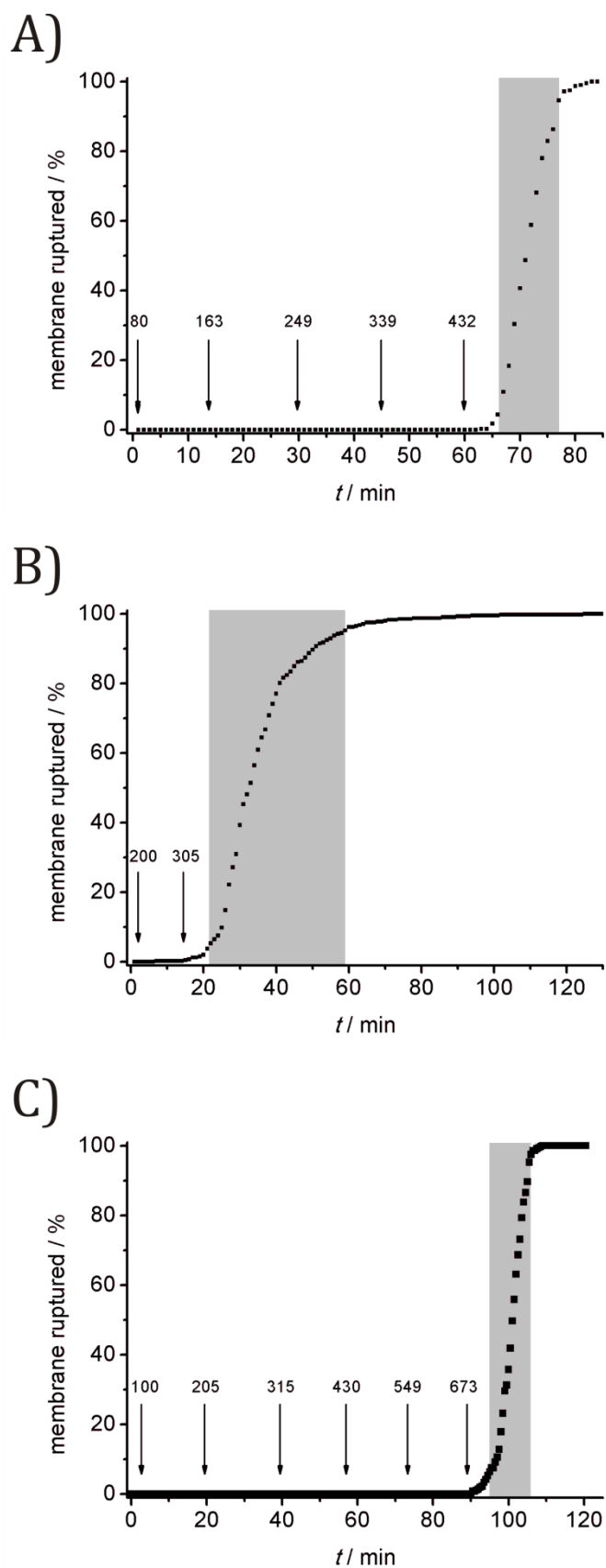


**Figure 4.6: Melittin titrations on pore-suspending membranes prepared from different lipid compositions on CPEO3 functionalised substrates, N pores are observed: A) POPC, N = 386; B) POPC/POPS (4:1) N = 397; C) DPhPC/chol (9:1), N = 358. Arrows indicate the addition of melittin to the sample with corresponding numbers showing [melittin] / nM after addition. Grey rectangles illustrate the time between 5% and 95% membrane ruptured with A) 11 min, B) 37 min, C) 11 min.**



#### 4.1.5 SICM TITRATION EXPERIMENTS

Pore-suspending membranes on CPEO3 functionalised substrates were subjected to SICM investigations. Similarly to experiments utilising fluorescence microscopy, titration experiments were performed in order to find out those CPP concentrations at which membranes are affected. In addition to these results, topographical information was obtained from SICM experiments and analysed.

##### *Topography of pore-suspending membranes*

The topography of pore-suspending membranes is not the main focus of this study but as recording of topographic data is inherent to the monitoring procedure of the CPP effect on lipid membranes, these experiments provide additional information on the architecture of pore-suspending membranes. Figure 4.7 displays topography information obtained from SICM experiments.

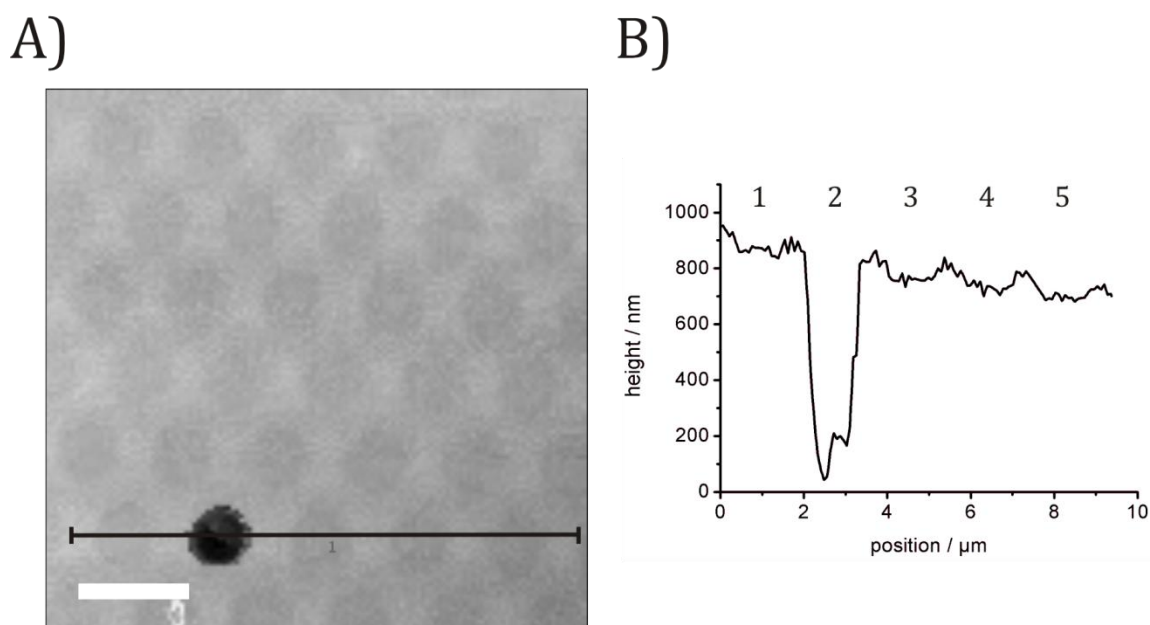


**Figure 4.7:** A) SICM image revealing typical topography of PSMs with profile line. Scale bar: 2.0  $\mu\text{m}$ . B) The corresponding profile reveals pore depths of PSMs of approximately 80 nm.

## RESULTS

Figure 4.8 shows a histogram comprising data obtained via analysis of a row of representative SICM images of pore-suspending membranes prepared on hydrophobically functionalised substrates. All images evaluated for this histogram were recorded without any manipulations after completion of spreading had been proven. The evaluation includes 269 pores suspended by lipid bilayers from nine different images and exhibits an average pore depth of 80 nm (median: 75 nm).

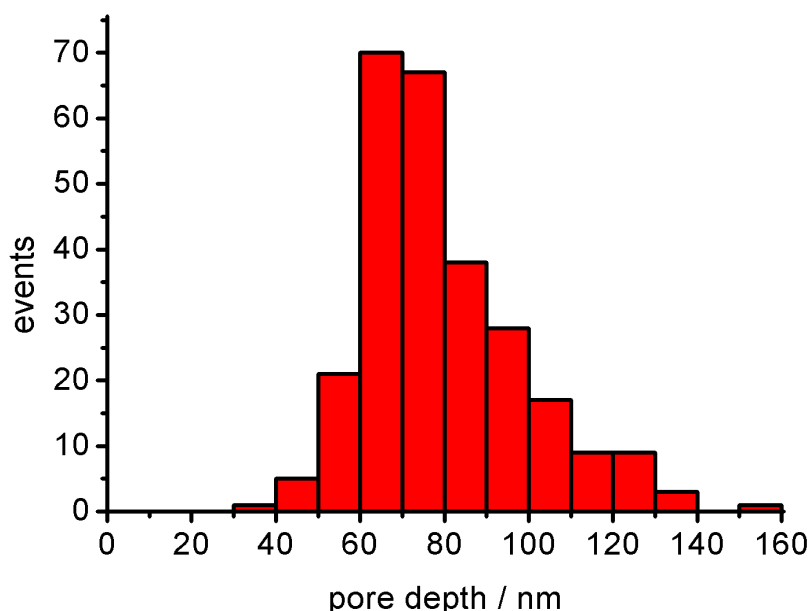


**Figure 4.8:** Pore depth distribution of a representative selection of SICM images of pore-suspending membranes on CPEO3 functionalised substrates. An average pore depth of 80 nm (median: 75 nm) is obtained.

### *Melittin titrations*

SICM experiments were performed to monitor the effect of melittin interacting with pore-suspending membranes. These were prepared from DPhPC/chol (9:1) GUVs as described in Chapter 3.2.2. In order to obtain critical CPP concentrations at which pore-suspending membranes are affected, the CPP is titrated to the lipid bilayers. The change in pore depth over time is correlated to the melittin concentration and reveals lipid-peptide interactions.

Similarly to CLSM based experiments, an excess of melittin was applied to PSMs to gain principal insights into the course of such an experiment and signals obtained by means of SICM from peptide membrane interactions. A melittin concentration in the  $\mu\text{M}$  range resulted in an increase in pore depths by several 100 nm for the whole sample from approximately 100 nm to 800 nm and more. This experiment completed preliminary investigations of the assay's applicability, and PSMs were then subjected to melittin titration experiments. At this point, the 'whitening' problem became obvious for lipid bilayers on CPEO3 functionalised substrates (cf. Fig. 5.4 A)–C)). This phenomenon – i.e. that increasing parts of the pixels recorded induced maximum deflexion of the z piezo such that these parts appeared as white spots – was overcome by a change in pipette geometry (cf. Fig. 5.4 D)). For titration

experiments on ME functionalised substrates, the same new pipette geometry was successfully used.

Figure 4.9 shows a typical series of SICM images recorded during a melittin titration experiment on a DPhPC/chol (9:1) membrane. The images shown, however, are not recorded equidistant in time but are chosen to illustrate the observations during a titration experiment well. A first application of melittin (Fig. 4.9 F)) results in a concentration of  $[\text{melittin}] = 349 \text{ nM}$ , and first few rupture events occur. The critical concentration of  $[\text{melittin}] = 452 \text{ nM}$  is reached after a second application of the CPP (Fig. 4.9 K)), leading to complete rupturing of pore-suspending membranes (Fig. 4.9 K)-O)). Rupture events do not follow a specific pattern but occur randomly, i.e. there is no cooperativity or interdependence with respect to positions of temporally subsequent rupture events. Membrane rupturing is not only revealed as discrete events with states 'membrane intact' and 'membrane ruptured', but intermediate states become obvious in some images, e.g. from the boxed membrane in Figure 4.9 J). The whole rupturing process is completed within 2.5 h.

Pore depths are extracted for every single pore-suspending membrane, and their development depending on melittin concentration and time is visualised to determine CPP concentrations at which membranes are affected and eventually caused to rupture. Plots of the pore depth development for single membranes (cf. Fig. 4.10) are summarised in plots of the whole ensemble of pores observed.

## RESULTS

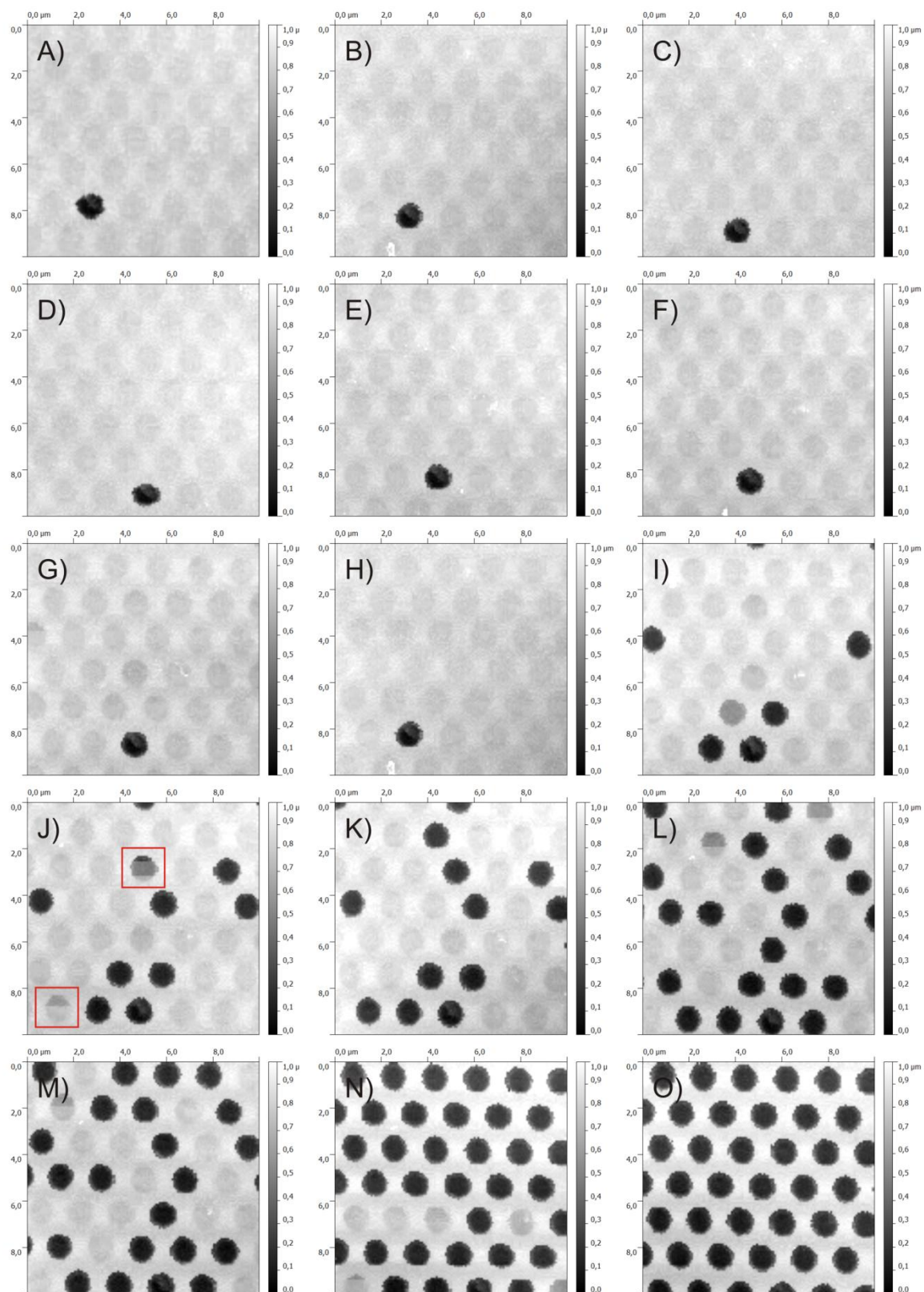


**Figure 4.9:** A series of SICM images taken during a typical melittin titration experiment on a DPhPC/chol (9:1) membrane. Melittin is applied to  $[\text{melittin}] = 349 \text{ nM}$  before F), leading to a slight increase in pore depth and first rupture events. At a critical concentration of  $[\text{melittin}] = 452 \text{ nM}$  (from K)), rupturing is completed (K-O)). J) shows membranes revealing intermediate states during rupturing (red boxes). The corresponding diagram with ruptured membranes plotted vs. time is shown in Figure 4.10 C).

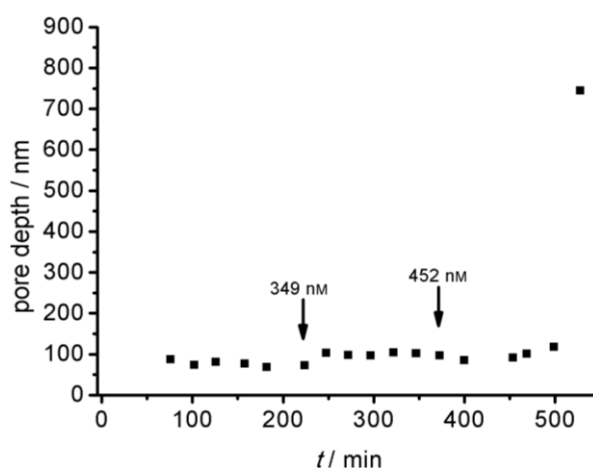


**Figure 4.10: Typical pore depth development over time of a single pore-suspending DPhPC/chol (9:1) membrane, depending on the melittin concentration. Melittin is applied to designated concentrations at time points indicated by arrows. An increase in pore depth of 21.1 nm (76.5 nm to 97.6 nm) is observed at [melittin] = 349 nm, rupturing of the membrane takes place at [melittin] = 452 nm.**

Three titration experiments were conducted with DPhPC/chol (9:1) membranes on hydrophobically functionalised substrates. Plots of the ensembles' pore depth developments are shown in Figure 4.11. Melittin induced membrane rupturing is found to be completed at 542 nm, 478 nm and 452 nm, respectively. At lower concentrations, a minor increase in pore depths is observed before rupturing occurs (cf. Fig. 4.11, [melittin] = 349 nm,  $t = 224$  min). These minor pore depth increases are observed in all three experiments prior to the actual rupturing and characterised by the small increase. Average values with standard deviations for this effect are observed as  $(33.2 \pm 8.9)$  nm,  $(21.8 \pm 7.8)$  nm and  $(31.7 \pm 9.8)$  nm, respectively (Fig. 4.11). However, not every pore-suspending membrane reveals such an intermediate state between the original intact membrane and the open pore, where the membrane has ruptured. The majority of membranes within one experiment as well as within the three experiments, however, displays similar behaviour as becomes obvious from the parallelism of data points and as shown in Figure 4.11 B), D) and F). This similarity is observed although melittin was applied in varying doses, i.e. the number of applications as well as the amount of melittin given differs between the three experiments. Figure 4.11 A) shows six additions of the CPP in  $\sim 90$  nm steps, the experiment shown in Figure 4.11 C) features four additions of two  $\sim 140$  nm and two  $\sim 90$  nm steps each, while the third experiment (Fig. 4.11 E)) was conducted with one large step ( $\sim 350$  nm) and one comparably small step ( $\sim 100$  nm).

## RESULTS

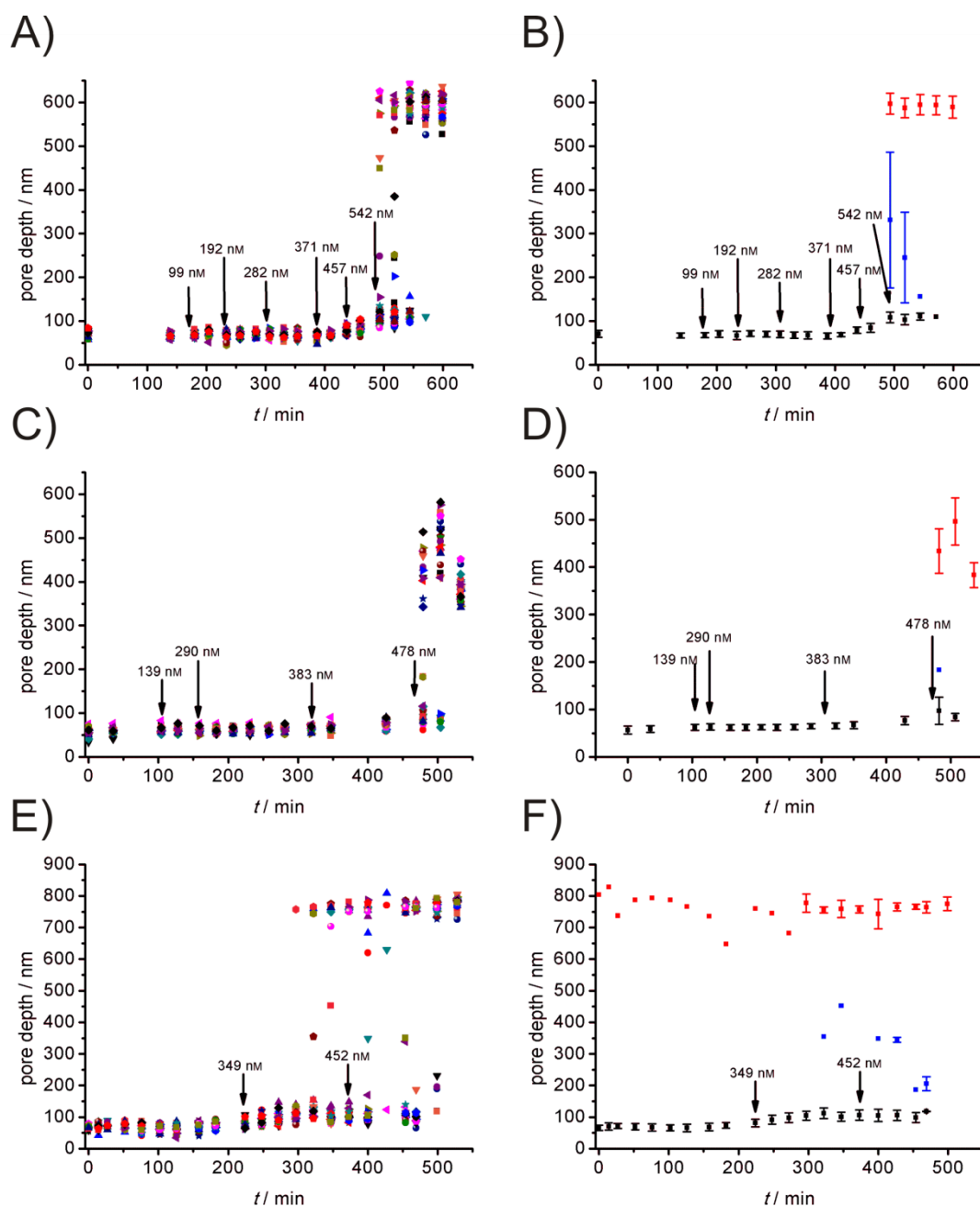


**Figure 4.11: Pore depth development for three melittin titration experiments on DPhPC/chol (9:1) membranes on CPEO3 functionalised substrates. A), C) and E) show raw pore depth data obtained during experiments, while averaged values and standard deviations were calculated for corresponding B), D) and F). Membrane rupturing is completed at [melittin] = A) 542 nM, B) 478 nM, C) 452 nM. All three experiments display highly parallel pore depth developments despite varying melittin concentration steps (number of arrows and positions) as becomes obvious from comparably small errors. Large errors are obtained for intermediate state pore depths which vary between 180 nm and 400 nm within images.**

## 4.2 INVESTIGATION OF PORE-SUSPENDING MEMBRANES ON HYDROPHILICALLY FUNCTIONALISED SUBSTRATES

This second major chapter describes experiments with pore-suspending membranes prepared on hydrophilically, i.e. ME functionalised substrates.

### 4.2.1 ESTABLISHMENT OF A SPREADING PROCEDURE

Similarly to pore-suspending membranes prepared on hydrophobically functionalised substrates, a protocol was needed to be found to reliably achieve solvent-free pore-suspending membranes. As the procedure applied for CPEO3 functionalised substrates worked reliably it was taken as a starting point. As the addition of  $\text{Ca}^{2+}$  facilitated spreading of GUVs containing negatively charged lipids it was tried whether advantages were also provided in the case of spreading on hydrophilically functionalised substrates where mediation of electrostatic interactions between ME hydroxy groups and lipid head groups might prove to be useful. Moreover, different spreading temperatures (0 °C, ambient temperature, 37 °C) and durations (15 min, 1 h, 3 h) were tried whereas sucrose concentration inside GUVs (300 mM), pore diameters (1.2  $\mu\text{m}$ ) and buffer (100 mM KCl, 10 mM Tris, pH 7.4) were adopted without further changes. Table 4.2 shows the parameters tested for improvements with respect to spreading success on hydrophilically functionalised substrates, where spreading success is defined as the ratio of substrates featuring sufficiently large membrane patches.

**Table 4.2: Parameters screened for spreading conditions of GUVs containing different lipids on ME functionalised substrates. Bold values are those adapted to a standard protocol (cf. Ch. 3.2.2).**

parameter	values tested		
spreading duration / h	0.25	<b>1</b>	3
$\theta$ / °C	<b>0</b>	ambient	37
[ $\text{Ca}^{2+}$ ] buffer content / mM	0		40

Experiments showed that the addition of  $\text{Ca}^{2+}$  did not result in enhanced spreading except for POPC/POPS (4:1) GUVs as was the case on hydrophobically functionalised substrates. 1 h was approved as the spreading duration of choice, the only major change was found to be the temperature at which spreading worked best. Independent of lipid composition, spreading was observed to be most successful at 0 °C.

GUV spreading on ME functionalised substrates, however, does not result in large porous areas covered with lipid bilayers as observed for spreading on CPEO3 (cf. Fig. 4.1 A)). In contrast to wholly covered porous regions, membrane patches corresponding to the GUVs' sizes are obtained. Figure 4.12 displays a patch of DPhPC/chol (9:1) membrane on hydrophilically functionalised substrates. It reveals one large (Fig. 4.12 A), top) and several small GUVs attached to the substrate surface. The top left corner of Figure 4.12 A) shows the narrow non porous region between porous rectangles (cf. Fig. 3.2 B)). The quality of GUV



## RESULTS

solutions is therefore more important for bilayer preparation on hydrophilically functionalised substrates than it is on hydrophobically functionalised substrates. In the former case, fewer but larger GUVs are favourable whereas in the latter case, a certain threshold diameter of few  $\mu\text{m}$  needs to be exceeded to achieve suitable patch sizes. On ME functionalised substrates, these would lead to many but small membrane patches. Within the membrane patches, however, homogeneous membrane coverage of pores is observed.

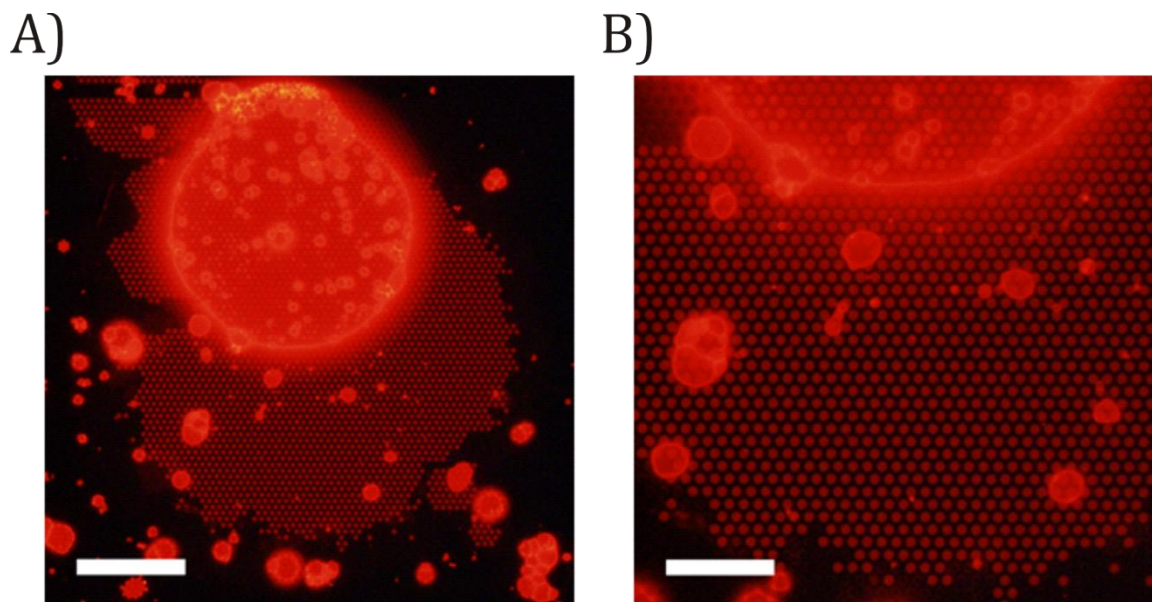


**Figure 4.12:** A DPhPC/chol (9:1) pore-suspending membrane imaged by means of fluorescence microscopy at different magnifications. A) The lack of continuous membrane coverage of a whole porous region is revealed. Pore-suspending membranes rather form patches resulting from spreading of individual GUVs – one of which is visible in the top half. B) Pore-suspending membranes on ME functionalised substrates look identical to those on CPEO3 functionalised substrates (cf. Fig. 4.1). Vesicles of various sizes remain attached to the substrate surface frequently. Scale bars: A) 27.0  $\mu\text{m}$ , B) 13.7  $\mu\text{m}$ .



#### 4.2.2 SICM IMAGING OF PORE-SUSPENDING MEMBRANES

Imaging of PSMs on hydrophilically functionalised substrates was found to be a delicate task, especially in comparison to imaging of PSMs on CPE03 (v.s.). These form patches covering whole porous rectangles of fluXXion substrates (cf. Fig. 4.1), whereas spreading on ME results in patches covered by the lipid material of a single GUV with circular areas of up to 30  $\mu\text{m}$  radii (cf. Fig. 4.12). It is thus more difficult to approach a suspended porous region of a ME based lipid bilayer with the SICM pipette due to the size of covered areas. A solution to this problem involved utilisation of an inverse optical microscope. This approach resulted in a higher probability to find a suspended patch, but was attended by consumption of more time as the pipette had to be localised with the optical microscope first before the substrate was moved underneath and directed such that the desired porous stripe and rectangle was approached. In addition to these problems specific for the imaging of PSMs on ME functionalised substrates, the obstacles discussed for PSMs on CPE03 (v.i.) had to be circumvented as well. While the first ME specific problem discussed here was related to finding the membrane patch, another was met during the imaging process on the ICNano, referred to as 'whitening' which is illustrated in Figure 4.13. When the pipette had approached the surface successfully and got in control, recording was initiated. At some point, mostly white pixels were recorded either abruptly (Fig. 4.13 A)), or the white area within pixels increased gradually (Fig. 4.13 B) and C)). This phenomenon was initially observed on membranes prepared on CPE03 during first melittin experiments but not during imaging of these membranes without melittin. The 'whitening' represents a surface of great height or, in other words, the set-point is met already before any lowering of the pipette was conducted during hopping. Blocking of the pipette was assumed as the reason for this behaviour. As samples had been rinsed with pure spreading buffer, it could only be induced by melittin or something inherent to PSMs on ME functionalised substrates. The problem was solved by a change of pipette geometry from a needle like to a bee stinger model (Fig. 4.13 D)), based on the assumption that particles blocked the pipette the more efficient the longer the narrow front part of the pipette was. The reasoning behind this assumption was that lipid material got attached to the pipette interior and blocked the pipette if it got stuck to the inner pipette wall in the narrow region. By changing the pipette geometry and shortening this narrow region, the probability for pipette blocking was reduced.

## RESULTS

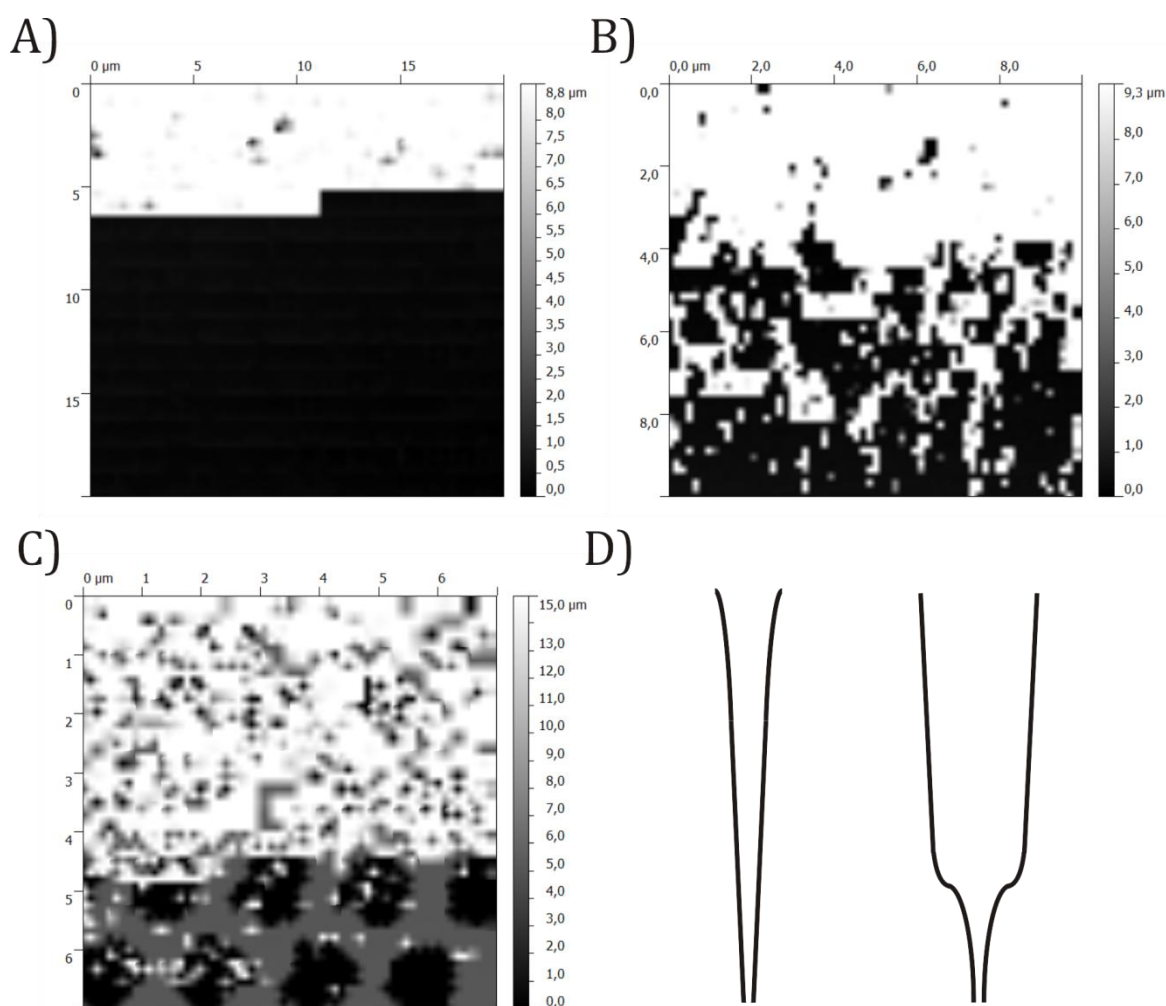


**Figure 4.13: Illustration of ‘whitening’ problem occurring during SICM imaging of lipid structures on ME in general or on CPEO3 after addition of melittin, especially on the ICNano instrument. A)-C) ‘Whitening’ of images recorded ME functionalisation. Abrupt ‘whitening’ (A)) is observed as well as gradually increasing, on non porous (A), B)) and non suspended porous regions (C)). D) shows the change in geometry from a needle like (left) to a bee stinger like model (right).**

### 4.2.3 TIME FRAME DEFINITION FOR EXPERIMENTS

The competence to distinguish between changes in measured signals induced and those not induced by CPPs is of pivotal importance as it has been described in Chapter 4.1.2. As pore-suspending membranes prepared on different functionalisations may behave differently and therefore may be usable within different time frames, additional blank experiments are needed to rule out that observed changes originate from inherent membrane instabilities rather than from the application of CPPs.

#### *Fluorescence*

A first blank experiment (Fig. 4.14) was conducted over 12 h with images taken every 10 min. There is no loss of pore-suspending membranes observed but rupturing of a single pore (top left quadrant). Another experiment was performed over 4 h where cooled buffer volumes comparable to CPP solution volumes were subsequently applied to mimic the addition of  $\mu$

volumes of ice-cooled peptide solution. It shows the same result as the experiment depicted in Figure 4.14 in terms of membrane loss. As conditions are exactly the same as applied for titration experiments, a time frame of 4 h can be securely used to conduct experiments on CPEO3 functionalised porous substrates since there is no pore rupturing induced by application of CLSM experimental conditions.

This time frame is regarded as sufficient since experiments can be started right after location of a suitable membrane covered area and preparation of CPP solutions of the desired concentration. Moreover, CLSM imaging is fast in contrast to SICM with chosen frame rates of about  $2 \text{ min}^{-1}$  (up to  $6 \text{ min}^{-1}$  possible at the resolutions chosen for most experiments) and about  $(3\text{--}4) \text{ h}^{-1}$ , respectively.

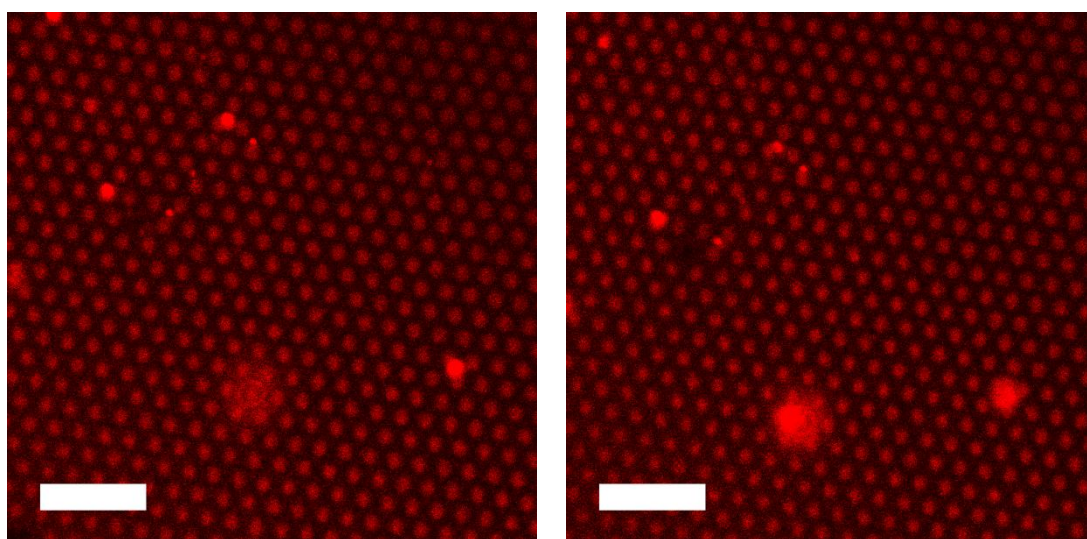


**Figure 4.14:** Images taken at the beginning ( $t = 0 \text{ min}$ ) and the end ( $t = 720 \text{ min}$ ) of a blank experiment, images were taken every 10 min. Fluorescent spots do not disappear throughout the whole experiment. Slight changes in fluorescence intensity may result from photobleaching or small shifts of the focal plane. Scale bars:  $7.6 \mu\text{m}$ .

#### 4.2.4 FLUORESCENCE TITRATION EXPERIMENTS

A variety of lipids was used to prepare pore-suspending membranes with different features as described in Chapter 3.2.2. Membranes consisting only of a neutral PC lipid (POPC) are compared to membranes comprising a PC lipid and different additions: either 10% cholesterol in addition to DPhPC, another neutral PC lipid, or 20% POPS, a negatively charged lipid, in addition to POPC. Melittin is used as a CPP and titrated to pore-suspending membranes (POPC, DPhPC/chol (9:1), POPC/POPS (4:1)). This process is monitored by means of CLSM (cf. Fig. 4.5) to investigate at which concentrations of CPP (critical concentration) the observed membranes rupture, i.e. at which  $[\text{CPP}]$  fluorescent circles indicating lipid bilayers vanish. Disappearance of fluorescence indicates rupturing of the membrane, and the number of ruptured membranes is compared to the overall number of suspended pores and plotted vs  $t$  (cf. Fig. 4.6).

## RESULTS

A typical series of fluorescence images is shown in Figure 4.5. As described above (cf. Ch. 4.1.3), the CPP's effect on the pore-suspending membrane starts between Figure 4.5 A) and B). Subsequent images reveal the random positions at which rupturing events take place. It has to be noticed that due to the patch nature of the membranes in contrast to wholly covered porous areas on hydrophobically functionalised substrates, the number of observed pores is by trend smaller on ME than on CPEO3.

Melittin has been applied to pore-suspending membranes prepared from various lipids on hydrophilically functionalised substrates as well as on hydrophobically functionalised substrates (cf. Ch. 4.1.3) to compare the influence the functionalisation type exerts on membranes and their reaction towards CPPs. Furthermore, penetratin as a second CPP has been applied to pore-suspending membranes on ME functionalised substrates to check for the assay's applicability to another CPP besides melittin.

### *Melittin*

When melittin is titrated to pore-suspending membranes on ME functionalised substrates, membranes behave in general as it is observed for those prepared on hydrophobically functionalised substrates. The number of lipid bilayers remains constant until a critical melittin concentration is reached. The whole membrane patch ruptures then within approximately 20 min in case of POPC and POPC/POPS (4:1) membranes as shown in Figure 4.12. In these two cases, the curve shape is found to be sigmoidal as it has been described for membranes on CPEO3 functionalised substrates as well, i.e. a short initial stage of slow increase in the number of ruptured pores is followed by a fast increase with an inflexion point when approximately 50% of the observed pores are ruptured. There is hardly any deceleration phase visible in the graphs obtained from CLSM experiments.

Membranes prepared from pure PC lipids (POPC) rupture at [melittin] = 1200 nM (Fig. 4.15 A)), for rupturing of membranes containing negatively charged lipids (POPC/POPS (4:1)) 700 nM of melittin are necessary (Fig. 4.15 B)). As stated above, both these lipid compositions show a sigmoidal curve in the rupturing vs  $t$  plot with completion of membrane disappearance within 20 min. In contrast to this, DPhPC/chol (9:1) shows a rupturing curve that has a much longer slow starting phase (Fig. 4.15 C)). Rupturing starts at [melittin] = 1600 nM but, another difference, completion of this process takes approximately 3.5 h which is not observed for any other experiment with melittin on pore-suspending membranes (penetratin induced rupturing processes take longer but are completed within 2.5 h, v.i.). While experiments on POPC and POPC/POPS (4:1) are reproducible (N = 2), the experiment on DPhPC/chol (9:1) is not reproduced, i.e. Figure 4.15 C) represents a single experiment. The random nature of the positions of subsequent rupturing events, however, holds throughout the whole series of melittin titration experiments on ME functionalised substrates.

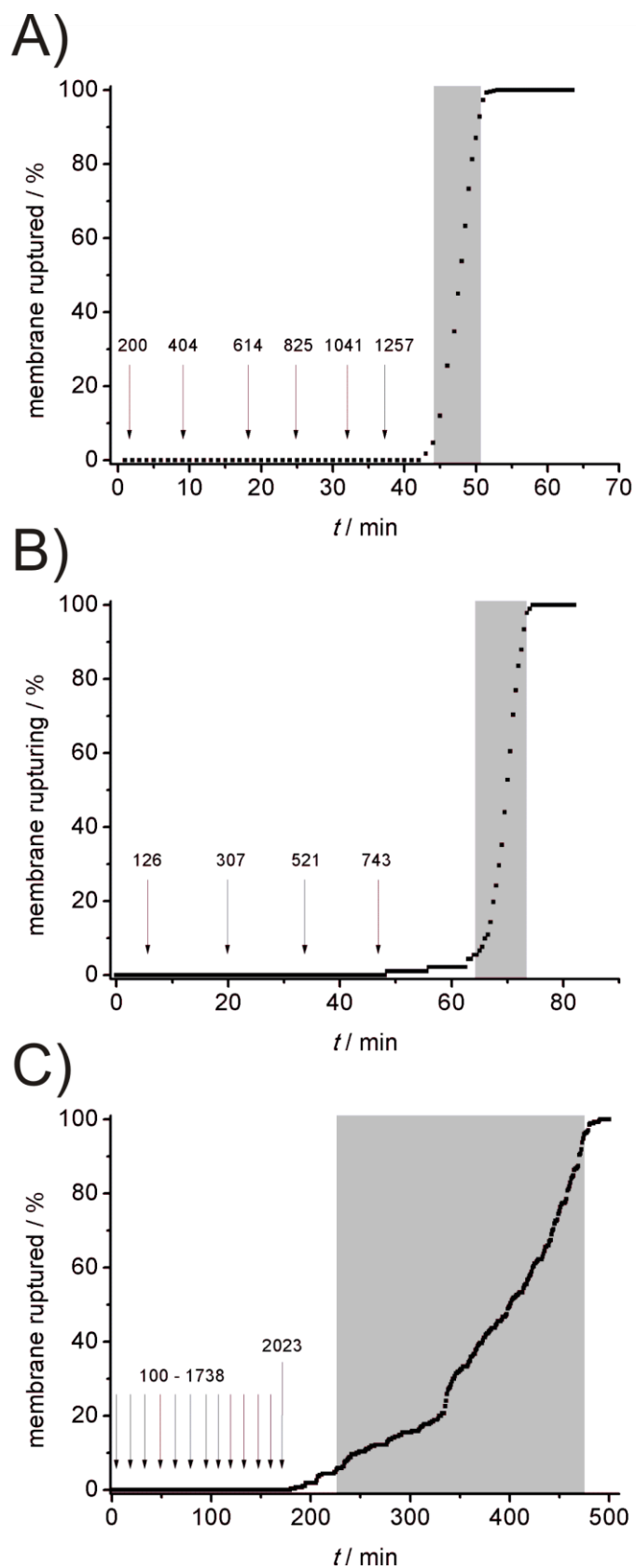


**Figure 4.15: Melittin titrations on pore-suspending membranes prepared from different lipid compositions on ME functionalised substrates, N pores are observed. A) POPC, N = 400; B) POPC/POPS (4:1) N = 91; C) DPhPC/chol (9:1), N = 270. There are 12 melittin additions in (100–150) nM steps before membranes start rupturing after the 13th. Arrows indicate the addition of melittin to the sample with corresponding numbers showing [melittin] / nM after addition. Grey rectangles illustrate the time between 5% and 95% membrane ruptured with A) 7 min, B) 9 min, C) 249 min.**

## RESULTS

### *Penetratin*

Titration of penetratin to pore-suspending membranes on ME functionalised substrates follows the same basic principles as is observed for titration of melittin, i.e. there is no loss of membranes until a critical penetratin concentration is reached. Pore-suspending lipid bilayers start rupturing at this critical concentration until fluorescence signals indicating these bilayers have disappeared completely. While penetratin and melittin titrations result in the same basic observations, there are differences with regard to details such as duration of the rupturing process and shape of the obtained curves of rupturing events vs  $t$ .

Curve shapes for penetratin experiments differ from those obtained in melittin experiments such that the number of ruptured pore-suspending lipid bilayers increases linearly with time, albeit with a straight linearity in the case of POPC/POPS (4:1) (Fig. 4.16 B)) only whereas POPC (Fig. 4.16 A)) and DPhPC/chol (9:1) (Fig. 4.16 C)) show alternating phases of rapid and slow increases in the number of ruptured membranes. Figure 4.16 reveals a sudden start of the rupturing process for every lipid composition without significant acceleration phases as is observed for melittin experiments. On the other hand, POPC/POPS (4:1) shows a pronounced deceleration phase whereas POPC and DPhPC/chol (9:1) exhibit constant rupturing velocities until the whole patch has disappeared. A second difference besides the curve shape is the duration of the rupturing processes. While melittin addition results in completion of rupturing within an average 20 min, penetratin effects complete disappearance of lipid bilayers fastest on POPC/POPS (4:1) (Fig. 4.16 B)) where it takes 40 min. Membranes consisting of POPC (Fig. 4.16 A)) and DPhPC/chol (9:1) (Fig. 4.16 C)) rupture within 140 min.

Compared to melittin CLSM experiments, penetratin effects lipid bilayers at significantly higher concentrations. The highest critical penetratin concentration is found for POPC/POPS (4:1) membranes where  $[\text{penetratin}] = 3 \mu\text{M}$  is necessary to observe vanishing of fluorescence signals. POPC membranes rupture at a critical concentration of  $2 \mu\text{M}$ , membranes prepared from DPhPC/chol (9:1) GUVs are affected at concentrations as low as  $1.6 \mu\text{M}$  (Fig. 4.16 C) shows an experiment where  $1.5 \mu\text{M}$  penetratin has not affected membrane rupturing, the next titration step has been to  $2 \mu\text{M}$ ). Experiments are reproducible ( $N = 2$ ) and result in the same critical concentrations for same lipid compositions.

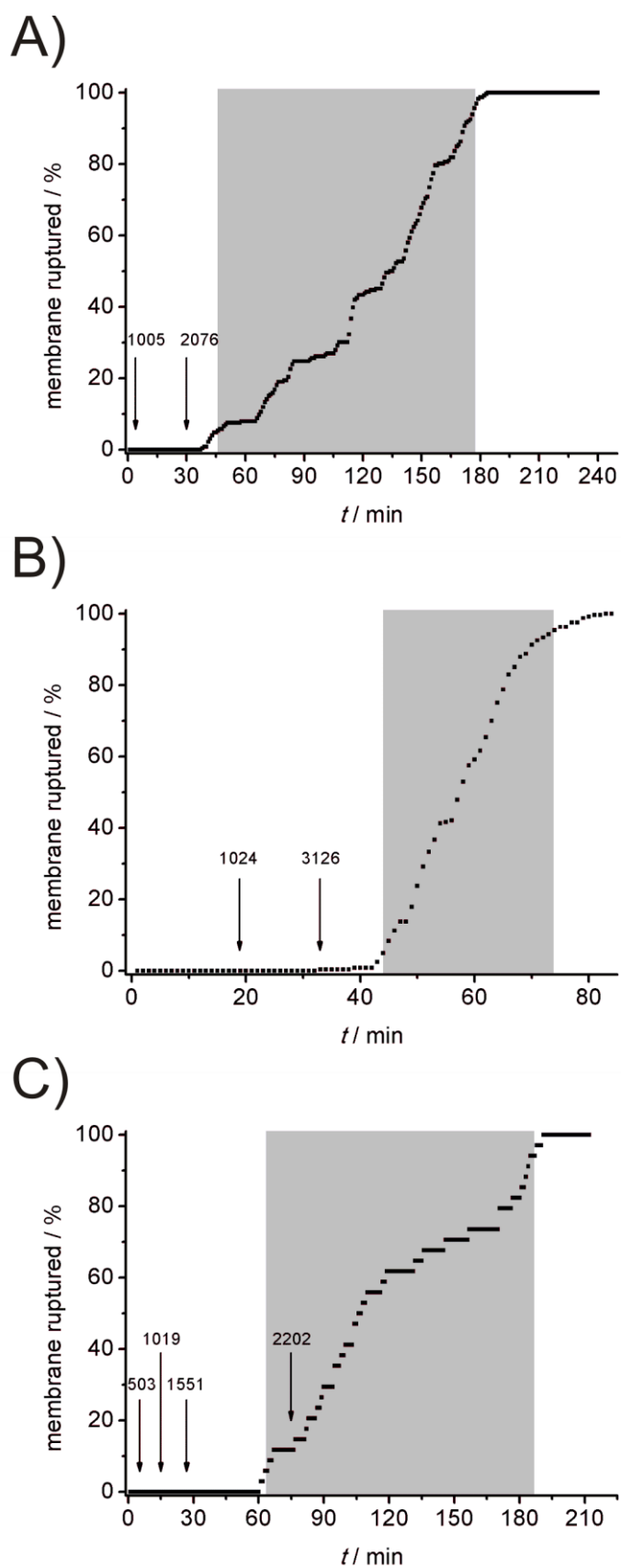
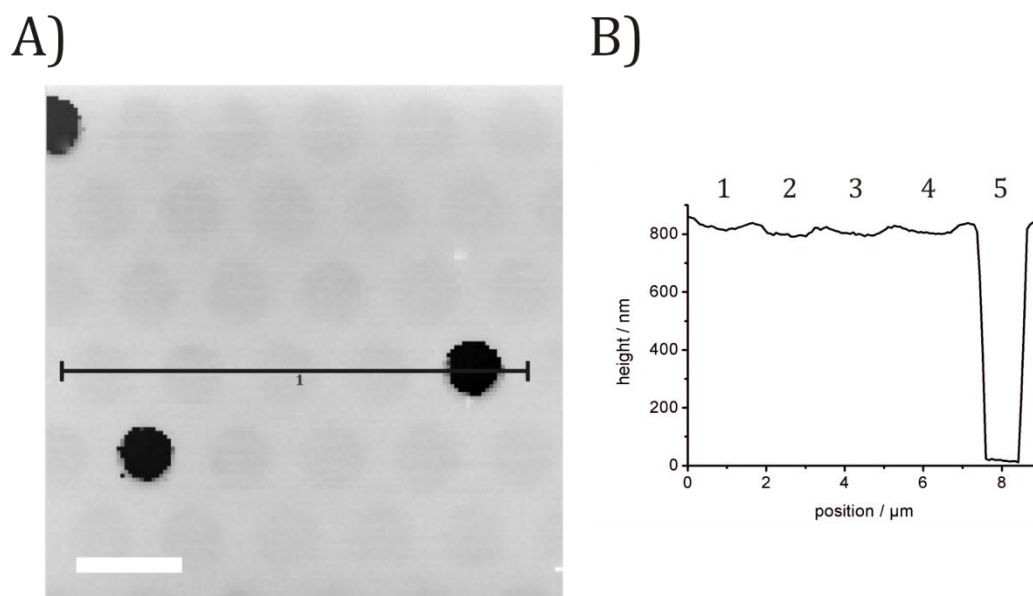


Figure 4.16: Penetratin titrations on pore-suspending membranes prepared from different lipid compositions on ME functionalised substrates, N pores are observed: A) POPC, N = 226; B) POPC/POPS (4:1) N = 240; C) DPhPC/chol (9:1), N = 34. Arrows indicate the addition of penetratin to the sample with corresponding numbers showing [penetratin] / nm after addition. Grey rectangles illustrate the time between 5% and 95% membrane ruptured with A) 131 min, B) 30 min, C) 123 min.

## RESULTS

### 4.2.5 SICM TITRATION EXPERIMENTS

Pore-suspending membranes on ME functionalised substrates were subjected to SICM investigations. Similarly to experiments utilising fluorescence microscopy, titration experiments were performed in order to find out those CPP concentrations at which membranes are affected. Lipid compositions were varied to investigate the interactions between melittin and different membranes. Figure 4.17 displays a typical SIC micrograph of pore-suspending membranes.



**Figure 4.17:** A) Typical SICM image of PSMs with suspended pores and non suspended pores. Topography data are obtained by profile lines as indicated. B) Corresponding profile. Suspended pores feature pore depths of approximately 30 nm (1-4), whereas non suspended pores are approximately 800 nm deep (5). Scale bar: 2.0 μm.

#### *Topography of pore-suspending membranes*

As described in Chapter 4.1.4, titration experiments entail topographic information which can be used to gain further insight into pore-suspending membranes' architecture.

Figure 4.18 shows a histogram comprising data obtained via analysis of a row of representative SICM images of pore-suspending membranes prepared on hydrophilically functionalised substrates. All images evaluated for this histogram were recorded without any manipulations conducted once the spreading buffer containing GUVs had been exchanged against SICM buffer. The evaluation includes 157 pores suspended by lipid bilayers from nine different images and exhibits an average pore depth of 59 nm (median: 57 nm).



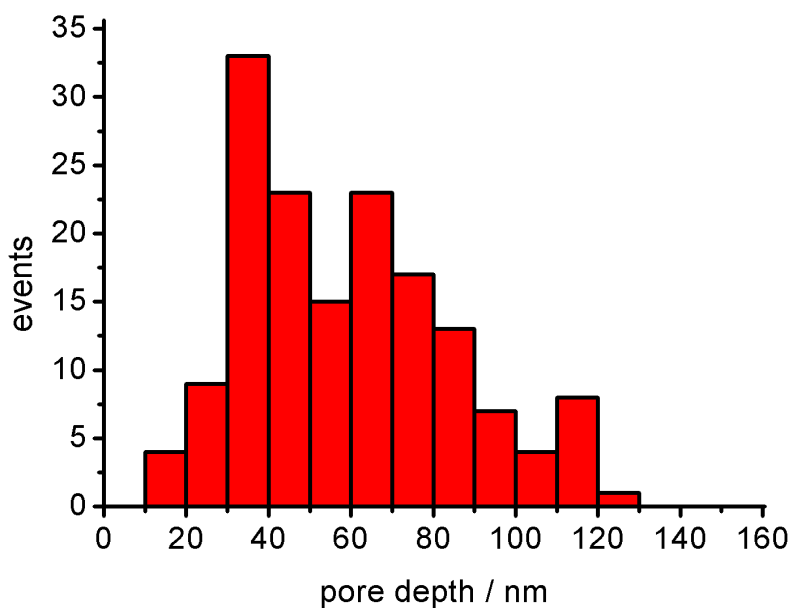


**Figure 4.18:** Pore depth distribution of a representative selection of SICM images of pore-suspending membranes on ME functionalised substrates. An average pore depth of 59 nm (median: 57 nm) is obtained.

#### *Melittin titrations*

SICM experiments were performed to monitor the effect of melittin interacting with pore-suspending membranes. In order to obtain critical CPP concentrations at which pore-suspending membranes are affected, the CPP is titrated to the lipid bilayers. The change in pore depth over time is correlated to the melittin concentration and reveals lipid-peptide interactions. Bilayers investigated by means of SICM were prepared from DPhPC/chol (9:1) or POPC GUVs as described in Chapter 3.2.2.

A typical example of a series of SICM images recorded during an experiment where melittin was titrated to a DPhPC/chol (9:1) membrane on CPEO3 has been shown above (cf. Ch. 4.1.4.). A similar course is obtained for experiments on membranes prepared on ME functionalised substrates. Several experiments, however, resulted in images not suitable for quantitative analysis with respect to pore depth development as shown in Figure 4.19.

The problem encountered and shown here, is the instrument's inability to work on substrates with open pores. After measuring squares with a high ratio of infinite depth (open pore), the pipette lost contact until the pipette was withdrawn and moved to the start of the next line in unidirectional scanning mode. Recording a larger image provides an insight to which extent rupturing is completed (Fig. 4.19 F)).

Quantitative analysis was possible for two experiments, one each on DPhPC/chol (9:1) and POPC on hydrophilically functionalised substrates.

## RESULTS

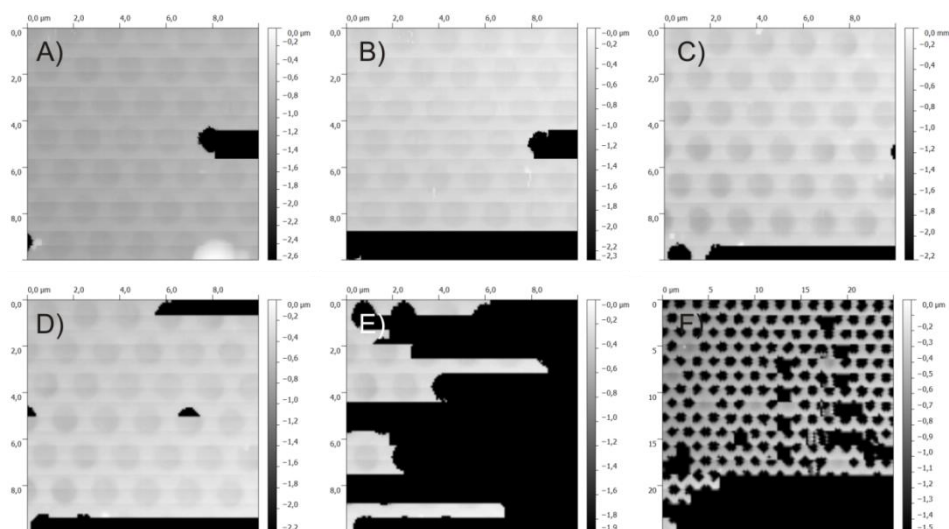


Figure 4.19: A selection of images from a titration experiment where melittin was added to a pore-suspending POPC membrane prepared on ME. The problem observed frequently and illustrated here in every image A)-F): the system did not tolerate open pores, especially for membranes prepared on ME.

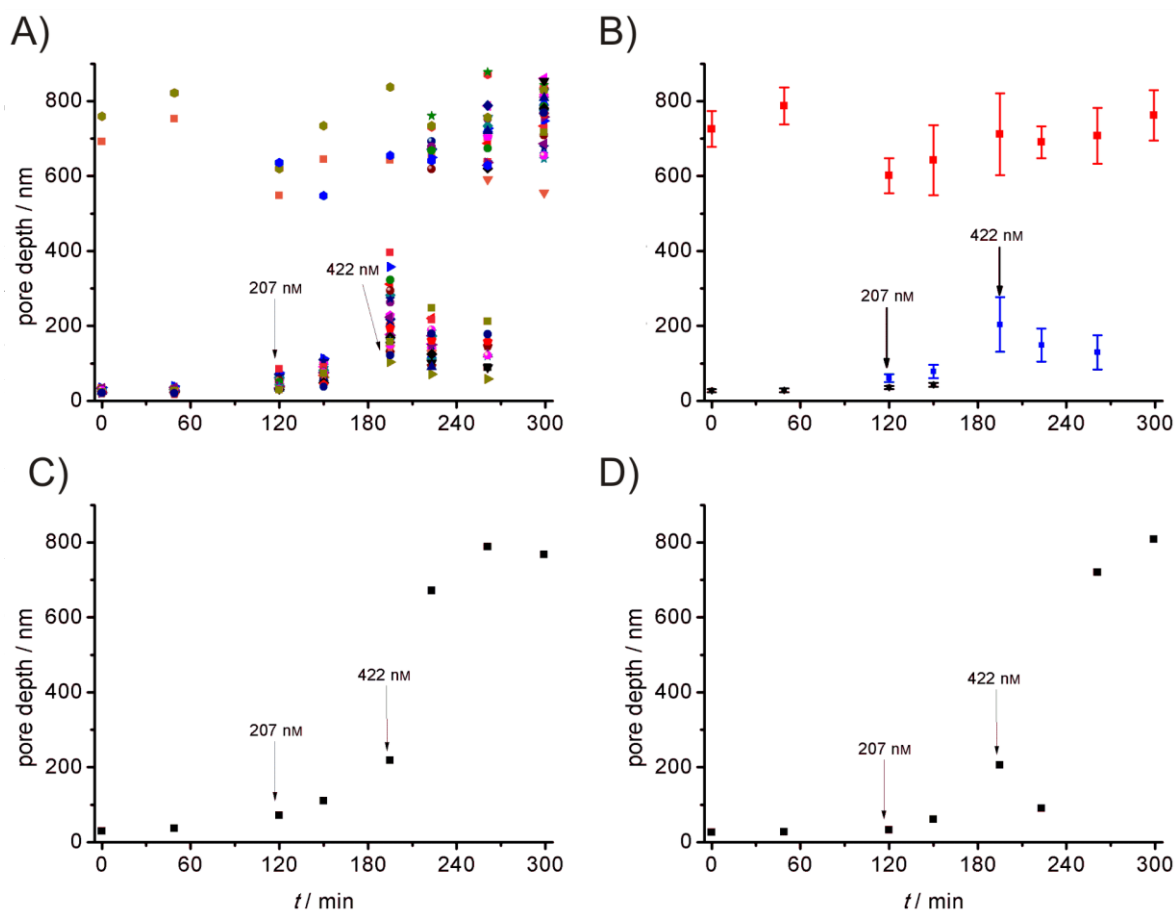
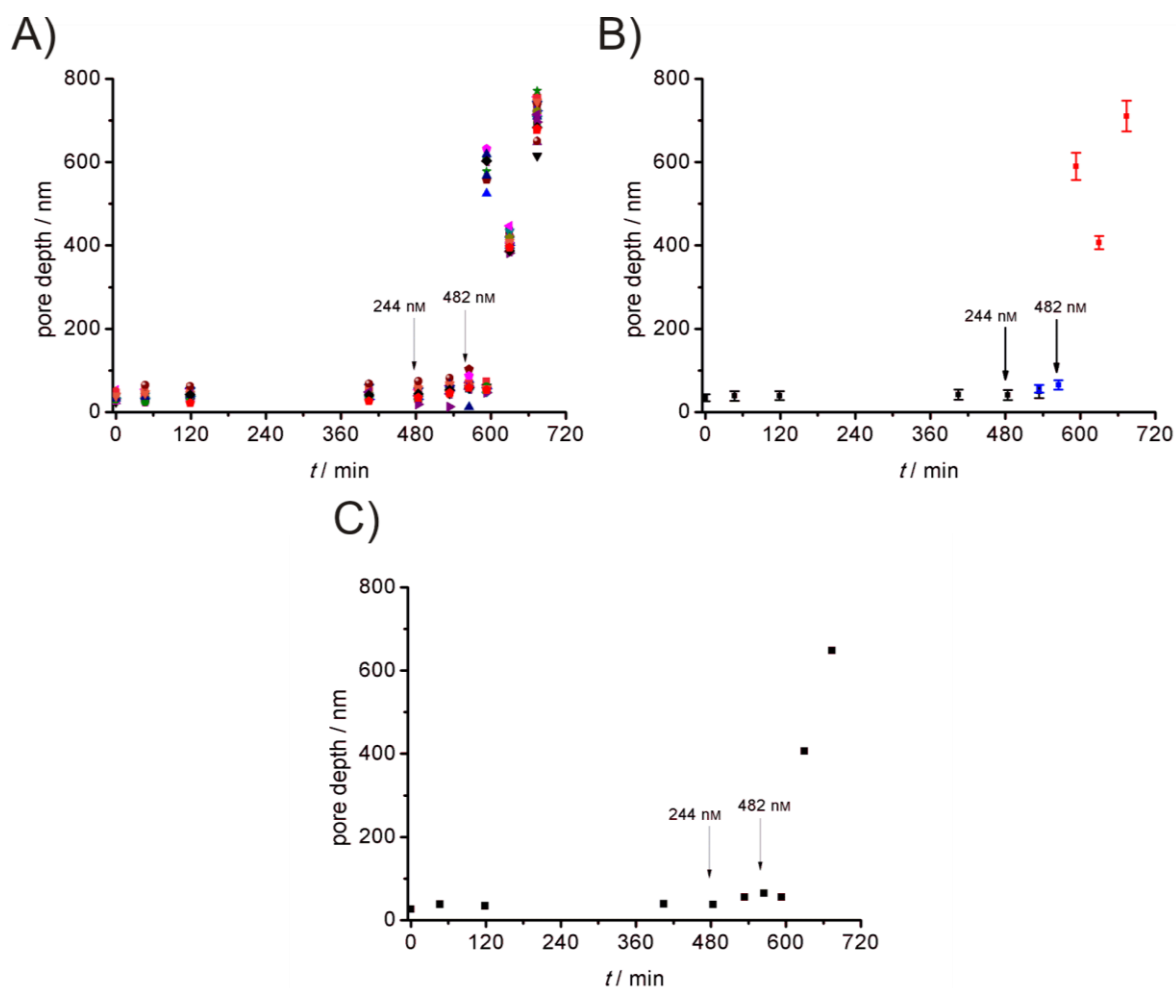


Figure 4.20: A) Pore depth development for the ensemble of a melittin titration experiment on a POPC membrane on ME functionalised substrate. B) Average pore depths and standard deviations for suspended pores (black), non suspended pores (red) and intermediate state membranes (blue) were calculated. Errors for intermediate state pore depths are comparably large as pore depths in the range of approximately (60–400) nm were considered as intermediate states. C) shows the typical course for a single membrane: at a melittin concentration of 207 nM an increase in pore depth is observed, membrane rupturing is completed at [melittin]=422 nM. D) shows a different course found several times. Remarkably, the pore depth increases first after addition of the critical melittin concentration by 145 nm, but decreases again by 115 nm before the membrane ruptures.



**Figure 4.21:** A) Pore depth development for the ensemble of a melittin titration experiment on a DPhPC/chol (9:1) membrane on ME functionalised substrate. B) Average pore depths and standard deviations for suspended pores (black), non suspended pores (red) and intermediate state membranes (blue) are displayed. C) shows the typical course for a single membrane: at a melittin concentration of 244 nM an increase in pore depth is observed, membrane rupturing is completed at [melittin] = 482 nM.

The ensemble's pore depth development for the DPhPC/chol (9:1) membrane is displayed in Figure 4.21 A), average values and standard deviations shown in Figure 4.21 B). Figure 4.21 C) reveals the typical course of the experiment for a single pore. With two exceptions in the ensemble plot, the pore depth increases when melittin is applied first to a concentration of 244 nM. Rupturing does not occur at this concentration but after the second application where [melittin] = 482 nM is reached, and rupturing of membranes is completed within 65 min. High variations in pore depths found when pores are not membrane-suspended anymore are due to the instrument's operation.

High parallelism in the course of pore depths throughout the experiments is observed as becomes obvious from Figure 4.21 A). A small increase in pore depths is found for most pore-suspending membranes before the second application of melittin after 565 min. The average increase amounts to  $(22 \pm 7)$  nm.



## 5 DISCUSSION

All experiments in this study were designed to be conducted by means of confocal laser scanning microscopy (CLSM) or scanning ion conductance microscopy (SICM). Artificial lipid membranes were chosen as the system observed as they allow for reduction of parameters such that a single variable determines potential differences in the system's behaviour. Pore-suspending membranes (PSMs) were used as the system of choice since they combine equally good accessibility for both CLSM and SICM with features mimicking cells more closely than other membrane model systems (cf. Ch. 1.3.4). Porous silicon nitride ( $\text{Si}_3\text{N}_4$ ) substrates with pore diameters of (800–2000) nm were utilised as pores of these dimensions are readily resolvable by means of both CLSM and SICM. This is not the case for porous substrates prepared from aluminum oxide with typical pore diameters of less than 60 nm. In order to develop and perform CLSM and SICM assays, pore-suspending membranes had to be prepared and inspected for sufficient quantity and quality, i.e. reliable preparation of sufficiently large and stable membrane patches. This examination was conducted by means of CLSM and SICM imaging before peptide titration experiments were developed and conducted.

### 5.1 ASSAY DEVELOPMENT

A variety of experiments involving pore-suspending membranes has been conducted demonstrating the potential advantage of this relatively recent improvement in membrane model system development. Fluorescence microscopy was utilised for the investigation of lipid domains within PSMs [Orth et al. 2012], electrophysiology was employed for the characterisation of ion channels [Gaßmann et al. 2009] and atomic force microscopy was used to evaluate bilayer mechanics [Mey et al. 2009; Kocun et al. 2011].

A wide range of assays has been conducted to elucidate melittin membrane interactions. In one major part of these assays, melittin was applied to erythrocytes. Typical experiments addressed the quantification of lytic activity by means of centrifugation or filtration assays. Melittin was added to a cell culture and the amount of haemoglobin in the supernatant was determined after centrifugation or filtration, respectively [DeGrado et al. 1982; Katsu et al. 1989; Oren and Shai 1997; Raghuraman and Chattopadhyay 2005]. Further assays included the quantification of inhibition of cell growth via cell density determination [Oren and Shai 1997] or colony counting as well as straightforward optical microscopy to monitor morphological changes [Katsu et al. 1989]. A second major part dealt with the investigation of interactions of melittin with membrane model systems, predominantly small or large unilamellar vesicles (SUVs or LUVs, respectively). Typical experiments include release assays to identify concentrations at which pores are formed or vesicles are lysed, to determine the size of these pores or to address questions with regard to mechanism or kinetics of melittin

## DISCUSSION

membrane interactions [Schwarz et al. 1992; Ohki et al. 1994; Benachir and Lafleur 1995; Benachir et al. 1997; Ladokhin et al. 1997; Allende and McIntosh 2003; Allende et al. 2005; van den Bogaart et al. 2008]. The effect of melittin membrane interactions on both the peptide and the bilayer as well as the peptide's affinity for membranes were investigated in a number of binding assays, e.g. by means of X-ray scattering to quantify membrane thicknesses, of phosphorous nuclear magnetic resonance (NMR) or fluorimetric analysis of the tryptophan residue's environment to investigate peptide orientation [Batenburg et al. 1988; Ghosh et al. 1997; Lee et al. 2001; Sheynis et al. 2003; Raghuraman and Chattopadhyay 2004; Lee et al. 2008]. Solid supported membranes (SSMs) were utilised to investigate membrane permeabilisation by means of impedance spectroscopy or to visualise the effect of melittin on lipid bilayers by means of AFM [Steinem et al. 2000], to examine the affinity of melittin for membranes of varying compositions or solve mechanistic questions by means of surface plasmon resonance (SPR) [Lee et al. 2001; Papo and Shai 2002].

In this study, assays based on CLSM and SICM were developed for the investigation of the interactions of the membrane active peptides melittin and penetratin with pore-suspending membranes. The main advantages of SICM are that imaging omits mechanical contact between probe and sample and that membrane permeability is an intrinsic parameter of the method. It is thus comparable with the impedance spectroscopy and AFM study on SSMs [Steinem et al. 2000] but provides the utilisation of PSMs as a further enhancement. Another advantageous feature is that rupturing of pores is observed individually and as part of a statistical ensemble by means of both CLSM and SICM which distinguishes these assays from e.g. vesicle leakage [Schwarz et al. 1992; Ohki et al. 1994; Benachir and Lafleur 1995; Benachir et al. 1997; Ladokhin et al. 1997; Allende and McIntosh 2003; Allende et al. 2005; van den Bogaart et al. 2008] or single GUV experiments [Mally et al. 2007; Lee et al. 2008].

## 5.2 PREPARATION OF PORE-SUSPENDING MEMBRANES

Membranes of various lipid compositions were desired, i.e. bilayers consisting of pure phosphocholine lipids, membranes of phosphocholine lipids with phosphoserine lipid content as well as those of phosphocholines and cholesterol. In addition to these three variations, membranes on both hydrophilically as well as hydrophobically functionalised substrates were intended. To this end, generalised protocols for the preparation of pore-suspending membranes were needed.

Since model membranes aimed at mimicking natural situations as closely as possible, GUV spreading was preferred to painting. The drawback of the latter – residual solvent near the rims – was circumvented, and the drawback of the former – impossibility of the formation of electrically insulating membranes – did not hamper the experiments in this study as they do not require insulation but sufficiently large membrane patches only.

A variety of spreading strategies has been developed. One possibility is the application of vesicle solution on non functionalised substrates such as silicon oxide (SiO<sub>2</sub>) [Mey et al. 2009]

or silicon nitride ( $\text{Si}_3\text{N}_4$ ) [Kresák et al. 2009]. A more frequently applied strategy is the coverage of the substrate rims with gold by means of evaporation. Thiolipids or analogues thereof are chemisorbed and form a monolayer on which vesicles can be spread. Early functionalisations aimed at utilisation of electrostatic interactions between negatively charged 3-mercaptopropionic acid (MPA) and vesicles comprising positively charged lipids such as *N,N*-dimethyl-*N,N*-dioctadecylammonium bromide (DODAB) [Hennesthal and Steinem 2000; Steltenkamp et al. 2006]. More recent approaches utilised hydrophobic or hydrophilic interactions where gold covered surfaces were further functionalised with octane thiol (OT) or cholesterylpolyethylenoxy thiol (CPEO3) in case of the former [Mey et al. 2009] and mercaptoethanol (ME) in the latter case [Kocun et al. 2011]. Another strategy circumvents the metal coverage by direct modification of silicon [Heinemann and Schwille 2011] or aluminium oxide substrates [Lazzara et al. 2011a; Lazzara et al. 2011b] with silanes. The principal difference between the latter strategies of gold evaporation and silanisation is that the metal is evaporated only on top of the covered substrate while simple silanisation does not discriminate between pore rims and interior such that the pore interior may be covered with lipids rather than bilayers suspending the pore. A more sophisticated approach, however, does lead to differently functionalised substrate surfaces [Lazzara et al. 2011b].

In this study, existing protocols for the preparation of specific PSMs on silicon nitride substrates were taken as starting points for the generalisation. These starting points included thiol chemistry, i.e. the use of Ti, Au and CPEO3 for hydrophobic functionalisation [Mey et al. 2009], while ME was chosen for hydrophilic functionalisation based on a study by Kocun et al. [Kocun et al. 2011]. The evaporation procedure results in sufficiently good discrimination of pore rims and interior such that spreading and PSM formation was achieved. Application of the same functionalisation strategy for both hydrophobically and hydrophilically functionalised substrates appears preferable with respect to comparability of results.

Variation of sucrose concentration inside GUVs, pore diameters, spreading duration, the buffer system and its  $\text{Ca}^{2+}$  buffer content as well as the spreading temperature resulted in a successfully applicable spreading protocol for CPEO3 functionalised porous substrates of all desired membrane types, i.e. pure PC membranes, PC membranes with PS content and those with cholesterol content. Similarly, slight variations of parameters mentioned above, resulted in successful preparation of PSMs on ME functionalised porous substrates. Thus the developed protocols provide fast and reliable access to the complete range of membrane varieties intended for CLSM and SICM investigations.

A caveat has to be considered for PSMs prepared on CPEO3 functionalised substrates. Due to hydrophobic substrate surfaces, persistence of air bubbles within the pores has to be considered, such that lipid monolayers on air would be achieved instead of bilayers separating two aqueous compartments. In order to prevent air bubbles from remaining in pores, the substrate was covered with ethanol to reduce the surface tension and induce gas emission. After extensive exchange of ethanol against buffer, the sample was carefully handled such that air contact was excluded. Complete removal of gas from the pores, however, cannot be guaranteed by careful handling alone.

## DISCUSSION

### 5.3 IMAGING OF PORE-SUSPENDING MEMBRANES

Prior to both assay development in the first place and assay conduction once it was established, imaging of PSMs was performed by CLSM and SICM. CLSM imaging was utilised to examine the success of PSM preparation, and SICM imaging was employed to gain topography information in addition to further proof of PSM existence.

#### 5.3.1 CLSM IMAGING

Imaging of fluorescently labelled pore-suspending membranes has been done frequently and routinely since the late 1970s [Edidin et al. 1977; Schlessinger et al. 1977; Derzko and Jacobson 1980; Klausner and Wolf 1980; Struck and Pagano 1980; Spiegel et al. 1984; Weiskopf et al. 2007; Mey et al. 2009; Windschiegl et al. 2009; Kocun et al. 2011; Orth et al. 2012]. The only requirement the fluorophore has to meet is a certain photostability as fluorescence titration experiments with image recording every 30-60 s are performed for up to several hours. Texas Red DHPE was tried successfully as shown by blank experiments (cf. Ch. 4.1.3 and 4.2.3) and used throughout this study.

#### 5.3.2 SICM IMAGING

Few studies have focused on the investigation of the topography of pore-suspending membranes. An early atomic force microscopy (AFM) study was performed to prove existence of PSMs on alumina substrates [Hennesthal and Steinem 2000]. Topographic information was obtained for membrane patches, however, but not for single pores suspended by lipid bilayers. Later experiments focused on mechanical features of lipid membranes but yielded topographical information of individual pores as well [Steltenkamp et al. 2006]. A first project dealt with alumina substrates with pore diameters in the range of 60–200 nm. Figure 5.1 A) displays the image recorded in contact mode in aqueous solution as well as a line profile. Non suspended pores appear to feature pore depths of approximately 18 nm whereas PSMs' pore depths depend on the load force: low force (0.9 nN) reveals pore depths of approximately 5 nm which changes to approximately 18 nm when stronger force is applied (2.7 nN) such that covered and non covered pores cannot be distinguished. Further projects investigated mechanics of PSMs prepared on the same substrates as used in this study which were functionalised similarly: OT or CPEO3 for hydrophobic [Mey et al. 2009] and ME for hydrophilic functionalisation [Kocun et al. 2011]. Membrane topographies obtained are displayed in Figure 5.1 B) and 5.1 C). While both experiments were performed in contact mode and reveal similar pore depths of approximately 90–100 nm for suspended pores, significant differences become obvious with respect to the profile lines: Mey et al. obtained symmetrical parabola profiles, Kocun et al. featured complete asymmetry. Pore diameters were overestimated by 0.1–0.2  $\mu\text{m}$  in both studies as values of 1.3–1.4  $\mu\text{m}$  are deduced from line profiles. For all AFM experiments conducted in contact mode, it has to be



taken into consideration that the membrane topography as recorded is influenced by the cantilever.

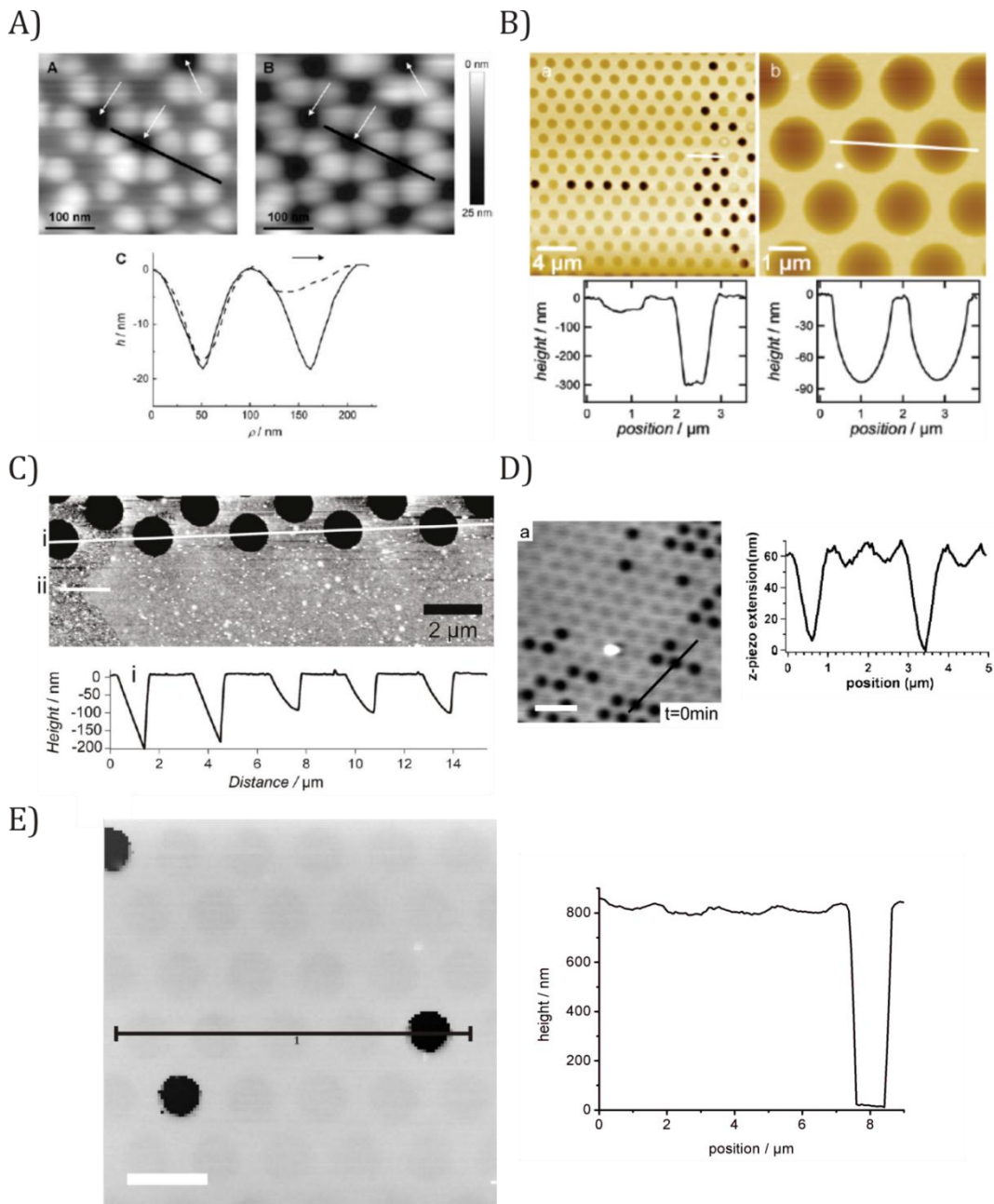


**Figure 5.1:** A comparison of images and line profiles obtained by AFM and SICM experiments. A) Topography image and profile line obtained from PSMs on an aluminium oxide substrate by means of AFM. The pore depth depends on the load force: low forces reveal pore depths of 5 nm for covered pores while high forces result in pore depths of 18 nm for both covered and uncovered pores [Hennesthal and Steinem 2000]. B) PSMs on hydrophobically functionalised  $\text{Si}_3\text{N}_4$  substrates with pore diameters of 800 nm (left) and 1.2  $\mu\text{m}$  (right). Contact mode AFM imaging reveals pore depths of 50 nm and 80 nm, respectively, for covered pores and almost perfect symmetry [Mey et al. 2009]. C) Similar pore depths of 90 nm are obtained from contact mode AFM imaging of PSMs on hydrophilically functionalised substrates with 1.2  $\mu\text{m}$  pore diameters. The profile, however, displays high asymmetry [Kocun et al. 2011]. D) SICM imaging of painted membranes on OT functionalised  $\text{Si}_3\text{N}_4$  with 450 nm pore diameters [Böcker et al. 2009]. Pore depth evaluation is complicated by the narrow pores as becomes obvious from the comparison with the E) typical image and profile obtained in experiments of this study where PSMs were prepared on hydrophilically functionalised  $\text{Si}_3\text{N}_4$  substrates with 1.2  $\mu\text{m}$  pore diameters. Membranes suspending 450 nm pores feature pore depths of approximately 10 nm but the profile shows an almost triangular shape for the pore (D)), whereas those suspending 1.2  $\mu\text{m}$  pores are approximately 30 nm deep (E)), and a profile with a flat bottom allowing for a more precise pore depth analysis. Scale bars: C) 2.1  $\mu\text{m}$ ,

## DISCUSSION

SICM provides a scanning probe microscopy (SPM) without mechanical contact between sample and probe. Experiments have so far mainly been conducted on living cells [Bustamante et al. 1991; Sigurdson et al. 1992; Green and Gillette 1983; Bossu and Feltz 1984; Gu et al. 2002; Ducholier 2005; Gao et al. 2009] or for development of new methods [Mannelquist et al. 2001; Pastré et al. 2001; Shevchuk et al. 2001; Novak et al. 2009, Mann et al. 2002; Happel et al. 2003; Takahashi et al. 2010a; Zhukov et al. 2012]; few publications have dealt with theoretic investigations [Nitz et al. 1998; Rheinlaender and Schäffer 2009; Edwards et al. 2009]. In the branch of living cell investigation, few generalised assays have been developed such as cell volume measurements. To date, imaging of membrane model systems has been conducted once by Böcker and co-workers [Böcker et al. 2009]. In that study, however, membranes were prepared from pure DPhPC and exclusively obtained via painting on octadecanethiol on pores of 450 nm diameter. In this study, on the contrary, PSMs containing a variety of lipids were prepared via spreading of GUVs on 1.2  $\mu\text{m}$  diameter pores and imaged by SICM for the first time. SICM images of PSMs by Böcker et al. [Böcker et al. 2009] as well as obtained in this study are displayed in Figure 5.1 D) and 5.1 E) and compared to AFM images (v.s.). It becomes obvious that 1.2  $\mu\text{m}$  diameter pores are much more suitable for pore depth analyses as their bottom appears as a much wider flat line (Fig. 5.1 E)) in contrast to the bottom of 450 nm pores with almost triangular profiles (Fig. 5.1 D)). Similarly to AFM experiments described above, pore diameters were overestimated by both the SICM study on painted as well as solvent-free PSMs. Pores appeared 160 nm wider in the former case which is in agreement with the approximately 1.4  $\mu\text{m}$  diameters found in this study on nominally 1.2  $\mu\text{m}$  diameter pores. This observation is in line with predictions by Edwards et al. [Edwards et al. 2009] based on finite element modelling. The degree of overestimation strongly depends on the set-point and the step height. In general, though, a change in the pipette z position is observed at lateral distances of the pipette from the step in the range of 1–3  $r_i$  (1–3fold inner pipette radius), but Edwards et al. point out that their assumed pipette sample distance is smaller than those typically used in experiments such that a step as considered would affect the pipette at even larger distances in practise.

In this study, there are not any differences revealed between membranes of various lipid compositions with respect to the shape of PSMs or their pore depth. Furthermore, there is no influence of the functionalisation (CPEO3 vs ME) on the PSM shape observed nor have differences been found in previous experiments. The pore depths, per contra, are revealed to be functionalisation dependent (v.i.). Differences with respect to geometry may exist, though, and be not resolvable by means of SICM as its vertical resolution is on the order of  $10^0$ – $10^1$  nm, while geometrical differences will, if at all, exist in the transition region between rim and free-standing membrane. Even if variations of bilayer courses had been revealed, it would have been necessary to consider the effect of the pore walls preventing unrestricted ion flow (cf. Ch. 1.2.3).

An evaluation of 269 PSMs on CPEO3 and 157 PSMs on ME results in average pore depths of  $(79.6 \pm 13)$  nm and  $(59.3 \pm 25.7)$  nm, respectively (cf. Fig. 4.8 and Fig. 4.18). The difference amounts thus to 20 nm with the value for PSMs on hydrophobic substrates lying within the error of that on PSMs on hydrophilic substrates. Relatively high errors are due to varying heights of Ti and – mainly – Au functionalisations. This is due to the fact that an even gold coating with relatively high evaporation velocity comes at the expense of variations of the nominal Au coating height of 30 nm. Nevertheless, an explanation approach for the pore depth difference shall be given here. Figure 5.2 illustrates the main difference between CPEO3 and ME, i.e. the protrusion of the cholesterol moiety of CPEO3 into the lower leaflet while a bilayer consisting solely of GUV lipids lies on the hydroxyl group of the ME molecules. Considering functionalisation of the Au coating over its whole surface and that exposition of CPEO3 to an aqueous environment is highly unfavourable compared to incorporation into the lower leaflet, the assumption of the bilayer ‘following’ the Au layer along the pore walls

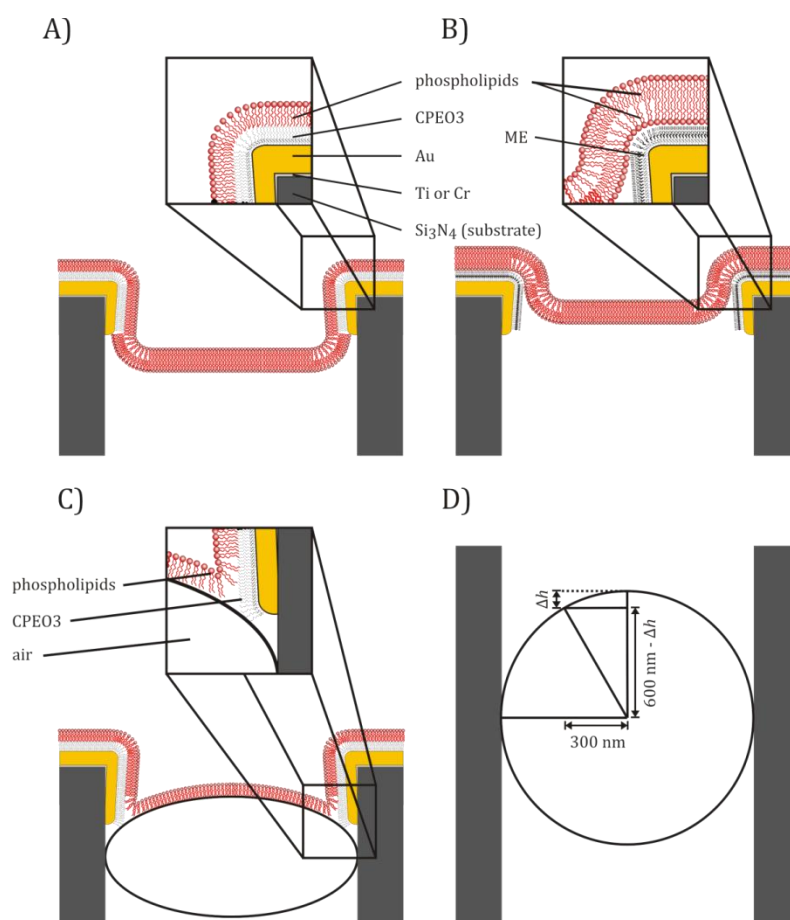


**Figure 5.2: Deduced geometry of PSMs. A) In case of hydrophobically (CPEO3) functionalised substrates, the bilayer adapts the shape of the supporting porous architecture as cholesterol moieties protrude into the lower leaflet. The suspending membrane area is relatively leveled as a result of the high lateral tension. B) In case of hydrophilically (ME) functionalised substrates, the bilayer lies on top of the functionalisation, but its shape is independent from the support's structure. C) If spreading of GUVs does not result in formation of PSMs but of lipid monolayers on residual air bubbles, the lipid monolayer follows the shape of the air/water interphase. D) Illustration of geometric consideration to determine the expected height difference  $\Delta h$  within an individual PSM.**

## DISCUSSION

becomes reasonable (Fig. 5.2 A)). On the contrary, there is no similar force driving the lipid bilayer on ME to bend and cover the top of the pore interior (Fig. 5.2 B)) as there is only hydrophilic interactions between the phospholipid head groups and the ME hydroxyl group which are not preferred to exposition of the phospholipid head group to the aqueous phase.

The question arises, why the pore depth difference found (20.3 nm) deviates from the nominal 30 nm height of the Au layer. Two conceivable reasons can be considered. Taking the errors of the pore depth evaluation into consideration, it becomes obvious that 30 nm lies well within the errors of the experimental value. Secondly, the Au layer's height may well deviate from 30 nm by several nm.

The hypothetical formation of lipid monolayers on air bubbles residing in pores causes a topography as displayed in Figure 5.2 C). On pore rims and at the top of the pore interior, the CPEO3 layer forms the lower leaflet of a bilayer. The top layer comprises lipids from spread GUVs which also assembles at the air/water interphase and follows the air bubble's shape. A simple geometrical consideration is illustrated in Figure 5.2 D). Assuming a perfectly spherical shape for the air bubble, the expected height difference within an individual pore-suspending membrane can be calculated. At a distance of 300 nm from the pore center, the Pythagorean theorem leads to an expected height difference  $\Delta h$  of:

$$\Delta h = 600 \text{ nm} - \sqrt{(600 \text{ nm})^2 - (300 \text{ nm})^2} = 80 \text{ nm}$$

Such a concave membrane shape and corresponding height difference was not observed in any experiment, independent of the functionalisation type. On the contrary, PSM shapes were either observed as planar or slightly convex which is considered as a first hint that monolayer formation on residual air was indeed prevented by careful handling during the spreading procedure.

## 5.4 CLSM TITRATION EXPERIMENTS

The fluorescence based assay for the investigation of CPP interactions with PSMs was conducted with a range of variables. The lipid composition, the functionalisation of the substrates and the peptides were varied to achieve a broad overview, and their influence on the course of the experiments is discussed in this chapter.

### 5.4.1 THE INFLUENCE OF LIPID COMPOSITION AND SUBSTRATE FUNCTIONALISATION IN MELITTIN EXPERIMENTS

It has been found that the interaction of melittin with membrane depends on the lipid composition of the latter, as described in Chapter 1.4.2. A surface plasmon resonance (SPR)

study of solid-supported hybrid bilayers of pure DMPC and pure DMPG on long-chain alkanethiols revealed  $K_D$  values of 30.3  $\mu\text{M}$  and 485 nM, respectively, amounting to a 100-fold increase in melittin affinity to the negatively charged PG bilayer when compared to the zwitterionic PC membrane [Lee et al. 2001]. Despite this increased affinity, melittin's lytic activity is reduced in the presence of PS lipids as found by means of vesicle release experiments [Benachir and Lafleur 1995; Hinch and Crowe 1996] and NMR experiments [Monette and Lafleur 1995; Pott et al. 2001]. A similar effect with regard to the decrease in lysis observed upon melittin application was found for cholesterol as a membrane constituent in release experiments [Benachir et al. 1997; Allende et al. 2005] and fluorescence studies [Raghuraman and Chattopadhyay 2004]. The latter study revealed, in contrast to negatively charged lipids, a decrease in melittin affinity towards cholesterol containing lipid bilayers. The effects of both cholesterol and PG or PG lipids were attributed to modified interactions of the peptide's tryptophan residue at position 19 [Chattopadhyay and Rukmini 1993; Benachir et al. 1997; Ghosh et al. 1997; Raghuraman and Chattopadhyay 2004; Allende et al. 2005]. In case of cholesterol, it was noted that erythrocytes as a major target for the bee venom comprise extraordinarily high ratios of cholesterol ( $\sim 45$  mol%) such that cholesterol is part of the cells' protective mechanism.

Penetratin was one of the first CPPs to be discovered [Joliot et al. 1991]. It is part of the Antennapedia homeodomain (AntHD) from *Drosophila melanogaster* and is readily internalised by various cell lines [Derossi et al. 1994; Brugidou et al. 1995; Derossi et al. 1996; Fenton et al. 1998; Derossi et al. 1998; Fischer et al. 2002] as well as GUVs [Thorén et al. 2000]. Concentrations at which penetratin is reported to be internalised range from as low as 75 nM [Fischer et al. 2002] (a value of 10  $\mu\text{M}$  is mentioned, but without reference given) to several  $10^1$   $\mu\text{M}$ . In that study, toxic effects on neurons were observed for concentrations of [penetratin]  $>100$   $\mu\text{M}$  [Brugidou et al. 1995]. To date, no dependence on lipid compositions of cells or vesicles has been reported with respect to the peptide's internalisation behaviour.

Mechanical features of PSMs were probed by means of AFM indentation experiments [Mey et al. 2009; Kocun et al. 2011]. Varying the substrate functionalisation revealed lateral membrane tensions  $\sigma$  in the range of  $10^1$   $\text{mN m}^{-1}$  for membranes prepared on hydrophobically functionalised surfaces (octanethiol (OT) or CPEO3). It was found that CPEO3 featured a tension reduced by 28% compared to OT and that  $\sigma$  increased with decreasing pore diameters. The most notable difference, however, was between PSMs on CPEO3 or OT and those prepared directly on the hydrophilic substrate surface: in the latter case,  $\sigma$  was reduced 100-fold to the range of  $10^{-1}$   $\text{mN m}^{-1}$  which is similar to that of plasma membranes with  $\sigma = (10^{-2}-10^{-1})$   $\text{mN m}^{-1}$  [Dai and Sheetz 1999; Sheets 2001]. This difference was attributed to the hydrophobic effect which can be described in terms of a free energy difference between the membrane parts suspending the pores and the part on the rim. As this scenario does not hold for a hydrophilically functionalised substrate with the lipid bilayer homogeneously covering pores as well as rims, there is no free energy difference and consequently a much reduced lateral tension  $\sigma$  observed. A subsequent study by Kocun and

## DISCUSSION

co-workers revealed tension values of  $\sigma \leq 3.5 \text{ mN m}^{-1}$  for PSMs on ME functionalised substrates.

In this study, fluorescence experiments were performed with PSMs prepared from purely zwitterionic GUVs as well as GUVs containing negatively charged lipids or cholesterol to investigate potential differences. All three types of PSMs were prepared on both hydrophobically and hydrophilically functionalised substrates. The results for different lipids are first discussed within the group of same functionalisation types before experiments on CPEO3 and ME are compared to each other.

### *The influence of various lipid compositions on melittin membrane interactions on hydrophobically functionalised substrates*

On CPEO3 functionalised substrates, it was found that  $[\text{melittin}] = 432 \text{ nM}$  was sufficient for rupturing of POPC PSMs, while POPC/POPS (4:1) PSMs ruptured at  $[\text{melittin}] = 305 \text{ nM}$  and DPhPC/chol (9:1) at  $[\text{melittin}] = 672 \text{ nM}$ . These values, however, cannot be regarded as exact concentrations at which membranes are affected. More accurately, the titration steps have to be taken into account. For pure POPC membranes, steps of 80 nM were applied, resulting in a concentration range of  $[\text{melittin}] = (340\text{--}432) \text{ nM}$  at which PSMs rupture. For POPC/POPS (4:1) and DPhPC/chol (9:1) PSMs, these concentration ranges are obtained as  $[\text{melittin}] = (201\text{--}305) \text{ nM}$  and  $[\text{melittin}] = (548\text{--}672) \text{ nM}$ , respectively. For an error discussion, the accuracy of the melittin stock solution's concentration needs to be considered. The concentration was determined by means of UV/Vis spectroscopy with an error of 6%. Aliquotation and absorbance of the peptide to container walls are further error sources such

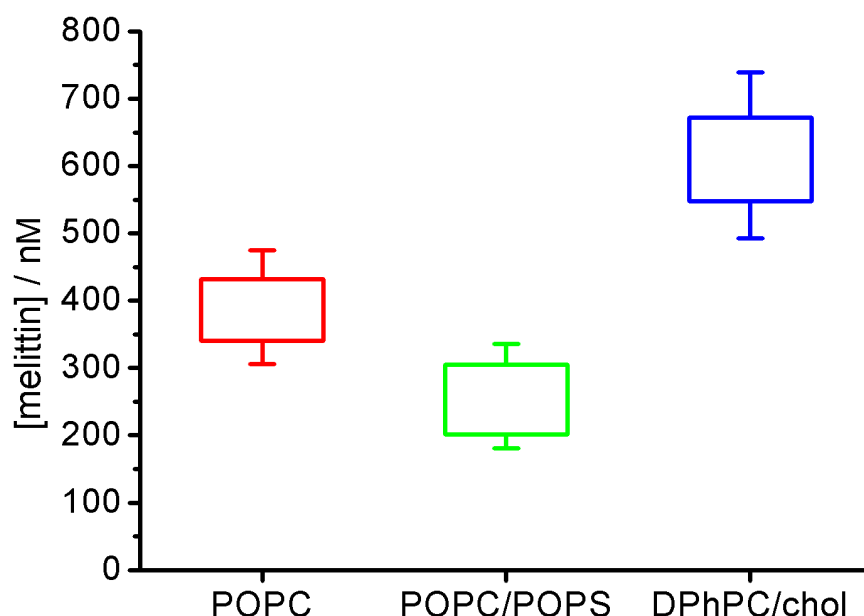


**Figure 5.3:** Graphic representation of results for melittin titrations on CPEO3 functionalised substrates investigated by fluorescence microscopy. Concentration ranges sufficient for membrane rupturing are shown as boxed with whiskers indicating the outer half of error bars for the border values – e.g. for POPC, the range of (340–432) nM is boxed, with whiskers reaching down to 306 nM and up to 475 nM. For POPC and POPC/POPS (4:1), error bars overlap, while DPhPC/chol (9:1) membranes rupture at higher concentrations than POPC bilayers.

that a total error  $\Delta[\text{melittin}]_{\text{stock solution}}$  of 10% is estimated. This error has to be calculated for each border of concentration ranges at which PSMs of various lipids rupture.

Figure 5.3 displays results and error considerations made above. It becomes obvious that a ratio of 20% POPS is insufficient to decrease melittin's lytic activity as reported in literature [Benachir and Lafleur 1995; Monette and Lafleur 1995; Hinch and Crowe 1996; Pott et al. 2001]. Instead, a slight decrease in [melittin] that is needed for rupturing is observed,  $(201 \pm 20) \text{ nM} - (305 \pm 31) \text{ nM}$  compared to  $(340 \pm 34) \text{ nM} - (432 \pm 43) \text{ nM}$  for POPC. Error bars of these [melittin] ranges overlap. On the other hand, DPhPC/chol (9:1) PSMs were found to be lysed by significantly higher concentrations of  $(548 \pm 55) \text{ nM} - (672 \pm 67) \text{ nM}$  than POPC bilayers. This result corresponds to release experiments [Benachir et al. 1997; Allende et al. 2005] and fluorescence studies [Raghuraman and Chattopadhyay 2004] which revealed the 'guarding' effect of cholesterol.

In order to evaluate the assay's quality, its results need to be compared to literature not only with respect to qualitative results as done above, but also with regard to quantitative findings. Melittin ruptures all three investigated types of PSMs (POPC, POPC/POPS (4:1), DPhPC/chol (9:1)) at concentrations in the range of  $10^2 \text{ nM}$ . This is in very good agreement with results from previous studies which revealed concentrations of  $(0.2 - 1) \mu\text{M}$  as sufficient for release of e.g. haemoglobin from erythrocytes or fluorescent markers from liposomes [Sessa et al. 1969; DeGrado et al. 1982; Tosteson et al. 1985; Katsu et al. 1989; Dempsey 1990; van den Bogaart et al. 2008]. In a study on solid-supported membranes by Steinem and co-workers, melittin concentrations of  $(1.6 - 6) \mu\text{M}$  were utilised for the disruption of lipid bilayers [Steinem et al. 2000].

As described in Chapter 4.1.3 (cf. Fig. 4.6), the sigmoidal curve shape of CLSM titration experiments remains the same, independent of the PSMs' lipid compositions. Moreover, the duration of rupturing amounts to approximately 25 min for all three lipid compositions. This demonstrates that the lipid composition does not influence kinetic parameters of membrane rupturing once the process is started. This suggests that the mechanism of membrane destruction is independent of lipid composition, unless different mechanisms appeared kinetically indifferent or with differences unrevealed at the employed temporal resolution.

## DISCUSSION

### *The influence of various lipid compositions on melittin membrane interactions on hydrophilically functionalised substrates*

For results of experiments on ME functionalised substrates, the same references are needed for discussion as have been for the discussion of experiments on CPEO3 functionalised substrates, i.e. the 'guarding' effect of negatively charged lipids or cholesterol and the concentration range in which melittin affects lipids membranes. Furthermore, the same error considerations have to be made as experiments were conducted exactly as those on hydrophobically functionalised substrates (v.s.). Pure POPC membranes ruptured at  $[\text{melittin}] = (1041 \pm 104) \text{ nM} - (1257 \pm 126) \text{ nM}$ , while PSMs comprising 20% POPS ruptured at a significantly lower peptide concentration range of  $[\text{melittin}] = (521 \pm 52) \text{ nM} - (743 \pm 74) \text{ nM}$ . There is hence no 'guarding' effect observed when negatively charged lipids are included into lipid bilayers as reported in literature [Benachir and Lafleur 1995; Monette and Lafleur 1995; Hinch and Crowe 1996; Pott et al. 2001]. On the other hand, the opposite effect is induced by cholesterol, i.e. an increase in  $[\text{melittin}]$  needed for PSM rupturing is observed, which is reached for  $[\text{melittin}] = (1738 \pm 174) \text{ nM} - (2023 \pm 202) \text{ nM}$ . This is according to literature where release experiments [Benachir et al. 1997; Allende et al. 2005] as well as fluorescence studies probing melittin's tryptophan signal [Raghuraman and Chattopadhyay 2004] reported the decrease in melittin's lytic activity in the presence of cholesterol in bilayers. Figure 5.4 displays the results found by CLSM experiments with 10% error bars after error considerations. It illustrates this study's results as according to literature with regard to quantity, i.e. peptide concentration ranges in the  $(10^2 - 10^3) \text{ nM}$  regime are sufficient for rupturing of PSMs as reported before for erythrocytes as well as liposomes [Sessa et al. 1969;

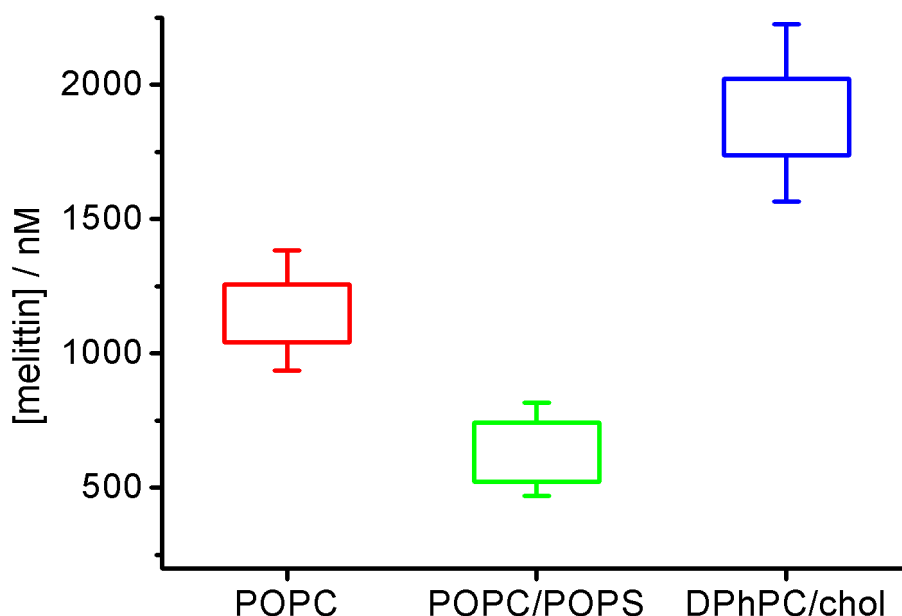


**Figure 5.4:** Graphic representation of results for melittin titrations on ME functionalised substrates investigated by fluorescence microscopy. Concentration ranges sufficient for membrane rupturing are shown as boxed with whiskers indicating the outer half of error bars for the border values.  $[\text{melittin}]$  ranges sufficient for PSM rupturing are found as  $(1041 \pm 104) \text{ nM} - (1257 \pm 126) \text{ nM}$ ,  $(521 \pm 52) \text{ nM} - (743 \pm 74) \text{ nM}$  and  $(1738 \pm 174) \text{ nM} - (2023 \pm 202) \text{ nM}$  for POPC, POPC/POPS (4:1) and DPhPC/chol (9:1), respectively.



DeGrado et al. 1982; Tosteson et al. 1985; Katsu et al. 1989; Dempsey 1990; van den Bogaart et al. 2008].

The kinetics of experiments on POPC and POPC/POPS (4:1) bilayers were found to be similar. In both cases, a sigmoidal curve shape was obtained, and the rupturing process was finished within approximately 20 min almost without deceleration phases, as described in Chapter 4.2.4 (cf. Fig. 4.15). In contrast to these PSM variations, the experiment on DPhPC/chol (9:1) did not reveal a similar curve shape or duration of the rupturing process. Instead, a duration of approximately 3.5 h was observed, and the curve shape displayed a very slow starting phase. The fact that there is only a single experiment on DPhPC/chol (9:1), which was not reproduced due to lack of spreading success, introduces a caveat with regard to the discussion of this particular experiment. The very similar kinetics of experiments on POPC and POPC/POPS (4:1), however, indicate that the mechanism of melittin membrane interaction is independent of lipid composition also on hydrophilically functionalised substrates as discussed for hydrophobically functionalised substrates (v.s.).

#### 5.4.2 THE INFLUENCE OF LIPID COMPOSITION AND SUBSTRATE FUNCTIONALISATION IN PENETRATIN EXPERIMENTS

In order to prove the general applicability of the fluorescence based assay, a row of experiments were conducted with penetratin on PSMs prepared on hydrophilically functionalised substrates. The same lipid compositions were used as in melittin titration experiments, i.e. POPC, POPC/POPS (4:1) and DPhPC/chol (9:1). Peptide concentrations found sufficient for rupturing of PSMs are [penetratin] = 2076 nM, 3126 nM and 2202 nM, respectively. As discussed for melittin, declaration of a concentration range instead of a specific concentration appears as more accurate. This renders results to (1005–2076) nM, (1024–3126) nM and (1551–2202) nM.

As discussed for melittin (v.s.), the concentration error needs to be taken into account. In contrast to melittin experiments, the concentration of the aliquot used for titrations was determined just before the experiment by means of UV/Vis. A steady decrease in concentration was observed which is ascribed to peptide adsorption to the test tube walls [Persson et al. 2003]. A quick row of three measurements gave an average error of 12%, and the total concentration error was hence estimated as 18% due to dilution and penetratin adsorption to the sample container walls. To minimise errors induced by dilution processes, concentration steps were relatively large which resulted in wide concentration ranges as displayed in Figure 5.5. For POPC and DPhPC/chol (9:1), a similar upper border of (2076±374) nM and (2202±396) nM, respectively, was observed. For POPC/POPS (4:1), the 2000 nM step was omitted in favour of 3000 nM, resulting in an upper border of (3126±563) nM. There is thus no difference observed in [penetratin] that results in membrane rupturing as the concentration range for DPhPC/Chol (9:1) lies almost completely in the range of that for POPC which in turn is nearly completely comprised by the range determined for POPC/POPS (4:1). More detailed titrations, i.e. titration experiments featuring

## DISCUSSION

smaller concentration steps are desirable. The observation, however, that penetratin acts on lipid bilayers independently of their lipid compositions is in accordance with literature as there are no reports of such dependencies to date.

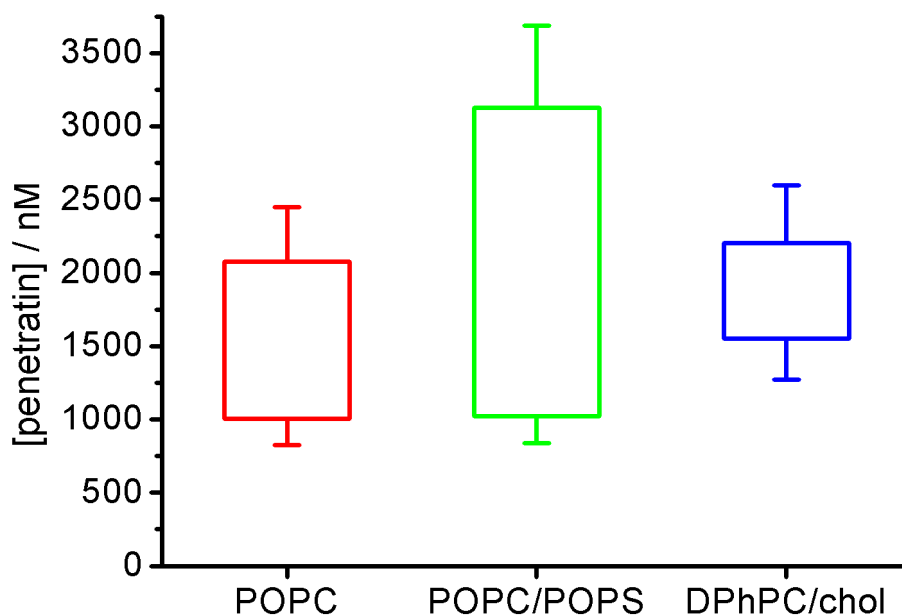


**Figure 5.5:** Graphic representation of results for penetratin titrations on ME functionalised substrates investigated by means of CLSM. Boxed concentration ranges are those sufficient for membrane rupturing, with whiskers indicating the outer half of 18% error bars for the border values. [penetratin] ranges sufficient for PSM rupturing are found as  $(1005 \pm 181) \text{ nM} - (2076 \pm 374) \text{ nM}$ ,  $(1024 \pm 184) \text{ nM} - (3126 \pm 563) \text{ nM}$  and  $(1551 \pm 279) \text{ nM} - (2202 \pm 396) \text{ nM}$  for POPC, POPC/POPS (4:1) and DPhPC/chol (9:1), respectively. There is hence no lipid composition dependency observed for penetratin on ME functionalised PSMs.

Analysis of curve shapes obtained from penetratin titrations reveals almost linear courses of experiments. While straight linearity is observed for POPC/POPS (4:1), POPC and DPhPC/chol (9:1) display an overall linear progress of membrane rupturing but with alternation of higher and lower velocities. Another difference is the fact that there is a significant deceleration phase found for POPC/POPS (4:1) whereas in case of both other PSM types, the linearity remains constant until the whole membrane patch is disturbed. The whole rupturing is completed much faster (within 35 min) in case of membranes comprising negatively charged lipids than in the other two where the process takes 4 times as long (approximately 140 min). One reason suggested for this difference is an increase in electrostatic interaction between the positively charged penetratin and the PS head groups.

### 5.4.3 COMPARATIVE DISCUSSION OF MELITTIN AND PENETRATIN TITRATIONS WITH PARTICULAR CONSIDERATION OF THE SUBSTRATE FUNCTIONALISATION INFLUENCE

A summary of the discussion above is presented in Figure 5.6. It compares the concentration ranges sufficient for membrane rupturing for melittin on CPEO3 functionalised, melittin on ME functionalised and penetratin on ME functionalised substrates.

The comparison of penetratin and melittin reveals that a higher penetratin concentration is needed for rupturing of the same membranes than the melittin concentration. This is in general accordance with literature [Thorén et al. 2000]. However, a larger difference was expected as Thorén and co-workers reported an approximately 60-fold increase in concentration when comparing penetratin and melittin: while leakage of carboxyfluorescein from asolectin GUVs was induced by melittin at peptide:lipid (P:L) ratios of 0.002–0.003, a ratio of 0.1 was needed for penetratin. Moreover, the amount of released dye was reduced by more than 95% in the case of penetratin. Additionally, penetratin's toxicity was reported as relatively low with usual concentrations in the  $10^2 \mu\text{M}$  range inducing cell destruction [Derossi et al. 1998]. For this reason, there had been no definite expectation prior to experiments whether PSM rupturing would be observed at all by means of CLSM. One possible reason is that either the assumed melittin concentration is higher than the actual concentration in the sample or that the penetratin concentration is underestimated. Consideration of the good accordance of [melittin] found for rupturing in this study with literature values leads to the conclusion that [penetratin] is more likely to be underestimated than [melittin] overestimated. Another explanation is that the difference between model membranes employed in this study and cellular systems investigated mainly in literature induces a larger difference in the behaviour of penetratin than it does in the behaviour of melittin, i.e. melittin affects PSMs similarly to erythrocytes, whereas penetratin reveals much higher activity at low concentrations on PSMs than it does on natural cells. The question arises, how this is possible. As described in Chapter 1.4.3, the translocation mechanism of penetratin remains to be elucidated. One reasonable scenario is that different pathways are possible, depending on the target, i.e. penetratin is able to directly translocate or to be internalised by endocytic mechanisms. It might be the case, although highly speculative, that neurons and other investigated cells internalise the peptide by means of endocytosis whereas pore-suspending membranes are directly translocated. Furthermore, there might be effective guarding measures active in cells which are not reflected by the model membranes in this study which therefore rupture at concentrations in the  $10^0 \mu\text{M}$  range which is not reported as toxic. The question remains unanswered why Thorén and co-workers [Thorén et al. 2000] found such large differences for melittin and penetratin in their GUV experiments. A highly speculative hypothesis would be that the lateral tension of GUVs influences penetratin lytic activity significantly stronger than melittin's.

Another difference found in this study is the kinetics of melittin and penetratin interactions with PSMs. While melittin experiments feature predominantly sigmoidal curves and rather

## DISCUSSION

short times in which bilayers are destructed completely, penetratin experiments follow a more linear shape and are completed up to seven times more slowly, the exception being POPC/POPS (4:1) membranes with less than twice the duration of the average melittin experiment (v.s.). The differences in curve shapes might indeed reflect different mechanisms. While pore formation is widely accepted as the mechanism of melittin [Vogel and Jähnig 1986; Sansom 1991; Lin and Baumgaertner 2000; Yang et al. 2001; Allende et al. 2005] and believed to be achieved after the carpet-like model [Pouny et al. 1992], translocation by formation of inverted micelles [Derossi et al. 1998] was discussed for penetratin as well as predominantly endocytic pathways more recently [Nakase et al. 2004; Maiolo et al. 2005; Duchardt et al. 2007]. The sigmoidal curve shape reflects the carpet-like model well, as there is cooperativity involved in this model (cf. Ch. 1.4.1) and sigmoidal curves a typical reflexion of such a behaviour as known from prominent examples such as O<sub>2</sub> binding to hemoglobin [Monod et al. 1963]. An inverted micelle pathway, per contra, does not necessarily involve such a pronounced cooperative behaviour as the interaction of single penetratin molecules with the membrane may be sufficient for the induction of translocation. The second major difference, i.e. the duration of rupturing processes, may be explained by the different natural roles of melittin and penetratin. While melittin as part of the bee venom acts to disturb cellular structures, penetratin belongs to the family of classic CPPs and is utilised by *Drosophila melanogaster* to interact with its own DNA which is why it translocates lipid membranes but does not reveal toxicity on natural cells up to the 10<sup>2</sup> μM range. The slower completion of the rupturing process of PSMs is thus explainable by a larger ratio of penetratin molecules passing the bilayer without causing enough damage that would result in destruction of the pore-suspending membrane.

For the first time, the interaction of melittin with lipid membranes was investigated with respect to mechanics of the bilayers, i.e. the tension within the bilayer ('prestress') was directly controlled via choice of functionalisation. As reported by Mey and co-workers, lateral tension within membranes is increased up to 100-fold on OT functionalised compared to non functionalised, i.e. hydrophilic, substrates [Mey et al. 2009]. Comparable values reported are 22 mN m<sup>-1</sup> and 0.15 mN m<sup>-1</sup>, respectively, with values on CPEO3 slightly lower than on OT. A further study specified the tension of membranes on ME functionalised substrates to  $\sigma \leq 3.5$  mN m<sup>-1</sup>, which means a tension value three to ten times smaller than for membranes on CPEO3 functionalised substrates [Kocun et al. 2011]:  $\sigma_{\text{CPEO3}}/\sigma_{\text{ME}} = 3-10$ . As becomes obvious from Figure 5.6, [melittin] ranges sufficient for membrane destruction were significantly higher on ME functionalised substrates for every lipid composition investigated. Moreover, the increase from CPEO3 to ME functionalised substrates was very similar for all types of PSMs investigated with factors of 3.0, 2.5 and 3.1 for POPC, POPC/POPS (4:1) and DPhPC/chol (9:1) membranes, respectively. This result reflects the reported membrane mechanics well, as a membrane subjected to higher 'prestress' is expected to be more vulnerable to destruction, i.e. it is expected to rupture at lower peptide concentrations. This is exactly the case for the investigated PSMs in this study where the increase in membrane tension on hydrophobically functionalised substrates is attended by a decrease in [melittin]

ranges by a factor of approximately  $2.9 \pm 0.3$ . This is in good agreement with the ratio of ‘prestress’ on CPEO3 and ME functionalised substrates of  $\sigma_{\text{CPEO3}}/\sigma_{\text{ME}} = 2-5$  as found by AFM.

As a summary, the comparison of penetratin and melittin interactions with pore-suspending membranes prepared on hydrophilically functionalised substrates reflects results from literature well, with the exception of the unexpectedly low [penetratin] values found sufficient for membrane destruction. It has to be taken into account, though, that results discussed in this study were obtained on a membrane model system different from those employed in previous studies. Establishment of the assay has to be regarded as successful and as establishment of a useful tool for the investigation of further membrane active peptides. Curve shapes may reveal hints at mechanisms, but it appears at best confined to confirmation of existing models rather than usable for elucidation of unknown mechanisms. The assay revealed the influence of lateral membrane tension in very good agreement with existing studies, illustrating its usefulness for the assessment of the ‘prestress’ influence in subsequent studies with other membrane compositions and/or other membrane active peptides.

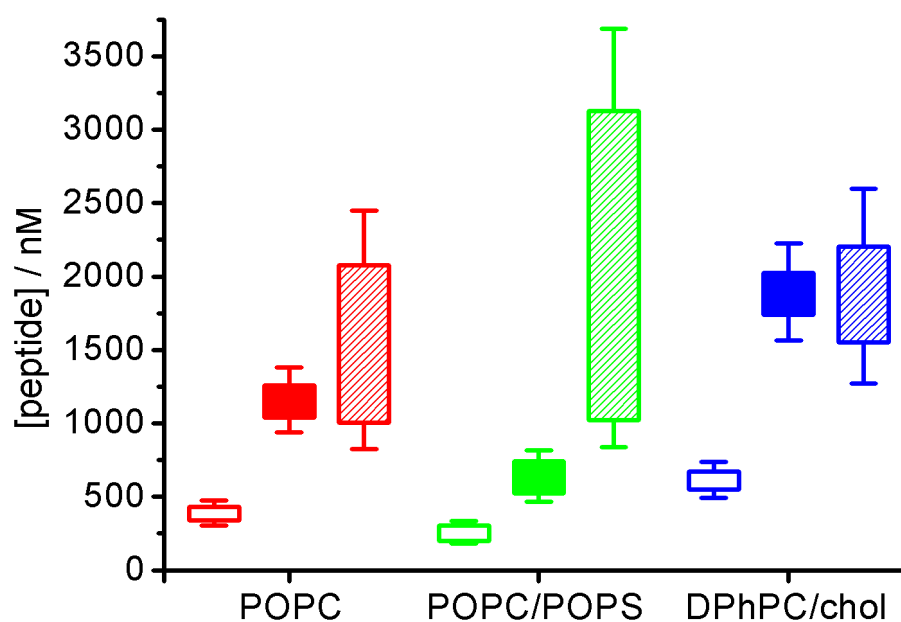


**Figure 5.6: Summary of results obtained from CLSM titration experiments with melittin on CPEO3 functionalised substrates (empty rectangles), melittin on ME functionalised substrates (full rectangles) and penetratin on ME functionalised substrates (shaded rectangles). The increase in [melittin] needed for PSM destruction for hydrophilically functionalised substrates is revealed. Even higher penetratin concentrations are needed on average but less higher than expected.**

## DISCUSSION

### 5.5 SICM TITRATION EXPERIMENTS

SICM titration experiments were conducted with melittin on pore-suspending membranes of various lipid compositions on both CPE03 and ME functionalised substrates. For a detailed discussion of melittin membrane interactions and membrane mechanics the reader is referred to Chapter 5.4.1. Briefly, it is reported that negatively charged lipids as well as cholesterol 'guard' lipid bilayers from destruction by melittin, i.e. higher melittin concentrations are needed for membrane rupturing than on pure PC membranes [Benachir and Lafleur 1995; Monette and Lafleur 1995; Hinch and Crowe 1996; Benachir et al. 1997; Pott et al. 2001; Raghuraman and Chattopadhyay 2004; Allende et al. 2005]. The mechanics of PSMs have been investigated in two AFM studies. It is found that a comparatively high lateral tension  $\sigma$  ('prestress') is featured by membranes on hydrophobically functionalised substrates in comparison to PSMs on hydrophilically functionalised substrates with differences in  $\sigma$  of a factor of 2–5 [Mey et al. 2009; Kocun et al. 2011].

#### 5.5.1 MELITTIN TITRATIONS ON DPhPC/CHOL (9:1) MEMBRANES ON HYDROPHOBICALLY FUNCTIONALISED SUBSTRATES

A row of three experiments was performed with melittin titrated onto PSMs prepared from DPhPC/chol (9:1) GUVs on CPE03 functionalised substrates. A similar course of the experiment was observed for all three of them despite variations in the concentration steps: one experiment was conducted with  $\sim 90$  nM steps, the second with two  $\sim 140$  nM and two  $\sim 90$  nM steps, the last with one  $\sim 350$  nM and one  $\sim 100$  nM step. The typical course of such a titration experiment was that pore depths were constant or showed minor increases until a certain melittin concentration was reached. This concentration was not sufficient for membrane destruction but resulted in an increase in pore depth of  $(29 \pm 16)$  nm for the majority of pores (69%, cf. Fig. 4.11). Application of another [melittin] step resulted in membrane destruction. Concentration ranges sufficient for membrane destruction are found as (457–542) nM, (383–478) nM and (349–452) nM, resulting in an average value of 444 nM. The time needed for destruction of all membranes differs within the row of experiments. While in one experiment approximately 45 min were sufficient for completion of rupturing, durations of approximately 100 and 160 min were observed as well.

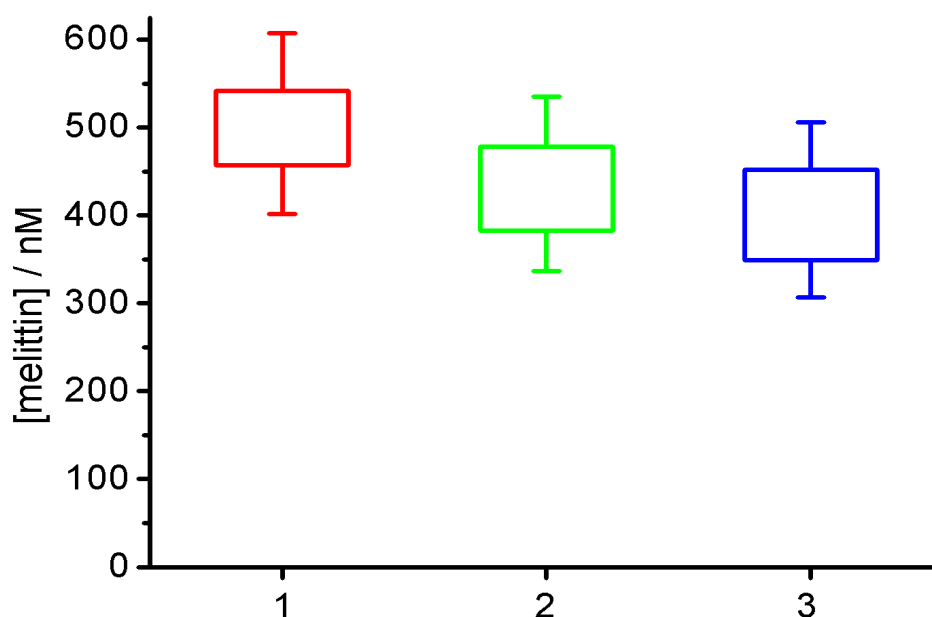


Figure 5.7: Illustration of three SICM titration experiments (1, 2, 3) on DPhPC/chol (9:1) on CPEO3 functionalised substrates. [melittin] ranges sufficient for membrane destruction are indicated by boxes, with whiskers representing 12% errors. An average range of  $(396 \pm 82)$  nM– $(491 \pm 102)$  nM is obtained.

An error discussion has been done for CLSM experiments. As the same melittin stock solution was used in CLSM and SICM experiments, a value of 6% for  $\Delta[\text{melittin}]$  of the stock solution holds here as well. Larger volumes were pipetted in case of SICM experiments, reducing the error slightly but back and forth pipetting of 1 ml of the sample solution increases the error such that a total error of 12% is estimated. The borders of [melittin] ranges given above have this error such that the three experiments result in Figure 5.7 and  $[\text{melittin}] = (457 \pm 55)$  nM– $(542 \pm 65)$  nM,  $(383 \pm 46)$  nM– $(478 \pm 57)$  nM and  $(349 \pm 42)$  nM– $(452 \pm 54)$  nM with an average range of  $(396 \pm 82)$  nM– $(491 \pm 102)$  nM.

As membrane destruction is represented by a large increase in pore depth from typical values of 100 nm to more than 500 nm (cf. e.g. Fig. 4.10), the question remains what the slight increase of  $(29 \pm 16)$  nm means. An explanation along the initial hypothesis is that melittin forms pores within the lipid bilayer as illustrated in Figure 5.8. As the membrane resistance is decreased, the ion current is increased (black line in the schematic diagram). This causes an ‘underdetermination’ of the pipette sample distance as the ion current has surpassed the set-point although there is no change in sample height except for the pore. The pipette z position is hence lowered (red line in the schematic diagram) which is attended by recording of a decrease in the surface z position. In case of recording the topography of pore-suspending membranes, pores would occur as deeper than before, the pore depths would increase. This is observed in pore depth development graphs (cf. Fig. 4.11, 4.20 and 4.21). It is questionable, however, whether enough pores can be formed for such an increase in ion current without inducing rupturing of the whole membrane. An exact answer to this question remains probably to be given by means of relatively sophisticated modelling, but a rough estimation implies that the formation of pores of up to 60 Å diameter is not sufficient for the increase in

## DISCUSSION

pore depth observed. The pore formation hypothesis does, however, remain a sensible explanation for the principal observation of an increase in pore depths.

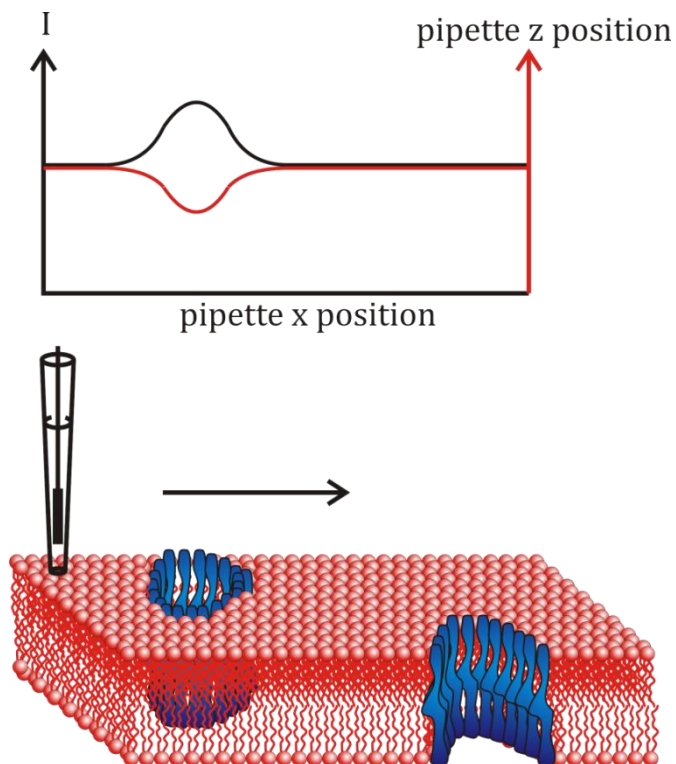


**Figure 5.8: Explanation model for the increase in pore depth prior to rupturing of PSMs. As the pipette is scanned across a pore (bottom), an increase in ion current is observed (black line in the top schematic). This results in correction of the pipette z position (red line in the top schematic) and thus in an underestimation of the sample surface z position: pore depths increase.**



### 5.5.2 MELITTIN TITRATIONS ON POPC AND DPhPC/CHOL (9:1) MEMBRANES ON HYDROPHILICALLY FUNCTIONALISED SUBSTRATES

Two experiments were conducted on ME functionalised substrates, one on PSMs prepared from POPC, one on PSMs prepared from DPhPC/chol (9:1). The course of both experiments was similar despite the variation in lipid composition. Considering the same errors as for experiments on CPEO3 functionalised substrates (cf. Ch. 5.5.1), [melittin] ranges of  $(207\pm 27)$  nM– $(422\pm 55)$  nM and  $(244\pm 32)$  nM– $(482\pm 63)$  nM were obtained for POPC and DPhPC/chol (9:1), respectively, as displayed in Figure 5.9. In both experiments, the second application of melittin resulted in a sufficiently high concentration that rupturing of PSMs was completed. The first application had also led to an increase in pore depths. For the titration onto POPC bilayers, an increase of  $(35\pm 13)$  nm was observed, whereas an increase of  $(22\pm 7)$  nm was obtained for DPhPC/chol (9:1) bilayers. The same discussion as for the experiments on CPEO3 functionalised substrates holds here (cf. Ch. 5.5.1). An increase in pore depth is expected before complete membrane destruction as melittin forms pores within the bilayer increasing the ion current (cf. Fig. 5.8), revealing an intermediate state between the intact pore-suspending membrane and the open pore but the size of the increase is higher than expected. The rupturing process was completed relatively slowly in both experiments with approximately 105 min for POPC and approximately 120 min for DPhPC/chol (9:1).

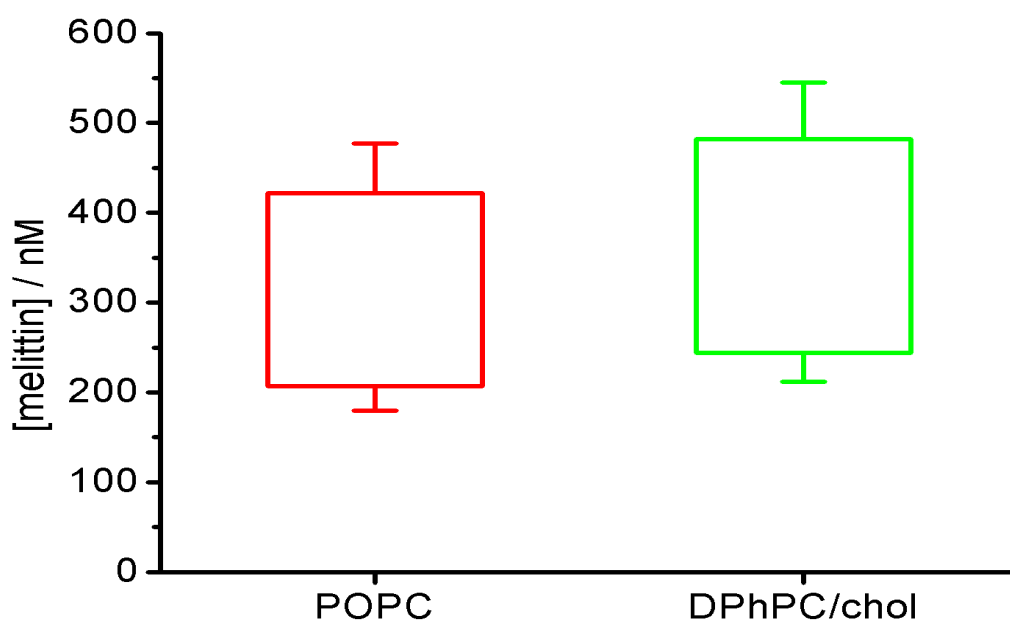


**Figure 5.9:** Illustration of SICM titration experiments on POPC and DPhPC/chol (9:1) on ME functionalised substrates. [melittin] ranges sufficient for membrane destruction are indicated by boxes, with whiskers representing 12% errors; values of  $(207\pm 27)$  nM– $(422\pm 55)$  nM and  $(244\pm 32)$  nM– $(482\pm 63)$  nM, respectively, were obtained.

A striking observation was made for some pores during the titration on pore-suspending membranes prepared from POPC. After the slight increase in pore depth after the first addition of melittin solution described above, a second increase was observed directly after the second application of melittin (cf. Ch. 4.2.4). In contrast to the slight increase of  $(35\pm 13)$  nm, an average increase of  $(123\pm 61)$  nm is found for these pores (cf. Fig. 4.20 D)). As

## DISCUSSION

this is well within the range of an operating pipette sample distance of (50–150) nm, the physical reason for this increase in pore depth remains obscure. After this increase, the pore depth decreases again, but does not reach as low a value as observed before. A qualitatively sensible explanation for such behaviour would be that pores are formed in the bilayer but are closed again and the intact membrane is regained. There is no explanation why this is not observed for the initial slight increase. It appears as rather improbable that larger damage of the bilayer, reflected by the large increase in pore depth, is more easily repaired and the intact membrane regained than the pores formed by melittin and reflected by the comparably slight increase in pore depth. As described above, the pore depth increase is of the same range as the pipette sample distance. This fact proposes the explanation that the pipette poked the membrane but this approach is not too convincing as destruction of the membrane would be expected rather than a decrease in pore depth which is observed instead.

It has to be noted that few data are available rendering a meaningful mutual comparison of SICM results difficult. A comparison of this study's results with literature reveals good accordance as all results are in the  $10^2$  nm range [Sessa et al. 1969; DeGrado et al. 1982; Tosteson et al. 1985; Katsu et al. 1989; Dempsey 1990; vanden Bogaart et al. 2008]. Comparison of the experiments performed on hydrophilically functionalised substrates shows that there is no dependence of the melittin membrane interaction on the lipid composition which is in contrast to literature where a 'guarding' effect of cholesterol is reported (cf. Ch. 5.4.1) [Benachir et al. 1997; Allende et al. 2005] and fluorescence studies [Raghuraman and Chattopadhyay 2004]. The comparison of melittin titration experiments on PSMs prepared from DPhPC/chol (9:1) on CPEO3 and ME does not reveal any influence of the functionalisation, i.e. there is no influence of lateral membrane tension detected. A slightly higher concentration range is required for membrane rupturing for CPEO3 functionalised substrates which is against the expectation that the higher 'prestress' in these PSMs results in a decrease in melittin concentration.

As the same peptide was used in every successful SICM experiment, it is not surprising that there is no principal difference observed with respect to the course of experiments. The slight increase in pore depth prior to the actual destruction of the bilayer hints at permeabilisation of the membrane but there is no proof for this hypothesis available, as discussed before (cf. Ch. 5.5.1). Titrations with non pore forming peptides such as penetratin would be interesting in this regard to elucidate whether mechanistic distinctions can be made from SICM experiments.

As a summary, the principal establishment of the SICM assay was successful, as rupturing of PSMs was detected and visualised in titration experiments such that concentration ranges sufficient for membrane destruction were determined. The experiments per se led to reasonable results, but the influence of lipid composition or substrates functionalisation was not revealed. Furthermore, questions remain with regard to the physical equivalent of particular observations.

## 5.6 COMPARISON OF CLSM AND SICM TITRATION EXPERIMENTS

In this study, two assays based on CLSM and SICM were developed and established for the investigation of interactions between lipid membranes and membrane affecting peptides. Both assays as such were established successfully. This is deduced from results obtained which were generally in good agreement with data reported in literature. Results from CLSM and SICM experiments are compared below which is why discussion in this chapter is mainly confined to melittin experiments while the reader is referred to Chapters 5.4.2 and 5.4.3 for discussion of penetratin experiments.

Figure 5.10 displays results of melittin titrations on CPEO3 and ME functionalised substrates investigated by means of CLSM and SICM. Every experiment per se led to reasonable concentrations in the range of  $10^2$  nM up to low  $10^3$  nM. The ‘guarding’ effect of negatively charged lipids as reported in literature [Benachir and Lafleur 1995; Monette and Lafleur 1995; Hinch and Crowe 1996; Pott et al. 2001] was not reflected in this study’s CLSM experiments (cf. Ch. 5.4.1) while there are no SICM experiments available with POPC/POPS (4:1) bilayers. The effect of cholesterol in PSMs was found according to literature by means of CLSM which revealed increased melittin concentrations necessary for membrane destruction for DPhPC/chol (9:1) compared to POPC (cf. Ch. 5.4.1) but not by means of SICM (cf. Ch. 5.5.2). Regardless of the functionalisation, concentrations found by means of SICM are almost the same as for POPC membranes on CPEO3 functionalised substrates. CLSM experiments revealed an influence of the functionalisation as expected after consideration of studies by Mey and co-workers and Kocun and co-workers (cf. Ch. 5.4.3) [Mey et al. 2009; Kocun et al. 2011]. This ‘prestress’ effect, however, was not observed by means of SICM (cf. Ch. 5.5.2). With regard to the determination of concentration ranges, sensible results are

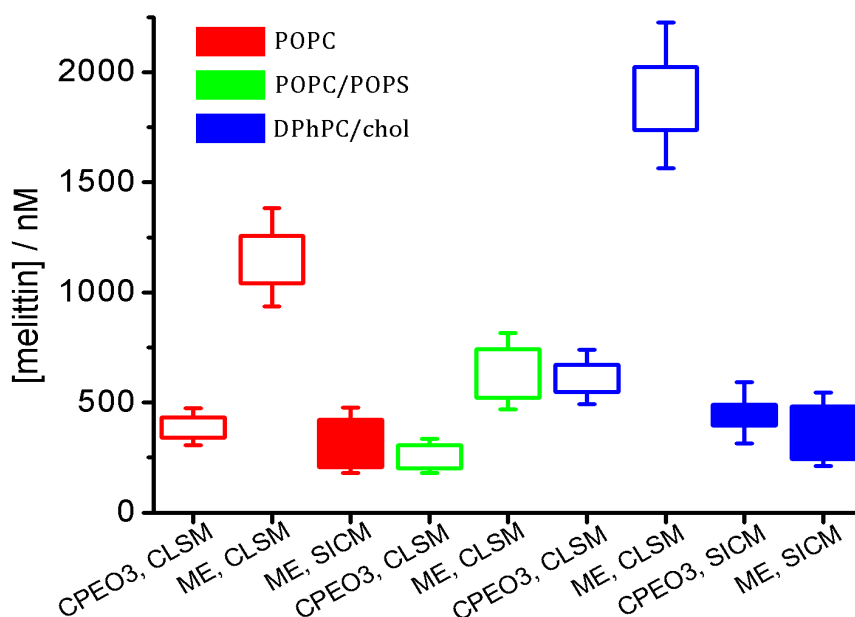


Figure 5.10: Graphic representation of melittin titrations investigated by means of SICM. Concentration ranges are boxed, with whiskers revealing the border values’ errors. Both CLSM (empty boxes) and SICM experiments (filled boxes) are included, with red, green and blue representing POPC, POPC/POPS (4:1) and DPhPC/chol (9:1), respectively.

## DISCUSSION

obtained from every individual experiment. Comparison of data reveals much better accordance with literature and expectations deduced from literature for the CLSM assay than for the SICM assay. This may partly be due to the more complete data set for CLSM experiments and contradictions within the SICM data set may be solved by further experiments. Experiments especially interesting are the completion of the range of melittin titration experiments by means of SICM. Moreover, it would be interesting, to conduct penetratin titrations by means of SICM to examine to what extent the putatively different mechanisms of melittin and penetratin are reflected by the SICM readout. Finally, experiments on hydrophobically functionalised substrates would serve to check for influence of tension on penetratin, as well.

Differences between CLSM and SICM experiments are furthermore found with regard to duration of rupturing. While the former generally observed membrane destruction completed in times close to 20 min (with the exception of DPhPC/chol (9:1) on ME functionalised substrates, as discussed in Chapter 5.4.1), the latter found times of 45 min and longer. A reason for this observation might be the constant stirring during fluorescence experiments which was not possible during SICM investigations. Measures were taken to enhance the fast and equal distribution of the peptide within the sample volumes as described in Chapter 3.3.2. Generally, a quick response was obtained if a peptide concentration sufficient for membrane affection was achieved but there is no further proof that SICM experiments did not suffer from imperfect sample solution mixing.

Both the CLSM as well as the SICM assay developed in this study were established successfully. Discussion and mutual as well as literature comparison of results obtained from both assays implies that the optical assay provides better and more precise results. It has to be taken into account, though, that scanning ion conductance microscopy is the less robust and by far the less utilised technique of the two. Further improvements and refinements as well as increasing experience will further enhance the quality of results and render it an increasingly powerful tool.





## 6 SUMMARY OF THESIS

Scanning ion conductance microscopy (SICM) provides a technique for the investigation of surface topography as well as the local ion conductance of a surface without any mechanical contact between probe and sample. This thesis aimed at the development and application of a SICM based assay for the investigation of the interactions of cell penetrating peptides (CPPs) with pore-suspending membranes (PSMs). It was desired to examine the influence of various lipid compositions of the PSMs and of membrane mechanics controlled by the substrate functionalisation.

A thiol chemistry based strategy was used for functionalisation of silicon nitride ( $\text{Si}_3\text{N}_4$ ) substrates with pore diameters of 1.2  $\mu\text{m}$ . Cholesteryl polyethylenoxy thiol (CPEO3) or mercaptoethanol (ME) were used to render the substrate surface hydrophobic or hydrophilic, respectively. Spreading protocols were developed that allowed for the preparation of solvent-free PSMs comprising various lipid compositions: pure 1-palmitoyl-2-oleoyl-*sn*-glycero-3-phosphatidylcholine (POPC), a 9:1 mixture of 1,2-diphytanoyl-*sn*-glycero-3-phosphatidylcholine (DPhPC) and cholesterol (chol) and a 4:1 mixture of POPC and 1-palmitoyl-2-oleoyl-*sn*-glycero-3-phosphatidyl-L-serine (POPS). Success rates of more than 50% were achieved, i.e. PSM preparation was observed on more than 50% of substrates. While large parts of the array were membrane covered on hydrophobically functionalised substrates, hydrophilically functionalised substrates typically featured few distinct bilayer patches of up to 50  $\mu\text{m}$  diameter (cf. Ch. 4.1.1 and 4.2.1).

Pore-suspending membranes were imaged by means of confocal laser scanning microscopy (CLSM) and SICM. The former was used to prove spreading success as described above, while the latter provided insight into topographies of PSMs. Height differences between rim regions and membranes covering the pores, referred to as 'pore depth', were revealed to depend on the substrate functionalisation. While an average pore depth of 80 nm was observed for hydrophobically functionalised substrates, hydrophilically functionalised substrates featured an average pore depth of 59 nm (cf. Ch. 4.1.5 and 4.2.4). This difference in pore depths is explained by the geometry of the functionalisation and the strength of interactions between the lipid bilayer and the functionalisation molecules. Reasoning against a hypothesis that lipid monolayers on residual air within the pores are formed rather than bilayers suspending the pores was obtained as the membrane topography recorded is not in agreement with the presumed topography of a monolayer on air. With respect to influence of the lipid composition on the membrane topography, there were not any differences observed.

The main part of this thesis addressed development and application of CPP titration experiments which were successfully established based on both the CLSM and the SICM technique. CLSM experiments were designed to gain insights into peptide membrane interactions, especially with regard to peptide concentration ranges at which membranes rupture, and facilitate development of the SICM assay. Three sets of titration experiments

## SUMMARY OF THESIS

were performed (cf. Ch. 4.1.4 and 4.2.3). Melittin was used on hydrophobically and -philically functionalised substrates, and penetratin was titrated onto hydrophilically functionalised substrates. Every set comprised experiments on all three different membrane compositions used throughout this thesis, i.e. purely zwitterionic PSMs (POPC) as well as PSMs comprising negatively charged lipids (POPC/POPS (4:1)) or cholesterol (DPhPC/chol (9:1)) in addition to zwitterionic lipids. Rupturing of PSMs was observed at varying melittin concentrations depending on the lipid composition as well as on the functionalisation. Bilayers on hydrophobically functionalised substrates were observed to rupture at three times lower [melittin] values than bilayers prepared on hydrophilically functionalised substrates, i.e. at [melittin] = (201–672) nM compared to (521–2023) nM. This finding is mainly attributed to the significantly higher lateral tension ('prestress') in PSMs on hydrophobically functionalised substrates. Comparably strong hydrophobic interactions between cholesterol moieties of functionalisation molecules and the lipid bilayer prevent the membrane from adapting to changes in the membrane architecture induced through pore formation by melittin to a larger extent than comparably weak hydrophilic interactions between mercaptoethanol hydroxyl groups and the bilayer. Moreover, it was found that, independent of the functionalisation, cholesterol presence leads to an increase in the melittin concentration range sufficient for PSM rupturing. On the contrary, the presence of POPS decreases the sufficient melittin concentration. It is presumed that cholesterol affects melittin's lytic activity by changing the membrane architecture and thereby melittin's local environment. Negative charges, introduced to the bilayer by POPS, are believed to enhance melittin binding which results in enhanced lytic activity. Penetratin concentration ranges were comparable with the higher melittin concentration ranges, values found are in the range of (1005–3126) nM. This is explained with the different roles played by melittin and penetratin in nature: while melittin is utilised by *Apis mellifera* to damage enemies' cells, penetratin belongs to a vital signal transduction pathway in *Drosophila melanogaster*. It was revealed that the [penetratin] range resulting in membrane rupturing does not depend on the PSM composition. A significant difference between melittin and penetratin titrations was observed with respect to kinetics. While melittin induced rupturing was typically completed within 15 min and the ruptured membrane ratio vs  $t$  plot revealed sigmoidal curves, penetratin curves followed a linear course and resulted in completion of PSM rupturing within more than 30 min. It is deduced that cooperative effects play an important role in the melittin mechanism whereas this is not the case for penetratin.

Melittin titration experiments were performed by means of SICM on DPhPC/chol (9:1) PSMs prepared on hydrophobically functionalised substrates and on POPC and DPhPC/chol (9:1) PSMs prepared on hydrophilically functionalised substrates (cf. Ch. 4.1.5 and 4.2.4). Unlike observed by CLSM, the SICM did not reveal any differences with respect to [melittin] ranges depending on membrane composition or substrate functionalisation. Titrations on hydrophobically functionalised substrates resulted in values between (350–452) nM, on hydrophilically functionalised substrates (207–482) nM were obtained. Prior to rupturing of membranes, an increase in pore depth was observed for individual membranes, corresponding to an increase in membrane permeability. This bilayer permeabilisation



reflects the formation of pores within PSMs induced by melittin. Completion of PSM rupturing did take place significantly slower than observed by means of CLSM which may be due to worse distribution of the peptide within the sample solution.



# APPENDIX

## A. ABBREVIATIONS

2D	Two-dimensional
3D	Three-dimensional
ac	Alternating current
AFM	Atomic force microscopy
AMP	Antimicrobial peptide
AnthD	Antennapedia homeodomain
BLM	Black lipid membrane
chol	Cholesterol
CPEO3	Cholesterylpolyethylenoxy thiol
CPP	Cell penetrating peptide
dc	Direct current
DHPE-TR	Dihexadecanoyl- <i>sn</i> -glycero-3-phosphoethanolamine- Texas Red
DPhPC	1,2-Diphytanoyl- <i>sn</i> -glycero-3-phosphatidylcholine
EM	Electron microscopy
ESC	Embryonic stem cell
GUV	Giant unilamellar vesicle
ITO	Indium tin oxide
L	Lipid
LUV	Large unilamellar vesicle
ME	Mercaptoethanol
MLV	Multilamellar vesicle
naCPP	Nonamphipathic cell penetrating peptide
P	Peptide
paCPP	Primary amphipathic cell penetrating peptide

## APPENDIX

PALM	Photo-activated localisation microscopy
POPC	1-Palmitoyl-2-oleoyl- <i>sn</i> -glycero-3-phosphatidylcholine
POPS	1-Palmitoyl-2-oleoyl- <i>sn</i> -glycero-3-phosphatidyl-L-serine
PSM	Pore-suspending membrane
PTFE	Polytetrafluoroethylene
QCM	Quartz crystal microbalance
saCPP	Secondary amphipathic cell penetrating peptide
SECM	Scanning electrochemical microscopy
SEM	Scanning electron microscopy
SICM	Scanning ion conductance microscopy
SNOM	Scanning near-field optical microscopy
SPM	Scanning probe microscopy
SPR	Surface plasmon resonance
SSCM	Scanning surface confocal microscopy
SSM	Solid supported membrane
STED	Stimulated emission depletion
STM	Scanning tunneling microscope
STORM	Stochastic optical reconstruction microscopy
SUV	Small unilamellar vesicle
Tris	Tris(hydroxymethyl)aminoethane
UV/Vis	Ultraviolet/visible

## B. SYMBOLS

$A$	Absorbance
$\alpha$	One half of the angular aperture
$c$	Concentration
$d$	Thickness
$\gamma$	Semiangle of a conical section
$E$	Electric field
$E_0$	Electronic ground state

$E_1$	Electronic excited state
$\varepsilon$	Extinction coefficient
$\varepsilon_0$	Electric constant
$f$	Frequency
$I$	Current
$I_{ac}$	Alternating current
$I_{cyl}$	Current of a hollow cylinder
$I_{dc}$	Direct current
$I_{dc,sat}$	Maximum dc current
$j$	Current density
$k$	Rate constant
$\kappa$	Specific conductance
$L_P$	Cone length
$\lambda$	Wavelength
$\lambda_{abs}$	Wavelength of absorption
$\lambda_{em}$	Wavelength of emission
$m$	Mass
$n$	Refractive index
$NA$	Numerical Aperture
$\nu', \nu''$	Vibrational states
$P$	Parameter
$p$	Pressure
$P_0$	Parameter set-point
$Q$	Charge
$R$	Resistance
$r$	Radius
$R_A$	Lateral contribution to $R_{l2}$
$r_a$	Outer pipette diameter
$R_B$	Vertical contribution to $R_{l2}$
$r_i$	Inner pipette diameter
$R_l$	Leakage resistance

## APPENDIX

$R_{l1}$	Leakage resistance beneath pipette glass
$R_{l2}$	Leakage resistance beneath pipette tip opening
$R_p$	Pipette resistance
$R_r$	Electrolyte resistance
$R_{tot}$	Total resistance
$\sigma$	Lateral tension ('prestress')
$t$	Time
$U$	Voltage
$V$	Volume
$z$	Probe-sample distance

## C. CHEMICALS

Argon	Air Liquide, Düsseldorf (Germany)
Calcium chloride	Merck, Darmstadt (Germany)
Chloroform	Merck, Darmstadt (Germany)
Cholesterol	Sigma-Aldrich (Taufkirchen)
Chromium	Umicore Materials, Balzers (Liechtenstein)
DHPE-TR	Sigma-Aldrich (Taufkirchen)
DPhPC	Avanti Polar Lipids, Alabaster (USA)
Ethanol p.a.	VWR International, Darmstadt (Germany)
Gold 99.99%	Allgemeine Gold- und Silberscheideanstalt, Pforzheim (Germany)
HCl	Merck, Darmstadt (Germany)
Hellmanex	Hellma, Müllheim (Germany)
Melittin	Sigma-Aldrich, Taufkirchen (Germany)
2-Mercaptoethanol	Carl Roth, Karlsruhe (Germany)
Mucosol	Merck, Darmstadt (Germany)
Nitrogen	Linde, München (Germany)
Penetratin	PolyPeptide Laboratories, Strasbourg (France)
Phosphorous acid	Merck, Darmstadt (Germany)
POPC	Avanti Polar Lipids, Alabaster (USA)

POPS	Avanti Polar Lipids, Alabaster (USA)
Potassium chloride	AppliChem, Darmstadt (Germany)
1-Propanol	Carl Roth, Karlsruhe (Germany)
Sodium hypochlorite	Carl Roth, Karlsruhe (Germany)
Sucrose	Carl Roth, Karlsruhe (Germany)
Tris/HCl	Carl Roth, Karlsruhe (Germany)

#### D. MATERIALS

Borosilicate capillaries	NPI electronic, Tamm (Germany)
Copper tape	Fritz Bossert, Hamburg (Germany)
ITO slides	Präzisions Glas & Optik, Iserlohn (Germany)
Eppendorf pipette	Eppendorf, Hamburg (Germany)
Eppendorf pipette tips	Sarstedt, Nürnbergrecht (Germany)
Gold target	Elektronen Optik Service, Dortmund (Germany)
Parafilm	Pechiney Plastic Packaging, Chicago (USA)
Petri dish	VWR International, Darmstadt (Germany)
Quartz cuvette	Hellma Optik, Halle (Germany)
Sand paper	AEG, Frankfurt/Main (Germany)
Silver wire	Goodfellow, Huntington (UK)
Si <sub>3</sub> N <sub>4</sub> substrates	fluXXion B.V., Eindhoven (Netherlands)
Sterile syringe filters	Sartorius, Göttingen (Germany)
Syringes	B Braun, Melsungen (Germany)
Titanium target	Elektronen Optik Service, Dortmund (Germany)

#### E. HARDWARE

Adventurer	OHAUS, Pine Brook (USA)
Agilent 3320A	Agilent Technologies, Santa Clara (USA)
Axopatch 200B Amplifier	Axon Instruments, Union City (USA)
B3-220PL	Motic, Wetzlar (Germany)

## APPENDIX

BX-51	Olympus, Hamburg (Germany)
Cary 50 UV spectrometer	Varian, Darmstadt (Germany)
ICNano Scanning Ion Conductance Microscope	Ionscope, Melbourn (UK)
ICNano2000 Scanning Ion Conductance Microscope	Ionscope, Melbourn (UK)
LSM 710 Examiner	Carl Zeiss, Jena (Germany)
MED 020 Modular High Vacuum Coating System	Bal-Tec, Balzers (Liechtenstein)
Milli-Q plus 185	Millipore, Eschborn (Germany)
Milli-RO 3	Millipore, Eschborn (Germany)
Objective W Plan-Achromat 63x/1.0 M27	Carl Zeiss, Jena (Germany)
P-1000 micropipette puller	Sutter Instruments, Novato (USA)
PDC 32 G-2	Harrick Plasma (Ithaca, USA)
pH-Meter Calimatic 766	Knick, Berlin (Germany)
Sartorius CP55D	Sartorius, Göttingen (Germany)
Sonorex RK 255 H	Bandelin, Berlin (Germany)
Sputter Coater 108 auto	Cressington Scientific Instruments (Watford, UK)
Thickness Controller MTM20	Cressington Scientific Instruments (Watford, UK)
Vacuum oven	Binder, Tuttlingen (Germany)
Variomag Electronicrührer	H+P Labortechnik, Oberschleißheim (Germany)

## F. SOFTWARE

Endnote X3	Thomson Reuters, New York (USA)
Gwyddion 2.23	<a href="http://gwyddion.net/">http://gwyddion.net/</a>
ICNano Hopping 2 1.9.3.73	Ionscope, Melbourn (UK)
ICNano 2000	Ionscope, Melbourn (UK)
Isis Draw 2.4	MDL Information Systems, Hayward (USA)
LabView 6.0.2	National Instruments, Austin (USA)



MATLAB R2011A	The Mathworks, Natick (USA)
Office 2010	Microsoft, Redmond (USA)
OriginPro 8	Origin Lab Corporation, Northampton (USA)
ScanIC Image	Ionscope, Melbourn (UK)
WSxM	<a href="http://www.nanotec.es/products/wsxm/">http://www.nanotec.es/products/wsxm/</a>
ZEN 2008	Carl Zeiss, Jena (Germany)
ZEN 2009 LE	Carl Zeiss, Jena (Germany)



## BIBLIOGRAPHY

Abbe, E. K. (1882). The Relation of Aperture and Power in the Microscope. *Journal of the Royal Microscopical Society* **2**: 300-9.

Allende, D. and McIntosh, T. J. (2003). Lipopolysaccharides in Bacterial Membranes Act Like Cholesterol in Eukaryotic Plasma Membranes in Providing Protection against Melittin-Induced Bilayer Lysis†. *Biochemistry* **42**: 1101-08.

Allende, D., Simon, S. A. and McIntosh, T. J. (2005). Melittin-Induced Bilayer Leakage Depends on Lipid Material Properties: Evidence for Toroidal Pores. *Biophysical Journal* **88**: 1828-37.

Allinquant, B., Hantraye, P., Mailleux, P., Moya, K., Bouillot, C. and Prochiantz, A. (1995). Downregulation of Amyloid Precursor Protein Inhibits Neurite Outgrowth in Vitro. *Journal of Cell Biology* **128**: 919-27.

Alonsoromanowski, S., Gassa, L. M. and Vilche, J. R. (1995). An Investigation by Eis of Gramicidin Channels in Bilayer-Lipid Membranes. *Electrochimica Acta* **40**: 1561-7.

Angelova, M. I. and Dimitrov, D. S. (1986). Liposome Electroformation. *Faraday Discussions of the Chemical Society* **81**: 303-11.

Angelova, M. I., Soléau, S., Méléard, P., Faucon, F. and Bothorel, P. (1992). Preparation of Giant Vesicles by External Ac Electric Fields. Kinetics and Applications. *Progress in Colloid & Polymer Science* **89**: 127-31.

Bacia, K., Schwille, P. and Kurzchalia, T. (2005). Sterol Structure Determines the Separation of Phases and the Curvature of the Liquid-Ordered Phase in Model Membranes. *Proceedings of the National Academy of Sciences* **102**: 3272-7.

Bamberg, E., Alpes, H., Apell, H. J., Bradley, R., Harter, B., Quelle, M. J. and Urry, D. W. (1979). Formation of Ionic Channels in Black Lipid-Membranes by Succinic Derivatives of Gramicidin-A. *Journal of Membrane Biology* **50**: 257-70.

Bamberg, E., Apell, H. J., Alpes, H., Gross, E., Morell, J. L., Harbaugh, J. F., Janko, K. and Lauger, P. (1978). Ion Channels Formed by Chemical Analogs of Gramicidin-A. *Federation Proceedings* **37**: 2633-8.

## BIBLIOGRAPHY

Batenburg, A. M., van Esch, J. H. and de Kruijff, B. (1988). Melittin-Induced Changes of the Macroscopic Structure of Phosphatidylethanolamines. *Biochemistry* **27**: 2324-31.

Bellet-Amalric, E., Blaudez, D., Desbat, B., Graner, F., Gauthier, F. and Renault, A. (2000). Interaction of the Third Helix of Antennapedia Homeodomain and a Phospholipid Monolayer, Studied by Ellipsometry and Pm-Irras at the Air-Water Interface. *Biochimica et Biophysica Acta* **1467**: 131-43.

Bello, J., Bello, H. R. and Granados, E. (1982). Conformation and Aggregation of Melittin: Dependence of Ph and Concentration. *Biochemistry* **21**: 461-5.

Benachir, T. and Lafleur, M. (1995). Study of Vesicle Leakage Induced by Melittin. *Biochimica et Biophysica Acta (BBA) - Biomembranes* **1235**: 452-60.

Benachir, T., Monette, M., Grenier, J. and Lafleur, M. (1997). Melittin-Induced Leakage from Phosphatidylcholine Vesicles Is Modulated by Cholesterol: A Property Used for Membrane Targeting. *European Biophysical Journal* **25**: 201-10.

Berlose, J.-P., Convert, O., Derossi, D., Brunissen, A. and Chassaing, G. (1996). Conformational and Associative Behaviours of the Third Helix of Antennapedia Homeodomain in Membrane-Mimetic Environments. *European Journal of Biochemistry* **242**: 372-86.

Betzig, E., Patterson, G. H., Sougrat, R., Lindwasser, O. W., Olenych, S., Bonifacino, J. S., Davidson, M. W., Lippincott-Schwartz, J. and Hess, H. F. (2006). Imaging Intracellular Fluorescent Proteins at Nanometer Resolution. *Science* **313**: 1642-45.

Binnig, G. and Rohrer, H. (1987). Scanning Tunneling Microscopy—from Birth to Adolescence. *Reviews of Modern Physics* **59**: 615-25.

Binnig, G., Rohrer, H., Gerber, C. and Weibel, E. (1982). Surface Studies by Scanning Tunneling Microscopy. *Physical Reviews Letters* **49**: 57-61.

Blodgett, K. (1935). Films Built by Depositing Successive Monomolecular Layers on a Solid Surface. *Journal of the American Chemical Society* **57**: 1007-22.

Böcker, M., Anczykowski, B., Wegener, J. and Schäffer, T. E. (2007). Scanning Ion Conductance Microscopy with Distance-Modulated Shear Force Control. *Nanotechnology* **18**.

Böcker, M., Muschter, S., Schmitt, E. K., Steinem, C. and Schäffer, T. E. (2009). Imaging and Patterning of Pore-Suspending Membranes with Scanning Ion Conductance Microscopy. *Langmuir* **25**: 3022-28.

Boisseau, S., Mabrouk, K., Ram, N., Garmy, N., Collin, V., Tadmouri, A., Mikati, M., Sabatier, J. M., Ronjat, M., Fantini, J. and de Waard, M. (2006). Cell Penetration Properties of Maurocalcine, a

Natural Venom Peptide Active on the Intracellular Ryanodine Receptor. *Biochimica Biophysica Acta* **1758**: 308-19.

Boll, A., Jatho, A., Czudnochowski, N., Geyer, M. and Steinem, C. (2011). Mechanistic Insight into the Translocation of Full Length Hiv-1 at across Lipid Membranes. *Biochimica et Biophysica Acta* **1808**: 2685-93.

Bossu, J. L. and Feltz, A. (1984). Patch-Clamp Study of the Tetrodotoxin-Resistant Sodium Current in Group C Sensory Neurones. *Neuroscience Letters* **51**: 241-6.

Bradford, M. M. (1976). A Rapid and Sensitive Method for the Quantitation of Microgram Quantities of Protein Utilizing the Principle of Protein-Dye Binding. *Analytical Biochemistry* **72**: 248-54.

Brown, L. R. and Wüthrich, K. (1981). Melittin Bound to Dodecylphosphocholine Micelles. H-Nmr Assignments and Global Conformational Features. *Biochimica et Biophysica Acta* **647**: 95-111.

Brozell, A. M., Muha, M. A., Sanii, B. and Parikh, A. N. (2006). A Class of Supported Membranes: Formation of Fluid Phospholipid Bilayers on Photonic Band Gap Colloidal Crystals. *Journal of the American Chemical Society* **128**: 62-3.

Bruckbauer, A., Ying, L., Rothery, A. M., Korchev, Y. E. and Klenerman, D. (2002). Characterization of a Novel Light Source for Simultaneous Optical and Scanning Ion Conductance Microscopy. *Analytical Chemistry* **74**: 2612-16.

Bustamante, J. O., Ruknudin, A. and Sachs, F. (1991). Stretch-Activated Channels in Heart Cells: Relevance to Cardiac Hypertrophy. *Journal of Cardiovascular Pharmacology* **17**: S110-3.

Chattopadhyay, A. and Rukmini, R. (1993). Restricted Mobility of the Sole Tryptophan in Membrane-Bound Melittin. *FEBS Letters* **335**: 341-4.

Cohen-Avrahami, M., Libster, D., Aserin, A. and Garti, N. (2012). Penetratin-Induced Transdermal Delivery from H(li) Mesophases of Sodium Diclofenac. *Journal of Controlled Release* **159**: 419-28.

Comstock, D. J., Elam, J. W., Pellin, M. J. and Hersam, M. C. (2010). Integrated Ultramicroelectrode-Nanopipet Probe for Concurrent Scanning Electrochemical Microscopy and Scanning Ion Conductance Microscopy. *Analytical Chemistry* **82**: 1270-76.

Condon, E. (1926). A Theory of Intensity Distribution in Band Systems. *Physical Review* **28**: 1182-201.

## BIBLIOGRAPHY

Cremer, P. S. and Boxer, S. G. (1999). Formation and Spreading of Lipid Bilayers on Planar Glass Supports. *Journal of Physical Chemistry B* **103**: 2554-9.

Czajlik, A., Mesko, E., Penke, B. and Perczel, A. (2002). Investigation of Penetratin Peptides. Part 1. The Environment Dependent Conformational Properties of Penetratin and Two of Its Derivatives. *Journal of Peptide Science* **8**: 151-71.

DeGrado, W. F., Musso, G. F., Lieber, M., Kaiser, E. T. and Kézdy, F. J. (1982). Kinetics and Mechanism of Hemolysis Induced by Melittin and by a Synthetic Melittin Analogue. *Biophysical Journal* **37**: 329-38.

Dempsey, C. E. (1990). The Actions of Melittin on Membranes. *Biochimica et Biophysica Acta (BBA) - Reviews on Biomembranes* **1031**: 143-61.

Derossi, D., Calvet, S., Trembleau, A., Brunissen, A., Chassaing, G. and Prochiantz, A. (1996). Cell Internalization of the Third Helix of the Antennapedia Homeodomain Is Receptorindependent. *Journal of Biological Chemistry* **271**: 18188-93.

Derossi, D., Chassaing, G. and Prochiantz, A. (1998). Trojan Peptides: The Penetratin System for Intracellular Delivery. *Trends in Cell Biology* **8**: 84-7.

Derossi, D., Joliot, A. H., Chassaing, G. and Prochiantz, A. (1994). The Third Helix of the Antennapedia Homeodomain Translocates through Biological Membranes. *Journal of Biological Chemistry* **269**: 10444-50.

Dertinger, T., von der Hocht, I., Benda, A., Hof, M. and Enderlein, J. (2006). Surface Sticking and Lateral Diffusion of Lipids in Supported Bilayers. *Langmuir* **22**: 9339-44.

Derzko, Z. and Jacobson, K. (1980). Comparative Lateral Diffusion of Fluorescent Lipid Analogues in Phospholipid Multibilayers. *Biochemistry* **19**: 6050-7.

Dietrich, C., Bagatolli, L. A., Volovyk, Z. N., Thompson, N. L., Levi, M., Jacobson, K. and Gratton, E. (2001). Lipid Rafts Reconstituted in Model Membranes. *Biophysical Journal* **80**: 1417-28.

Doeven, M. K., Folgering, J. H. A., Krasnikov, V., Geertsma, E. R., van den Bogaart, G. and Poolman, B. (2005). Distribution, Lateral Mobility and Function of Membrane Proteins Incorporated into Giant Unilamellar Vesicles. *Biophysical Journal* **88**: 1134-42.

Drin, G., Mazel, M., Clair, P., Mathieu, D., Kaczorek, M. and Tamsamani, J. (2001). Physico-Chemical Requirements for Cellular Uptake of Pantp Peptide. Role of Lipid Binding Affinity. *European Journal of Biochemistry* **268**: 1304-14.

Duchardt, F., Fotin-Mleczek, M., Schwarz, H., Fischer, R. and Brock, R. (2007). A Comprehensive Model for the Cellular Uptake of Cationic Cell-Penetrating Peptides. *Traffic* **8**: 846-66.

Duclohier, H. (2005). Neuronal Sodium Channels in Ventricular Heart Cells Are Localized near T-Tubules Openings. *Biochemical and Biophysical Research Communications* **334**: 1135-40.

Dupont, E., Prochiantz, A. and Joliot, A. H. (2005). Penetratins. Handbook of Cell-Penetrating Peptides. Florida, CRC Press: 5-28.

Dutta, A. K., Korchev, Y. E., Shevchuk, A. I., Hayashi, S., Okada, Y. and Sabirov, R. Z. (2008). Spatial Distribution of Maxi-Anion Channel on Cardiomyocytes Detected by Smart-Patch Technique. *Biophysical Journal* **94**: 1646-55.

Edidin, M., Zagzansky, Y. and Lardner, T. J. (1977). Measurement of Membrane Protein Lateral Diffusion in Single Cells. *Science* **191**: 466-8.

Edwards, M. A., Williams, C. G., Whitworth, A. L. and Unwin, P. R. (2009). Scanning Ion Conductance Microscopy: A Model for Experimentally Realistic Conditions and Image Interpretation. *Analytical Chemistry* **81**: 4482-92.

El-Andaloussi, S., Holm, T. and Langel, Ü. (2005). Cell-Penetrating Peptides: Mechanisms and Applications. *Current Pharmaceutical Design* **11**: 3597-611.

El-Andaloussi, S., Järver, P., Johansson, H. J. and Langel, Ü. (2007a). Cargo-Dependent Cytotoxicity and Delivery Efficacy of Cell-Penetrating Peptides: A Comparative Study. *Biochemical Journal* **407**: 285-92.

El-Andaloussi, S., Johansson, H. J., Holm, T. and Langel, Ü. (2007b). A Novel Cell-Penetrating Peptide, M918, for Efficient Delivery of Proteins and Peptide Nucleic Acids. *Molecular Therapy* **15**: 1820-6.

Elmqvist, A., Lindgren, M., Bartfai, T. and Langel, Ü. (2001). "Vecadherin-Derived Cell-Penetrating Peptide, Pvec with Carrier Functions. *Experimental Cell Research* **269**: 237-44.

Engelman, D. M. (2005). Membranes Are More Mosaic Than Fluid. *Nature* **438**: 578-80.

Faucon, J. F., Dufourcq, J. and Lussan, C. (1979). The Self-Association of Melittin and Its Binding to Lipids: An Intrinsic Fluorescence Polarization Study. *FEBS Letters* **102**: 187-90.

Favero, G., Campanella, L., Cavallo, S., D'Annibale, A., Perrella, M., Mattei, E. and Ferri, T. (2005). Glutamate Receptor Incorporated in a Mixed Hybrid Bilayer Lipid Membrane Array, as a Sensing Element of a Biosensor Working under Flowing Conditions. *Journal of the American Chemical Society* **127**: 8103-11.

## BIBLIOGRAPHY

Fittipaldi, A., Ferrari, A., Zoppe, M., Arcangeli, C., Pellegrini, V., Beltram, F. and Giacca, M. (2003). Cell Membrane Lipid Rafts Mediate Caveolar Endocytosis of Hiv-1 Tat Fusion Proteins. *Journal of Biological Chemistry* **278**: 34141-9.

Florin, E. L. and Gaub, H. E. (1993). Painted Supported Lipid Membranes. *Biophysical Journal* **64**: 375-83.

Franck, J. and Dymond, E. G. (1926). Elementary Processes of Photochemical Reactions. *Transactions of the Faraday Society* **21**: 536-42.

Frankel, A. D. and Pabo, C. O. (1988). Cellular Uptake of the Tat Protein from Human Immunodeficiency Virus. *Cell* **55**: 1189-93.

Fujiwara, T., Ritchie, K., Murakoshi, H., Jacobson, K. and Kusumi, A. (2002). Phospholipids Undergo Hop Diffusion in Compartmentalized Cell Membrane. *Journal of Cell Biology* **157**: 1071-82.

Futaki, S., Suzuki, T., Ohashi, W., Yagami, T., Tanaka, S., Ueda, K. and Sugiura, Y. (2001). Arginine-Rich Peptides. An Abundant Source of Membrane-Permeable Peptides Having Potential as Carriers for Intracellular Protein Delivery. *Journal of Biological Chemistry* **276**: 5836-40.

Gabriel, O. (2007). "Depiction of Franck Condon Principle in Absorption and Fluorescence.". Retrieved 6 February, 2013, from <http://en.wikipedia.org/wiki/File:Franck-Condon-diagram.png>.

Gao, Y.-J., Zhang, L., Samad, O. A., Suter, M. R., Yasuhiko, K., Xu, Z.-Z., Park, J.-Y., Lind, A.-L., Ma, Q. and Ji, R.-R. (2009). Jnk-Induced Mcp-1 Production in Spinal Cord Astrocytes Contributes to Central Sensitization and Neuropathic Pain. *Journal of Neuroscience* **29**: 4096-108.

Gaßmann, O., Kreir, M., Ambrosi, C., Pranskevich, J., Oshima, A., Röling, C., Sosinsky, G., Fertig, N. and Steinem, C. (2009). The M34a Mutant of Connexin26 Reveals Active Conductance States in Pore-Suspending Membranes. *Journal of Structural Biology* **168**: 168-76.

Gasteiger, E., Gattiker, A., Hoogland, C., Ivanyi, I., Appel, R. D. and Bairoch, A. (2003). ExPASy: The Proteomics Server for in-Depth Protein Knowledge and Analysis. *Nucleic Acids Research* **31**: 3784-88.

Ghosh, A. K., Rukmini, R. and Chattopadhyay, A. (1997). Modulation of Tryptophan Environment in Membranebound Melittin by Negatively Charged Phospholipids: Implications in Membrane Organization and Function. *Biochemistry* **36**: 14291-305.



Girard, P., Pecreaux, J., Lenoir, G., Falson, P., Rigaud, J. L. and Bassereau, P. (2004). A New Method for the Reconstitution of Membrane Proteins into Giant Unilamellar Vesicles. *Biophysical Journal* **87**: 419-29.

Gomezlagunas, F., Pena, A., Lievano, A. and Darszon, A. (1989). Incorporation of Ionic Channels from Yeast Plasma-Membranes into Black Lipid-Membranes. *Biophysical Journal* **56**: 115-9.

Gorelik, J., Ali, N. N., Sheikh Abdul Kadir, S. H., Lab, M., Stojkovic, P., Armstrong, L., Sviderskaya, E. V., Negulyaev, Y. A., Klenerman, D., Bennett, D. C., Lako, M., Harding, S. E., Stojkovic, M. and Korchev, Y. E. (2008). Non-Invasive Imaging of Stem Cells by Scanning Ion Conductance Microscopy: Future Perspective. *Tissue Eng Part C Methods* **14**: 311-8.

Gorelik, J., Gu, Y., Spohr, H. A., Shevchuk, A. I., Lab, M. J., Harding, S. E., Edwards, C. R. W., Whitaker, M., Moss, G. W. J., Benton, D. C. H., Sánchez, D., Darszon, A., Vodyanoy, I., Klenerman, D. and Korchev, Y. E. (2002a). Ion Channels in Small Cells and Subcellular Structures Can Be Studied with a Smart Patch-Clamp System. *Biophysical Journal* **83**: 3296-303.

Gorelik, J., Harding, S. E., Shevchuk, A. I., Koralage, D., Lab, M., de Swiet, M., Korchev, Y. and Williamson, C. (2002b). Taurocholate Induces Changes in Rat Cardiomyocyte Contraction and Calcium Dynamics. *Clinical Science* **103**: 191-200.

Gorelik, J., Zhang, Y., Shevchuk, A. I., Frolenkov, G. I., Sánchez, D., Lab, M. J., Vodyanoy, I., Edwards, C. R. W., Klenerman, D. and Korchev, Y. E. (2004). The Use of Scanning Ion Conductance Microscopy to Image A6 Cells. *Molecular and Cellular Endocrinology* **217**: 101-08.

Green, D. J. and Gillette, R. (1983). Patch-Clamp and Voltage-Clamp Analysis of Cyclic Amp-Stimulated Inward Current Underlying Neuron Bursting. *Nature* **306**: 784-5.

Green, M. and Loewenstein, P. M. (1988). Autonomous Functional Domains of Chemically Synthesized Human Immunodeficiency Virus Tat Trans-Activator Protein. *Cell* **55**: 1179-88.

Gu, Y., Gorelik, J., Spohr, H. A., Shevchuk, A., Lab, M. J., Harding, S. E., Vodyanoy, I., Klenerman, D. and Korchev, Y. E. (2002). High-Resolution Scanning Patch-Clamp: New Insights into Cell Function. *The FASEB Journal* **16**: 748-50.

Habermann, E. and Jentsch, J. (1967). Sequenzanalyse Des Melittins Aus Den Tryptischen Und Peptischen Spaltstücken. *Hoppe-Seyler's Zeitschrift für Physiologische Chemie* **348**: 37-50.

Hansma, P. K., Drake, B., Marti, O., Gould, S. A. and Prater, C. B. (1989). The Scanning Ion-Conductance Microscope. *Science (New York, N.Y.)* **243**: 641-43.

## BIBLIOGRAPHY

Happel, P., Hoffmann, G., Mann, S. A. and Dietzel, I. D. (2003). Monitoring Cell Movements and Volume Changes with Pulse-Mode Scanning Ion Conductance Microscopy. *Journal of Microscopy* **212**: 144-51.

Heinemann, F. and Schwille, P. (2011). Preparation of Micrometer-Sized Free-Standing Membranes. *A European Journal of Chemical Physics and Physical Chemistry* **12**: 2568-71.

Hell, S. W. and Wichmann, J. (1994). Breaking the Diffraction Resolution Limit by Stimulated Emission: Stimulated-Emission-Depletion Fluorescence Microscopy. *Opt. Lett.* **19**: 780-82.

Hennesthal, C. and Steinem, C. (2000). Pore-Spanning Lipid Bilayers Visualized by Scanning Force Microscopy. *Journal of the American Chemical Society* **122**: 8085-6.

Henriques, S. T., Melo, M. N. and Castanho, M. A. R. B. (2006). Cell-Penetrating Peptides and Antimicrobial Peptides: How Different Are They? *Biochemical Journal* **399**: 1-7.

Hess, S. T., Giriajan, T. P. and Mason, M. D. (2006). Ultra-High Resolution Imaging by Fluorescence Photoactivation Localization Microscopy. *Biophysical Journal* **91**: 4258-72.

Hincha, D. K. and Crowe, J. H. (1996). The Lytic Activity of the Bee Venom Peptide Melittin Is Strongly Reduced by the Presence of Negatively Charged Phospholipids or Chloroplast Galactolipids in the Membranes of Phosphatidylcholine Large Unilamellar Vesicles. *Biochimica et Biophysica Acta (BBA) - Biomembranes* **1284**: 162-70.

Horcas, I., Fernandez, R., Gomez-Rodriguez, J. M., Colchero, J., Gomez-Herrero, J. and Baro, A. M. (2007). Wsxn: A Software for Scanning Probe Microscopy and a Tool for Nanotechnology. *Review of Scientific Instruments* **78**: 013705.

James, A. F., Sabirov, R. Z. and Okada, Y. (2010). Clustering of Protein Kinase  $\alpha$ -Dependent Cftr Chloride Channels in the Sarcolemma of Guinea-Pig Ventricular Myocytes. *Biochemical and Biophysical Research Communications* **391**: 841-45.

Jass, J., Tjarnhage, T. and Puu, G. (2000). From Liposomes to Supported, Planar Bilayer Structures on Hydrophilic and Hydrophobic Surfaces: An Atomic Force Microscopy Study. *Biophysical Journal* **79**: 3153-63.

Joliot, A. H., Pernelle, C., Deagostini-Bazin, H. and Prochiantz, A. (1991). Antennapedia Homeobox Peptide Regulates Neural Morphogenesis. *Proceedings of the National Academy of Sciences* **88**: 1864-8.

Jones, A. T. (2007). Macropinocytosis: Searching for an Endocytic Identity and Role in the Uptake of Cell Penetrating Peptides. *Journal of Cellular and Molecular Medicine* **11**: 670-84.

Katsu, T., Kuroko, M., Morikawa, T., Sanchika, K., Fujita, Y., Yamamura, H. and Uda, M. (1989). Mechanism of Membrane Damage Induced by the Amphipathic Peptides Gramicidin S and Melittin. *Biochimica et Biophysica Acta* **983**: 135-41.

Keller, C. A., Glasmästar, K., Zhdanov, V. P. and Kasemo, B. (2000). Formation of Supported Membranes from Vesicles. *Physical Reviews Letters* **84**: 5443-6.

Klausner, R. D. and Wolf, D. E. (1980). Selectivity of Fluorescent Lipid Analogues for Lipid Domains. *Biochemistry* **19**: 6199-203.

Klocek, G., Schulthess, T., Shai, Y. and Seelig, J. (2009). Thermodynamics of Melittin Binding to Lipid Bilayers. Aggregation and Pore Formation†. *Biochemistry* **48**: 2586-96.

Kocun, M., Lazzara, T. D., Steinem, C. and Janshoff, A. (2011). Preparation of Solvent-Free, Pore-Spanning Lipid Bilayers: Modeling the Low Tension of Plasma Membranes. *Langmuir* **27**: 7672-80.

Köper, I., Schiller, S. M., Giess, F., Naumann, R. and Knoll, W. (2006). Functional Tethered Biomolecular Lipid Membranes (Tbblms). *Advances in Planar Lipid Bilayers and Liposomes* **3**: 37-53.

Korchev, Y. E., Bashford, C. L., Alder, G. M., Apel, P. Y., Edmonds, D. T., Lev, A. A., Nandi, K., Zima, A. V. and Pasternak, C. A. (1997a). A Novel Explanation for Fluctuations of Ion Current through Narrow Pores. *The FASEB Journal* **11**: 600-08.

Korchev, Y. E., Bashford, C. L., Milovanovic, M., Vodyanoy, I. and Lab, M. J. (1997b). Scanning Ion Conductance Microscopy of Living Cells. *Biophysical Journal* **73**: 653-58.

Korchev, Y. E., Gorelik, J., Lab, M. J., Sviderskaya, E. V., Johnston, C. L., Coombes, C. R., Vodyanoy, I. and Edwards, C. R. W. (2000a). Cell Volume Measurement Using Scanning Ion Conductance Microscopy. *Biophysical Journal* **78**: 451-57.

Korchev, Y. E., Milovanovic, M., Bashford, C. L., Bennett, D. C., Sviderskaya, E. V., Vodyanoy, I. and Lab, M. J. (1997c). Specialized Scanning Ion-Conductance Microscope for Imaging of Living Cells. *Journal of Microscopy* **188**: 17-23.

Korchev, Y. E., Negulyaev, Y. A., Edwards, C. R. W., Vodyanoy, I. and Lab, M. J. (2000b). Functional Localization of Single Active Ion Channels on the Surface of a Living Cell. *Nat Cell Biol* **2**: 616-19.

Korlach, J., Schwille, P., Webb, W. W. and Feigensohn, G. W. (1999). Characterization of Lipid Bilayer Phases by Confocal Microscopy and Fluorescence Correlation Spectroscopy. *Proceedings of the National Academy of Sciences* **96**: 8461-66.

## BIBLIOGRAPHY

Kresák, S., Hianik, T. and Naumann, R. L. C. (2009). Giga-Seal Solvent-Free Lipid Membranes: From Single Nanopores to Nanopore Arrays. *Soft Matter* **5**: 4021-32.

Krishna, G., Schulte, J., Cornell, B. A., Pace, R. J. and Osman, P. D. J. (2001). Thethered Bilayer Membranes Containing Ionic Reservoirs: The Interfacial Capacitance. *Langmuir* **17**: 4858-66.

Kusumi, A., Nakada, C., Ritchie, K., Murase, K., Suzuki, K., Murakoshi, H., Kasai, R. S., Kondo, J. and Fujiwara, T. (2005). Paradigm Shift of the Plasma Membrane Concept from the Two-Dimensional Continuum Fluid to the Partitioned Fluid: High-Speed Single-Molecule Tracking of Membrane Molecules. *Annual Review of Biophysics and Biomolecular Structure* **34**: 351-U54.

Ladha, S., Mackie, A. R., Harvey, L. J., Clark, D. C., Lea, E. J., Brullemans, M. and Duclouhier, H. (1996). Lateral Diffusion in Planar Lipid Bilayers: A Fluorescence Recovery after Photobleaching Investigation of Its Modulation by Lipid Composition, Cholesterol, or Alamethicin Content and Divalent Cations. *Biophysical Journal* **71**: 1364-73.

Ladokhin, A. S., Selsted, M. E. and White, S. H. (1997). Sizing Membrane Pores in Lipid Vesicles by Leakage of Co-Encapsulated Markers: Pore Formation by Melittin. *Biophysical Journal* **72**: 1762-66.

Ladokhin, A. S. and White, S. H. (2001). 'Detergent-Like' Permeabilization of Anionic Lipid Vesicles by Melittin. *Biochimica et Biophysica Acta* **1514**: 253-60.

Lakowicz, J. R. (2006). Principles of Fluorescence Spectroscopy. New York, Springer.

Lang, H., Duchl, C. and Vogel, H. (1994). A New Class of Thiolipids for the Attachment of Lipid Bilayers on Gold Surfaces. *Langmuir* **10**: 197-210.

Langmuir, I. and Schäfer, V. (1938). Activities of Urease and Pepsin Monolayers. *Journal of the American Chemical Society* **60**: 1351-60.

Lazzara, T. D., Carnarius, C., Kocun, M., Janshoff, A. and Steinem, C. (2011a). Separating Attoliter-Sized Compartments Using Fluid Pore-Spanning Lipid Bilayers. *ACS Nano* **5**.

Lazzara, T. D., Kliesch, T.-T., Janshoff, A. and Steinem, C. (2011b). Orthogonal Functionalization of Nanoporous Substrates: Control of 3d Surface Functionality. *ACS Appl. Mater. Interfaces* **3**: 1068-76.

Lee, M.-T., Hung, W.-C., Chen, F.-Y. and Huang, H. W. (2008). Mechanism and Kinetics of Pore Formation in Membranes by Water-Soluble Amphipathic Peptides. *Proceedings of the National Academy of Sciences* **105**: 5087-92.

Lee, M. T., Hung, W. C., Chen, F. Y. and Huang, H. W. (2005). Manybody Effect of Antimicrobial Peptides: On the Correlation between Lipid's Spontaneous Curvature and Pore Formation. *Biophysical Journal* **89**: 4006-16.

Lee, T. H., Mozsolits, H. and Aguilar, M. I. (2001). Measurement of the Affinity of Melittin for Zwitterionic and Anionic Membranes Using Immobilized Lipid Biosensors. *Journal of Peptide Research* **58**: 464-76.

Li, A. P., Müller, F., Birner, A., Nielsch, K. and Gösele, U. (1998). Hexagonal Pore Arrays with a 50-420 Nm Interpore Distance Formed by Self-Organization in Anodic Alumina. *Journal of Applied Physics* **84**: 6023-6.

Lichtman, J. W. and Conchello, J.-A. (2005). Fluorescence Microscopy. *Nature Methods* **2**: 910-9.

Lin, J.-H. and Baumgaertner, A. (2000). Stability of a Melittin Pore in a Lipid Bilayer: A Molecular Dynamics Study. *Biophysical Journal* **78**: 1714-24.

Lindberg, M., Biverståhl, H., Gräslund, A. and Måler, L. (2003). Structure and Positioning Comparison of Two Variants of Penetratin in Two Different Membrane Mimicking Systems by Nmr. *European Journal of Biochemistry* **270**: 3055-63.

Lopez, A., Dupou, L., Altibelli, A., Trotard, J. and Tocanne, J. F. (1988). Fluorescence Recovery after Photobleaching (Frap) Experiments under Conditions of Uniform Disk Illumination. Critical Comparison of Analytical Solutions, and a New Mathematical Method for Calculation of Diffusion Coefficient D. *Biophysical Journal* **53**: 963-70.

Lowry, O. H., Rosebrough, N. J., Farr, A. L. and Randall, R. J. (1951). Protein Measurement with the Folin Phenol Reagent. *Journal of Biological Chemistry* **193**: 265-75.

MacDonald, R. C., MacDonald, R. I., Menco, B. P., Takeshita, K., Subbarao, N. K. and Hu, L. R. (1991). Small-Volume Extrusion Apparatus for Preparation of Large, Unilamellar Vesicles. *Biochimica Biophysica Acta* **1061**: 297-303.

Madani, F., Lindberg, S., Langel, #220, lo, Futaki, S., Gr, #228 and slund, A. (2011). Mechanisms of Cellular Uptake of Cell-Penetrating Peptides. *Journal of Biophysics* **2011**.

Magzoub, M., Kilk, K., Eriksson, L. E., Langel, Ü. and Gräslund, A. (2001). Interaction and Structure Induction of Cell-Penetrating Peptides in the Presence of Phospholipid Vesicles. *Biochimica et Biophysica Acta* **1512**: 77-89.

Maiolo, J. R., Ferrer, M. and Ottinger, E. A. (2005). Effects of Cargo Molecules on the Cellular Uptake of Arginine-Rich Cell-Penetrating Peptides. *Biochimica et Biophysica Acta* **1712**: 161-72.

## BIBLIOGRAPHY

Mally, M., Majhenc, J., Svetina, S. and Žekš, B. (2007). The Response of Giant Phospholipid Vesicles to Pore-Forming Peptide Melittin. *Biochimica et Biophysica Acta (BBA) - Biomembranes* **1768**: 1179-89.

Mann, S. A., Hoffmann, G., Hengstenberg, A., Schuhmann, W. and Dietzel, I. D. (2002). Pulse-Mode Scanning Ion Conductance Microscopy—a Method to Investigate Cultured Hippocampal Cells. *Journal of Neuroscience Methods* **116**: 113-17.

Mannelquist, A., Iwamoto, H., Szabo, G. and Shao, Z. (2001). Near-Field Optical Microscopy with a Vibrating Probe in Aqueous Solution. *Applied Physics Letters* **78**: 2076-78.

Mannelquist, A., Iwamoto, H., Szabo, G. and Shao, Z. (2002). Near Field Optical Microscopy in Aqueous Solution: Implementation and Characterization of a Vibrating Probe. *Journal of Microscopy* **205**: 53-60.

Matsuzaki, K., Yoneyama, S. and Miyajima, K. (1997). Pore Formation and Translocation of Melittin. *Biophysical Journal* **73**: 831-38.

Matsuzaki, K., Yoneyama, S., Murase, O. and Miyajima, K. (1996). Transbilayer Transport of Ions and Lipids Coupled with Mastoparan X Translocation. *Biochemistry* **35**: 8450-6.

Mayor, S. and Pagano, R. E. (2007). Pathways of Clathrin-Independent Endocytosis. *Nature Reviews Molecular Cell Biology* **8**: 603-12.

Mey, I., Stephan, M., Schmitt, E. K., Muller, M. M., Ben Amar, M., Steinem, C. and Janshoff, A. (2009). Local Membrane Mechanics of Pore-Spanning Bilayers. *Journal of the American Chemical Society* **131**: 7031-9.

Minsky, M. (1988). Memoir on Inventing the Confocal Scanning Microscope. *Scanning* **10**: 128-38.

Mironov, V. L. (2004). Fundamentals of Scanning Probe Microscopy. Nizhniy Novgorod, NT-MDT.

Monette, M. and Lafleur, M. (1995). Modulation of Melittin-Induced Lysis by Surface Charge Density of Membranes. *Biophysical Journal* **68**: 187-95.

Monod, J., Changeux, J.-P. and Jacob, F. (1963). Allosteric Proteins and Cellular Control Systems. *Journal of Molecular Biology* **6**: 306–29.

Morone, N., Fujiwara, T., Murase, K., Kasai, R. S., Ike, H., Yuasa, S., Usukura, J. and Kusumi, A. (2006). Three-Dimensional Reconstruction of the Membrane Skeleton at the Plasma Membrane Interface by Electron Tomography. *Journal of Cell Biology* **174**: 851-62.

Müller, P., Rudin, H. T., Tien, H. T. and Wescott, W. C. (1963). Methods for the Formation of Single Bimolecular Lipid Membranes in Aqueous Solution. *Journal of Physical Chemistry* **67**: 534-5.

Naito, A., Nagao, T., Norisada, K., Mizuno, T., Tuzi, S. and Saitô, H. (2000). Conformation and Dynamics of Melittin Bound to Magnetically Oriented Lipid Bilayers by Solid-State <sup>31</sup>p and <sup>13</sup>c Nmr Spectroscopy. *Biophysical Journal* **78**: 2405-17.

Nakase, I., Niwa, M., Takeuchi, T., Sonomura, K., Kawabala, N., Koike, Y., Takehashi, M., Tanaka, S., Ueda, K., Simpson, J. C., Jones, A. T., Sugiura, Y. and Futaki, S. (2004). Cellular Uptake of Arginine-Rich Peptides: Roles for Macropinocytosis and Actin Rearrangement. *Molecular Therapy* **10**: 1011-22.

Neumann, W., Habermann, E. and Hansen, H. (1953). Differenzierung Von Zwei Hämolysierenden Faktoren Im Bienengift. *Naunyn-Schmiedebergs Archiv für experimentelle Pathologie und Pharmakologie* **217**: 130-43.

Nitz, H., Kamp, J. and Fuchs, H. (1998). A Combined Scanning Ion-Conductance and Shear-Force Microscope. *Probe Microscopy* **1**: 187-200.

Novak, P., Li, C., Shevchuk, A. I., Stepanyan, R., Caldwell, M., Hughes, S., Smart, T. G., Gorelik, J., Ostanin, V. P., Lab, M. J., Moss, G. W. J., Frolenkov, G. I., Klenerman, D. and Korchev, Y. E. (2009). Nanoscale Live-Cell Imaging Using Hopping Probe Ion Conductance Microscopy. *Nat Meth* **6**: 279-81.

Ohki, S., Marcus, E., Sukumaran, D. K. and Arnold, K. (1994). Interaction of Melittin with Lipid Membranes. *Biochimica et Biophysica Acta (BBA) - Biomembranes* **1194**: 223-32.

Oren, Z. and Shai, Y. (1997). Selective Lysis of Bacteria but Not Mammalian Cells by Diastereomers of Melittin: Structure-Function Study†. *Biochemistry* **36**: 1826-35.

Orth, A., Johannes, L., Römer, W. and Steinem, C. (2012). Creating and Modulating Microdomains in Pore-Spanning Membranes. *A European Journal of Chemical Physics and Physical Chemistry* **13**: 108-14.

Palm, C., Netzereab, S. and Hallbrink, M. (2006). Quantitatively Determined Uptake of Cell-Penetrating Peptides in Non-Mammalian Cells with an Evaluation of Degradation and Antimicrobial Effects. *Peptides* **27**: 1710-6.

## BIBLIOGRAPHY

Papo, N. and Shai, Y. (2002). Exploring Peptide Membrane Interaction Using Surface Plasmon Resonance: Differentiation between Pore Formation Versus Membrane Disruption by Lytic Peptides†. *Biochemistry* **42**: 458-66.

Pastré, D., Iwamoto, H., Liu, J., Szabo, G. and Shao, Z. (2001). Characterization of Ac Mode Scanning Ion-Conductance Microscopy. *Ultramicroscopy* **90**: 13-19.

Pellegrino, M., Orsini, P. and De Gregorio, F. (2009). Use of Scanning Ion Conductance Microscopy to Guide and Redirect Neuronal Growth Cones. *Neuroscience Research* **64**: 290-96.

Perez, F., Lledo, P. M., Karagogeos, D., Vincent, J. D., Prochiantz, A. and Ayala, J. (1994). Rab3a and Rab3b Carboxy-Terminal Peptides Are Both Potent and Specific Inhibitors of Prolactin Release by Rat Cultured Anterior Pituitary Cells. *Molecular Endocrinology* **8**: 1278-87.

Persson, D., Thorén, P. E. G., Herner, M., Lincoln, P. and Nordén, B. (2003). Application of a Novel Analysis to Measure the Binding of Membrane-Translocating Peptide Penetratin to Negatively Charged Liposomes. *Biochemistry* **42**: 421-29.

Persson, D., Thorén, P. E. G. and Nordén, B. (2001). Penetratin-Induced Aggregation and Subsequent Dissociation of Negatively Charged Phospholipid Vesicles. *FEBS Letters* **25245**: 2918-26.

Plant, A. L. (1993). Self-Assembled Phospholipid/Alkanethiol Biomimetic Bilayers on Gold. *Langmuir* **9**: 2764-7.

Pooga, M., Hällbrink, M., Zorko, M. and Langel, Ü. (1998). Cell Penetration by Transportan. *FASEB Journal* **12**: 67-77.

Pott, T., Maillet, J. C., Abad, C., Campos, A., Dufourcq, J. and Dufourc, E. J. (2001). The Lipid Charge Density at the Bilayer Surface Modulates the Effects of Melittin on Membranes. *Chemistry and Physics of Lipids* **109**: 209-23.

Pouny, Y., Rapaport, D., Mor, A., Nicolas, P. and Shai, Y. (1992). Interaction of Antimicrobial Dermaseptin and Its Fluorescently Labeled Analogues with Phospholipid Membranes. *Biochemistry* **31**: 12416-23.

Prater, C. B., Hansma, P. K., Tortonese, M. and Quate, C. F. (1991). Improved Scanning Ion-Conductance Microscope Using Microfabricated Probes. *Review of Scientific Instruments* **62**: 2634-38.

Proksch, R., Lal, R., Hansma, P. K., Morse, D. and Stucky, G. (1996). Imaging the Internal and External Pore Structure of Membranes in Fluid: Tappingmode Scanning Ion Conductance Microscopy. *Biophysical Journal* **71**: 2155-57.



Quay, S. C. and Condie, C. C. (1983). Conformational Studies of Aqueous Melittin: Thermodynamic Parameters of the Monomer-Tetramer Self-Association Reaction. *Biochemistry* **22**: 695-700.

Raghuraman, H. and Chattopadhyay, A. (2004). Interaction of Melittin with Membrane Cholesterol: A Fluorescence Approach. *Biophysical Journal* **87**: 2419-32.

Raghuraman, H. and Chattopadhyay, A. (2005). Cholesterol Inhibits the Lytic Activity of Melittin in Erythrocytes. *Chemistry and Physics of Lipids* **134**: 183-9.

Raghuraman, H. and Chattopadhyay, A. (2006). Effect of Ionic Strength on Folding and Aggregation of the Hemolytic Peptide Melittin in Solution. *Biopolymers* **83**: 111-21.

Raghuraman, H. and Chattopadhyay, A. (2007). Melittin: A Membrane-Active Peptide with Diverse Functions. *Biosci Rep* **27**: 189-223.

Raguse, B., Braach-Maksvytis, V., Cornell, B. A., King, L. G., Osman, P. D. J. and Ron, J. (1998). Tethered Lipid Bilayer Membranes: Formation and Ionic Reservoir Characterization. *Langmuir* **14**: 648-59.

Rex, S. (1996). Pore Formation Induced by the Peptide Melittin in Different Lipid Vesicle Membranes. *Biophysical Chemistry* **58**: 75-85.

Rheinlaender, J. and Schäffer, T. E. (2009). Image Formation, Resolution, and Height Measurement in Scanning Ion Conductance Microscopy. *Journal of Applied Physics* **105**: 094905.

Riedel, E. and Janiak, C. (2007). Anorganische Chemie. Berlin, de Gruyter.

Ritchie, K., Iino, R., Fujiwara, T., Murase, K. and Kusumi, A. (2003). The Fence and Picket Structure of the Plasma Membrane of Live Cells as Revealed by Single Molecule Techniques. *Molecular Membrane Biology* **20**: 13-8.

Römer, W. and Steinem, C. (2004). Impedance Analysis and Single-Channel Recordings on Nano-Black Lipid Membranes Based on Porous Alumina. *Biophysical Journal* **86**: 955-65.

Ruiz, M. (2007). "Cell Membrane: Detailed Diagram." Retrieved 27 February, 2013, from [http://en.wikibooks.org/wiki/File:Cell\\_membrane\\_detailed\\_diagram\\_en.svg](http://en.wikibooks.org/wiki/File:Cell_membrane_detailed_diagram_en.svg).

Rust, M. J., Bates, M. and Zhuang, X. (2006). Sub Diffraction-Limit Imaging by Stochastic Optical Reconstruction Microscopy (Storm). *Nature Methods* **6**: 793-96.

## BIBLIOGRAPHY

Säälik, P., Elmquist, A., Hansen, M., Padari, K., Saar, K., Viht, K., Langel, Ü. and Pooga, M. (2004). Protein Cargo Delivery Properties of Cell-Penetrating Peptides. A Comparative Study. *Bioconjugate Chemistry* **15**.

Sansom, M. S. P. (1991). The Biophysics of Peptide Models of Ion Channels. *Progress in Biophysics and Molecular Biology* **55**: 139-235.

Schlessinger, J., Axelrod, D., Koppel, D. E., Webb, W. W. and Elson, E. L. (1977). Lateral Transport of a Lipid Probe and Labeled Proteins on a Cell Membrane. *Science* **195**: 307-8.

Schmalz, G. (1929). Über Glätte Und Ebenheit Als Physikalisches Und Physiologisches Problem. *Zeitschrift des Verbandes Deutscher Ingenieure* **73**: 144-61.

Schmitt, E. K., Nurnabi, M., Bushby, R. J. and Steinem, C. (2008). Electrically Insulating Pore-Suspending Membranes on Highly Ordered Porous Alumina Obtained from Vesicle Spreading. *Soft Matter* **4**: 250-3.

Schraml, S. (2003). Setup and Application of a Scanning Ion Conductance Microscope. Vienna, Vienna Univ. Technol.

Schutze-Redelmeider, M. P., Gournier, H., Garcia-Pons, F., Moussa, M., Joliot, A. H., Volovitch, M., Prochiantz, A. and Lemonnier, F. A. (1996). Introduction of Exogenous Antigens into the Mhc Class I Processing and Presentation Pathway by *Drosophila* Antennapedia Homeodomain Primes Cytotoxic T Cells in Vivo. *Journal of Immunology* **157**: 650-5.

Schwarz, G., Zong, R.-t. and Popescu, T. (1992). Kinetics of Melittin Induced Pore Formation in the Membrane of Lipid Vesicles. *Biochimica et Biophysica Acta (BBA) - Biomembranes* **1110**: 97-104.

Sessa, G., Freer, J. H., Colacicco, G. and Weissmann, G. (1969). Interaction of Alytic Polypeptide, Melittin, with Lipid Membrane Systems. *Journal of Biological Chemistry* **244**: 3575-82.

Shevchuk, A., Hobson, P., Lab, M., Klenerman, D., Krauzewicz, N. and Korchev, Y. (2008). Endocytic Pathways: Combined Scanning Ion Conductance and Surface Confocal Microscopy Study. *Pflugers Arch - Eur J Physiol* **456**: 227-35.

Shevchuk, A. I., Frolenkov, G. I., Sánchez, D., James, P. S., Freedman, N., Lab, M. J., Jones, R., Klenerman, D. and Korchev, Y. E. (2006). Imaging Proteins in Membranes of Living Cells by High-Resolution Scanning Ion Conductance Microscopy. *Angewandte Chemie International Edition* **45**: 2212-16.

Shevchuk, A. I., Gorelik, J., Harding, S. E., Lab, M. J., Klenerman, D. and Korchev, Y. E. (2001). Simultaneous Measurement of Ca<sup>2+</sup> and Cellular Dynamics: Combined Scanning Ion

Conductance and Optical Microscopy to Study Contracting Cardiac Myocytes. *Biophysical Journal* **81**: 1759-64.

Sheynis, T., Sykora, J., Benda, A., Kolusheva, S., Hof, M. and Jelinek, R. (2003). Bilayer Localization of Membrane-Active Peptides Studied in Biomimetic Vesicles by Visible and Fluorescence Spectroscopies. *European Journal of Biochemistry* **270**: 4478-87.

Sigurdson, W., Ruknudin, A. and Sachs, F. (1992). Calcium Imaging of Mechanically Induced Fluxes in Tissuecultured Chick Heart: Role of Stretch-Activated Ion Channels. *American Journal of Physiology: Heart and Circulatory Physiology* **262**: 1110-5.

Simons, K. and Ikonen, E. (1997). Functional Rafts in Cell Membranes. *Nature* **387**: 569-72.

Simons, K. and Sampaio, J. L. (2011). Membrane Organization and Lipid Rafts. *Cold Spring Harbor Perspectives in Biology* **3**.

Simons, K. and Toomre, D. (2000). Lipid Rafts and Signal Transduction. *Nature Reviews Molecular Cell Biology* **1**: 31-9.

Singer, C. (1914). Notes on the Early Story of Microscopy. *Proceedings of the Royal Society of Medicine* **7**: 247-79.

Singer, S. J. (1972). A Fluid Lipid-Globular Protein Mosaic Model of Membrane Structure. *Annals of the New York Academy of Sciences* **195**: 16-23.

Singer, S. J. and Nicolson, G. L. (1972). The Fluid Mosaic Model of Structure of Cell-Membranes. *Science* **175**: 720-31.

Sonnleitner, A., Schutz, G. J. and Schmidt, T. (1999). Free Brownian Motion of Individual Lipid Molecules in Biomembranes. *Biophysical Journal* **77**: 2638-42.

Soomets, U., Lindgren, M., Gallet, X., Hällbrink, M., Elmquist, A., Balaspiri, L., Zorko, M., Pooga, M., Brasseur, R. and Langel, Ü. (2000). Deletion Analogues of Transportan. *Biochimica et Biophysica Acta* **1467**: 165-76.

Spiegel, S., Kassis, S., Wilchek, M. and Fishman, P. H. (1984). Direct Visualization of Redistribution and Capping of Fluorescent Gangliosides on Lymphocytes. *Journal of Cell Biology* **99**: 1575-81.

Spinke, J., Yang, J., Wolf, H., Liley, M. and Knoll, W. (1992). Polymer-Supported Bilayer on a Solid Substrate. *Biophysical Journal* **63**: 1667-71.

## BIBLIOGRAPHY

Steinem, C., Galla, H.-J. and Janshoff, A. (2000). Interaction of Melittin with Solid Supported Membranes. *Physical Chemistry Chemical Physics* **2**: 4580-85.

Steinem, C., Janshoff, A., Ulrich, W. P., Sieber, M. and Galla, H. J. (1996). Impedance Analysis of Supported Lipid Bilayer Membranes: A Scrutiny of Different Preparation Techniques. *Biochimica Biophysica Acta* **1279**: 169-80.

Steltenkamp, S., Müller, M., Deserno, M., Hennesthal, C., Steinem, C. and Janshoff, A. (2006). Mechanical Properties of Pore-Spanning Lipid Bilayers Probed by Atomic Force Microscopy. *Biophysical Journal* **91**: 217-26.

Stokes, G. G. (1852). On the Change of Refrangibility of Light. *Philosophical Transactions of the Royal Society of London* **142**: 463-562.

Struck, D. K. and Pagano, R. E. (1980). Insertion of Fluorescent Phospholipids into the Plasma Membrane of a Mammalian Cell. *Journal of Biological Chemistry* **255**: 5405-10.

Takahashi, Y., Murakami, Y., Nagamine, K., Shiku, H., Aoyagi, S., Yasukawa, T., Kanzaki, M. and Matsue, T. (2010a). Topographic Imaging of Convolved Surface of Live Cells by Scanning Ion Conductance Microscopy in a Standing Approach Mode. *Physical Chemistry Chemical Physics* **12**: 10012-17.

Takahashi, Y., Shevchuk, A. I., Novak, P., Murakami, Y., Shiku, H., Korchev, Y. E. and Matsue, T. (2010b). Simultaneous Noncontact Topography and Electrochemical Imaging by Scm/Sicm Featuring Ion Current Feedback Regulation. *Journal of the American Chemical Society* **132**: 10118-26.

Talbot, J. C., Dufourcq, J., de Bony, J., Faucon, J. F. and Lussan, C. (1979). Conformational Change and Self Association of Monomeric Melittin. *FEBS Letters* **102**: 191-3.

Tanaka, M. and Sackmann, E. (2005). Polymer-Supported Membranes as Models of the Cell Surface. *Nature* **437**: 656-63.

Theodore, L., Derossi, D., Chassaing, G., Llibat, B., Kubes, M., Jordan, P., Chneiweiss, H., Godement, P. and Prochiantz, A. (1995). Intraneuronal Delivery of Protein Kinase C Pseudosubstrate Leads to Growth Cone Collapse. *Journal of Neuroscience* **15**: 7158-67.

Troy, C. M., Derossi, D., Prochiantz, A., Greene, L. A. and Shelanski, M. L. (1996). Downregulation of Cu/Zn Superoxide Dismutase Leads to Cell Death Via the Nitric Oxide - Peroxynitrite Pathway. *Journal of Neuroscience* **16**: 253-61.

Tseng, A. A. and Li, Z. (2007). Manipulations of Atoms and Molecules by Scanning Probe Microscopy. *Journal of Nanoscience and Nanotechnology* **7**: 2582-95.

Tünnemann, G., Martin, R. M., Haupt, S., Patsch, C., Edenhofer, F. and Cardoso, M. C. (2006). Cargo-Dependent Mode of Uptake and Bioavailability of Tat-Containing Proteins and Peptides in Living Cells. *FASEB Journal* **20**: 1775-84.

Ulman, A. (1996). Formation and Structure of Self-Assembled Monolayers. *Chemical Reviews* **96**: 1533-54.

Ulrich, A. S. (2002). Biophysical Aspects of Using Liposomes as Delivery Vehicles. *Biosci Rep* **22**: 129-50.

van den Bogaart, G., Guzmán, J. V., Mika, J. T. and Poolman, B. (2008). On the Mechanism of Pore Formation by Melittin. *Journal of Biological Chemistry* **283**: 33854-57.

Van Gelder, P., Dumas, F. and Winterhalter, M. (2000). Understanding the Function of Bacterial Outer Membrane Channels by Reconstitution into Black Lipid Membranes. *Biophysical Chemistry* **85**: 153-67.

Vivès, E., Brodin, P. and Lebleu, B. (1997). A Truncated Hiv-1 Tat Protein Basic Domain Rapidly Translocates through the Plasma Membrane and Accumulates in the Cell Nucleus. *Journal of Biological Chemistry* **272**: 16010-7.

Vogel, H. and Jähnig, F. (1986). The Structure of Melittin in Membranes. *Biophysical Journal* **50**: 573-82.

Wedler, G. (1997). Lehrbuch Der Physikalischen Chemie. Weinheim, Wiley-VCH.

Weiskopf, D., Schmitt, E. K., Kluhr, M. H., Dertinger, S. K. and Steinem, C. (2007). Micro-BIms on Highly Ordered Porous Silicon Substrates: Rupture Process and Lateral Mobility. *Langmuir* **23**: 9134-9.

Williams, L. M., Evans, S. D., Flynn, T. M., Marsh, A., Knowles, P. F., Bushby, R. J. and Boden, N. (1997). Kinetics of the Unrolling of Small Unilamellar Phospholipid Vesicles onto a Self-Assembled Monolayer. *Langmuir* **13**: 751-7.

Windschiegl, B., Orth, A., Römer, W., Berland, L., Stechmann, B., Bassereau, P., Johannes, L. and Steinem, C. (2009). Lipid Reorganization Induced by Shiga Toxin Clustering on Planar Membranes. *PLoS One* **4**: e6238.

Xia, H., Gao, X., Gu, G., Liu, Z., Hu, Q., Tu, Y., Song, Q., Yao, L., Pang, Z., Jiang, X., Chen, J. and Chen, H. (2012). Penetratin-Functionalized Peg-Pla Nanoparticles for Brain Drug Delivery. *International Journal of Pharmaceutics* **436**: 840-50.

Yang, L., Harroun, T. A., Weiss, T. A., Ding, L. and Huang, H. W. (2001). Barrel-Stave Model or Toroidal Model? A Case Study on Melittin Pores. *Biophysical Journal* **81**: 1475-85.

## BIBLIOGRAPHY

Yeagle, P. L. (1985). Cholesterol and the Cell Membrane. *Biochimica et Biophysica Acta* **822**: 267-87.

Young, R., Ward, J. and Scire, F. (1971). Observation of Metal-Vacuum-Metal Tunneling, Field Emission, and the Transition Region. *Physical Reviews Letters* **27**: 922-4.

Young, R., Ward, J. and Scire, F. (1972). The Topographiner: An Instrument for Measuring Surface Microtopography. *Review of Scientific Instruments* **43**: 999-1011.

Zhang, H., Wu, L. and Huang, F. (1999). Electrochemical Microprocess by Scanning Ion-Conductance Microscopy. *Journal of Vacuum Science & Technology B: Microelectronics and Nanometer Structures* **17**: 269-72.

Zhang, W. and Smith, S. O. (2005). Mechanism of Penetration of Antp(43-58) into Membrane Bilayers. *Biochemistry* **44**: 10110-8.

Zhang, Y., Gorelik, J., Sanchez, D., Shevchuk, A., Lab, M., Vodyanoy, I., Klenerman, D., Edwards, C. and Korchev, Y. (2005). Scanning Ion Conductance Microscopy Reveals How a Functional Renal Epithelial Monolayer Maintains Its Integrity. *Kidney Int* **68**: 1071-77.

Zhukov, A., Richards, O., Ostanin, V., Korchev, Y. and Klenerman, D. (2012). A Hybrid Scanning Mode for Fast Scanning Ion Conductance Microscopy (Sicm) Imaging. *Ultramicroscopy* **121**: 1-7.

Ziegler, A. (2008). Thermodynamic Studies and Binding Mechanisms of Cell-Penetrating Peptides with Lipids and Glycosaminoglycans. *Advanced Drug Delivery Reviews* **60**: 580-97.

Zorko, M. and Langel, Ü. (2005). Cell-Penetrating Peptides: Mechanism and Kinetics of Cargo Delivery. *Advanced Drug Delivery Reviews* **57**: 529-45.

# CURRICULUM VITAE

## CHRISTOPH SÄSEN

christoph.sassen@gmail.com

Citizenship: Germany

### EDUCATION

- PRESENT                    **Ph.D. Thesis, Georg-August Universität Göttingen (Germany)**
- MAY 2009                Title: *A scanning ion conductance microscopy assay to investigate interactions between cell penetrating peptides and pore-suspending membranes*
- Supervisor: Prof. Dr. Claudia Steinem
- MARCH 2010            **Admission to graduate program “Physics of Biological and Complex Systems “**
- within Göttingen Graduate School for Neurosciences, Biophysics, and Molecular Biosciences (GGNB)
- MARCH 2009            **Diploma Thesis, Georg-August-Universität Göttingen (Germany)**
- MARCH 2008            Title: *The role of metal ions in catalytic promiscuity*
- Supervisor: Prof. Dr. Ulf Diederichsen
- External at Cambridge University (UK)**
- Supervisor: Dr. Florian Hollfelder
- MARCH 2009            **Diploma Studies in Chemistry,**
- APRIL 2003              **Georg-August-Universität Göttingen (Germany)**
- JUNE 2007                **Chinese Language and Culture Studies,**
- SEPTEMBER 2006        **Anhui University (Hefei, PR China)**
- JUNE 2002                **Abitur (University Entrance Diploma)**
- Maximilian-Kolbe-Gymnasium Wegberg (Germany)**

# CURRICULUM VITAE

## SELECTED PRESENTATIONS

- NOVEMBER 2011      **Poster** „*Monitoring Membrane Permeability: A SICM Approach*”  
GGNB Science Day, Göttingen (Germany)
- AUGUST 2011      **Poster** „*Monitoring Membrane Permeability: A SICM Approach*”  
8<sup>th</sup> European Biophysics Congress (EBSA), Budapest (Hungary)
- MARCH 2011      **Talk** „*Monitoring Membrane Permeability: Development of a SICM Approach*”  
GGNB PBCS doctoral retreat, Goslar (Germany)
- FEBRUARY 2011    **Talk** “Monitoring Membrane Permeability: Development of a SICM Approach”  
SFB 803 Winter School, Eisenach (Germany)
- JUNE 2010      **Poster** „*New applications of pore-suspending membranes*”  
Annual Meeting of the German Biophysical Society,  
Bochum (Germany)

## SCHOLARSHIPS

- AUGUST 2011      **GGNB Travel Grant**  
for participation at 8<sup>th</sup> European Biophysics Congress
- AUGUST 2008      **DAAD (German Academic Exchange Service) Scholarship**
- MARCH 2008      for accomplishment of a diploma thesis







## ACKNOWLEDGMENTS - DANKSAGUNG

Prof. Dr. Claudia Steinem danke ich für die stete Unterstützung und Freiheit bei dieser Arbeit, für alles, was ich dabei gelernt habe und die interessanten Gespräche und Diskussion.

I wish to thank the members of my thesis committee, Prof. Dr. Ulf Diederichsen and Dr. Iwan Schaap, for being easily convinced to take these and referee positions and pleasant discussion atmosphere during meetings.

I am grateful to Dr. Ingo Mey and the ionscope people, especially Dr. Giovanna de Filippi, for all the help with regard to SICM questions, problems and desasters – there were quite some; and for sharing the beauty of this instrument.

Jutta Gerber-Nolte und Michaela Klingebiel danke ich für wertvolle Assistenz bei allerlei Laborpräparation, insbesondere für ihre Funktion als nie versiegende Substratequelle. Marianne Wagener möchte ich danken für Unterstützung in den unvermeidlichen Orga-Fragen und die Motivationshilfe.

Meinen Master- und Bachelorstudenten Carmen und Janek danke ich für die gemeinsam durchlebte Laborzeit und dafür, dass sie zum Gelingen dieser Arbeit beigetragen haben. Euch beiden für die Zukunft nur das Beste.

Für das gewissenhafte und höchst lehrreiche Korrekturlesen danke ich Dr. Gretel, Dr. Julia, Dr. Dany und Ole, der – wenn bisher auch ohne Dr. – diese Arbeit vielleicht besser kennt als ich.

Beiden Arbeitskreisen danke ich für die schöne Zeit. Ich bin dankbar für die gemeinsamen Erlebnisse, Pausen, das (Ver-)Teilen der Messzeiten und den Zusammenhalt während dieser Jahre; vor Allem Dany, Gretel, Julia und Sabine haben das Labor zu einem besseren Ort gemacht – dabei waren wir nur Kollegen.

Ich danke den Lehrern, die mich geprägt haben: Frau Dichans, die vor langer Zeit einen mutigen Vorschlag gemacht hat; Frau Heese, die uns früh ernst genommen hat; Herrn Schmidt, der uns gezeigt hat, wie spannend Chemie ist; Herrn Mätje, der mich noch mehr (heraus-)gefordert hat als gefördert; Frau Rab, die mir das leuchtendste Vorbild darstellt; Frau Wang, die die Tradition und die Moderne aus Ost und West verbunden hat und Herrn Wang, der immer mit vollem Eifer dabei war.

Muito obrigado to the VIP Göttingen Capoeiristas. You've been a light to me at the end of daily tunnels. Thanks for sharing this world full of energy and fun, especially to Batata, Beijaflor, Careca, Curinga, Dendê, Piao, Piranha and Tixitita who have become friends to me.

Auch der besten WG der Welt sei an dieser Stell gedankt. Ich habe mich immer zu Hause gefühlt, besonders natürlich in der Fußball-WG mit Elli, Andi und Mary.

Keinesfalls missen möchte ich die unvergleichliche Zeit, die ich in und um Göttingen mit Benni, Christian, Frieda, Gretel, Marta und Sascha und Sylvia verbracht habe. Ich kann mir nicht vorstellen, dass es irgendwie anders auch nur halb so gut gewesen sein könnte.

Fast zu guter Letzt möchte ich mich bei meiner Familie bedanken, ohne deren Rückhalt und nie in Frage stehende Unterstützung ich nicht so weit gekommen wäre, auch wenn ich es wohl meist leichter mit euch hatte als umgekehrt.

Zu wirklich guter Letzt: Danke Toni. Ohne Dich würde es diesen Moment, da ich diese Worte schreibe, nicht geben. Ich kann nicht sagen, wie viel Du mir bedeutest.







